ADVANCED PROCESSING AND ANALYSIS OF SOUTH WEST HUB 3D SEISMIC DATA

Final report

ANLEC R&D Project 7-0314-0231

Prepared by:

R. Pevzner[1], L. Langhi [3], J. Shragge[2], S. Ziramov[1], J. Strand[3], T. Potter[2], K. Tertyshnikov[1], A. Bona[1] and M. Urosevic[1]

CURTIN UNIVERSITY (1), UNIVERSITY OF WESTERN AUSTRALIA (2), CSIRO (3)

12/17/2015

CONTENTS

ACKNOWLEDGEMENTS

The authors wish to acknowledge financial assistance provided through Australian National Low Emissions Coal Research and Development (ANLEC R&D). ANLEC R&D is supported by Australian Coal Association Low Emissions Technology Limited and the Australian Government through the Clean Energy Initiative. We also would like to acknowledge the Western Australia's Department of Mines and Petroleum for managing and financial support of the SW Hub project. This work was supported by resources provided by The Pawsey Supercomputing Centre with funding from the Australian Government and the Government of Western Australia.

EXECUTIVE SUMMARY

The South West Hub (SW Hub) project, one of the first Australian commercial-scale CO_2 geosequestration efforts, is currently going through a detailed site characterisation. As a part of this process a 3D seismic survey has been acquired in Q1 2014 by Geokinetics over a 115 km^2 area in the vicinity of potential future injection sites. The main aim of the 3D seismic survey acquisition is to provide the data for high-quality imaging of geologic structures up to 5 km depths that will assist in the mapping and characterisation of geologic structures of direct importance to the SW Hub project. One of the key issues revealed after the initial processing carried out by a contractor was that patchy source/receiver distribution caused by the presence of a number of so-called 'NO GO' zones (subareas/ land parcels with no access to the seismic crews) in the area and complex geological structure of the subsurface affected quality of the image. This project was aiming to attempt to resolve these by applying a number of seismic data processing techniques available to National Geosequestration Laboratory (NGL) research team.

One of the principal approaches to mitigate the irregular geometry was utilisation of pre-stack Kirchhoff migration algorithm and pre-conditioning data in the offset planes. Operations performed in the offset planes involved zeroing all the extrapolated migration artefacts. In order to evaluate effect of lateral velocity variations and improve the imaging of steeply dipping interfaces, a range of pre-stack depth migration algorithms was deployed. Overall, the 3D Kirchhoff PSDM results showed a modest uplift in imaging of the steeply dipping interfaces over the fast-track pre-stack time-migration (PSTM) results while imaging with 3D RTM operators was less successful.

The post-stack diffraction imaging was used as a complimentary method for fault detection to conventional attribute-based detection of faults followed by steered post-stack migration of the data. The results clearly emphasize the discontinuities in the image compared to the standard post-stack migration and image certain faults even better than the pre-stack imaging.

In order to evaluate elastic properties at the upper part of the section and test the hypothesis of having faults propagating close to the surface in the vicinity of Harvey-4

well a multichannel analysis of surface waves was tested on the Nested seismic 3D survey data acquired in December 2014 (*ANLEC R&D Project 7-1213-0224)*.

In 2013 a first-order assessment of the CO_2 containment for the SW Hub suggested possible migration pathways across faults with potential for improving reservoir connectivity but also bypassing the primary and secondary seal (Langhi et al., 2013; *ANLEC R&D project 7-1111-0201 Integration of data from Harvey-1 well to support decision*). In this study we update this initial assessment of the CO_2 containment potential by integrating the newly acquired 3D seismic dataset and available data from Harvey-2 and Harvey-4 wells. We investigate the structural architecture of the SW Hub, potential for lateral and vertical circulation of CO_2, geomechanical controls on reactivation and sub-seismic fractures affecting structural permeability in the Wonnerup and Yalgorup Members.

In case of juxtaposition of the Wonnerup Member against another aquifer across a fault, the membrane (or capillary) seal is assessed using the Shale Gouge Ratio (SGR) predictive algorithm that is considered as a proxy of up-scaled fault-rock composition. Empirical calibration is used to derive a fault-seal failure envelope and to calculate a maximum fluid column height able to be trapped by a fault without leaking. The relationship between the modelled faults and the present-day stress field is investigated to analyse the effects of stress field changes on fault kinematic behaviour and to define which critically stressed fault segments are most likely to be forced into failure with pore-pressure build-up. Finally, elastic dislocation theory is used to predict the spatial distribution, orientation and mode of sub-seismic fractures in the Wonnerup and the Yalgorup Members and assess their relative likelihood of reactivation under the present-day stress field.

1. INTRODUCTION

The South West Hub (SW Hub) project, one of the first Australian commercial-scale CO_2 geosequestration efforts, is currently going through a detailed site characterisation. As a part of this process a 3D seismic survey has been acquired in 2013-2014 by Geokinetics (Australasia) Pty Ltd over a 115 km^2 area in the vicinity of potential future injection sites. The main aim of the 3D seismic survey acquisition is to provide the data for high-quality imaging of geologic structures up to 5 km depths that will assist in the mapping and characterisation of geologic structures of direct importance to the SW Hub project. One of the key issues revealed after the initial processing carried out by a contractor was that patchy source/receiver distribution caused by the presence of a number of so-called 'NO GO' zones (subareas/ land parcels with no access to the seismic crews) in the area and complex geological structure of the subsurface affected quality of the image. This project was aiming to attempt to resolve these by applying a number of seismic data processing techniques available to National Geosequestration Laboratory (NGL) research team. Some of the specific targets identified included the improved fault imaging and extended reservoir definition. Various data regularisation techniques and migration algorithms were deployed to address this.

At the first stage data was processed to DMO (Dip Moveout corrected) stack / migrated volume. DMO stacking was needed to deploy 3D diffraction imaging (Alonaizi et al., 2013) to improve fault characterisation and steered Kirchhoff imaging (Tertyshnikov et al., 2013) to improve the signal-to-noise ratio of the migrated image.

In order to improve velocity model and prepare for application of the data regularisation and depth imaging techniques, a pre-stack time Kirchhoff migration was used to produce a pre-stack time migrated (PSTM) volume. Despite not being a principal deliverable for this project, that volume was used by most of the groups working on SW Hub geological models.

3D pre-stack depth migration (PSDM) is commonly applied in exploration seismology to accurately position seismic energy reflected from the boundaries of subsurface geologic

strata within 3D image volumes. The previous two decades have seen the development of first 3D Kirchhoff, then 3D wave-equation migration (WEM), and more recently 3D reverse-time migration (RTM) migration techniques. This sequence represents a gradual improvement in the accuracy – and computational complexity – of wave-propagation physics that is fundamental to all seismic imaging techniques. The main reason to evaluate performance of PSDM in the area is structural complexity and presence of both steeply dipping interfaces (fault places) and some lateral velocity variation. We apply both Kirchhoff and RTM algorithms to the data and compare their performance. In order to apply RTM a significant 5D interpolation effort is required to regularise the input dataset.

In parallel to that a dedicated high-density 3D seismic survey was acquired in December 2014 by NGL around Harvey 4 well location (Urosevic et al., 2015; *ANLEC R&D Project 7-1213-0224*). Data from this survey was used to evaluate multichannel analysis of surface waves (MASW) as a tool for the near-surface characterisation applicable in the area.

In 2013 a first-order assessment of the CO_2 containment for the SW Hub suggested possible migration pathways across faults with potential for improving reservoir connectivity but also bypassing the primary and secondary seal (Langhi et al., 2013; *ANLEC R&D project 7-1111-0201 Integration of data from Harvey-1 well to support decision*). The assessment was based on a geological model built upon sparse 2D seismic data with locally high uncertainties specifically regarding the structural architecture.

This work continues this initial assessment of the CO_2 containment potential by integrating the newly acquired 3D seismic dataset and available data from Harvey-2 and Harvey-4 wells. We investigate the structural architecture of the SW Hub, potential for lateral and vertical circulation of CO_2, geomechanical controls on reactivation and sub-seismic fractures affecting structural permeability in the Wonnerup and Yalgorup Members.

In case of juxtaposition of the Wonnerup Member against another aquifer across a fault, the membrane (or capillary) seal (Jennings, 1987; Watts, 1987) is assessed using the Shale Gouge Ratio (SGR) predictive algorithm (Yielding et al., 1997; Freeman et al.,

1998) that is considered as a proxy of up-scaled fault-rock composition (Bretan et al., 2011). Empirical calibration is used to derive a fault-seal failure envelope and to calculate a maximum fluid column height able to be trapped by a fault without leaking (Yielding, 2002; Bretan et al., 2003). Ciftci et al. (2012) demonstrate that SGR calculated on faults intersecting, but not offsetting completely, a caprock can also be used to qualitatively assess along-fault hydrocarbon migration potential and caprock bypass.

The relationship between the modelled faults and the present-day stress field is investigated to analysis the effects of stress field changes on fault kinematic behaviour and to define which critically stressed fault segments are most likely to be forced into failure with pore-pressure build-up. Areas of fault reactivation are associated with an increase in structural permeability and therefore with the potential for along-fault flow (Ferril et al., 1999, Mildren et al, 2005, Bretan et al., 2011).

Elastic dislocation theory (Okada, 1985; 1992; Dee et al., 2007) is used to predict the spatial distribution, orientation and mode of sub-seismic fractures in the Wonnerup and the Yalgorup Members and assess their relative likelihood of reactivation under the present-day stress field.

2. SEISMIC DATA ANALYSIS AND IMAGING

2.1. Seismic data available for analysis

To improve the subsurface characterisation of proposed South West Hub area the Department of Mines and Petroleum Western Australia acquired a large 3D seismic reflection survey in December 2013 – April 2014. The survey is officially known as DMPWA 2013 Harvey-Waroona 3D seismic survey; for simplicity in this report we refer to it as Harvey 3D seismic survey.

The seismic survey was carried out by Geokinetics (Australasia) Pty Ltd in the Shires of Harvey and Waroona, approximately 140 km South of Perth. It covered a total land area of 114.81 km^2 (Geokinetics, 2014). Table 1 provides the principal data acquisition parameters of the survey.

As the survey area comprises of the land parcels owned/operated by the multiple individual landowners, there was a significant period spent prior to commencement to the actual seismic data acquisition scouting out and identifying the so called ‘GO’ and ‘NO GO’ zones. This resulted in a survey of both long total duration and patchy acquisition coverage and fold (see Figure 2).

Table 1: DMPWA 2013 Harvey-Waroona 3D seismic survey parameters

Geometry	
Number of receiver lines	73
Receiver line interval	200 m
Receiver spacing	50 m
Number of source lines	41
Source line interval	200 m
Source interval	50 m
Recording patch	Rectangular template 22 Receiver Lines @159 channels each In-line max offset 7,925 metres Cross-line max offset 2,175 metres In-line: static spread, Cross-line: Roll on Roll off
Number of live channels	3498
Near offset	25 m
Far offset	8218 m
Binning / Nominal fold	25 x 25 m / 440
Source / receiver parameters	
Source	Vibroseis Input / Output Inc. AHV-IV (60,000 lb.) @ 80% 2 units per fleet
Sweep parameters	12 s 5-100 Hz linear upsweep with 350 ms tapers; 2 sweeps per VP
Listen time	5 s
Receivers	SM-24 10 Hz geophones Linear group, 6 elements with 1 m spacing

In order to improve characterisation of the upper part of the section, a dedicated small (2.12 km^2) 3D seismic survey was acquired in December 2014 by NGL/Curtin crew (Urosevic et al., 2015) around Harvey 4 well location. In this report we refer to it as Nested Harvey 3D seismic survey. Table 2 summarises the acquisition parameters for this survey, while Figure 1 shows the relative location of the surveys and the existing Harvey data wells.

In this study we use large Harvey 3D seismic survey for all data analysis, except for a feasibility study of application of multichannel analysis of surface waves (MASW) for near-surface characterisation, which uses the Nested 3D dataset.

Table 2: Nested Harvey 3D seismic survey

Geometry	
Number of receiver lines	21
Receiver line interval	90 m
Receiver spacing	15 m
Number of source lines	16
Source line interval	90 m
Source interval	15 m
Recording patch	Fixed receiver spread
Number of live channels	2331 (582 vertical geophones + 583 3C geophones)
Near offset	8 m
Far offset	2340 m
Binning / fold	7.5 x 7.5 / up to ~150
Source / receiver parameters	
Source	Vibroseis Inova UNIVIB (26,000 lb.) @ 70% 1 units per fleet
Sweep parameters	24 s 6-150 Hz linear upsweep with 500 ms tapers; 1 sweeps per VP
Listen time	4 s
Receivers	10 Hz 1C (vertical) and 3C geophones Single geophone per station

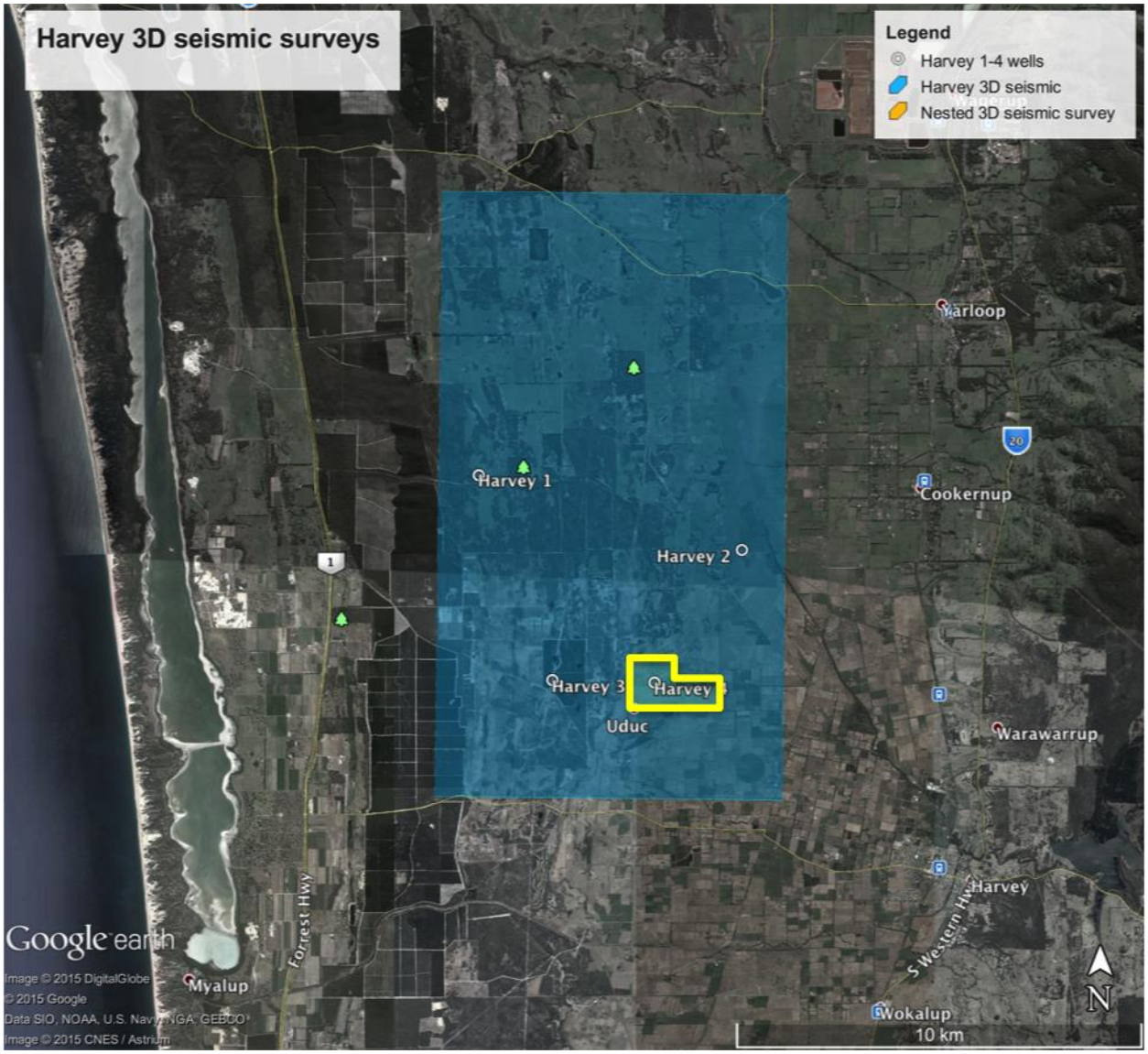

Figure 1. Harvey 3D seismic surveys location scheme

2.2. Shot domain processing

The pre-processing flow chart is shown in the Table 3.

Table 3: Harvey 3D seismic survey pre-processing flow chart.

Procedure	Parameters
Data conversion	**SEG-D data Input and conversion to ProMAX internal format**
Geometry assignment	**Applied from SPS files**
Binning	**Bin size 25m x 25m**
Vertical stacking	**Stacking of two sweeps per position**
Trace Editing	**Kill bad traces**
Air Blast Attenuation	**Attenuation mode for air velocity at 331 m/s**
Elevation Statics	**Final datum elevation – 40 m, Replacement Velocity – 2500 m/s**
Residual Static	**Application of residual statics**
Deconvolution	**Minimum phase predictive Decon Operator length – 120ms Operator predictive distance 8ms Operator 'white noise' level – 0.1%**
Band-pass Filtering	**4-10-150-250 (Hz)**
Surface wave noise attenuation	**Velocity 1200m/s, frequencies 4-40Hz**
Automatic Gain Control	**500ms**

Geometry

All data were loaded into the processing system and reformatted to an internal ProMax format. Geometry information was extracted from the SPS files (Figure 2). The chosen bin size was 25m x 25m, resulting in maximum fold coverage of 550 (Figure 3)

***Figure 2. Harvey 3D seismic* survey layout for Source (white) and receiver (black) locations where X and Y coordinates are Easting and Northing, respectively. Distances are in metres.**

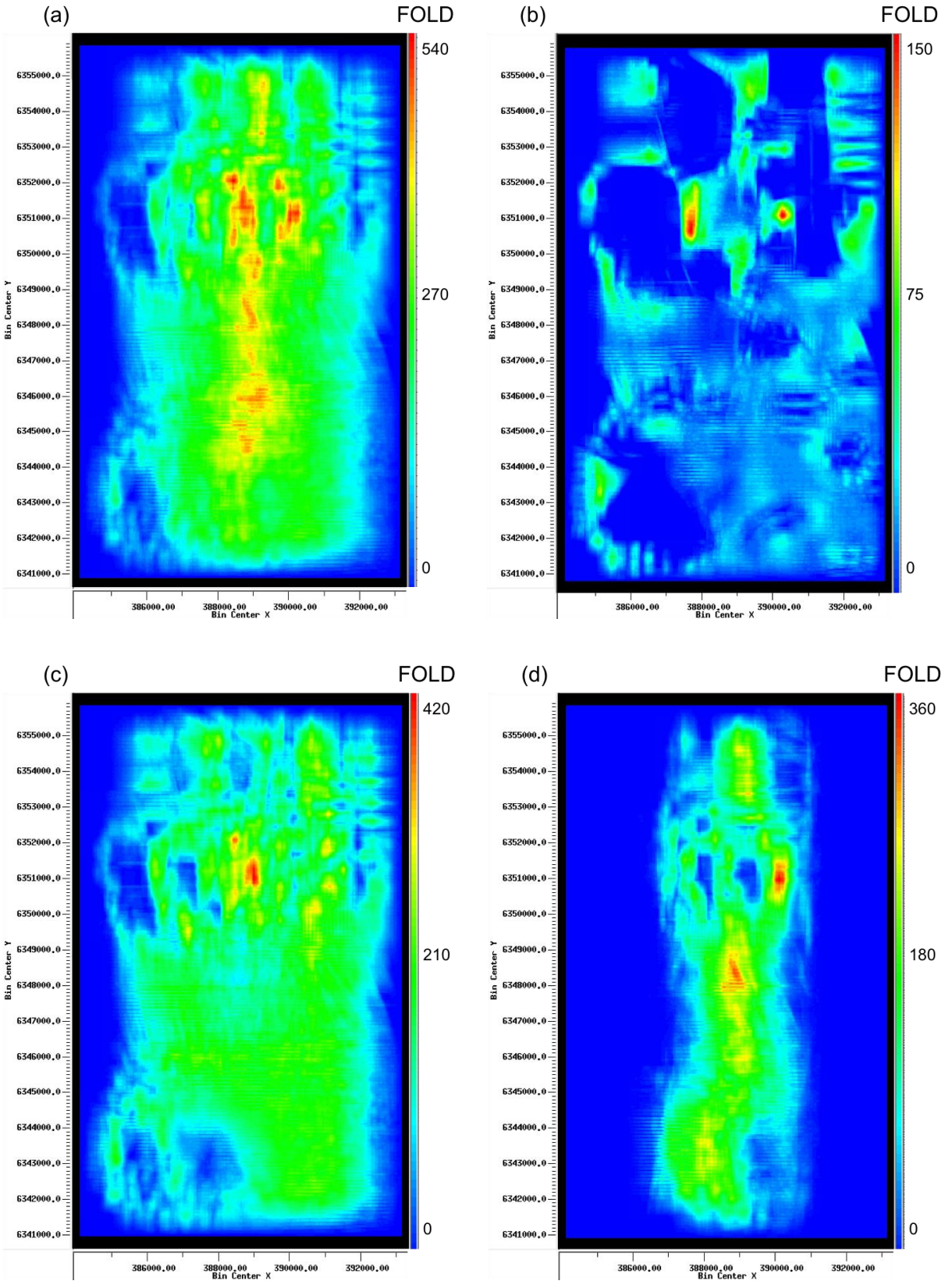

Figure 3. Harvey 3D seismic CMP fold coverage for bin size of 25m x 25m. Full offset range (a), near offset range 0-2Km (b), middle offset range 2-6km (c) and far offset range 6-9km (d).

Trace Editing

Killing bad traces was conducted automatically, based on a RMS amplitude variation at late times. Gain compensation for loss in offset direction was applied prior to the selection of the threshold and the application of automatic trace editing.

Statics

The topography is mostly flat over the survey area. Variation in elevation is a maximum of 32 m with values varying from 10 to 42 m, resulting in the following parameters.

Final datum elevation – 40 m, Replacement Velocity – 2500 m/s.

Replacement velocity is estimated from refraction velocity measured from near offsets (500m-2km). The maximum time shift is about 11 ms (see Figure 4).

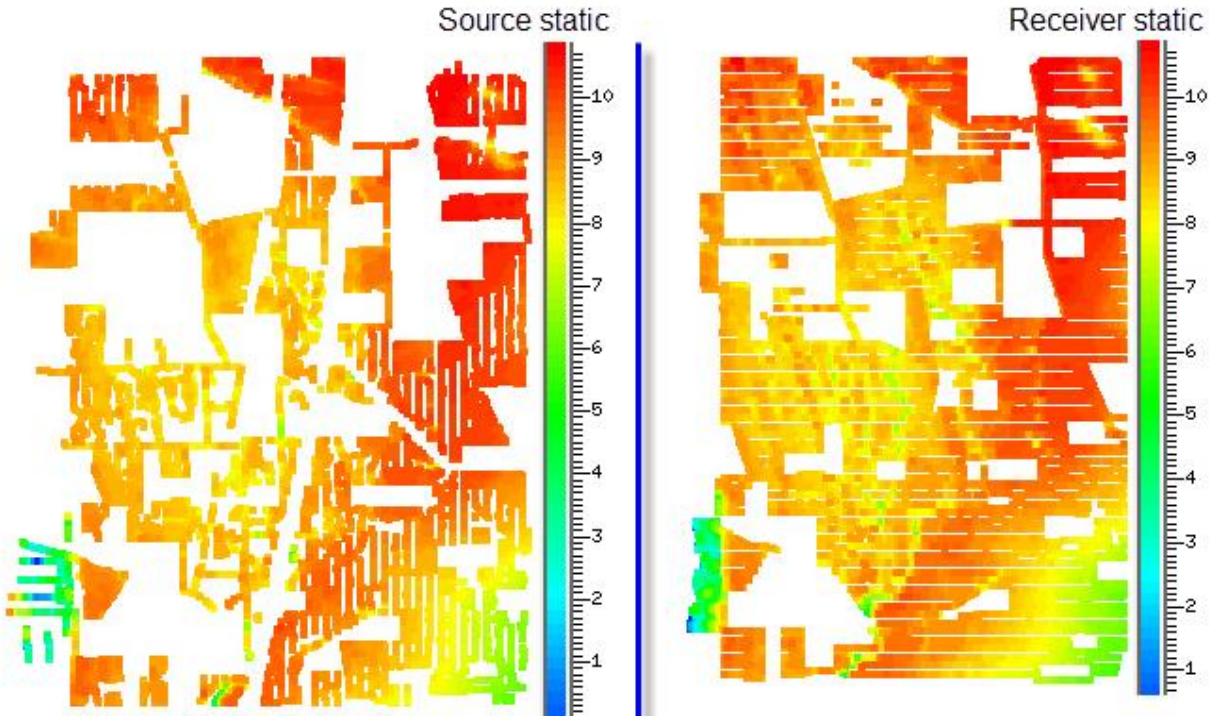

***Figure 4. Applied Harvey 3D seismic* elevation statics shown in *ms*.**

Following the elevation statics, residual static corrections were applied. Due to irregular offset distribution, refraction and high-resolution LMO (Linear move out) statics did not result in stable solution.

Air Blast Attenuation and Noise Reduction

Air blast attenuation, based on filtering in frequency-wavenumber (FK) domain was applied in attenuation mode for an air-wave velocity of 331 m/s. Time-Frequency Domain (TDF) noise rejection applied to the data isolated noise by replacing it with the median spectral amplitudes calculated from 21 adjacent traces. This operation was done in time-frequency domain using Short Time Fourier Transform algorithm. The frequency range was set to 0-125 Hz.

Predictive Deconvolution

In order to improve the shape of the wavelet and increase temporal resolution a deconvolution was applied. After testing different algorithms the following parameters were chosen:

Type – predictive, least squares, minimum phase.

The deconvolution operator length was chosen based on examining autocorrelation functions and seismograms post-deconvolution with different operator lengths. The operator length of 120 ms and operator predictive distance of 8 ms was chosen.

Bandpass Filter

At this stage of processing, an Ormsby bandpass filter was applied with the following parameters – 4-10-150-250 Hz. This filter effectively removed low frequency deconvolution artefacts. However, it does not affect high frequencies at this stage, which have been left untouched at this stage.

Surface wave noise attenuation

A frequency-wavenumber (F-K) based, surface wave noise attenuation was applied for coherent noise attenuation. The main goal was to remove ground roll from the shot records, with otherwise minimum effect on the signal. Shots were separated for each receiver line and traces were sorted from maximum negative offsets to maximum positive offset.

Automatic gain control (AGC) with small window size (150ms) was applied before all filtering steps for the purpose of trace normalisation and then removed from the data.

This way FK filtering keeps relative amplitudes of the signal preserved, and filtering artefacts are reduced. Input to pre-processing sequence is shown in the Figure 5, the output of pre-processing is illustrated in Figure 6. Figures 5 and 6 are showing success in attenuating source generated noise and improved resolution; however it is hard to see obvious reflection hyperbolas at this stage.

Automatic Gain Control (AGC)

As a final step in pre-processing AGC was applied using 500ms window length for scalar computation. AGC was used to both normalise noise/weak traces and as an overall gain recovery.

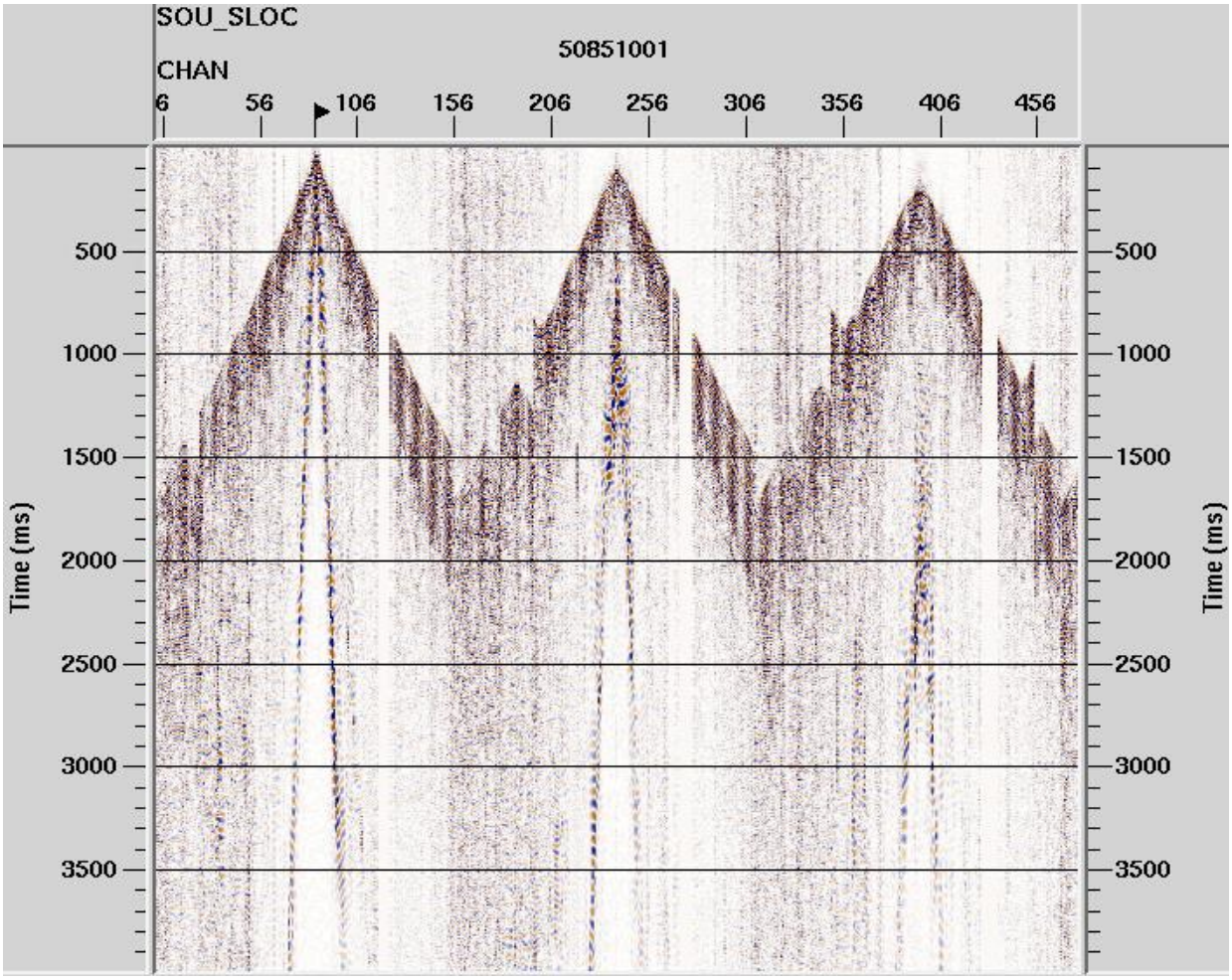

Figure 5. **Raw shot gather, for three receiver lines.**

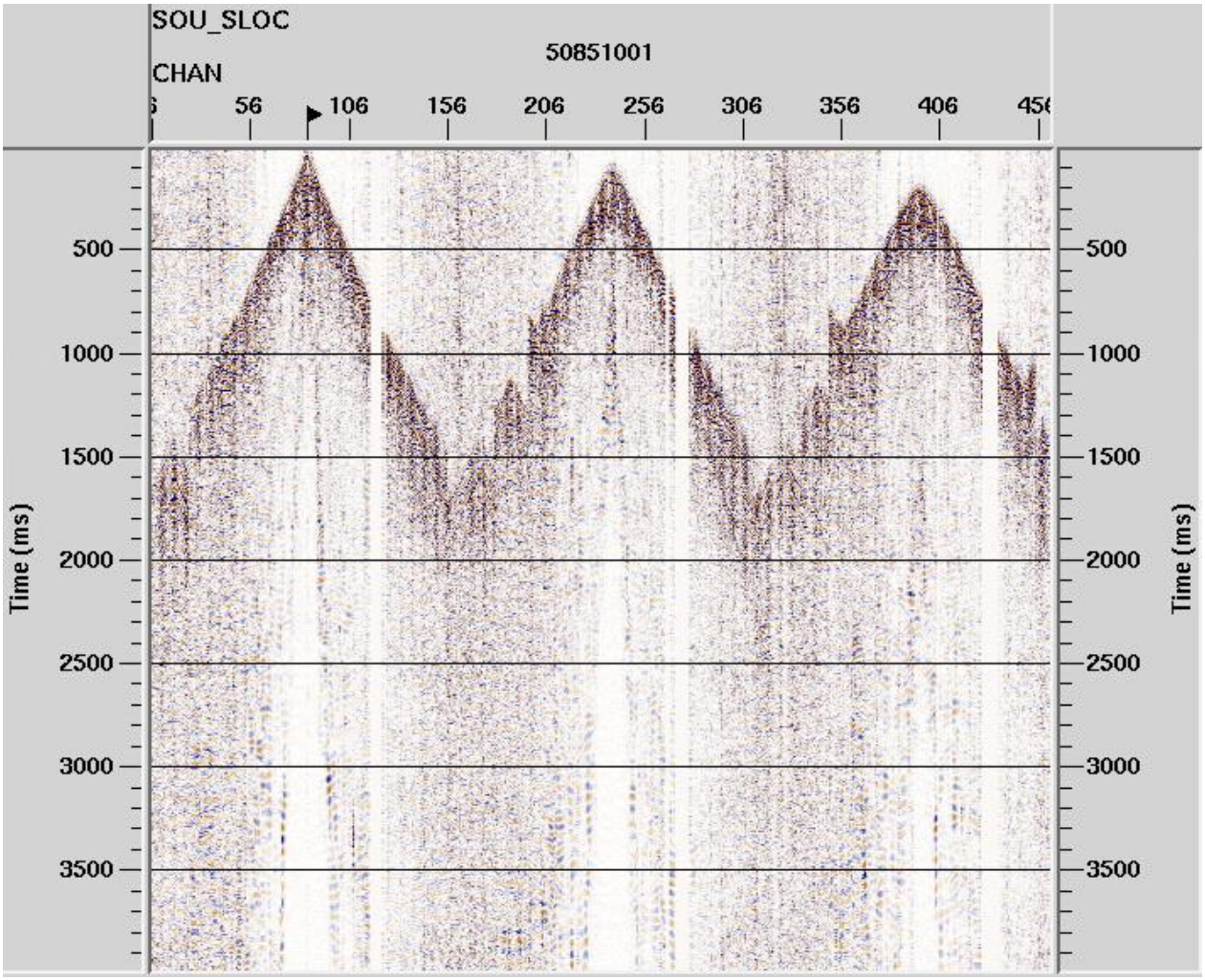

Figure 6. **Pre-processed shot gather, for three receiver lines.**

2.3. Velocity analysis

In order to improve the continuity of reflections, special pre-processing was applied to the data for enhanced velocity analysis and statics correction calculations. Temporary bandpass filter (8-14-40-60 Hz) was applied to common middle point (CMP) gathers to reduce low and high frequency noise and strengthen reflections for velocity estimation.

Only for velocity analysis purposes, 3D super-gathers were formed from the data.

A total of three velocity analyses were carried out.

1. The first velocity field was obtained from Harvey 2D test seismic survey, acquired in 2013 along the Riverdale Rd (ANLEC R&D Project 7-1213-0223). Due to better offset distribution in 2D profile, these velocities proved better for velocity analysis than any of the pre-processed 3D dataset at this stage. 2D velocity field was used for computation of residual statics.
2. The second velocity field was analysed after dip move-out correction (DMO) on 3D seismic data. This field was used for post DMO stacking, post-stack migration and as initial velocity field for PSTM.
3. As a separated imaging technique, pre-stack time imaging was conducted on pre-process dataset in offset domain. The final velocity field was computed for image gathers and used for second run of PSTM. Figures 7-12 shows velocity field at different stages, preliminary NMO velocity field v1, DMO velocity field v2 and PSTM velocity filed v3. Velocity field at the bottom part of the section is significantly different for the three iterations which can be explained by complexity of the structure and difficulties in doing the velocity analysis.

2.4. Dip-moveout correction

Dip-moveout (DMO) correction is a dip-dependent partial migration, applied so that non-zero-offset seismic data exhibit the same zero-offset reflection times and reflection points for all offsets. This transformation from non-zero-offset to zero-offset yields improved (less dip-dependent) velocity estimates and higher lateral resolution, as well as producing a few other desirable characteristics, such as the attenuation of coherent noise. To compensate for variations in coverage, this processing step tries to maintain time-dependent fold information and scale each output trace accordingly. This is done by offset regularisation with offset bin size of 80m x 80m. Areas with large offset gaps couldn't have good interpolation, and the gaps introduced so-called "V" shape in stacked volumes. This could only be populated during imaging, by migrating data inside of "V" shapes; however, this would not be reliable for interpretation and thus we recommend its omission. Gathers in the CMP, DMO and PSTM domain with semblance values and velocity estimate are presented in Figure 7-through Figure 9.

An alternative to performing a DMO correction is undertaking a common reflection surface stack (CRS) analysis. CRS processing provides tools to bring structural information into time processing. During this process, the coherence of wavefield dip is

used to mix data across bins to create stacks or regularized CMP gathers with improved signal-to-noise levels. We tested The CRS method on this dataset; however, it yielded poor results attributed the artefacts created by large offset gaps that overpowered observed reflectivity.

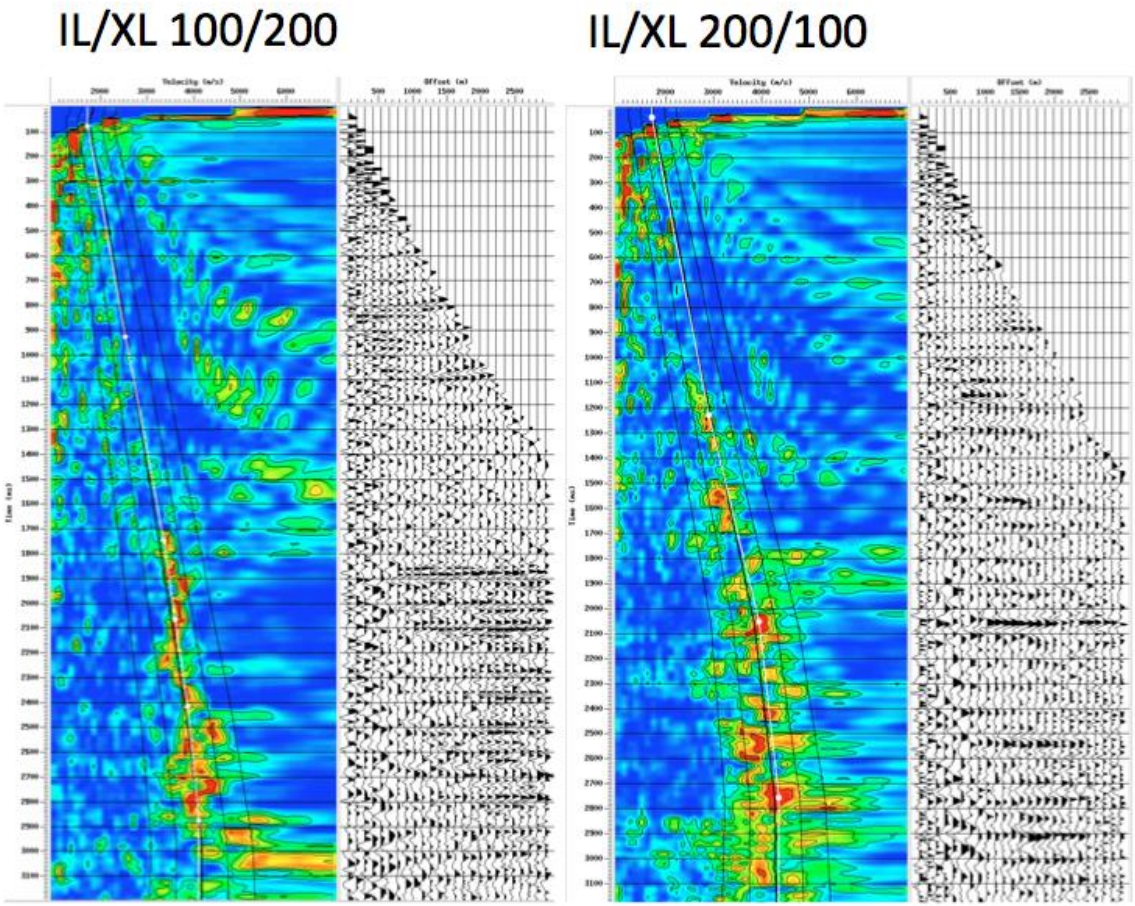

Figure 7. **Velocity field for the first velocity interactive velocity analysis procedure.**

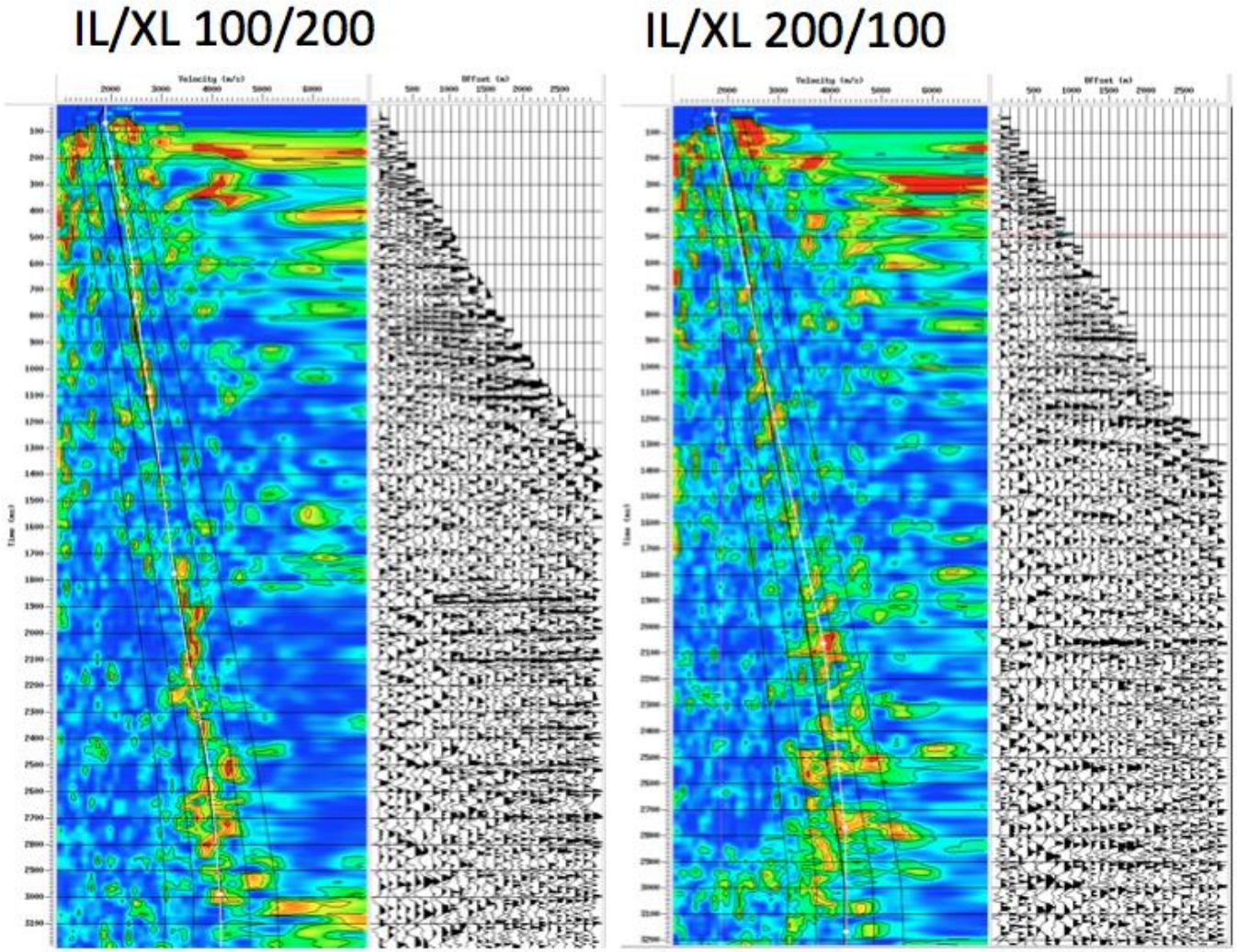

Figure 8. **Velocity field for the second velocity interactive velocity analysis procedure (after application of DMO).**

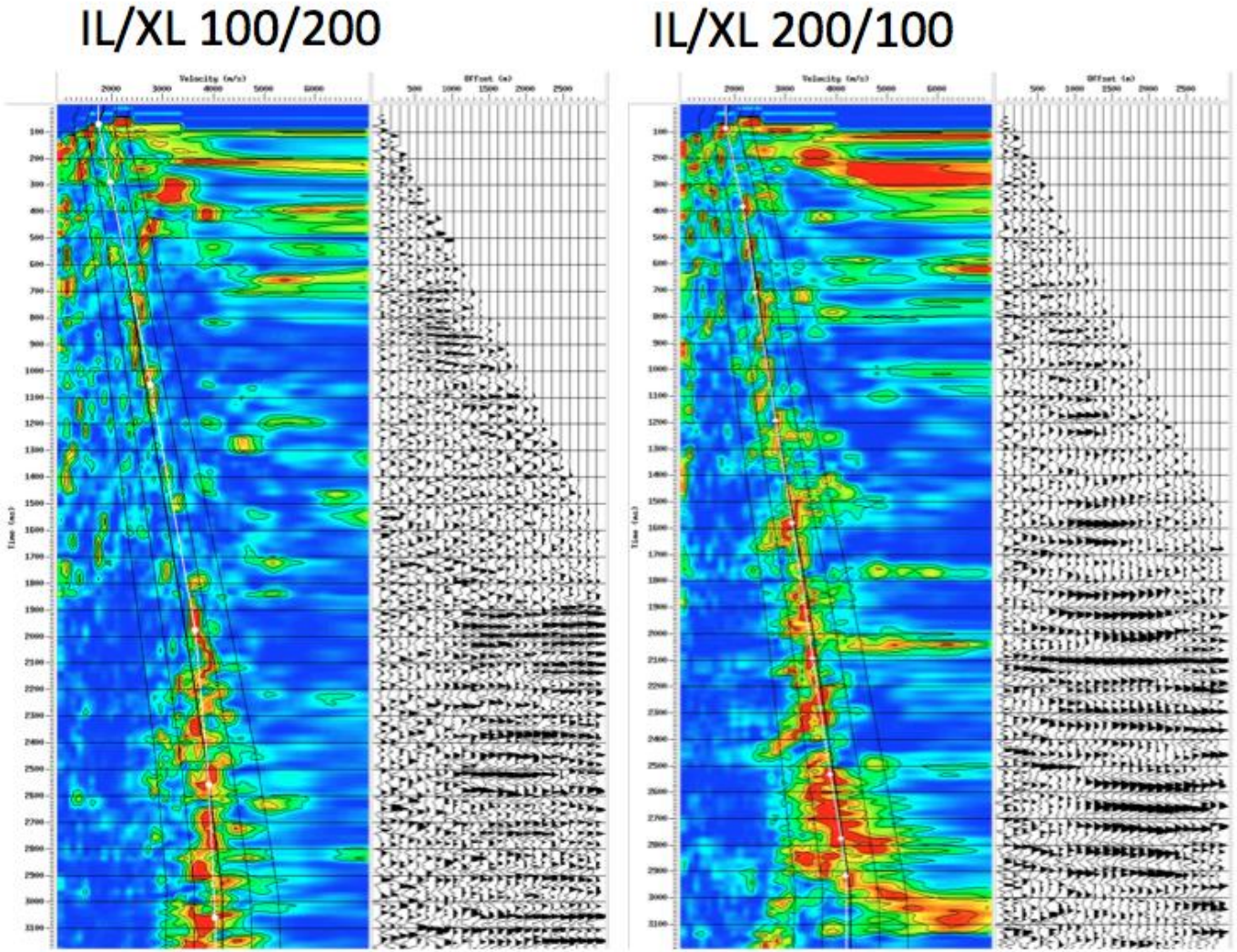

Figure 9. **Velocity field for the third velocity interactive velocity analysis procedure (after application of PSTM).**

A section showing velocity fields used for CMP, DMO and PSTM stacking are given in Figure 10-Figure 12.

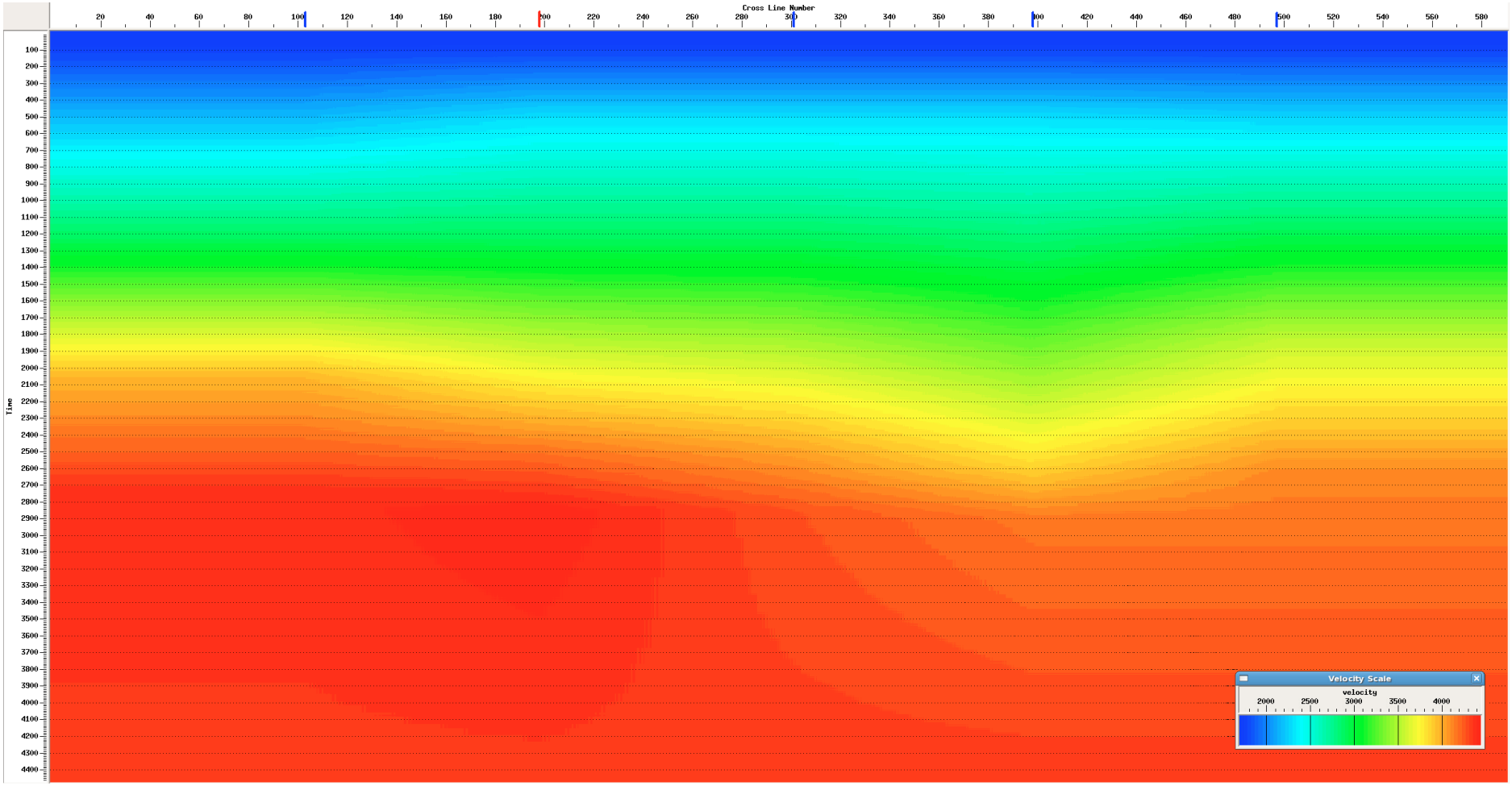

Figure 10. **NMO velocity field of IL 200, velocity field I.**

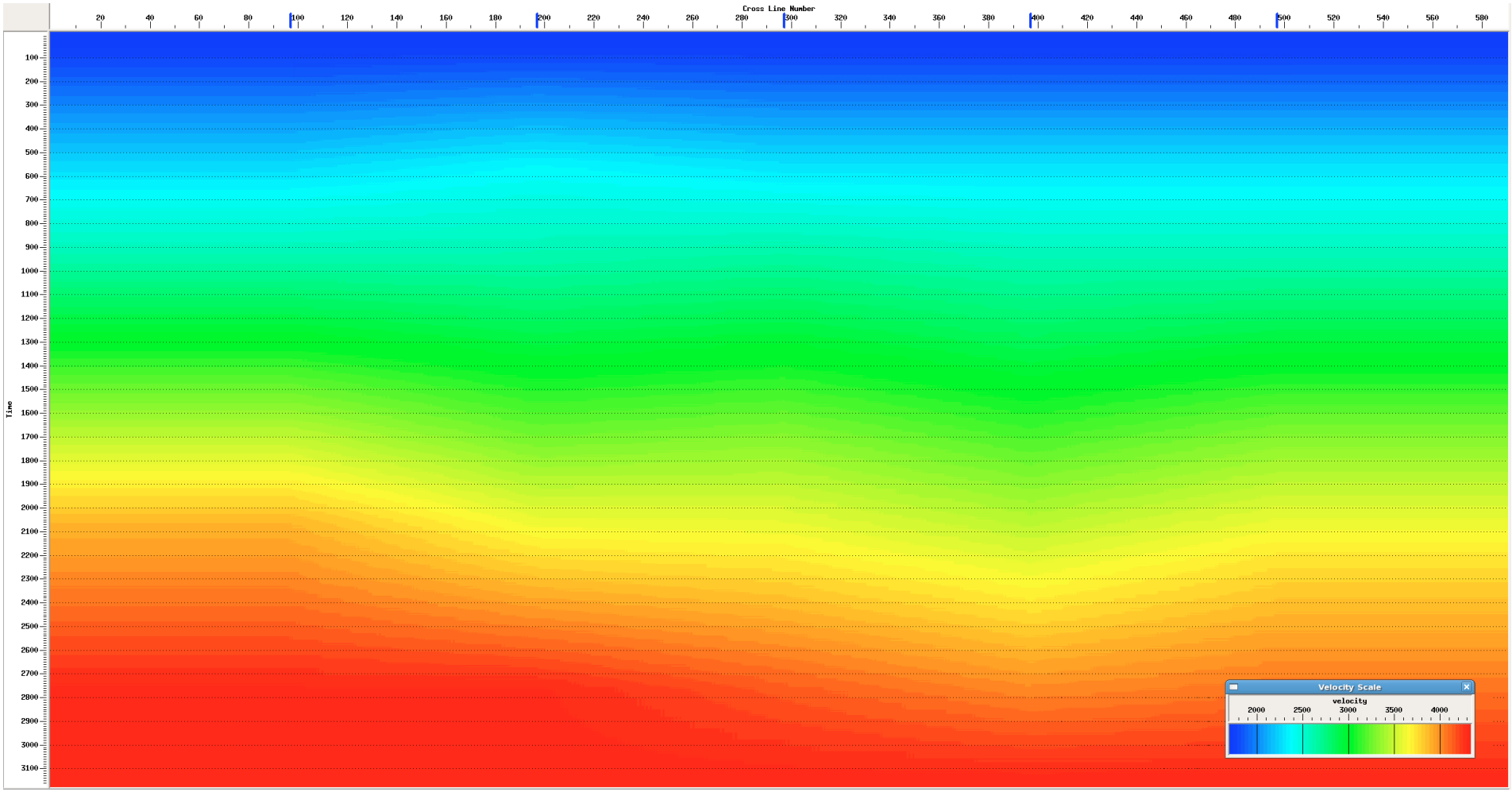

Figure 11. **DMO velocity field of IL 200, velocity field II.**

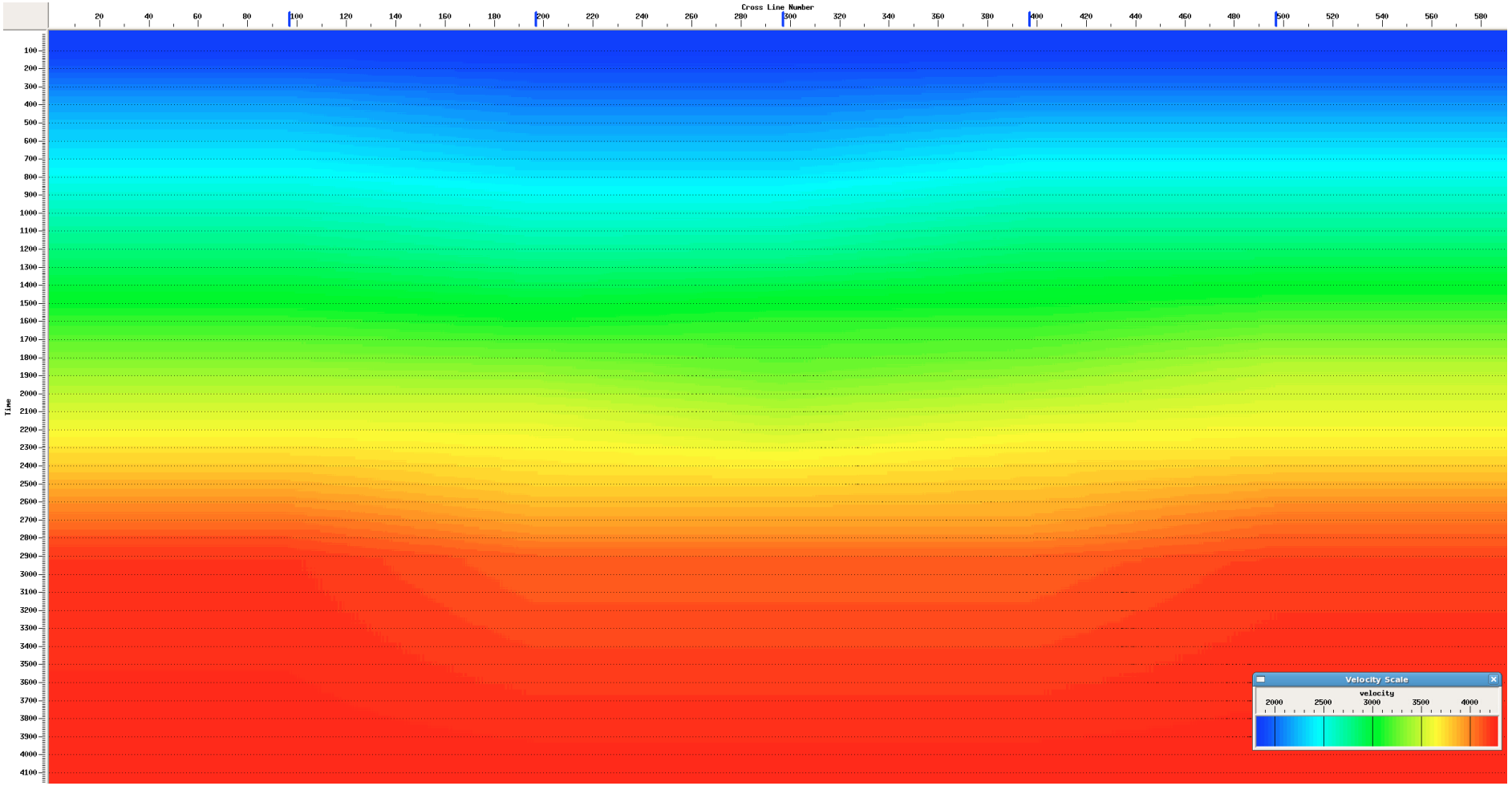

Figure 12. **PSTM velocity field of IL 200, velocity field III.**

2.5. Time-domain imaging techniques

2.5.1. Post stack migration

Two migration algorithms were used for imaging Harvey 3D dataset. First, the fast-track migrated 3D volume was imaged using post-stack phase-shift migration algorithm. At this stage, processing and imaging was accelerated to meet deadlines. Although this phase of work was restricted to the post stack migration algorithm, never the less the resultant product achieved good resolution of the complex structural setting. The flow chart for post-stack migration is shown in Table 4.

Table 4. Post-stack migration flow chart.

Procedure	Parameters
Data input	**Pre-processed dataset**
NMO Iteration I	**Velocity field I (from 2D survey)**
DMO to Gathers 3D Iteration I	**Offset binning: 30/80/8550**
Velocity analysis	**Compute velocity field II**
NMO Iteration II	**Velocity field II**
DMO to Gathers 3D Iteration II	**Offset binning: 30/80/8550**
60% stretch mute	**Post-NMO top mute**
Band-pass filter	**1-20-80-120 (HZ)**
3D stack	**Normalisation scalar 0.5**
FXY deconvolution	**Window 200/800ms**
Post-stack migration	**Velocity field II converted to interval velocities**
Depth conversion	**Velocity field II converted to average velocity**
SEGY output	**Standard SEG Rev1**

2.5.2. Pre-stack time migration

Initially, the velocity field used for pre-stack migration was obtained from CMP gathers after DMO correction had been applied. However, it became apparent that a conventional DMO correction followed by post-stack migration was insufficient to handle the lateral changes in velocity field around major faults. Therefore, we applied pre-stack Kirchhoff time migration, based on the Kirchhoff integral formula, to help handle velocity field complexity. The goal of pre-stack time migration (PSTM) is to derive a velocity model appropriate for the geologic setting and migration algorithm in use. The measure of the success of the model building and migration process is the ability to satisfy the needs of the algorithm, to place events at the proper position, to properly focus the energy, to avoid introduction of a false structure, and to flatten the image gathers.

The PSTM work consisted of three stages:

1. Initial velocity preparation and 1st pass of pre-stack time migration;
2. Residual velocity model modification; and
3. Final PSTM analysis.

Step 1 involved the building of the initial stacking velocity model followed by a first iteration of PSTM. The initial model was built through the use of the RMS velocity model from DMO corrected gathers. The imaging was done on pre-processed offset gathers, without applying a DMO correction. Typically, many reflection events in the image gathers produced by the first pass of migration are inaccurately imaged. This suggests the presence of errors in the initial velocity model, which required futher updates to better image the data.

Step 2 involved several iterations of residual velocity analysis on image gathers. The residual velocity error or residual move out error is determined by analysis of the gathers. This analysis proposes changes to the original velocity model that will more accurately image the gathers. After updating the velocity model it is then used in the PSTM work to produce revised and, ideally improved, image gathers.

Upon achieving a satisfactory imaging of the gathers, one performs Step 3; the final PSTM of the full project using the final velocity model. After the final migration, several post-migration processes were applied to the data, such as elimination of extrapolated migration smiles, filtering and time-to-depth scaling. Table 5 presents the PSTM processing flow.

.

Table 5: Pre-stack Migration Flow Chart.

Procedure	Parameters
Data input	**Pre-processed dataset**
Data datuming	**Moving seismic and velocities to final datum**
PSTM Iteration I	**Offset binning: 30/120/8550, Velocity field II**
Velocity analysis	**Compute velocity field III**
PSTM Iteration II	**Offset binning: 30/120/8550, Velocity field III**
60% stretch mute	**Post-NMO top mute**
3D stack	**Normalization scalar 0.5**
FXY deconvolution	**Window 200/800ms**
SEGY output	**Standard SEG Rev1**

2.5.3. Time-domain imaging results

The comparison of two migration algorithms is illustrated in Figure 13 through -Figure 28. The total of four inline (ILINE) stacks in receiver direction and four crossline (XLINE)

stacks in source line direction are displayed (top 5 seconds). Post-stack imaging applied on a DMO stack was a fast-track, preliminary phase shift migration that was much improved when the pre-stack time imaging was computed. The vertical resolution of post-stack migrated and PSTM volume is different. Post-stack migrated volume includes DMO correction and phase-shift migration algorithm, while PSTM is based on a Kirchhoff integral solution. During process of DMO some of the low frequencies have been suppressed, while in PSTM they remain present. This is one of the reasons why PSTM has higher S/N ratio when compared to post-stack migration.

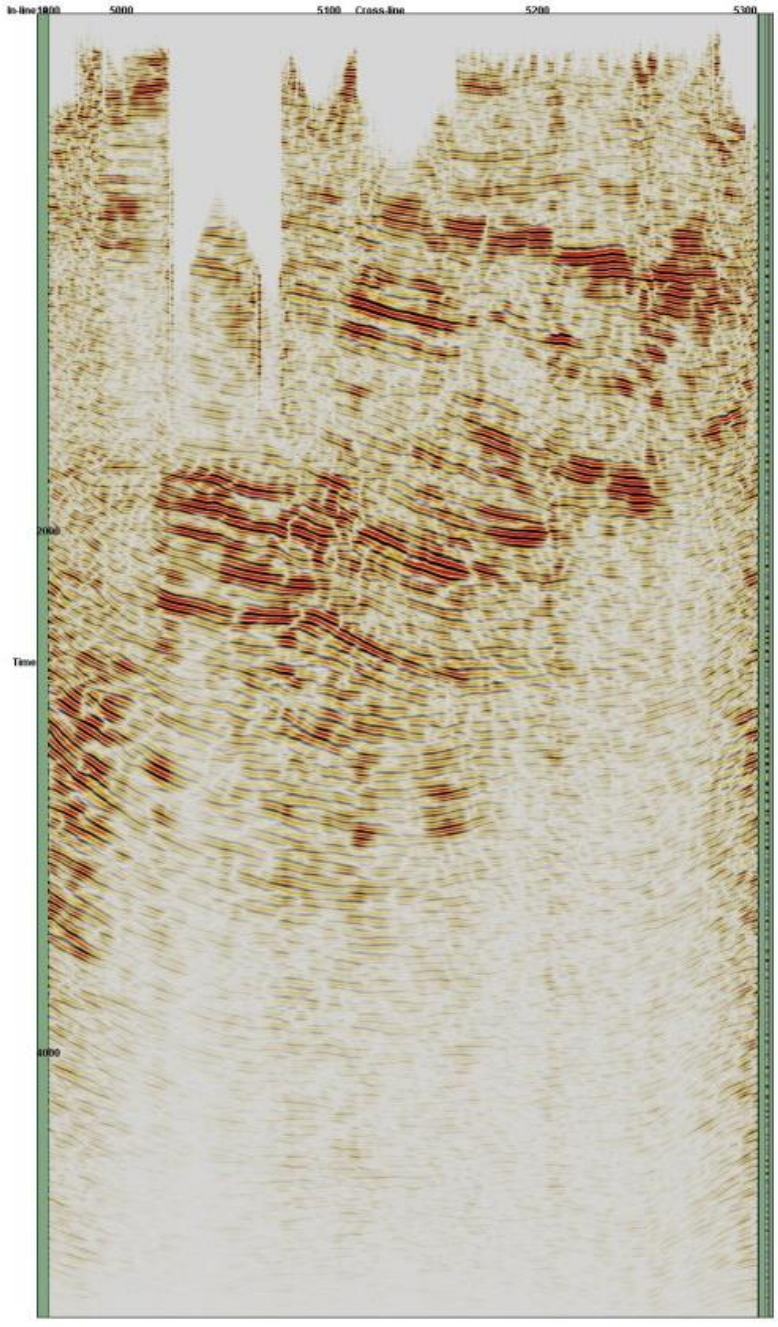

Figure 13. **Phase shift post-stack migration, ILINE1100.**

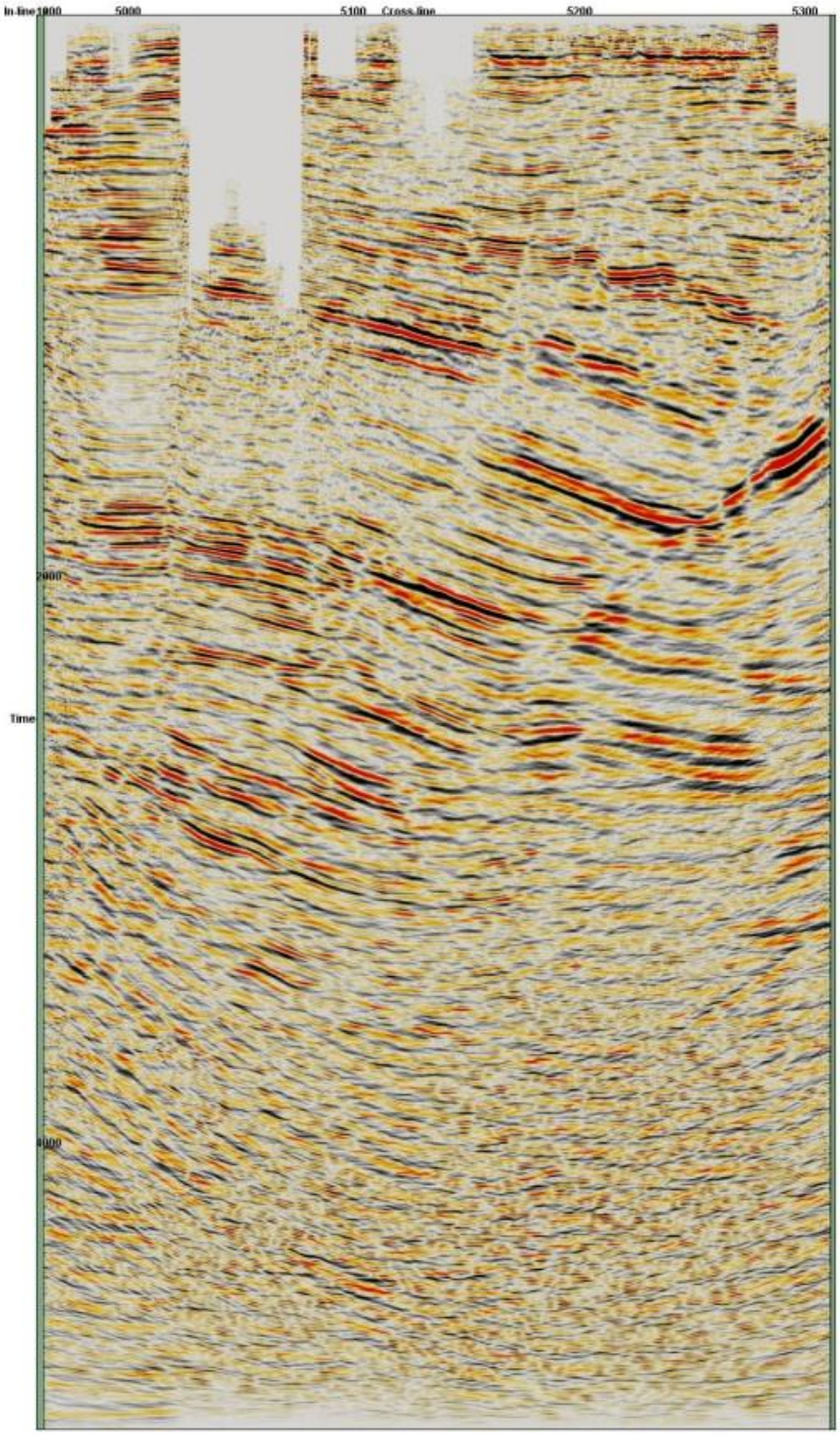

***Figure 14. Kirchhoff* pre-stack time migration, ILINE1100.**

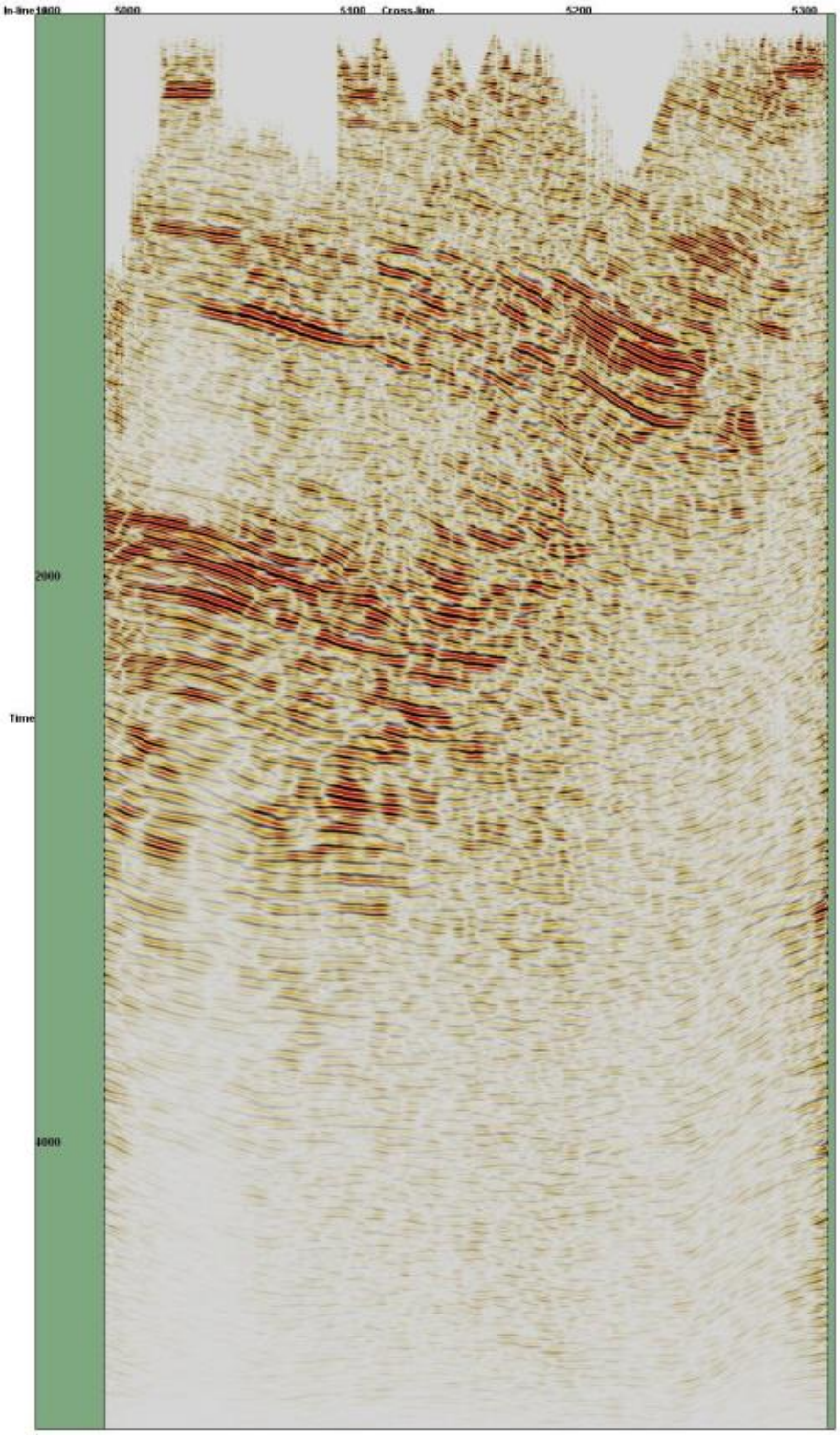

Figure 15. **Phase shift post-stack migration, ILINE1200.**

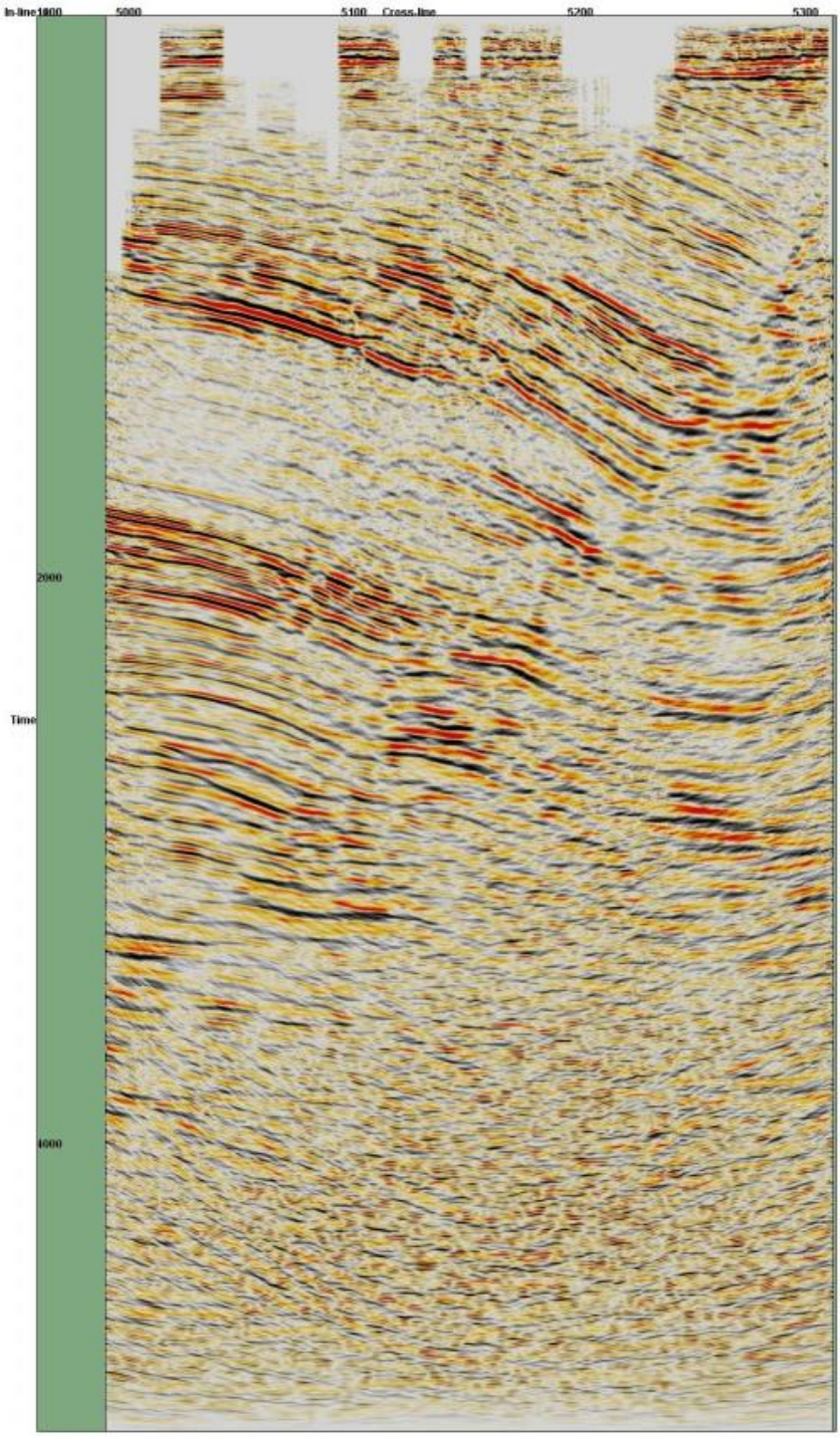

Figure 16. **Pre-stack time migration, ILINE1200.**

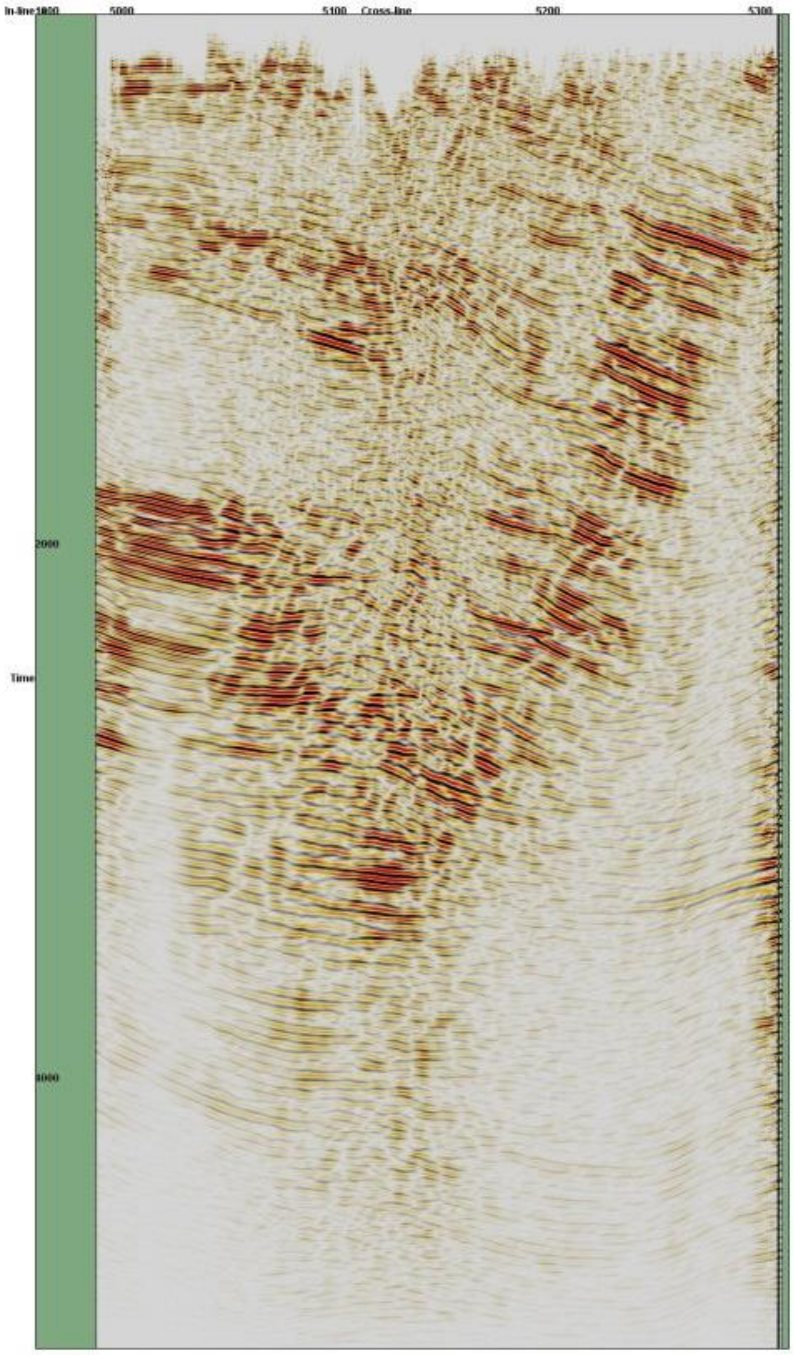

Figure 17. **Phase shift post-stack migration, ILINE1300.**

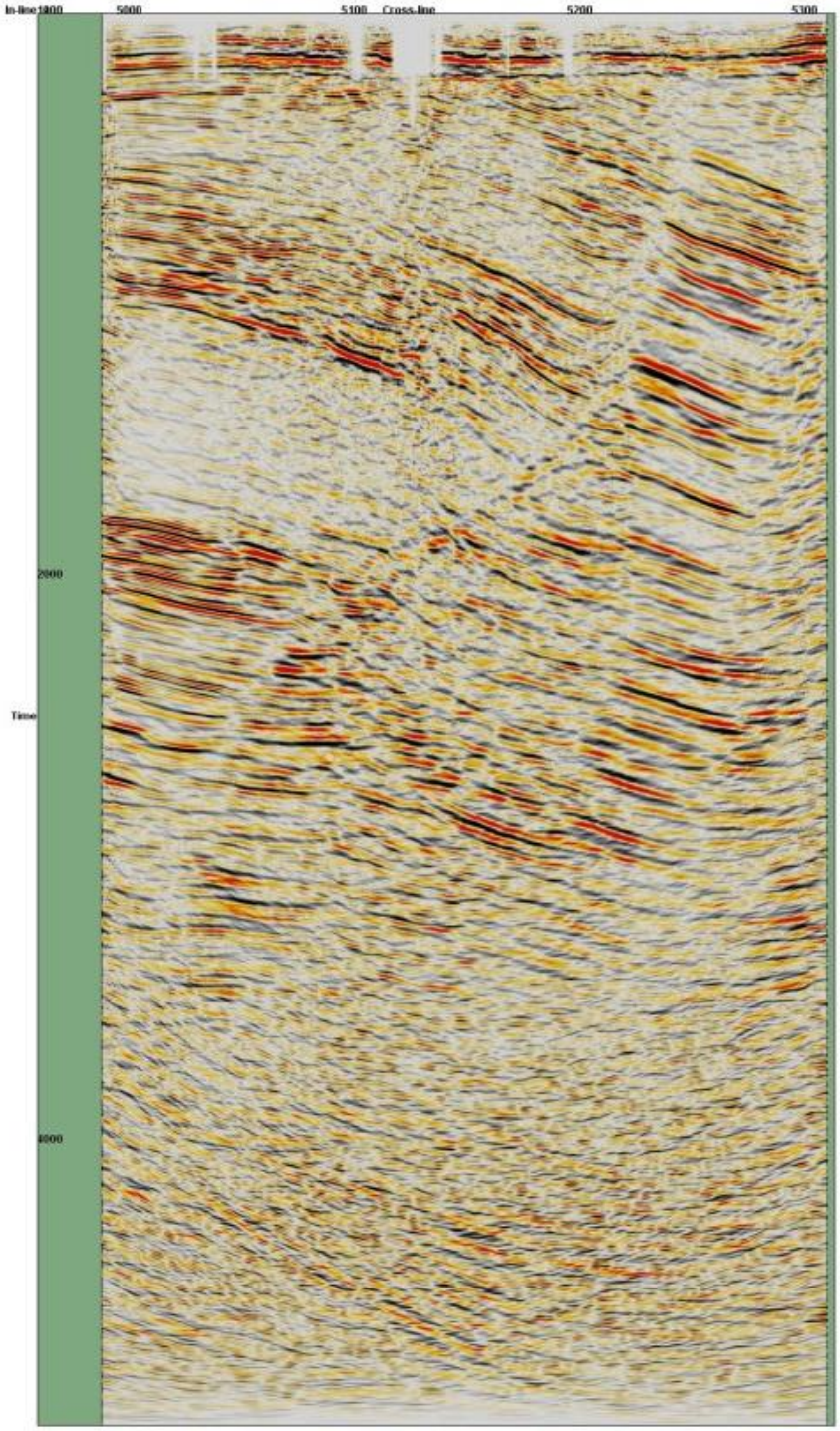

Figure 18. **Pre-stack time migration, ILINE1300.**

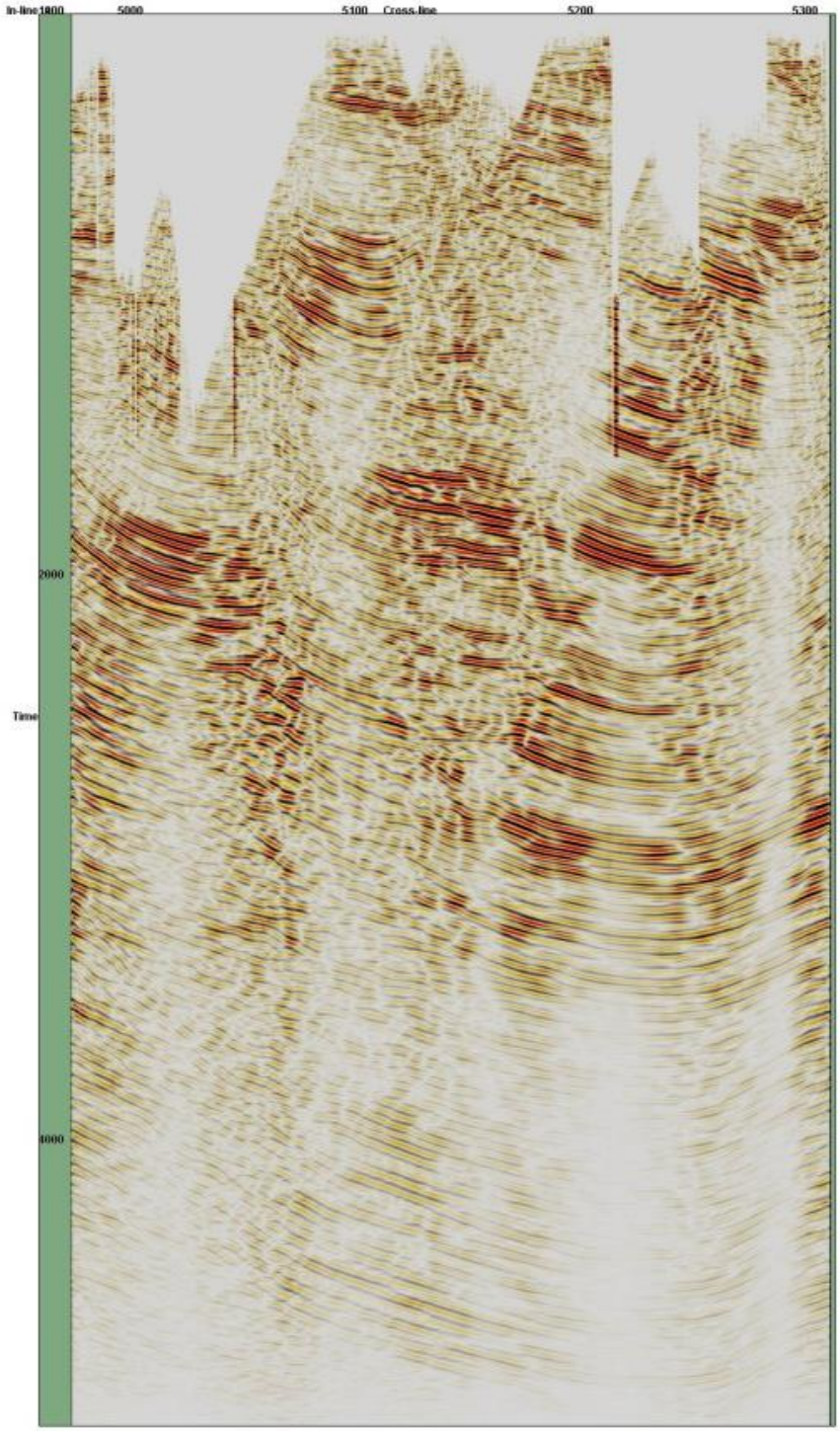

Figure 19. **Phase shift post-stack migration, ILINE1400.**

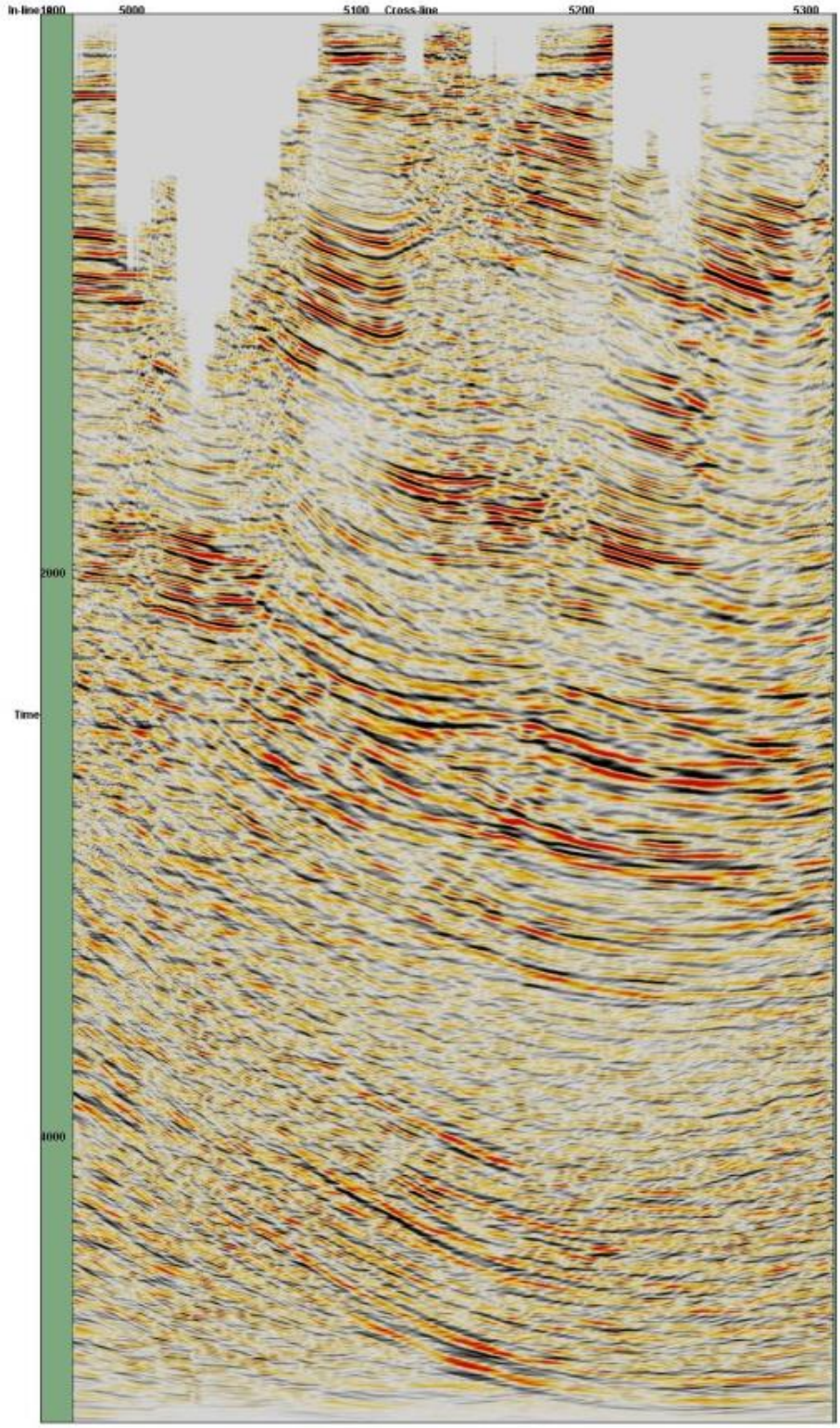

Figure 20. **Pre-stack time migration, ILINE1400.**

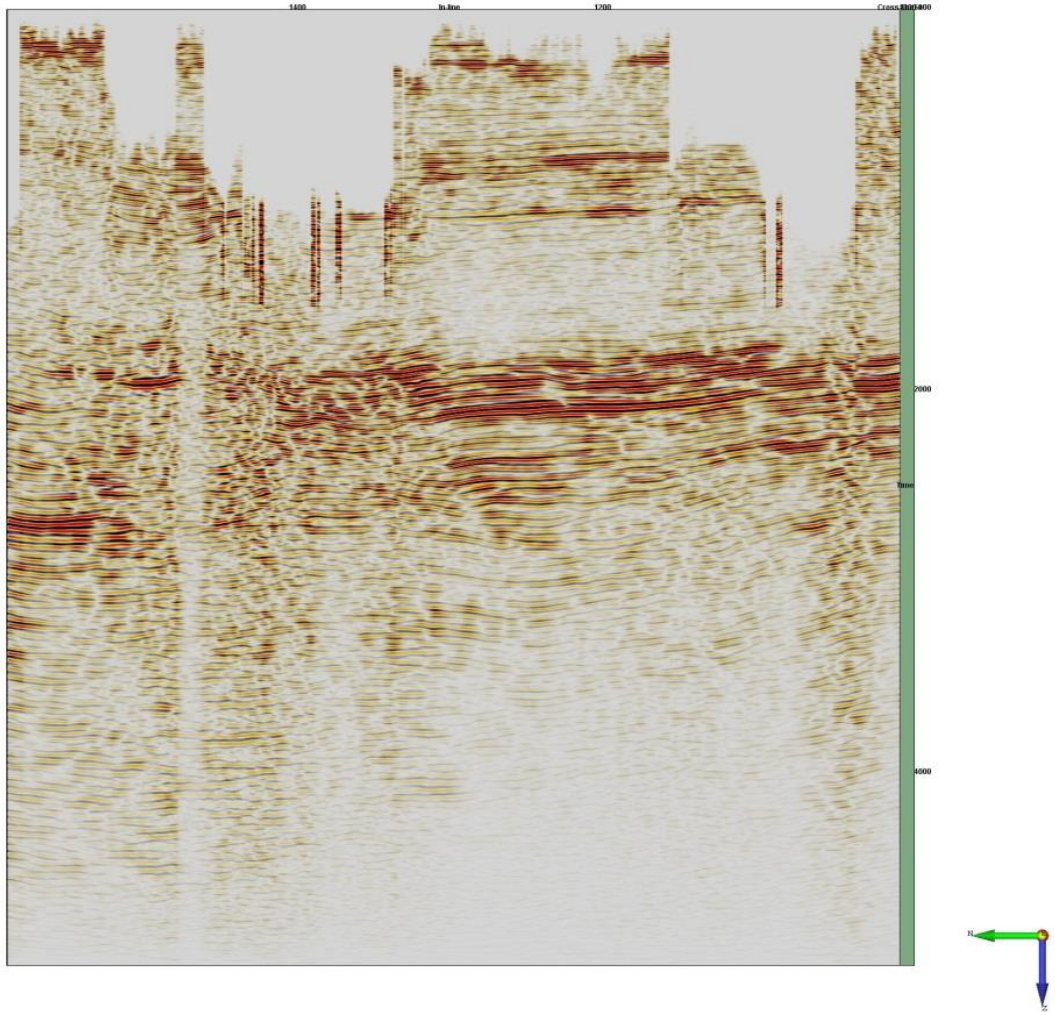

Figure 21. **Phase shift post-stack migration, XLINE5050.**

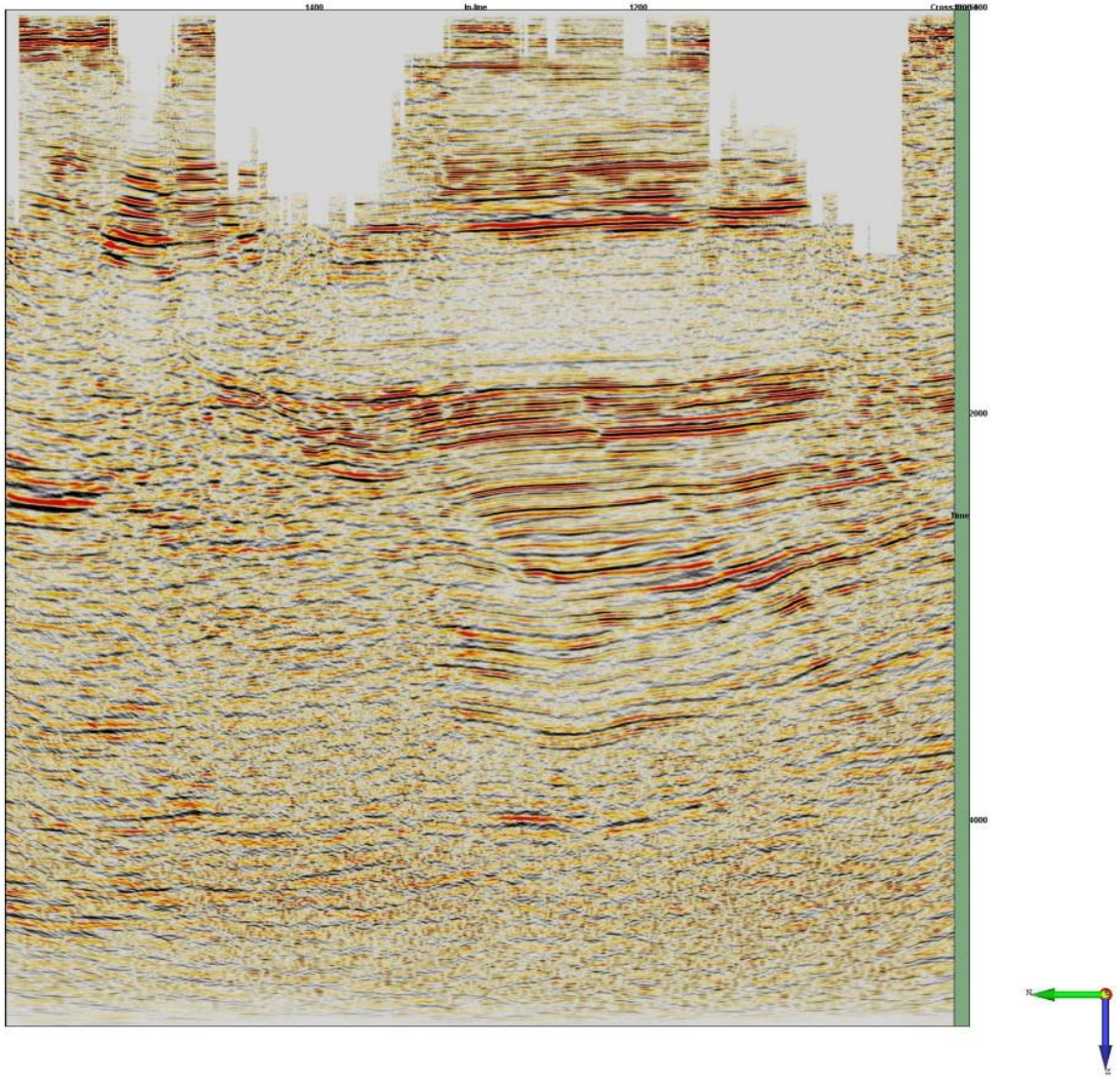

Figure 22. **Pre-stack time migration, XLINE5050.**

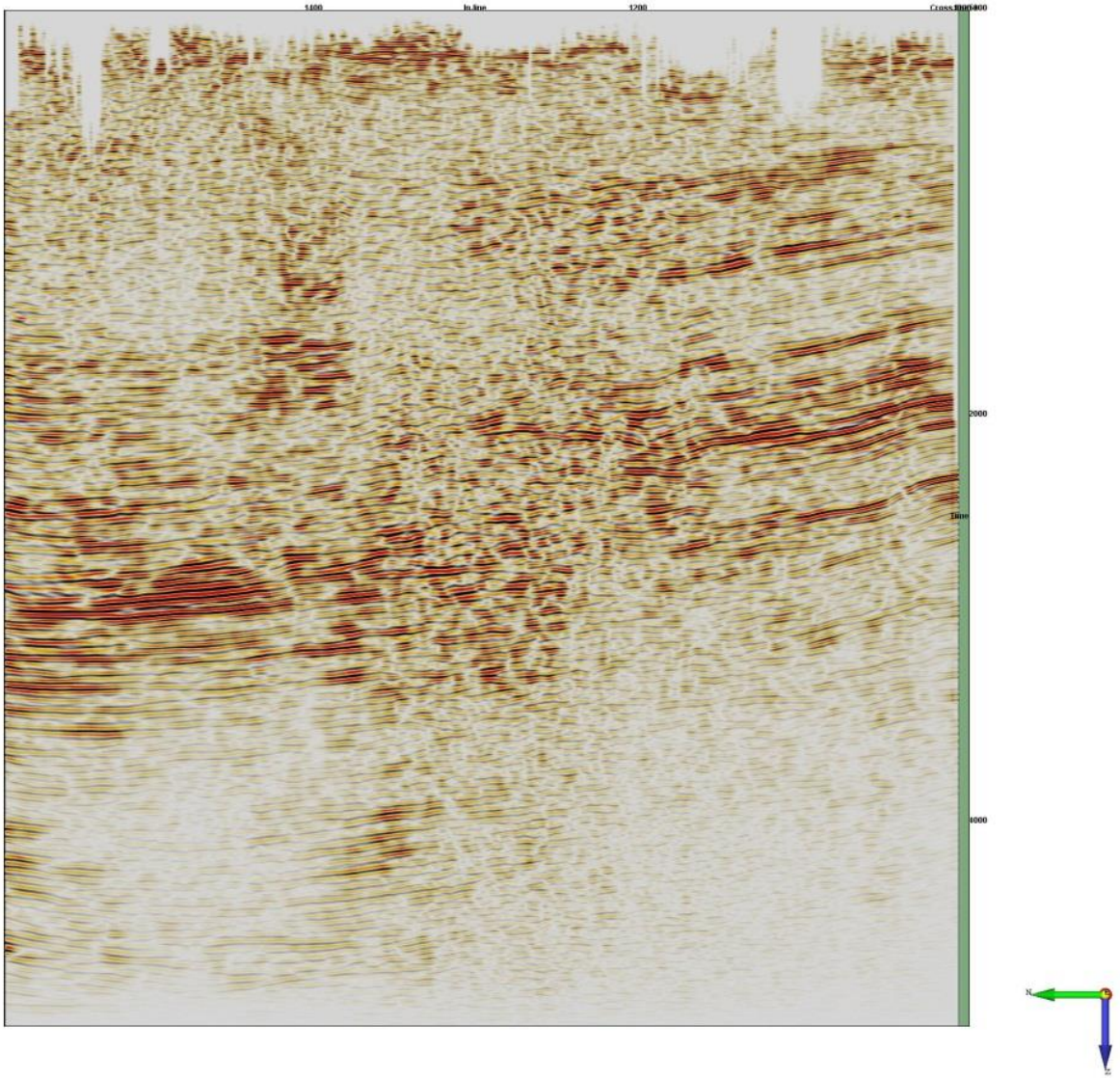

Figure 23. **Phase shift post-stack migration, XLINE5150.**

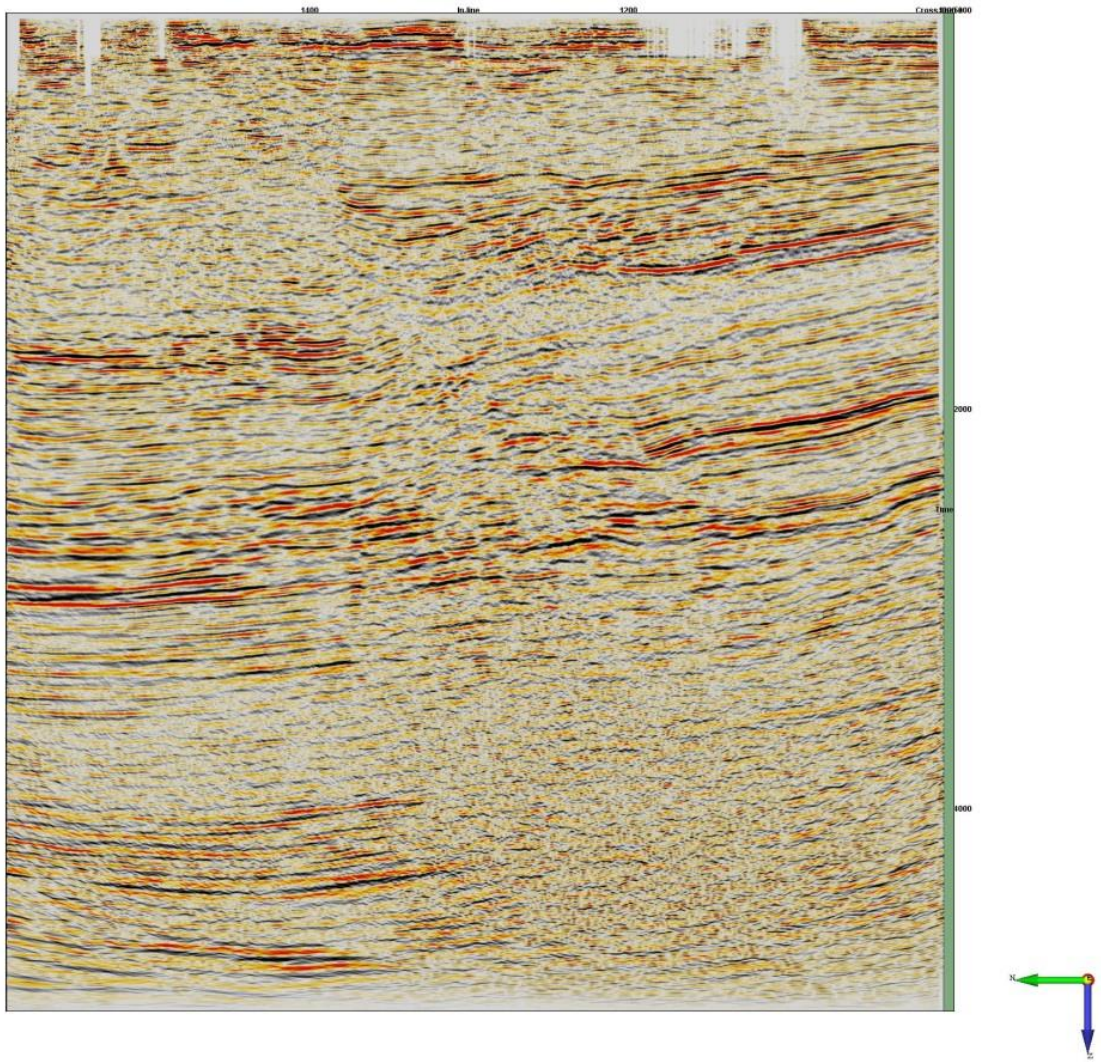

Figure 24. **Pre-stack time migration, XLINE5150.**

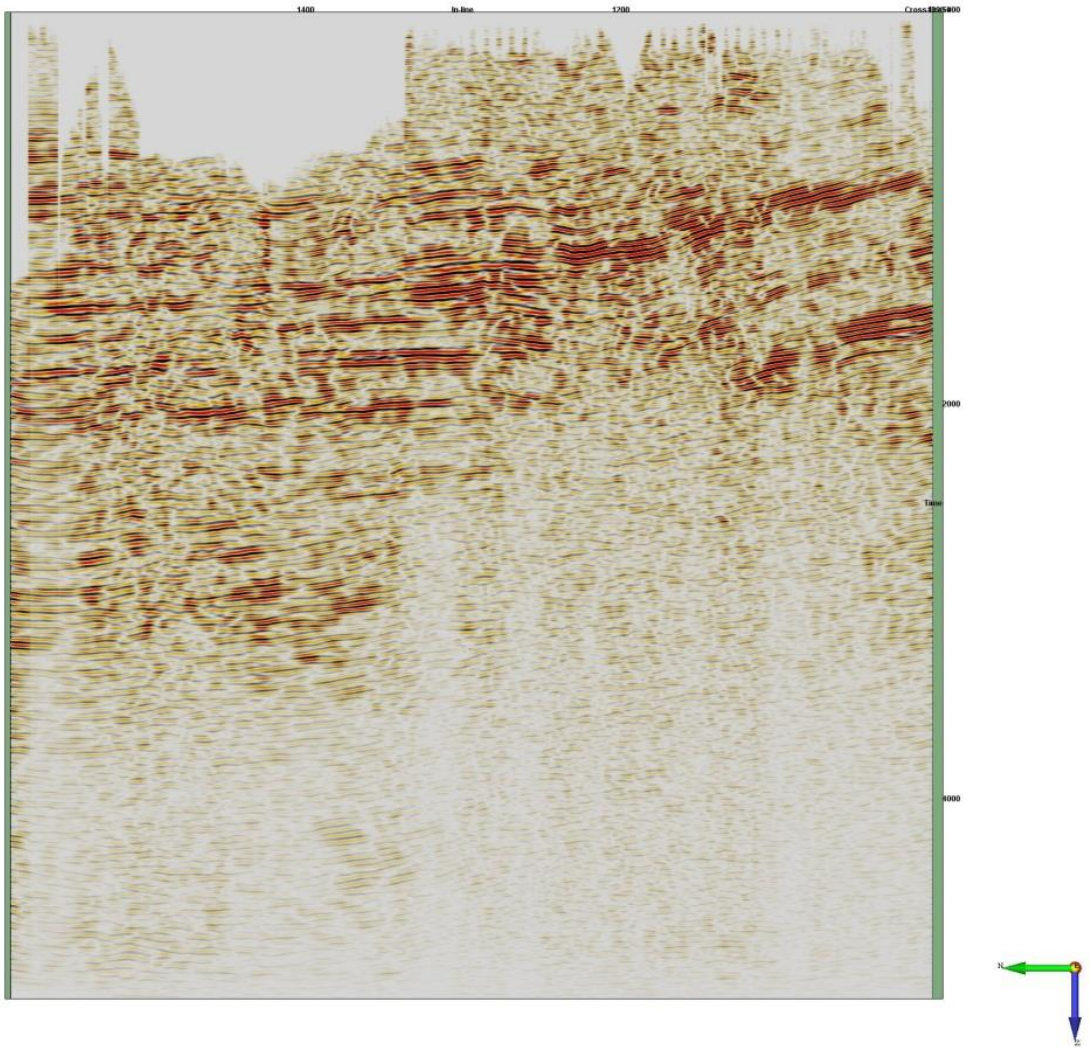

Figure 25. **Phase shift post-stack migration, XLINE5250.**

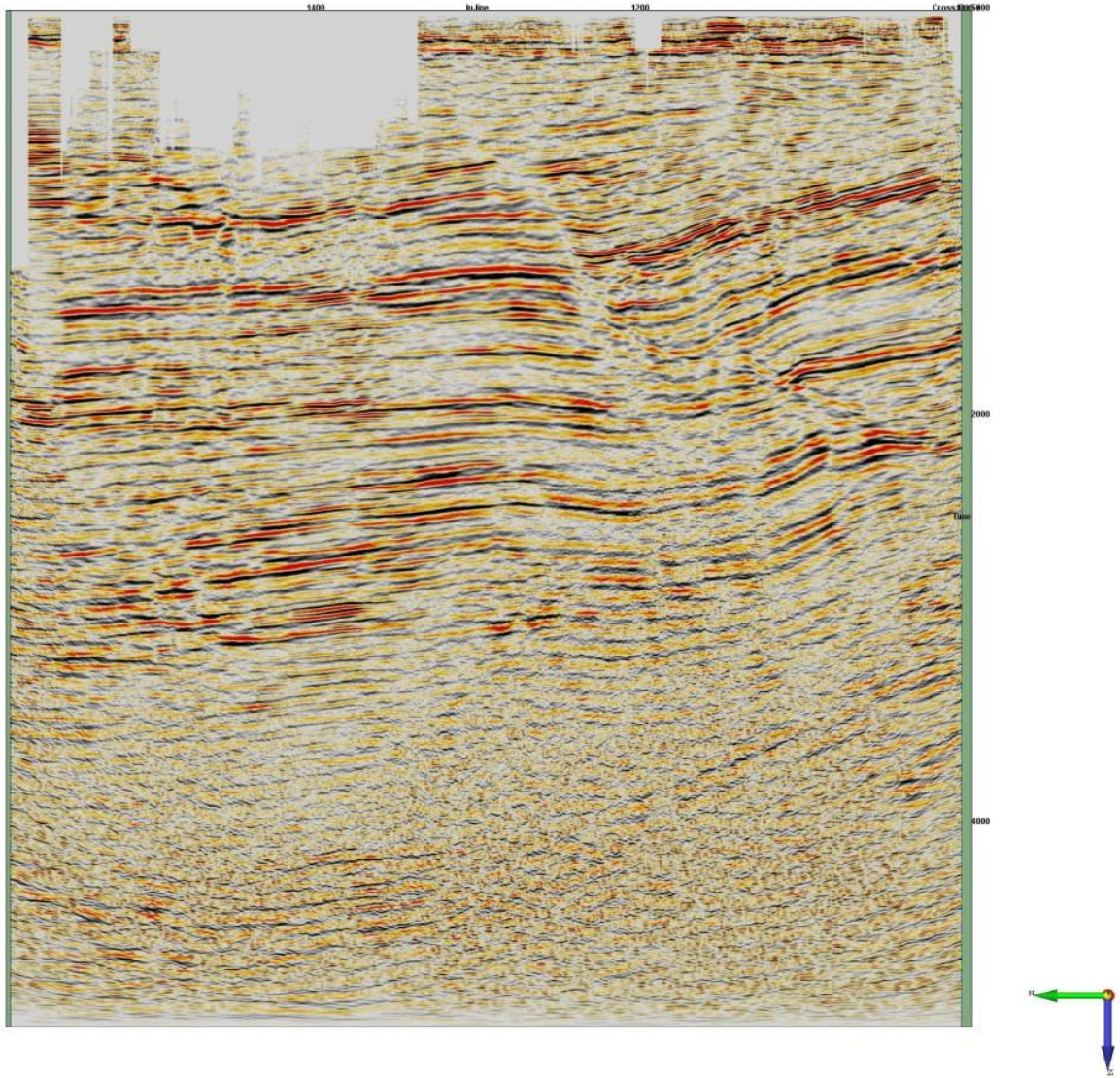

Figure 26. **Pre-stack time migration, XLINE5250.**

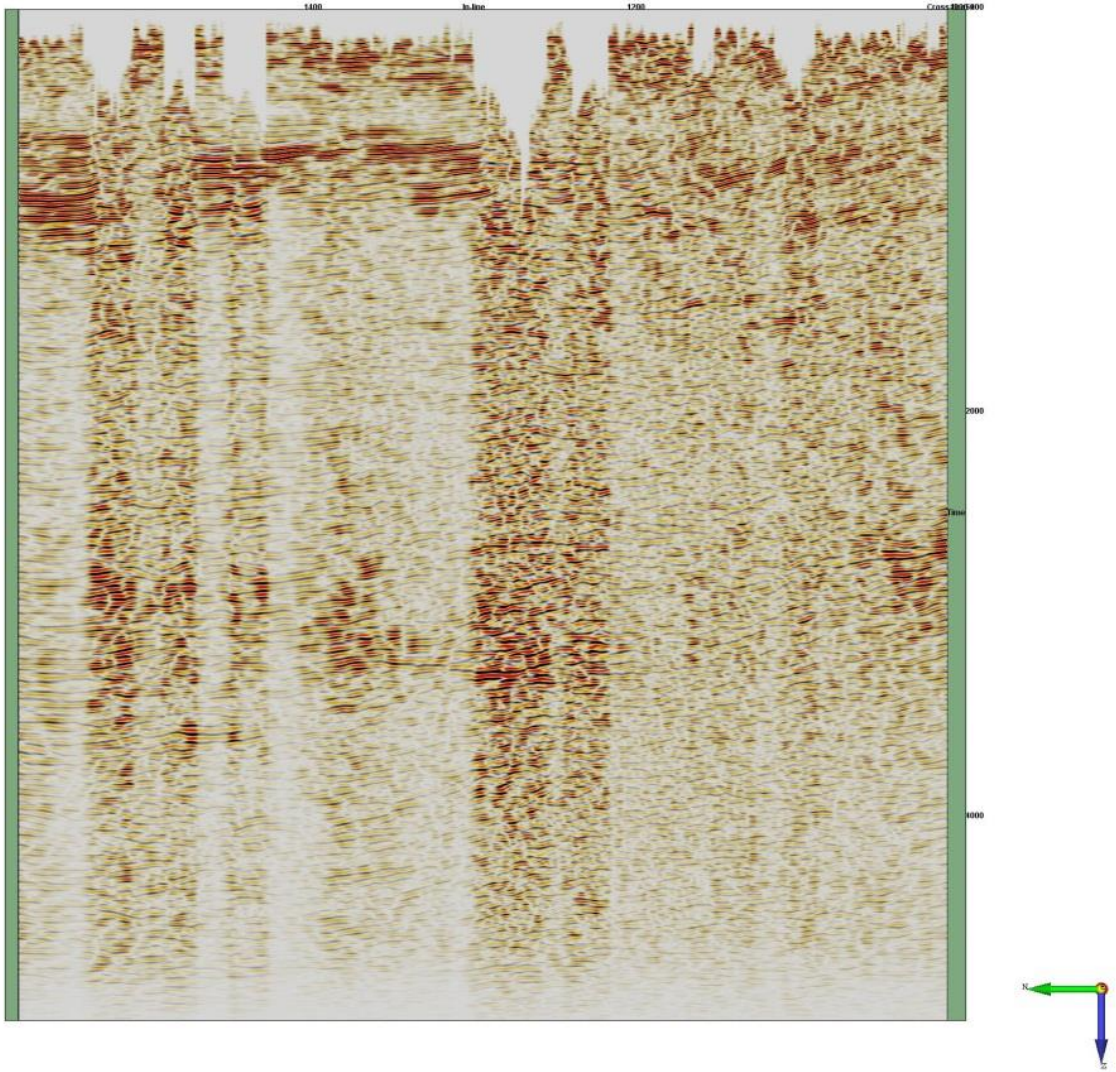

Figure 27. **Phase shift post-stack migration, XLINE5350.**

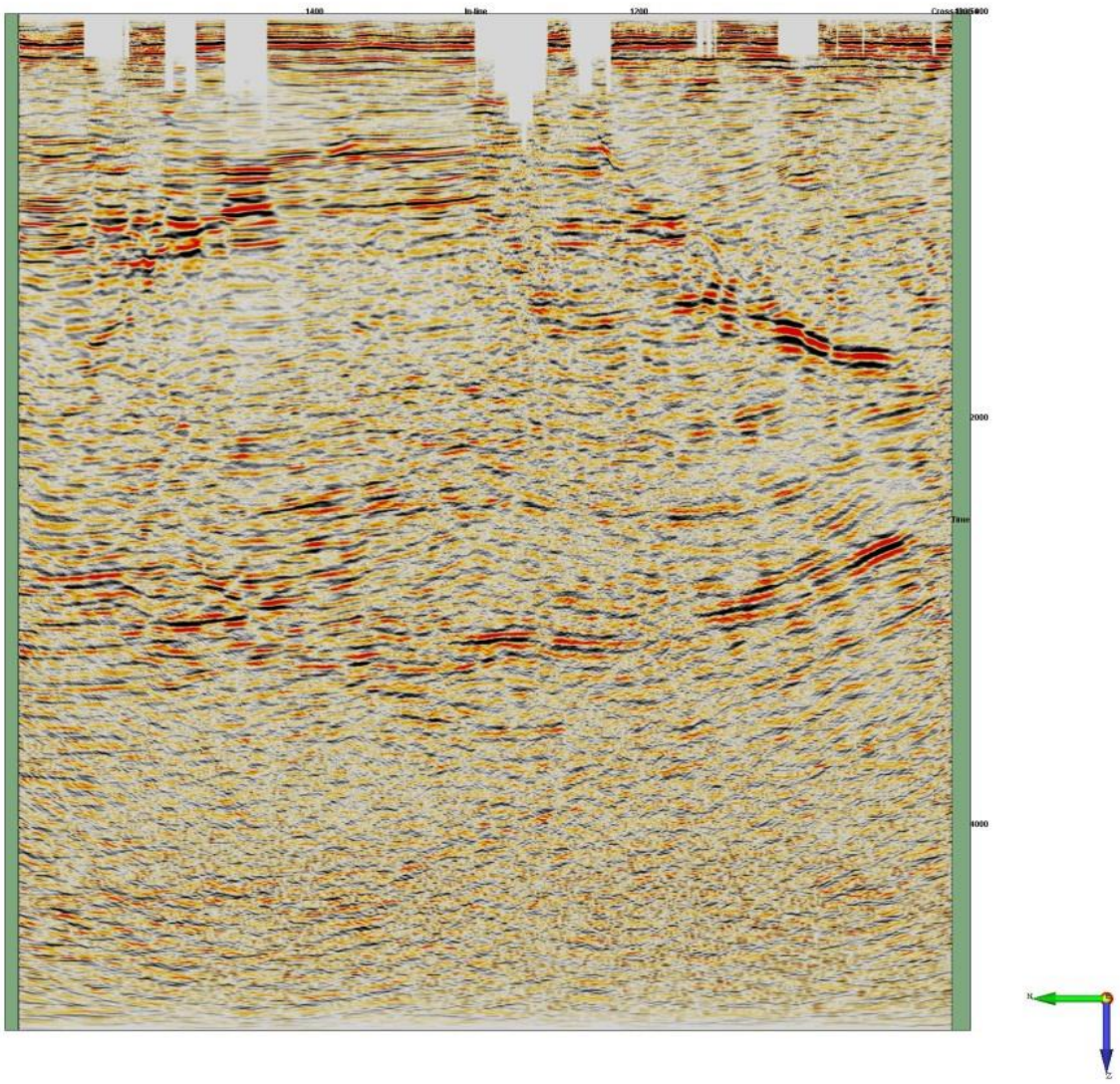

Figure 28. **Pre-stack time migration, XLINE5350.**

2.6. Pre-stack depth migration

3D pre-stack depth migration (PSDM) is commonly applied in exploration seismology to accurately position seismic energy reflected from the boundaries of subsurface geologic strata within 3D image volumes. The previous two decades have seen the development of first 3D Kirchhoff, then 3D wave-equation migration (WEM), and more recently 3D reverse-time migration (RTM) migration techniques. Kirchhoff migration uses an infinite frequency, ray-based approximation to the wave equation and employs ray-tracing methods to image the subsurface. The WEM method is based on more accurate solutions to a one-way acoustic wave equation; however, it assumes the wave is uni-directional and has steep-dip imaging limitations. RTM imaging uses more accurate full two-way solutions to the acoustic wave equation. The Kirchhoff-WEM-RTM sequence represents a gradual improvement in the accuracy – and computational complexity – of wave-propagation physics that is fundamental to all seismic imaging techniques. In marine settings, 3D RTM operators have led to a significant improvement in the exploration community's ability to image complex geological structure (e.g., sub-salt, rugose near-surface velocity lensing) over the less accurate Kirchhoff imaging techniques. However, for many scenarios involving more straightforward geology (i.e., flat lying or moderately dipping strata), communal experience has demonstrated that applying 3D RTM analyses can often be ``overkill'' and does not lead to measurable improvement – especially considering its significant computational overhead.

The application of 3D RTM in land seismic settings is far less commonly reported than 3D Kirchhoff migration applications. One of the key reasons for this is that land data acquisition is often significantly more sparsely sampled than marine scenarios, and suffers from more acquisition holes usually due to access limitations. One way to address this problem is to use physical or statistical multidimensional seismic data interpolation methods that help establish a more regularised 5D data volume consisting of four spatial (x- and y- receiver and shot locations) and one time dimension. Regularisation is an important factor for a successful application of finite-difference-based RTM operators that are quite sensitive to irregular data sampling since they

require regular spatial data sampling. Conversely, one of the strengths of integral-based 3D Kirchhoff methods is that they are less sensitive to acquisition irregularities and are thus far more commonly applied in land seismic scenarios. However, an open and strongly data-dependent question remains regarding the point at which 3D RTM imaging of land seismic data yields better results than 3D Kirchhoff migration.

The Harvey 3D seismic survey is a land dataset characterised by sparse, irregular data acquisition and significant acquisition holes that arose due to site access restrictions. Thus, given these acquisition challenges key research questions to be addressed in the Harvey 3D PSDM work are the following:

- How well can 3D Kirchhoff PSDM image the reflectivity from geologic structure within the target-oriented volume?
- Will 3D RTM be an effective imaging solution for the Harvey 3D seismic survey?
- How do the 3D RTM results compare to those from 3D Kirchhoff PSDM analysis?

We will address these research questions in the sections below.

2.6.1 Harvey 3D Seismic Survey – data selection for pre-stack depth imaging

The 3D PSDM analyses were applied to a target-oriented subset of the full Harvey 3D seismic volume. The black bounding box in Figure 29 shows the 10x10km^2 area chosen for the 3D PSDM work. The rationale behind this choice is two-fold: (1) it represents the location where, according to our understanding, future CO_2 injection activities are most likely to occur; and (2) it has a relatively more regular 3D seismic coverage that affords a more fair comparison between the two PSDM methods.

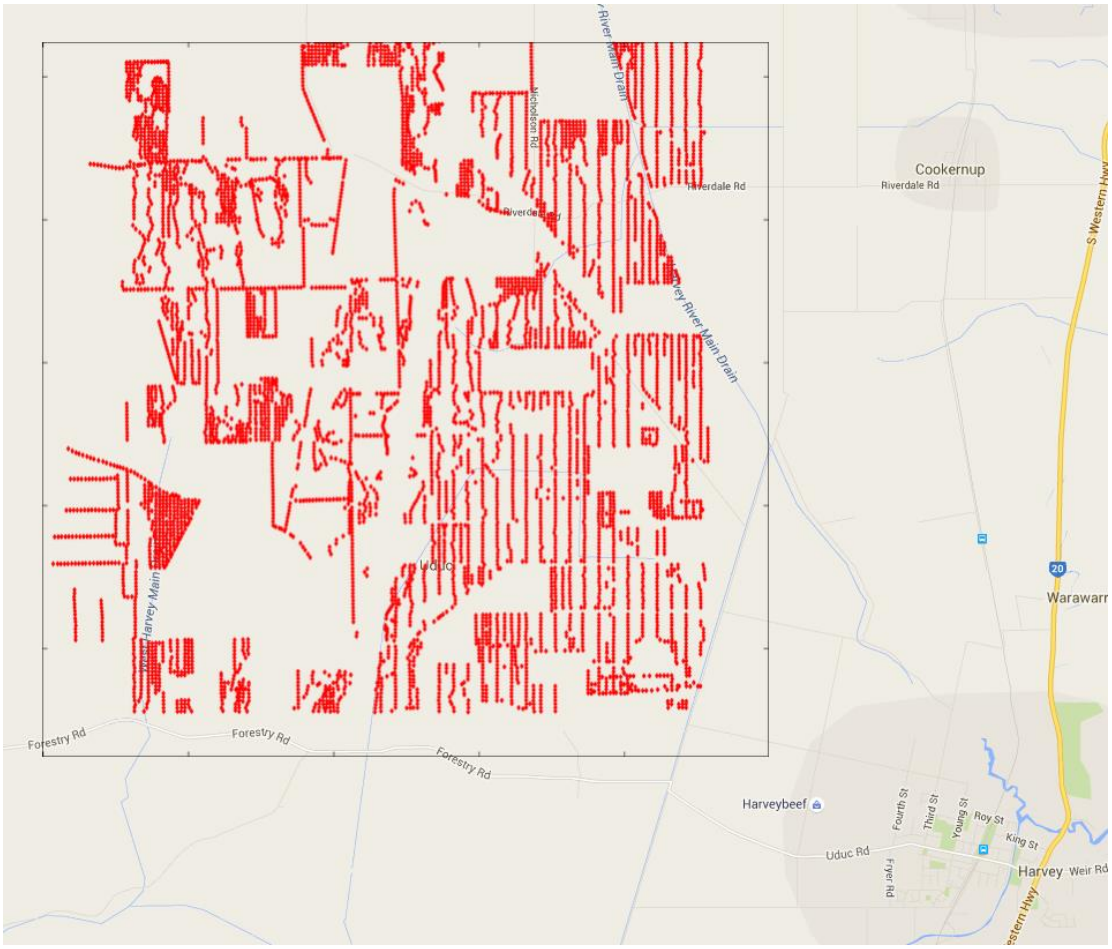

Figure 29. Harvey 3D seismic shot locations in the target-oriented area to the northwest of Harvey, WA, chosen for 3D PSDM work. The black bounding box represents the 10x10km2 imaging area with a cell-centered origin in the lower left corner at [384000, 6340500] m.

We prepared two slightly different datasets for the two PSDM analyses. The Kirchhoff PDSM dataset was generated by extracting a data subset with CMP locations falling within 10x10km^2 square bounded by the UTM Zone 50 coordinate limits between 384000m and 394000m in the easting (x) direction and between 6340500m and 6350500m in the northing (y) direction. For the image volume grid we used a 25m-cell spacing for both the x and y coordinates, and a 6.25m interval in depth (z). We set the cell-centred origin of the grid at the UTM coordinate pair of [x,y]=[384000,6340500]m in the southwest of the grid, which we refer to as [x,y]=[0,0]km in the images below. The mesh extends for a total of 10km in both the easterly and northerly directions, with 400 bins in both the inline (y) direction and crossline (x) directions. The data subset reduces the total number of traces to 22,601,499 and seismic shots to 7945 (including some

midpoints where shot locations fall outside of the image area). Table 6 summarises the gridding parameters used for the Kirchhoff 3D PDSM procedure.

The data set for 3D RTM work was generated by binning shot gathers with shot locations falling within the same 10x10km^2 area as described above. We used a bin interval of $\Delta x=\Delta y=50$m for both source and receiver bin coordinates. This represented 5224 total shot locations, with significant variation in shot density due to issues arising from site access challenges. Figure 29 presents the available areal shot coverage in the target-oriented area nominally oriented in a north-south direction, while Figure 30 presents the receiver locations that are predominantly oriented in an east-west direction. Table 7 summarises all gridding parameters used for the 3D RTM work.

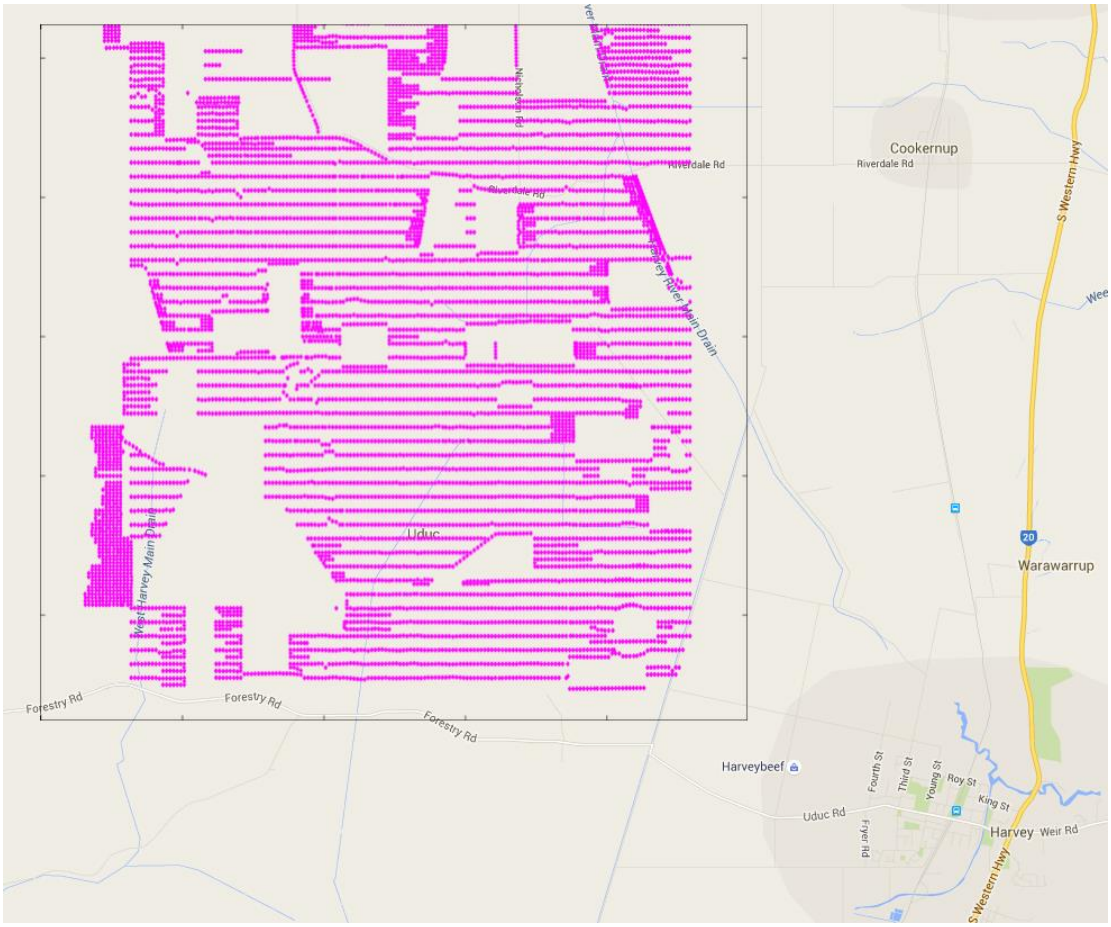

Figure 30. Harvey 3D seismic receiver locations in the target-oriented region to the northwest of Harvey, WA.

Both PDSM data sets were subject to the same data pre-processing steps as discussed in Table 3. This workflow consisted of the following procedural steps:

- Geometry assignment
- Trace editing
- Air blast attenuation
- Elevation statics shift to a single final datum
- Residual statics shift;
- Deconvolution
- Band-pass filtering
- Surface-wave noise attenuation
- Trace balance through long-window (500 ms) automatic gain control (AGC).

The 3D interval depth velocity model developed for PSDM work was based on the 3D PSTM velocity model derived by optimising stack semblance described as the third velocity model building procedure in Section 2.3 above. We used the Promax time-to-depth conversion utility (Time/Depth Conversion) to convert the PSTM velocity model to a PSDM depth velocity model. The initial velocity model covering the 10x10km^2 target-oriented area was interpolated to 25m in all dimensions to match the data binning using smooth 3D *sinc*-based operators.

2.6.2. 3D Kirchhoff PSDM

We imaged the 10x10km^2 area using the Kirchhoff pre-stack migration code (KDMIG) from the *Promax* software package. We used *Promax's* 3D Eikonal solver to generate the travel-time tables required for Kirchhoff PDSM using the 3D interval depth velocity model . We set the migration aperture to a limit of 32º in both lateral directions and used *Promax* anti-aliasing filter in order to reduce the adverse effects of operator aliasing. The depth sampling of the migrated volume for the 3D Kirchhoff migration was set to 6.25m to enable a high-resolution recovery of reflectivity from the surface to a maximum depth of 5.75km. Table 6 summarises the migration parameters used in the 3D Kirchhoff work.

The 3D Kirchhoff PDSM analyses were run on the University of Western Australia (UWA) Geophysics cluster using single 32-core AMD Opteron server with 256GB of RAM connected to a fast *Infiniband* storage array. Numerous initial migration tests were run at coarser sampling intervals and for smaller 3D sub-volumes to test parameters, examine the utility of additional processing and data conditioning steps, and

incrementally verify successes in subsurface reflectivity imaging. We computed the final migration results on the full grid described above, which required an overall run time of roughly 24 hours.

The output image volume from the KDMIG procedure was a 4D ``hypercube'' with the four dimensional axes: offset, inline, cross-line and depth. Prior to stacking over the offset dimension we applied a top mute in both depth and offset, which we truncated at a depth of 500m to ensure the inclusion of near-surface reflectivity in the final image volume. The final Kirchhoff migration volume was ouput as a *segy* file, and then re-oriented and re-gridded so as to be directly comparable with *segy* image volumes previously delivered to ANLEC. This image volume represents the 3D PSDM results that were made available to ANLEC as part of the project deliverables.

Table 6: Table of gridding and migration parameters for the 3D Kirchhoff work.

Parameter	**Value**
Coordinate system	UTM Zone 50 H (South)
Grid min x (cell centered, Easting)	384000m
Grid max x (cell centered, Easting)	393975m
Grid min y (cell centered, Northing)	6340500m
Grid max y (cell centered, Northing)	6350475m
Grid min z (cell centered, depth)	0m
Grid max z (cell centered, depth)	5750m
Δx	25m
$\mathrm{Number\ of\ cross\text{-}line\ bins}$	400
Δy	25m
$\mathrm{Number\ of\ inline\ bins}$	400
Δz	6.25m
$\mathrm{Number\ of\ depth\ bins}$	921
Offset bin increment	100m
Minimum offset	50m
Maximum offset	9350m
Number of offset bins	94
Number of shots	7945
Migration aperture	32°
Traces	22,601,499
Data format	16-bit integer

Imaging Results

We have extracted a number of cross sections and depth slices from the final 3D Kirchhoff image volume and present them in the figures below. We plot the figures in a ``cube plot" view where the lower-left panel shows the easting (x) cross-section, the lower-right panel shows the northing cross-section (y), and the upper panel shows a

map-view depth or time slice. Each panel has three thin dark blue lines indicating the location in the cube through which the three slices were extracted. All image plots are shown at an equal aspect ratio such that reflector and fault dips are shown at their true angles. We note that the PSDM images are lower frequency than the PSTM images reported above. We emphasise that the main reason for this is that migration images in depth domain suffer from a vertical stretch roughly proportional to the velocity field relative to time-domain images. Thus, for the 3D Harvey velocity model this means that near-surface reflectors appear approximately four times higher frequency than at depth.

Figure 31 illustrates the influence of seismic acquisition holes on the resulting image cube. The depth slice (top panel) of Figure 31, extracted at z=0.2km, indicates the presence of significant data holes – especially to the southwest of the image – as well as a hatch pattern arising from the acquisition footprint. However, the depth slice extracted at z=1.45km and shown in Figure 31b is observed to no longer show significant acquisition holes (though does exhibit reflector dimming), indicating the holes have been substantially ``healed'' by undershooting at wider offsets source-receiver pairs.

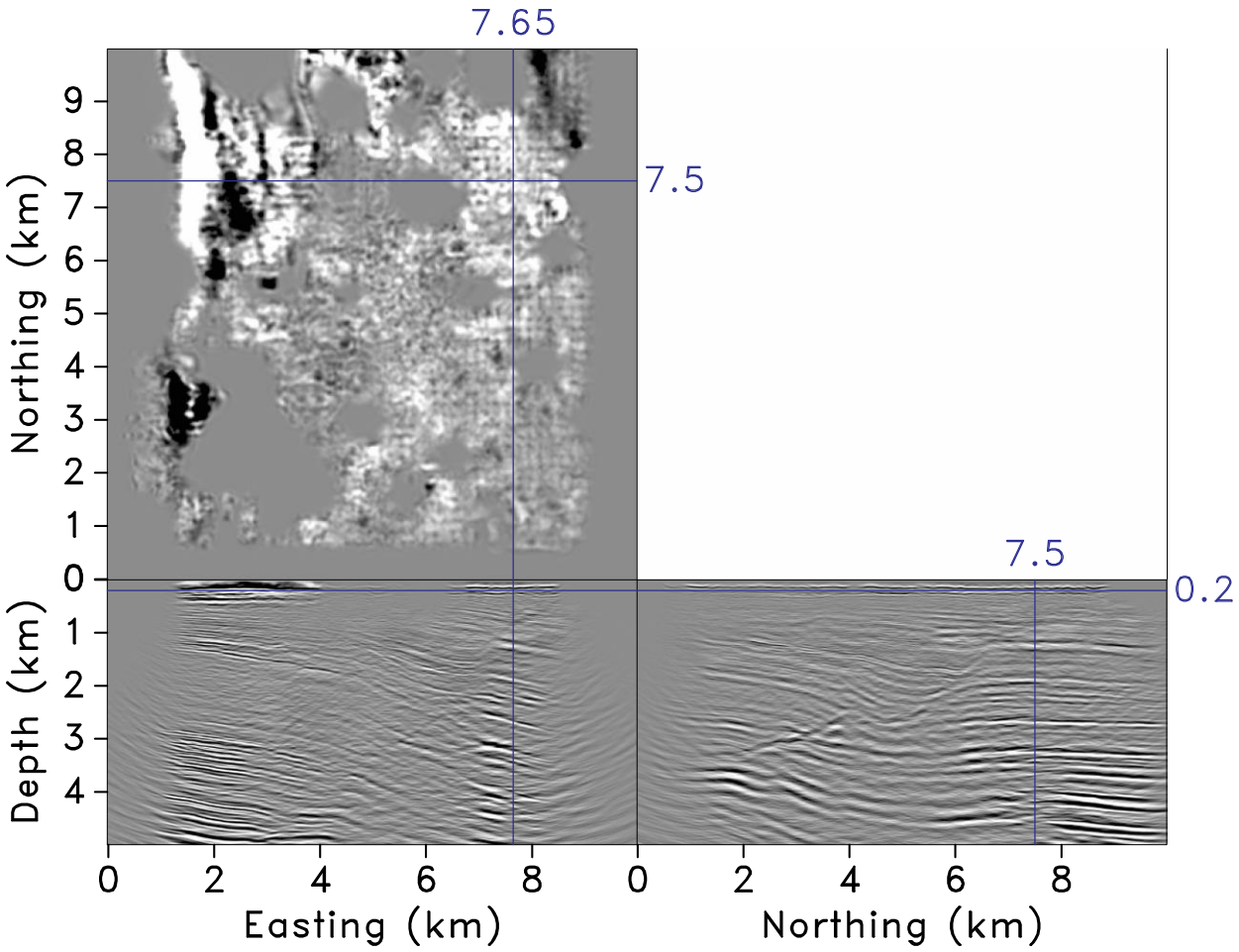

Figure 31a. Cubeplot view extracted from the 3D KPSDM. Depth slice taken at z=0.2km illustrating the variability and sparsity of CMP sampling – especially in the vicinity of the large acquisition hole in the southwest corner. (con't)

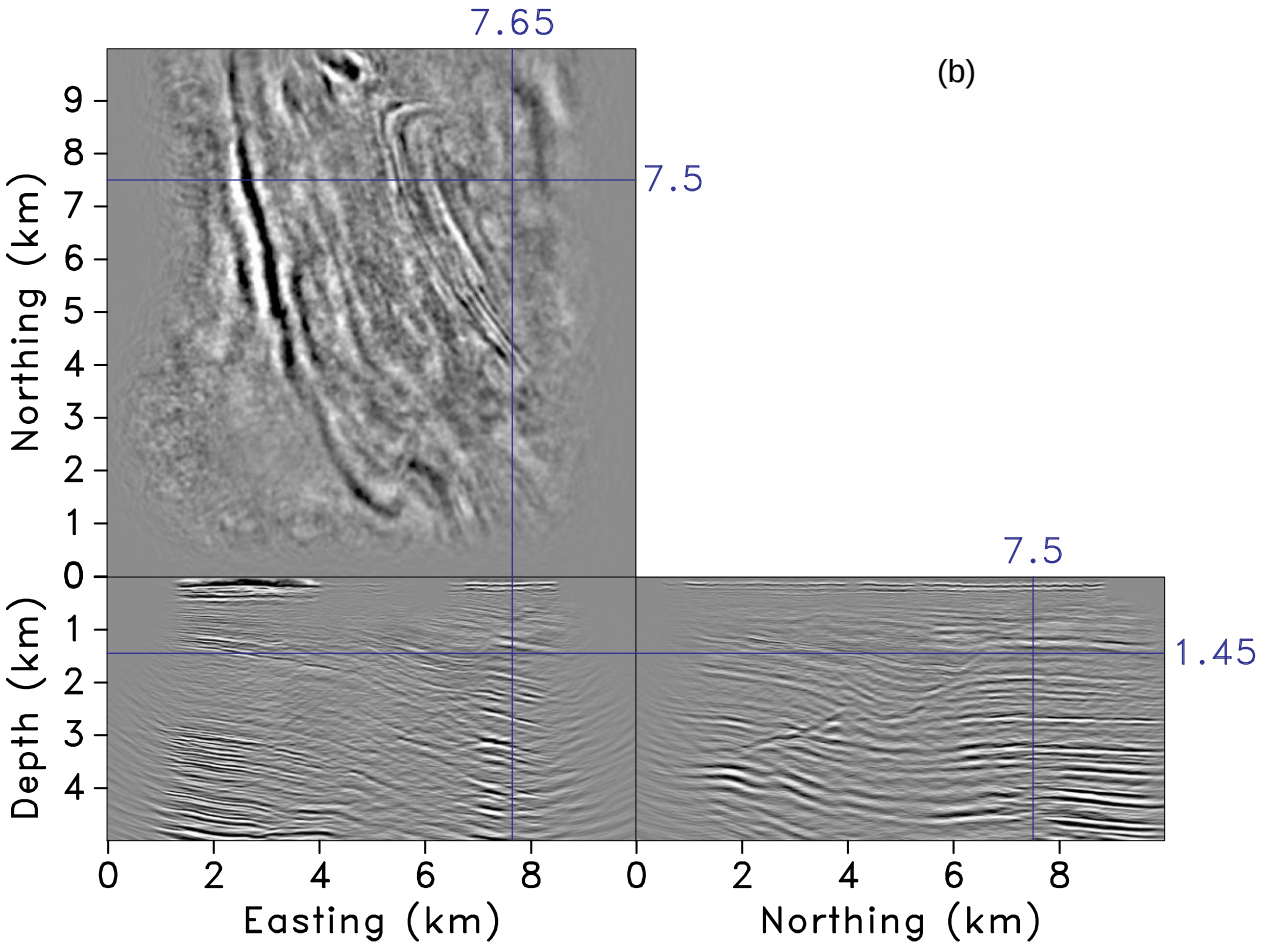

Figure 31b. Cubeplot view extracted from the 3D Kirchhoff. Depth slice extracted at z=1.45km showing the infilling of acquisition holes through undershooting by wider offset source-receiver pairs

The northing cross-sections of these panels, extracted at *x*=7.65km, show a prominent fault reflector interpreted to associated with the F10 Fault. These reflectors extend from about *z*=3.0km depth toward the south end of the volume to less than *z*=1.0km depth near the north end. The easting cross-section extracted at *y*=7.5km also shows the fault; however, the fault-plane reflection is weaker and is more obviously indicated by the abrupt truncations in reflectivity. The F10 fault is also visible in the northeast portion of the depth slice in Figure 311b, and is traceable for about 6-7km in length throughout the image volume.

Figure 32 presents another cube plot view extracted at *x*=1.9km, *y*=6.25km and *z*=3.19km depth. The easting panel shows a 1.5km-thick geologic unit at between 1.5-3.0km depth between *x*=1-5km, as well as the previously discussed F10 fault between *x*=5-8km. This thick geologic unit, interpreted to be the Wonnerup Formation, is better

observed in the Northing cross-section. We note that this package has a limited amount of internal reflectivity; an observation consistent with previously reported 2D imaging results from earlier ANLEC projects. This northing panel also illustrates the acquisition holes between *y*=1-4km, which manifests in weaker amplitudes, less coherent reflectivity and a corresponding greater uncertainty. The depth slice again cross cuts the F10 Fault, which shows up as a somewhat sinuous reflector of approximately 6-7 km in length.

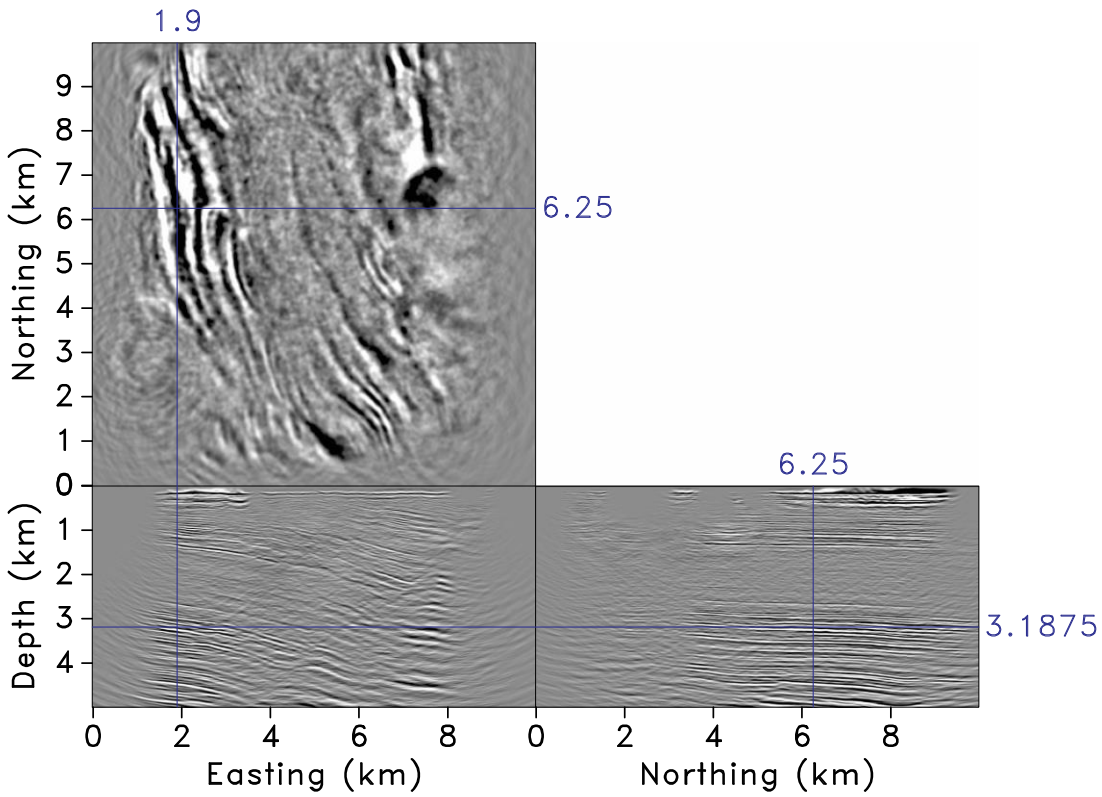

Figure 32. Cube plot through easting coordinate 3902500m (front face), northing coordinate 6356750~m (side panel) and depth 3.19km.

Figure 333 presents a cube plot view through *x*=7.65km, *y*=6.0km and at *z*=3.13km depth. The easting and northing cross-sections show reflections from F10 Fault, with the fault truncating the reflectivity in the easting cross-section between *x*=6-8km. The near-surface reflector at between *z*=0.1-0.2km depth is also well imaged in this section.

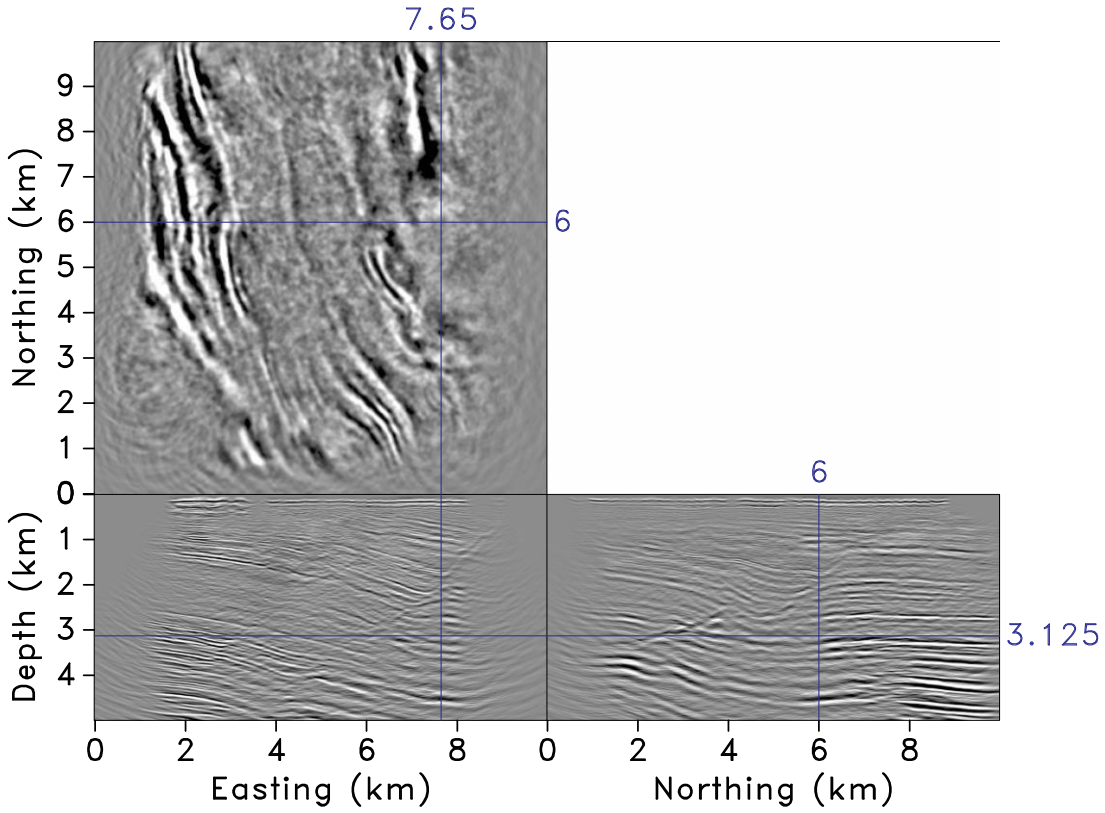

Figure 33. Cube plot through easting coordinate 390000m (front face), northing coordinate 6352400m (side panel) and depth 3125m.

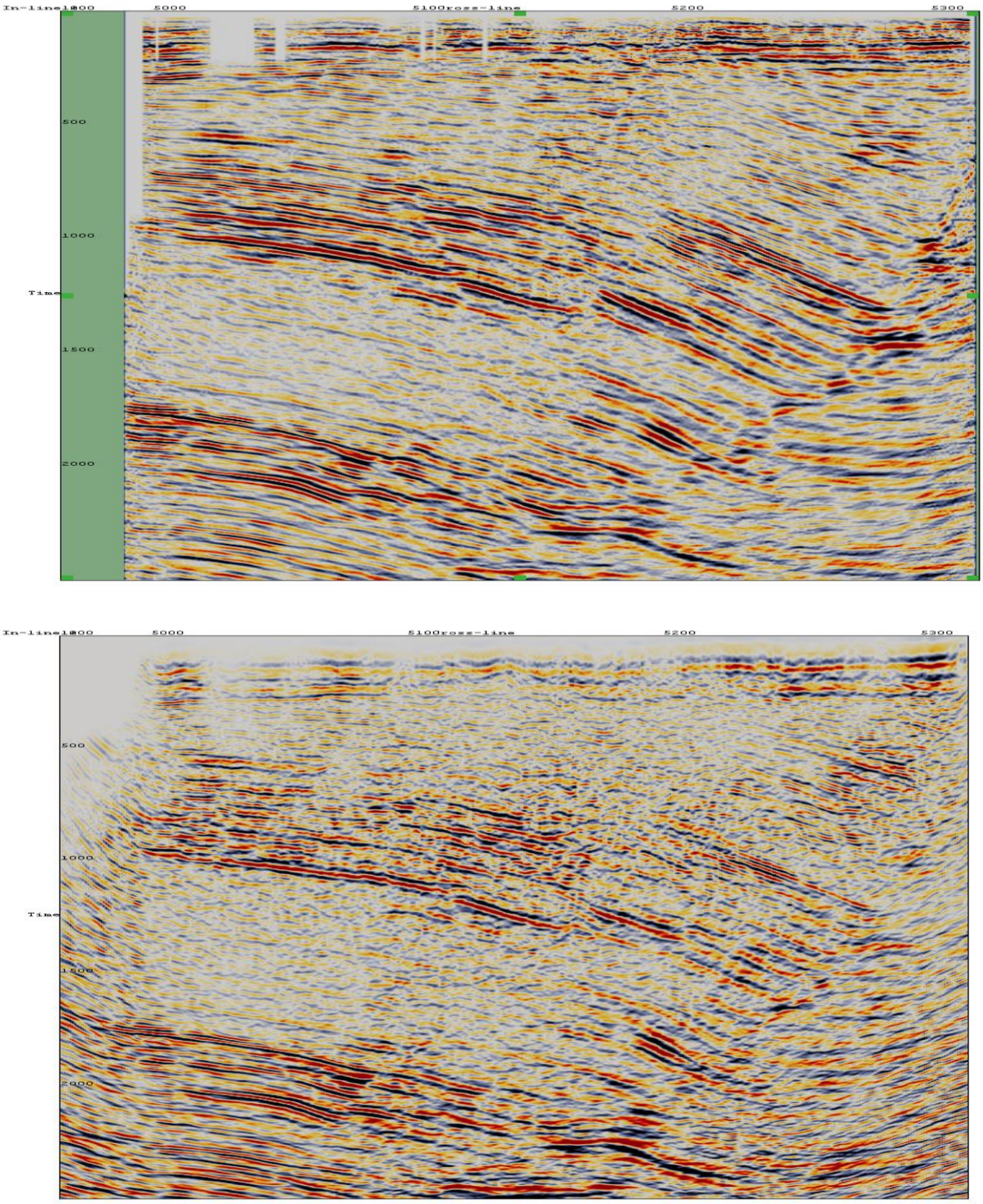

Figure 34. Comparative section for inline 1175. (a) PSTM. (b) Kirchhoff PSDM.

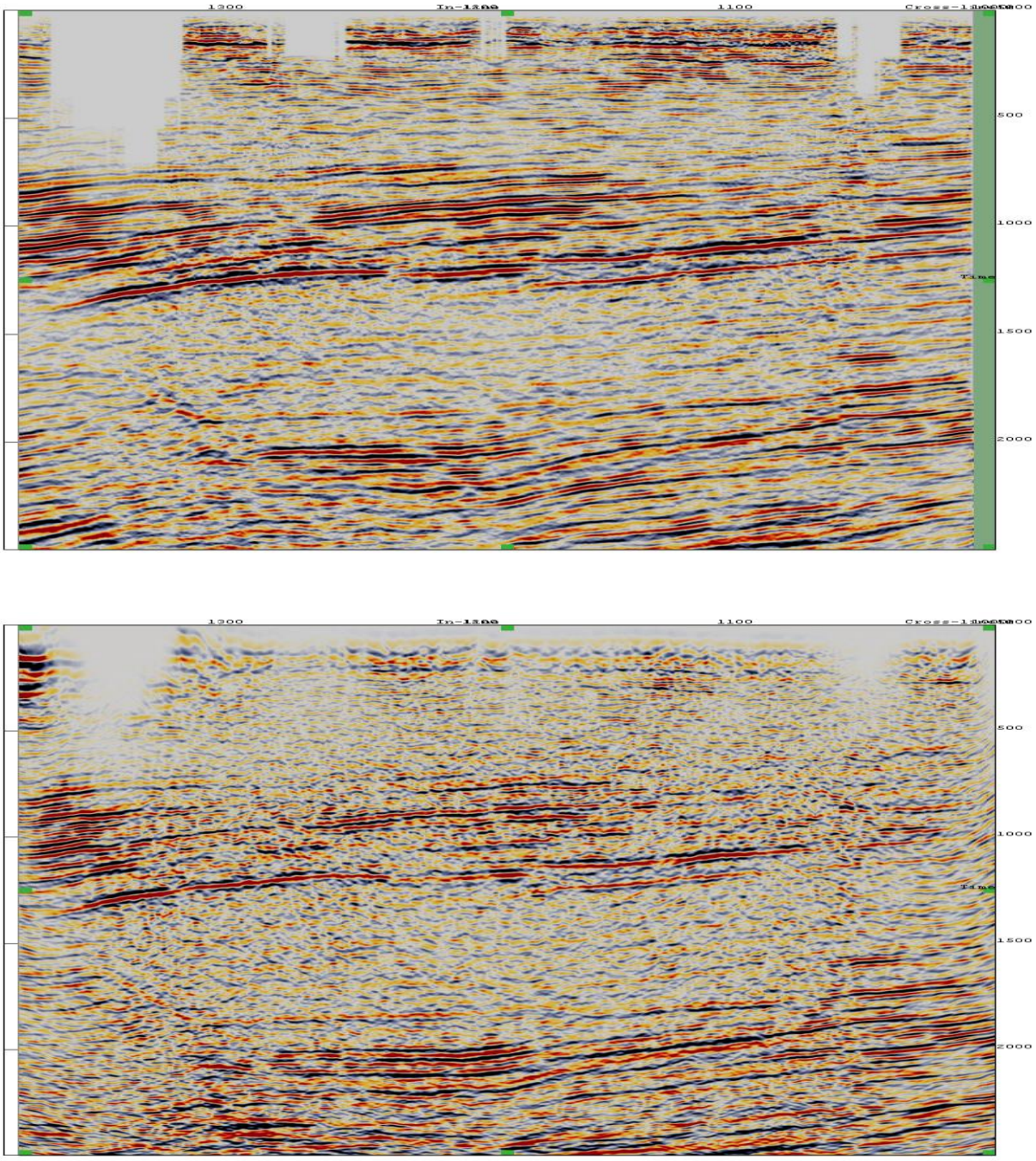

Figure 35. Comparative section for crossline 5119. (a) PSTM. (b) Kirchhoff PSDM.

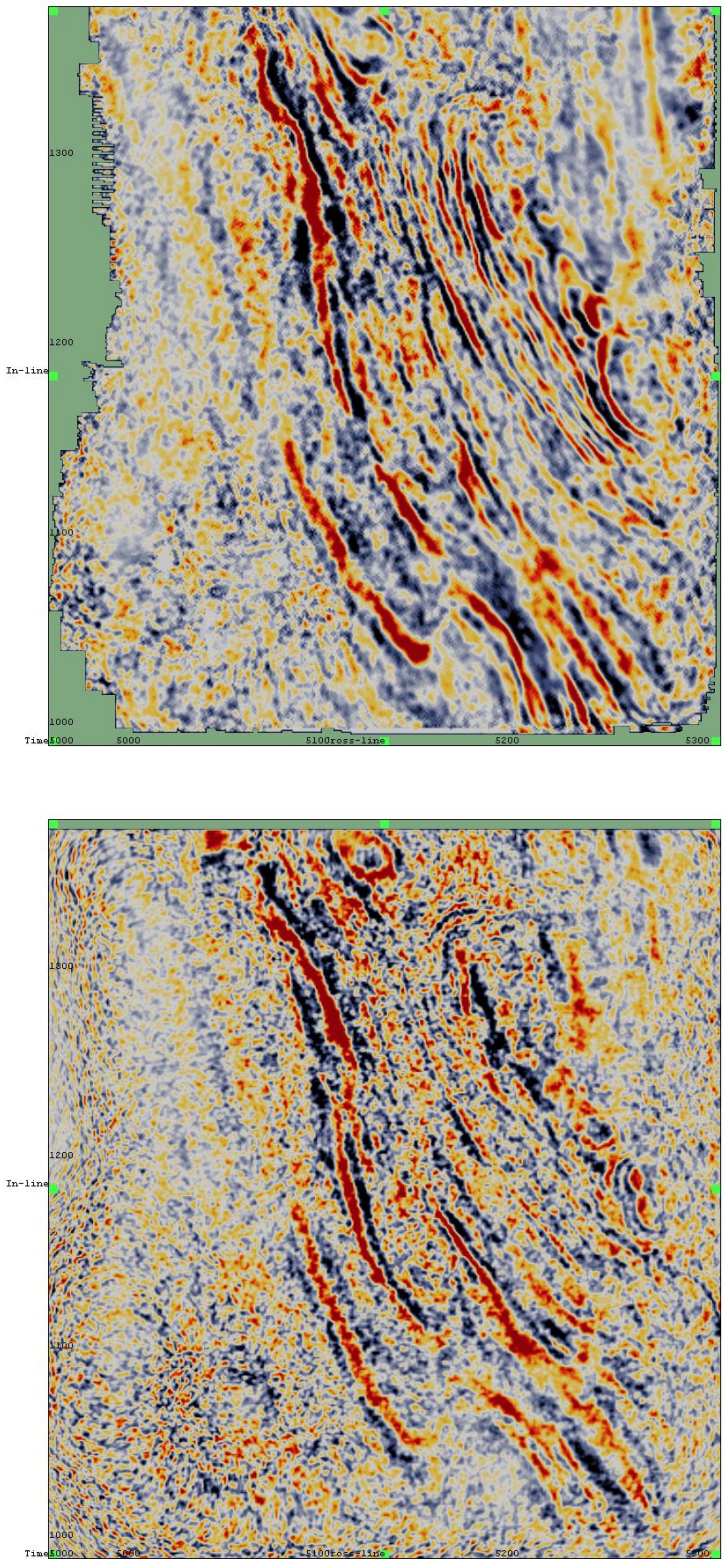

Figure 36. Comparative time slice extracted at 1197ms. (a) PSTM. (b) Kirchhoff PSDM.

Figures 34-36 show comparative inline, crossline and time slice sections from the same locations at the same colour scale for the PSTM (upper panels) and Kirchhoff PSDM (lower panel) image volumes. Overall, the images are fairly comparable with the PSTM results having a better recovery of the top 500m and showing overall better lateral continuity and less high-frequency speckle (that could be reduced in the PSDM results through additional post-migration filtering). Subtle differences in the imaging around faults are noticed in the three figures; however, the differences are noticeable when comparing the time slices shown in Figure 36.

2.6.3. Multi-dimensional Data Interpolation

Initial tests of the 3D RTM imaging code were carried out on gridded but non-regularised shot-record data. The resulting image volumes were observed to be substandard and exhibited the effects of strong image aliasing due to the irregular and sparse seismic acquisition. To help mitigate these issues we trialled a number of multi-dimensional interpolation routines with the aim of infilling some axes of the 5D data hypercube and thereby helping to diminish the effects of both the acquisition holes and to a lesser extent the nominal 0.2km receiver line sampling. In the course of this investigation we examined two different 3D and one 5D interpolation methods: adaptive prediction error filtering (APEF), plane-wave destructors (PWDs), and azimuthal moveout (AMO), respectively.

APEF is a two-stage interpolation technique that represents an extension of the prediction error filter (PEF) research undertaken at the Stanford Exploration Project (Claerbout and Fomel, 2001). A PEF is a compact non-stationary filter whose coefficients are computed directly from the data. Applying the computed PEF filter back on this data effectively annihilates the signal, leaving only a random white spectrum. Filter operators of this type are quite useful for non-stationary interpolation because the inverse (or more commonly the adjoint) of a PEF filter, when applied to a random field with a white spectrum, can be used to reconstruct data *with the same characteristics as the original data*. Thus, by training a PEF filter where one have data and then applying the filter to where one does not represents an effective way for performing multidimensional seismic data interpolation. Moreover, an advantage of this approach

is that it can estimate and reconstruct multiple reflector dips at the same location. Thus, a PEF-based interpolation approach can model weak seismic signals even in the presence of significant noise of different dips – which is definitely the case for 3D shot gathers in the Harvey Seismic data set.

Herein, we apply the APEF approach of Liu and Fomel (2011), who extend the computation of PEF filter coefficients beyond conventional practice to include scenarios exhibiting a highly irregular distribution of traces within a 3D shot gather. Data reconstruction using this technique is a two-stage approach. The first step involves estimating PEF coefficients in a [5,3,3] neighbourhood of each sample on live traces within the [N_t, N_x, N_y] volume. One then smooths the estimated coefficients over a [20,5,5] radius to better ensure reflector continuity. The second phase involves applying the inverse PEF filter to a random field of white noise that results in an infilling of traces at unknown locations. While recovering phase information proved straightforward, establishing the amplitudes proved to be more difficult. To address this issue Liu and Fomel (2011) set up an inverse problem with the goal minimising the roughness of the 3D shot gather volume. We ran ten iterations of the solver, after which additional iterations did not greatly affect the results. We restricted the interpolation radius to no greater than 200m because distances greater than this started to yield poorer 3D interpolation results.

Figure 37 presents an example of the APEF interpolation results. Before performing the interpolation we applied a fairly conservative first-arrival mute to remove the direct arrivals. This proved to be an important step because otherwise the inverse problem focused on fitting the much stronger direct arrivals, which threw off the amplitudes of the remaining components within the 3D shot gather.

Figure 37a presents a binned 3D shot gather prior to interpolation. The easting cross-section is fairly well sampled in this view; however, the northing cross-section is somewhat sparse with an average interval of 200m between receiver lines. The constant time slice in the upper panel better shows the acquisition sparsity, and highlights three holes in the middle of shot record. Figure 37b presents the shot gather in Figure 37a after applying the 3D APEF interpolation. Traces that were live in the upper panel are reconstructed exactly, while the missing traces have been filled in up to

a maximum distance of 200m, which has reduced the extent of acquisition holes accordingly.

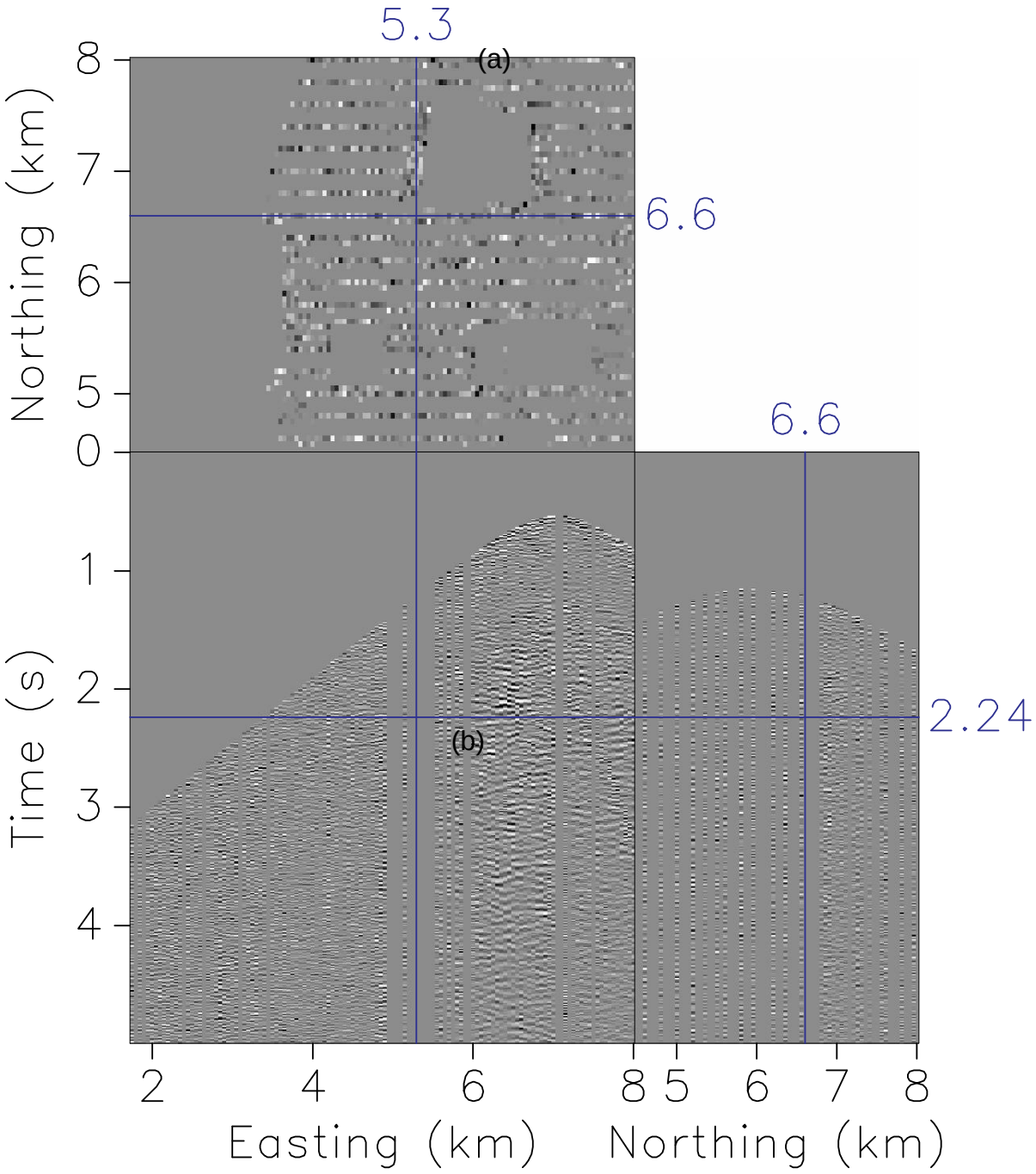

Figure 37a. APEF interpolation example. Binned 3D shot record.

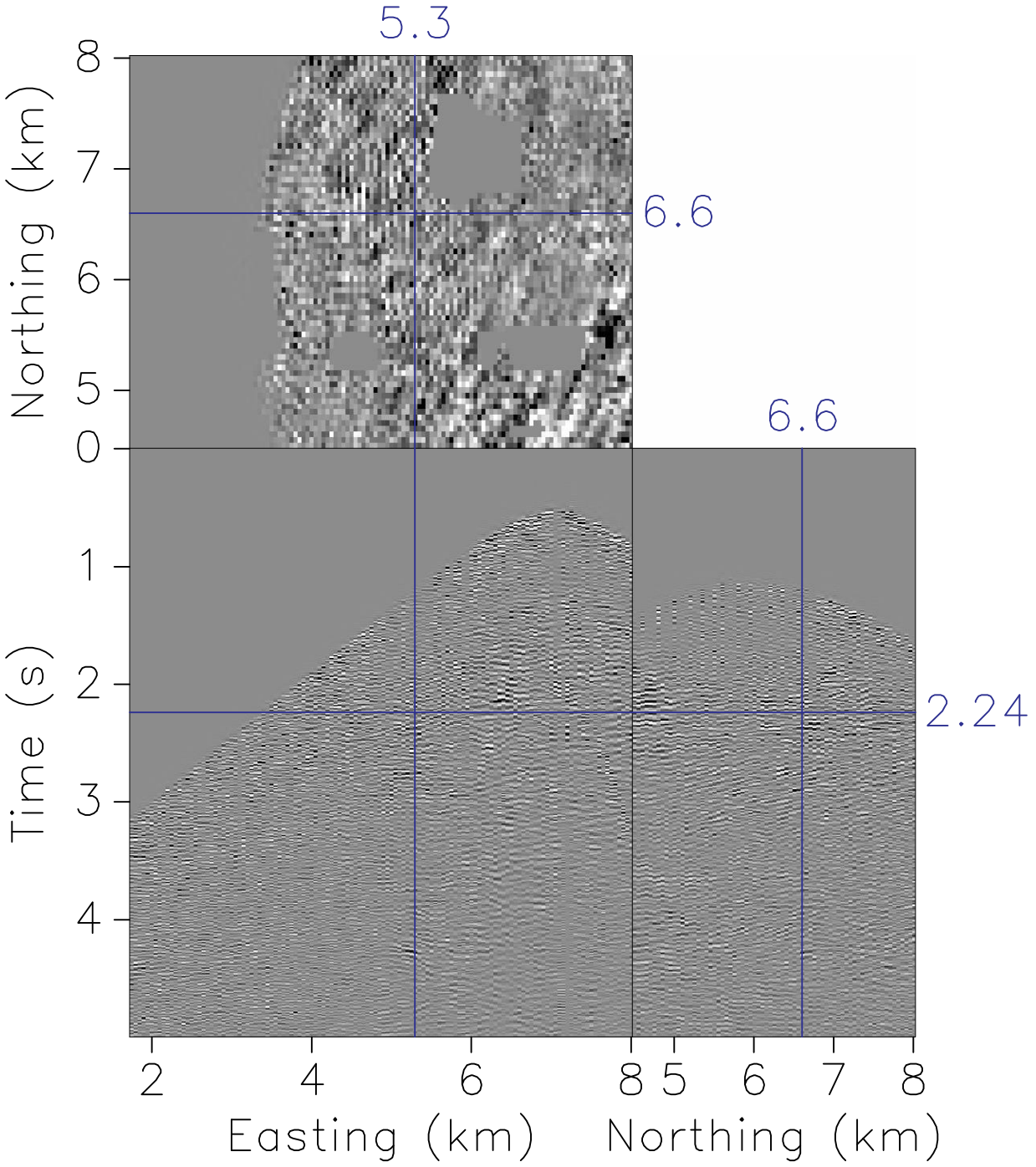

Figure 37b. APEF interpolation example. The same 3D shot record as for Figure 34a after applying 3D APEF interpolation routine

Figure 385 presents RTM imaging results for both the non-interpolated (Figure 385a) and interpolated (Figure 385b) results. The cube plot view in the upper panel suggests that some reflectivity has been successfully imaged. However, the depth slice illustrates that the migrated volume has fairly significant levels of noise throughout the migrated volume, but especially in the near surface (i.e., top 300m). The single-shot RTM result shown in the lower panel has significantly higher signal relative to the result in the upper panel, and has an overall higher signal-to-noise ratio and a lower level of noise within the top 300m. These results suggest that interpolated data set should be better for RTM analysis.

Other interpolation tests

Two additional interpolation techniques were investigated during the course of the PSDM work: 3D plane-wave destructors (PWDs) and 5D azimuthal moveout (AMO). The two-stage 3D PWD approach (Fomel, 2002) is quite closely related to the aforementioned APEF technique. The first stage involves estimating the local plane-wave dip field on live seismic traces. A smoothed version of these coefficients are then used during the second stage filtering operation is used to infill missing traces. While this technique proved to be useful for interpolating by a factor of two or three in well-sampled components of the 3D shot gathers, it suffered from being only able to estimate a single dip (i.e., no crossing events) representing the stronger event. Accordingly, interpolations of 3D shot gathers that exhibit low signal-to-noise levels were strongly and adversely affected by noise (e.g., contaminating residual surface wave). Thus, this approach was disregarded as not well suited for seismic data from the Harvey seismic survey.

AMO (Biondi et al., 1998) takes significantly different approach than the above two interpolation methods. This technique applies the AMO operator to the full 5D prestack volume in the midpoint-offset domain. This operator is analogous to the cascade of a forward dip moveout (DMO) operator for a known midpoint-offset location followed by an adjoint DMO operator to a neighbouring unknown midpoint-offset location. This allows for wavefield energy to be moved around a neighbourhood of the 5D hypercube to infill missing traces. The AMO operator represents a composite operator that can be applied in a mixed log-frequency (ω), Fourier-midpoint-wavenumber ($\mathbf{k_m}$) and spatial-

offset (**h**) domain. Although this approach works quite well for well-sampled data sets, the level of uneven sampling in the midpoint domain of the Harvey seismic survey data caused significant difficulties for the AMO approach. We attribute this to severe aliasing of the Fourier-midpoint-domain ($\mathbf{k_m}$) operators, which did not lead to useful interpolation results. Again, after initial tests we decided to not follow this approach.

Based on these experiences, we suggest using fully 5D temporal-spatial (i.e., t-**m**-**h**) or 5D frequency-spatial (i.e., ω-**m**-**h**) operators. Attempts were made to contact researchers specializing in these approaches for collaboration; however, we were unable to secure proprietary research codes for the present analysis, and this remains a topic for future study.

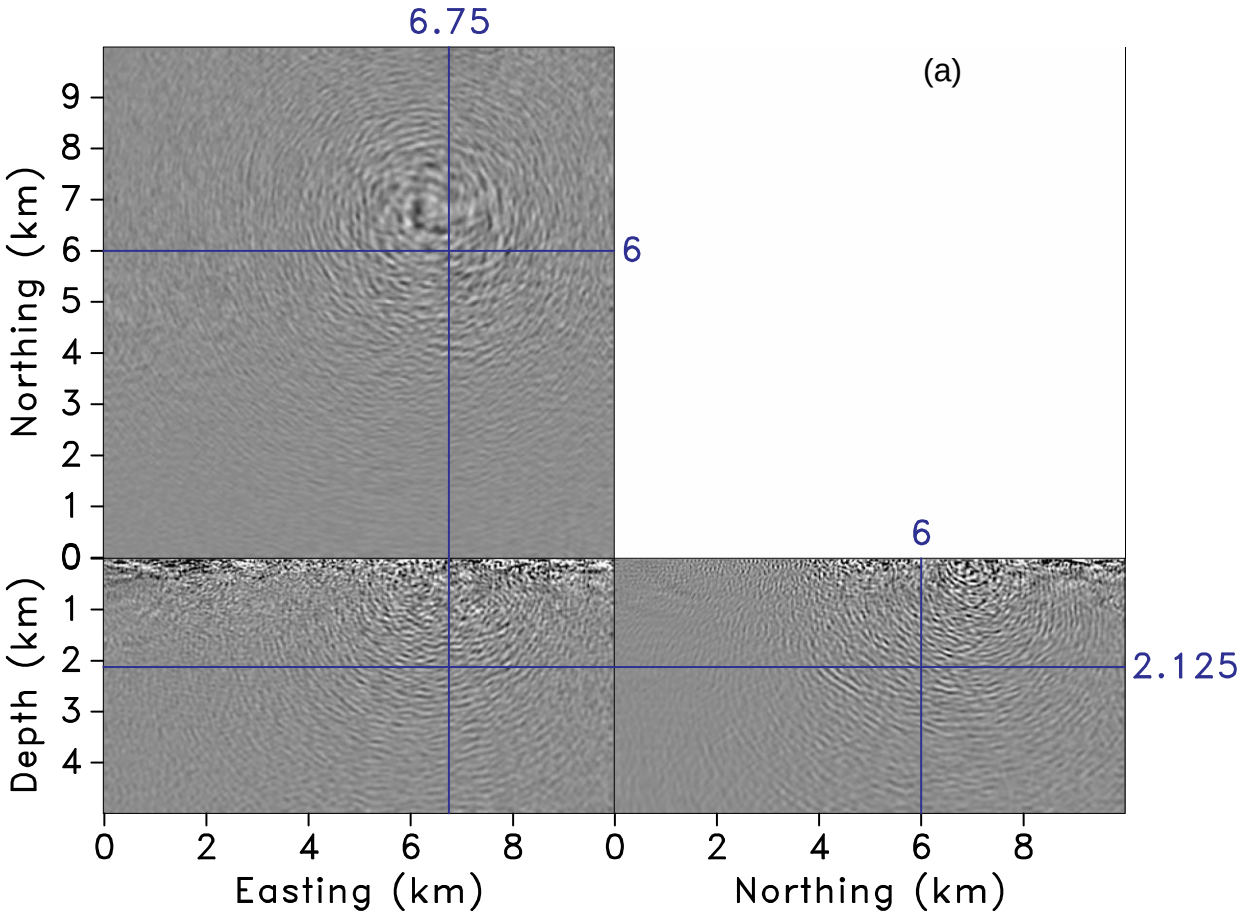

Figure 38a. Single-shot RTM result showing the benefits of interpolation on a 3D shot gather with one of the best signal-to-noise ratios - RTM of a non-interpolated shot gather.

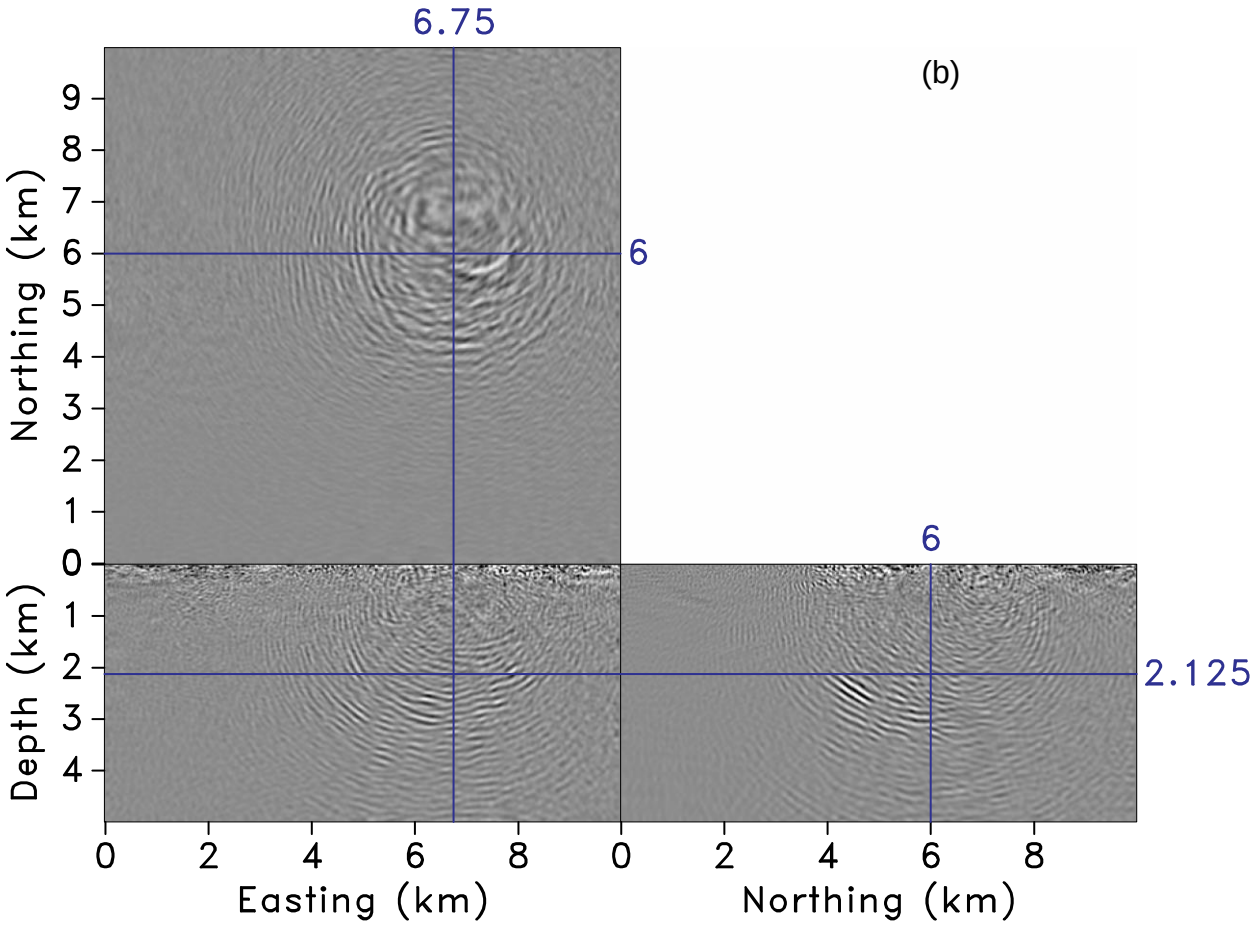

Figure 38b. Single-shot RTM result showing the benefits of interpolation on a 3D shot gather with one of the best signal-to-noise ratios. RTM of an interpolated shot gather.

2.6.4. 3D Reverse-time Migration

We applied a UWA proprietary GPU-based 3D RTM imaging code to the Harvey 3D survey data described above. The RTM code has been previously benchmarked against a number of industry benchmark 3D (marine) velocity models and is known to generate high-quality results for typical marine 3D exploration seismic data. The Harvey imaging test represents the authors' first attempt at using this RTM code on a 3D land data set exhibiting significantly sparser acquisition.

The RTM code has two different options for ``imaging condition'': (1) conventional cross-correlation (CC); and (2) inverse-scattering (IS) (Stolk et al., 1999). Using the CC imaging condition is known to lead to low-frequency noise in the result, which can then

be removed through filtering before generating a final image. One advantage of the IS imaging condition is that it applies a physics-based combination of spatial and temporal derivatives in the neighbourhood of the imaged point to automatically remove low frequency noise (Whitmore and Crawley, 2012) without the need for an additional processing step. Figure 39 illustrates the two different types of RTM imaging conditions applied to the same shot as presented in Figure 37. Figure 39a-b present the conventional CC and IS imaging condition, respectively. Note that the CC result without post-filtering exhibits low-frequency noise as expected, while the IS imaging condition results is comparatively noise-free.

All of the RTM results reported below were computed using the IS imaging condition on three nodes each with dual NVIDIA K10 GPU cards and connected to a fast *Infiniband* storage array. The RTM results were run at $\Delta x=\Delta y=\Delta z=25$m spacing in a model of dimension $[N_z,N_x,N_y]=[208,400,400]$, which was nearing the available memory limits of the K10 GPU. We used random boundary conditions in the model domain, which are designed to make any reflections from the boundary incoherent in the resulting imaging. The total wall time for the full 3D run of 5224 shots was 1.25 days, making these approximately 3-4X more computational expensive as the 3D Kirchhoff operators described above.

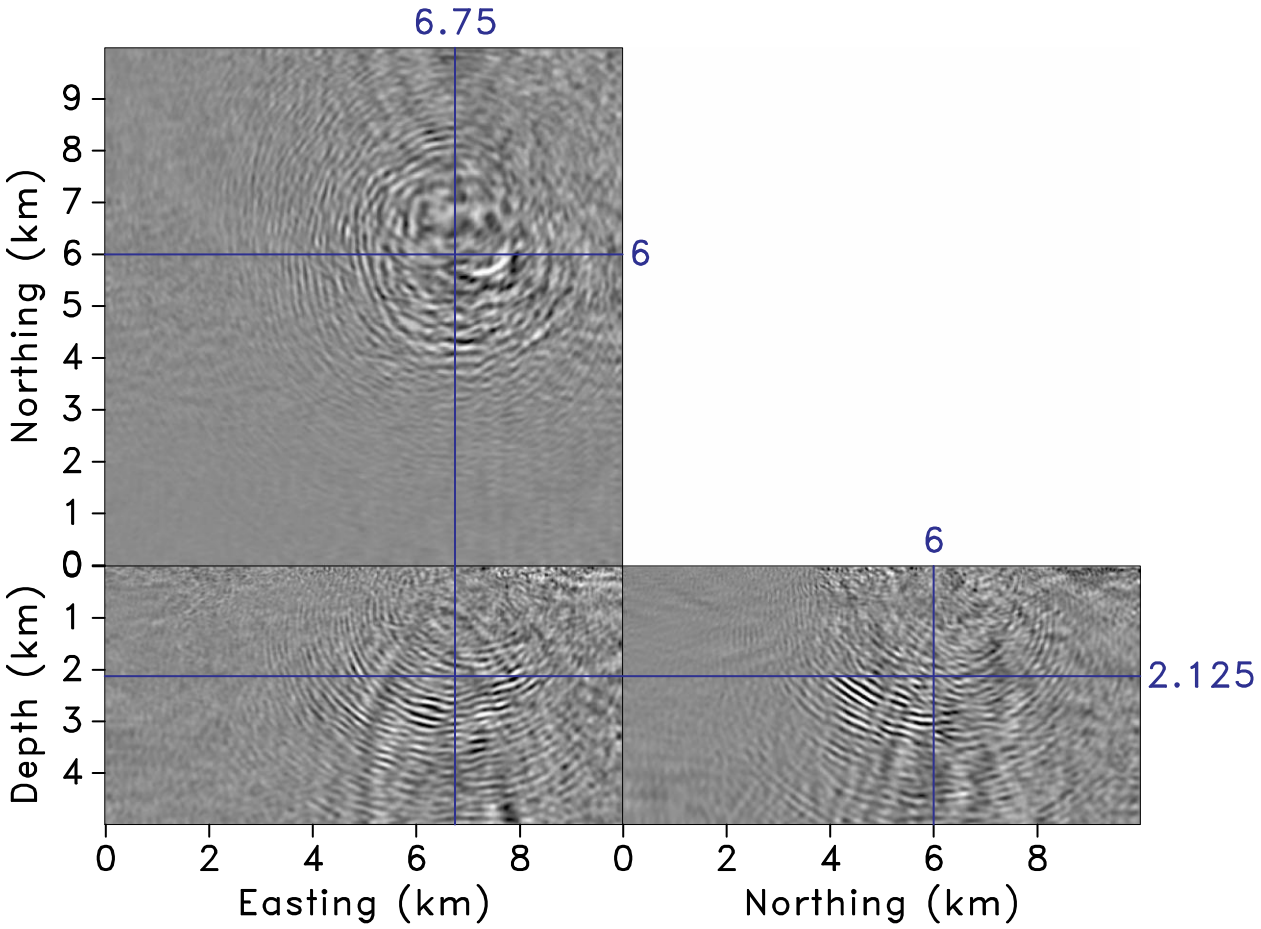

Figure 39a. Demonstration of the different RTM imaging conditions applied to the same single shot as in Figure 31(a,b) - Cross-correlation imaging condition.

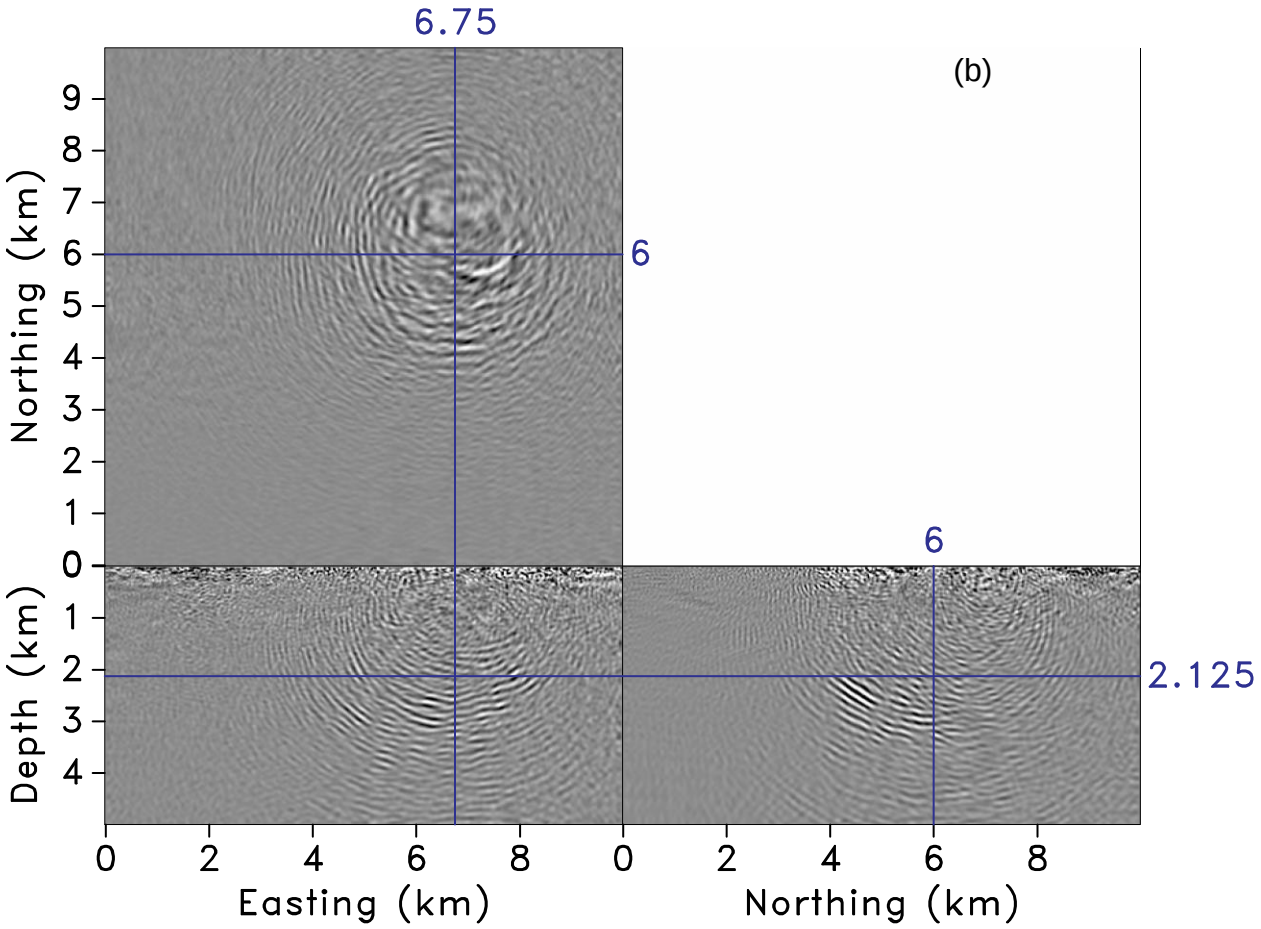

Figure 39b. Demonstration of the different RTM imaging conditions applied to the same single shot as in Figure 31. Inverse-scattering imaging condition.

Imaging results

Figure 417 presents a comparison of Kirchhoff and RTM 3D PSDM results for cross-sections taken at *x*=7.65km, *y*=7.5km and *z*=3.125km depth. Overall, the Kirchhoff result exhibits a much better and more broadband recovery of reflectivity as explained later - especially in the top 1km where little reflectivity can observed in the RTM results. The northing cross-section in the Kirchhoff results shows fairly flat strata that are separated by the F10 fault-plane reflection (or potentially two sub-parallel faults). The same panel in 3D RTM results does not show the fault-plane reflector; however, the presence of a fault can be inferred by an abrupt change in reflectivity, perhaps with a steeper dip. This observation is echoed by the more weakly imaged fault in the easting panels. The depth slice show similar structure, though illustrates that the 3D RTM result is more band-limited and of lower resolution. Table 7 provides a summary of the parameters used for the 3D RTM imaging analysis.

Figure 42 presents an additional cube plot comparison taken at *x*=5.9km, *y*=8.0km and *z*=3.19km depth. The northing RTM panel shows reflectivity between 1-5km depth that is similar to the Kirchhoff results. However, the near surface is again poorly resolved and some of the reflectivity is not well imaged between X=3-6km. A third comparison showing similar results is presented in Figure 50.

The 3D PDSM results demonstrate that 3D Kirchhoff migration operators are able to successfully image reflectivity from the large-scale 3D geologic structure contained within a target-oriented 10x10km^2 area of the Harvey 3D seismic survey to depths of nearly 6km. The western half of imaged area shows a 1.5km-thick geologic unit of broad lateral extent with little internal reflectivity that dips slightly to the west. The eastern half of the image volume highlights a prominent fault reflector, presumably associated with the F10 fault. Overall, the 3D Kirchhoff PSDM results showed a modest uplift over the fast-track pre-stack time-migration (PSTM) results, and represent a worthwhile exercise to be applied at future Australian CO_2 geosequestration sites.

Table 7: Table of gridding and migration parameters for 3D RTM work.

Parameter	**Value**
Coordinate system	UTM Zone 50 H (South)
Grid min x (cell centered, Easting)	384000m
Grid max x (cell centered, Easting)	393975m
Grid min y (cell centered, Northing)	6340500m
Grid max y (cell centered, Northing)	6350475m
Grid min z (cell centered, depth)	0.0m
Grid max z (cell centered, depth)	5750.0m
Δx	25m
$\text{Number of cross-line bins}$	400
Δy	25m
$\text{Number of inline bins}$	400
Δz	25m
$\text{Number of depth levels}$	208
Offset bin increment	100m
Shot bin sampling in *x* and *y*	50m
Receiver bin sampling in *x* and *y*	50m
Number of offset bins	94
Number of shots	5224
Maximum aperture in *x* and *y*	10km

PSDM imaging with the 3D RTM approach was less successful than with the corresponding 3D Kirchhoff operators. The RTM image volumes generated demonstrated an ability to image reflectivity at depths greater than 1km; however, the numerical experiments indicated this technique was not that well suited due imaging issues largely associated with to the irregular source and receiver sampling and large acquisition holes. While 3D APEF interpolation within shot records was observed to improve the RTM results relative to non-interpolated data, the resulting RTM images were more band-limited and suffered from significant aliasing within the top 1km. Moreover, the 3D RTM analysis was roughly 3-4x computationally more expensive then Kirchhoff. Thus, even though RTM has become an accepted 3D technique for imaging

complex geologic structure in industry-oriented marine seismic settings, applying RTM in 3D land seismic scenarios may only be warranted for scenarios where: (1) data are more regular sampling throughout the full 5D seismic data volume; and (2) the true velocity models are of sufficient complexity to cause the breakdown of the approximations underlying Kirchhoff migration operators.

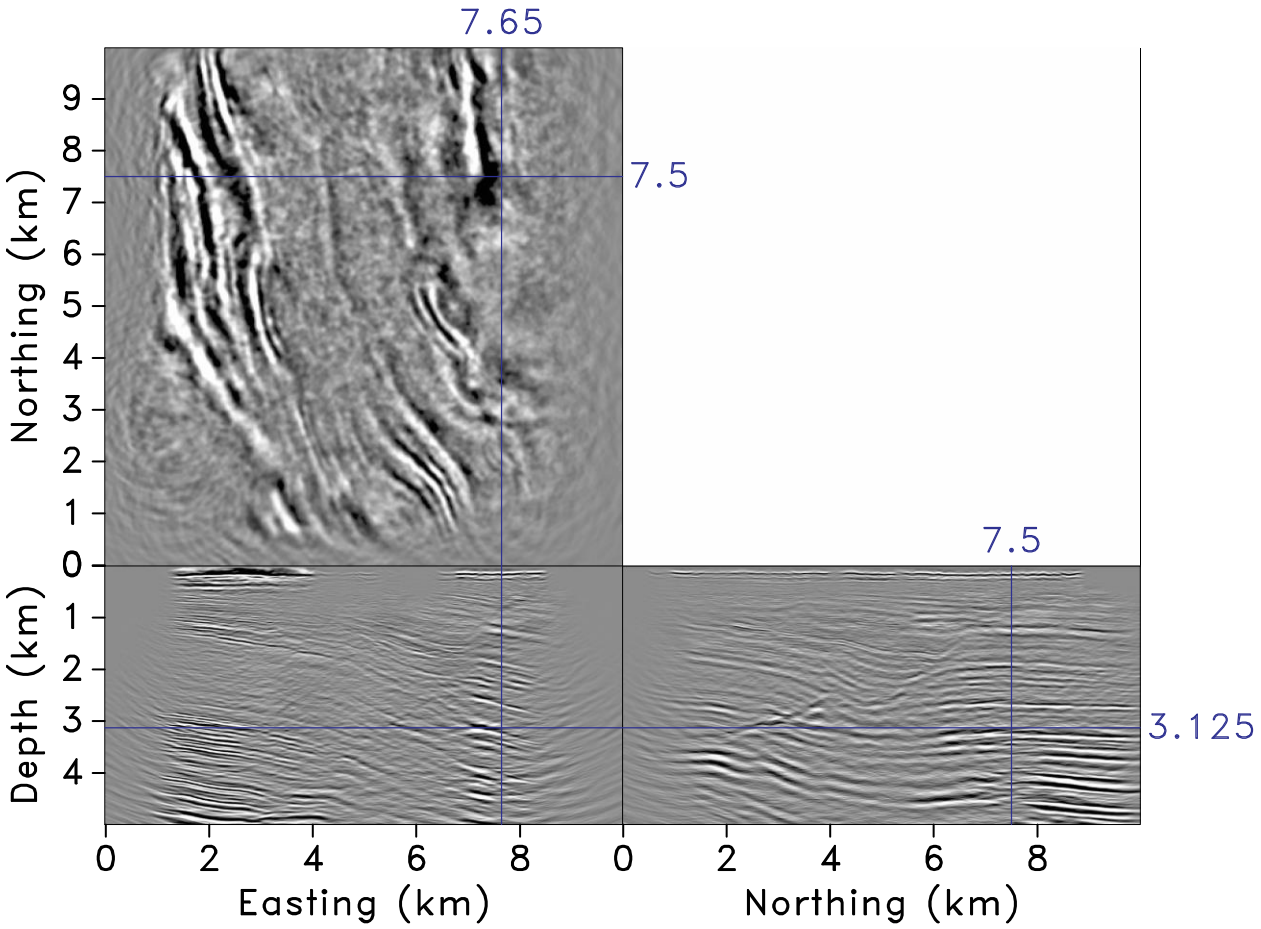

Figure 40a. Comparison of two different 3D PSDM results extracted at constant slices locations [x,y,z]=[7.65,7.5,3.13]km. Kirchhoff migration.

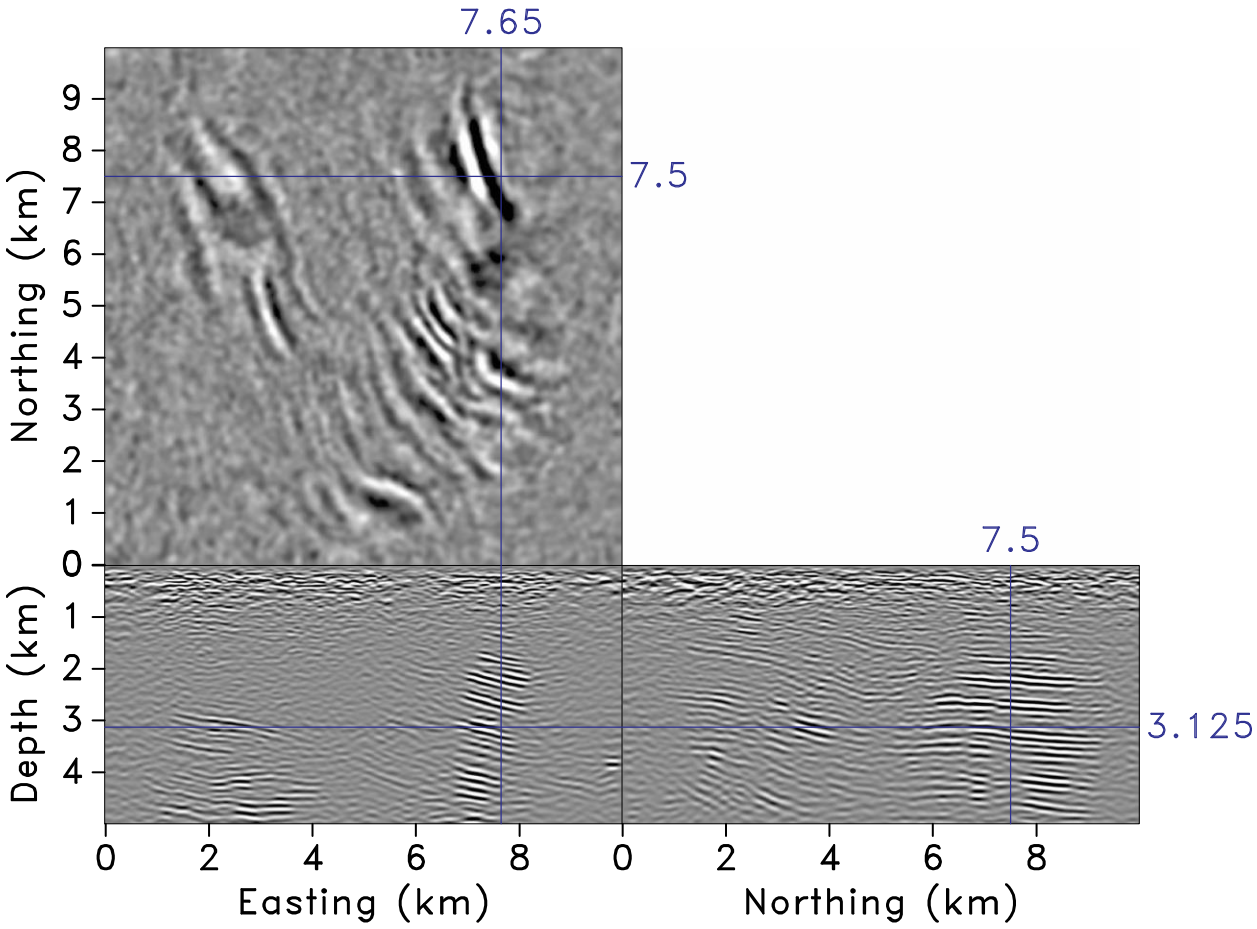

Figure 40b. Comparison of two different 3D PSDM results extracted at constant slices locations [x,y,z]=[7.65,7.5,3.13]km. (Reverse-time migration (inverse-scattering imaging condition).

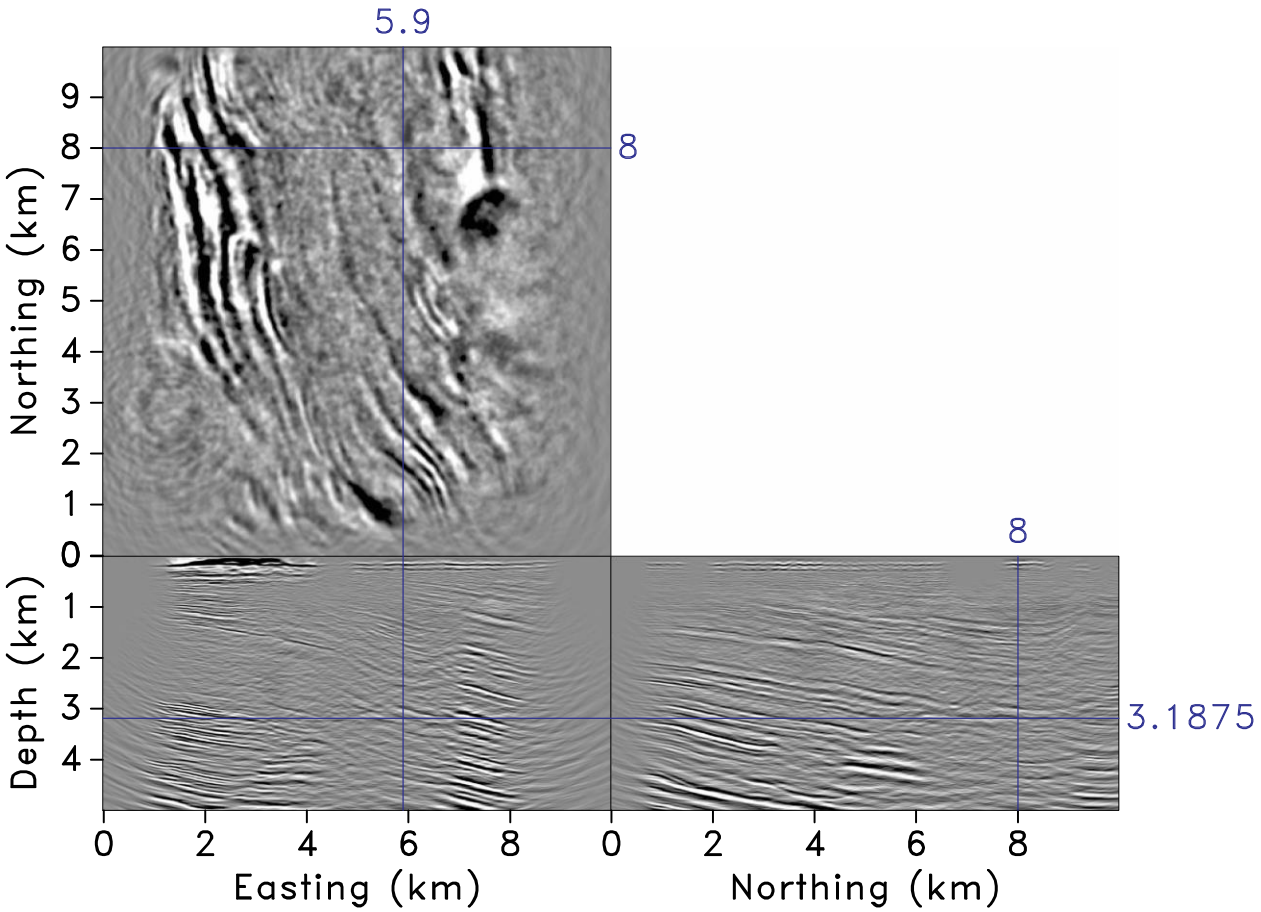

Figure 41a. Comparison of two different PSDM results extracted at constant slices locations [x,y,z]=[5.9,8.0,3.19]km. Kirchhoff migration.

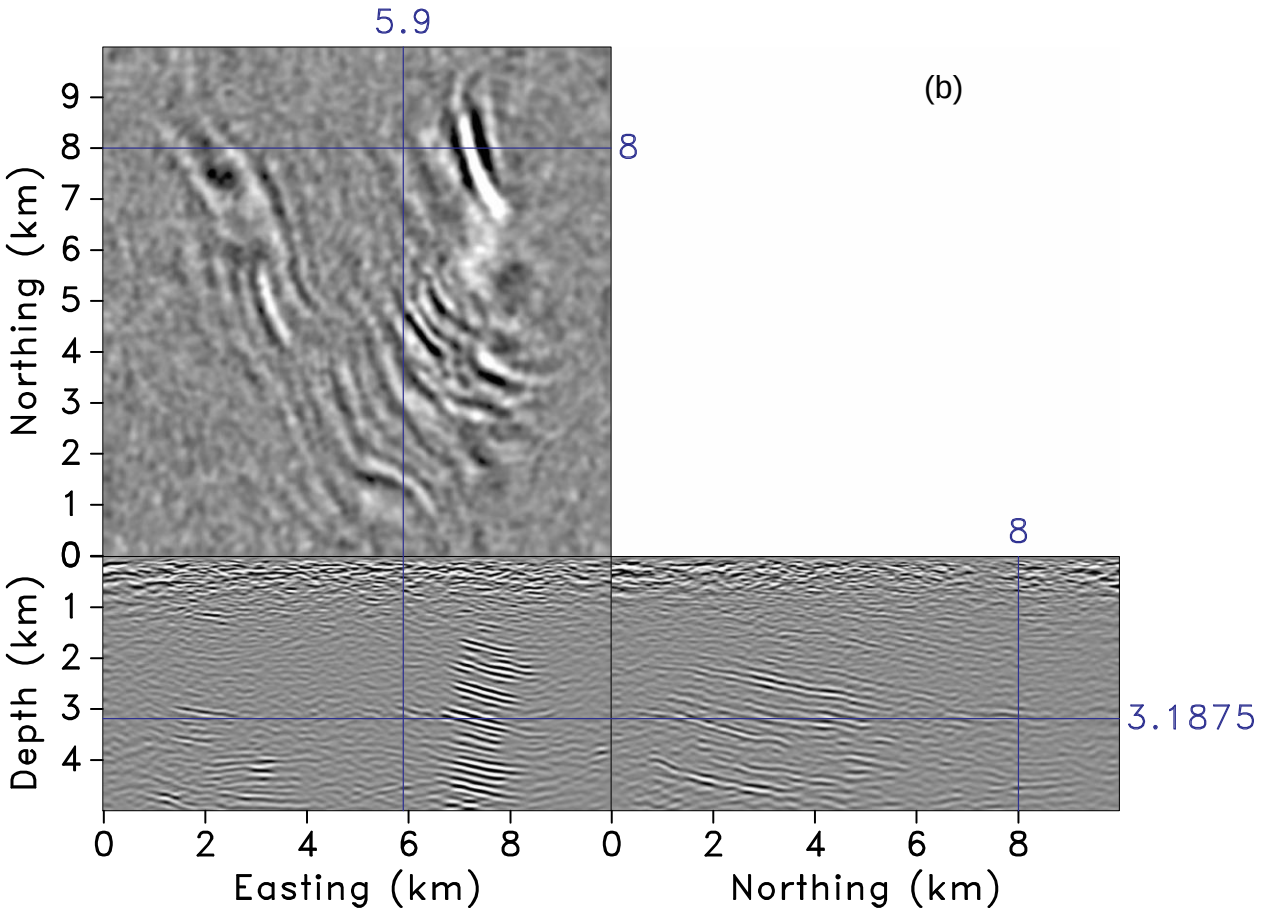

Figure 41. Comparison of two different PSDM results extracted at constant slices locations [x,y,z]=[5.9,8.0,3.19]km Reverse-time migration (inverse-scattering imaging condition).

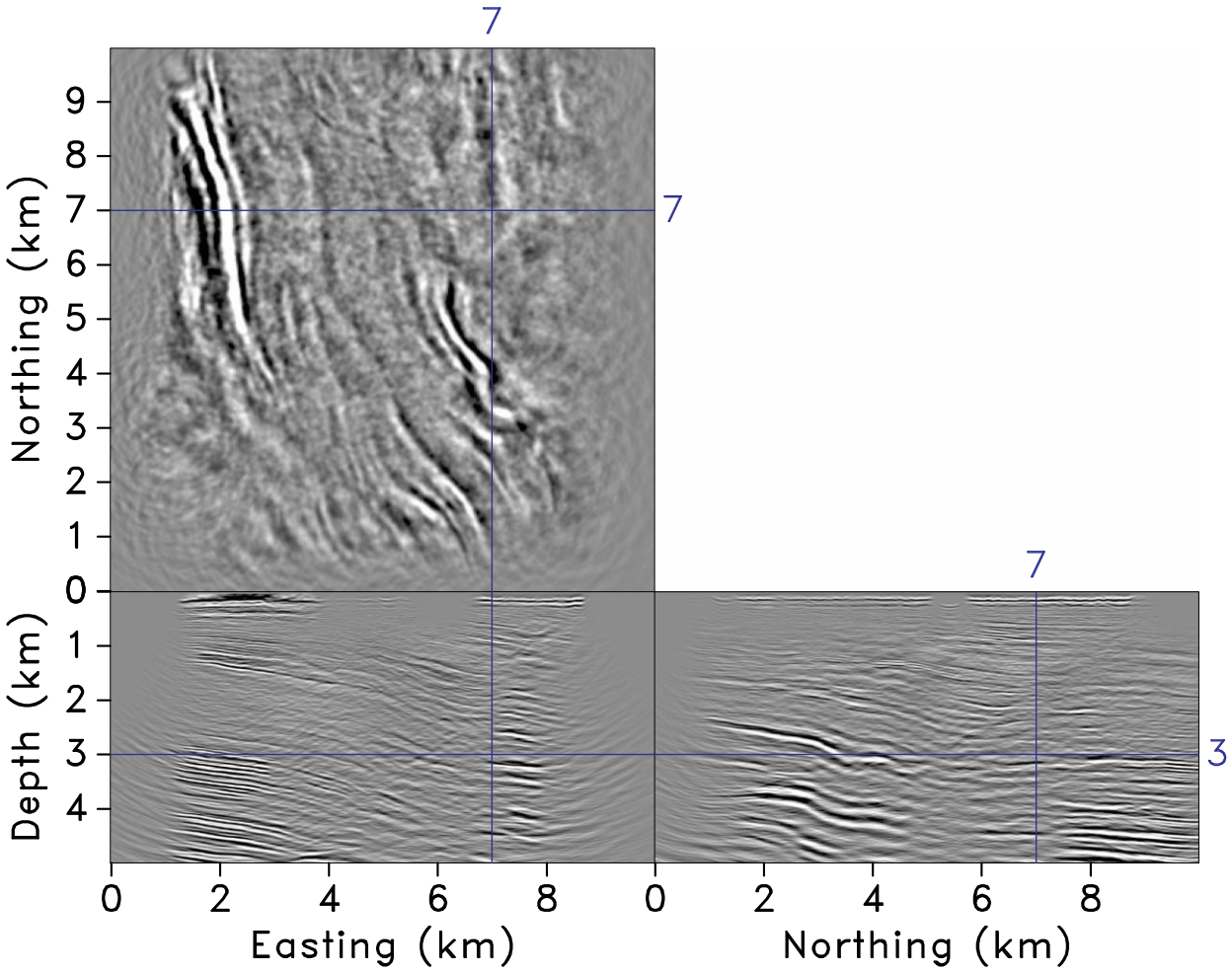

Figure 42a. Comparison of two different PSDM results extracted at constant slices locations [x,y,z]=[7.0,7.0,3.0]km - Kirchhoff.

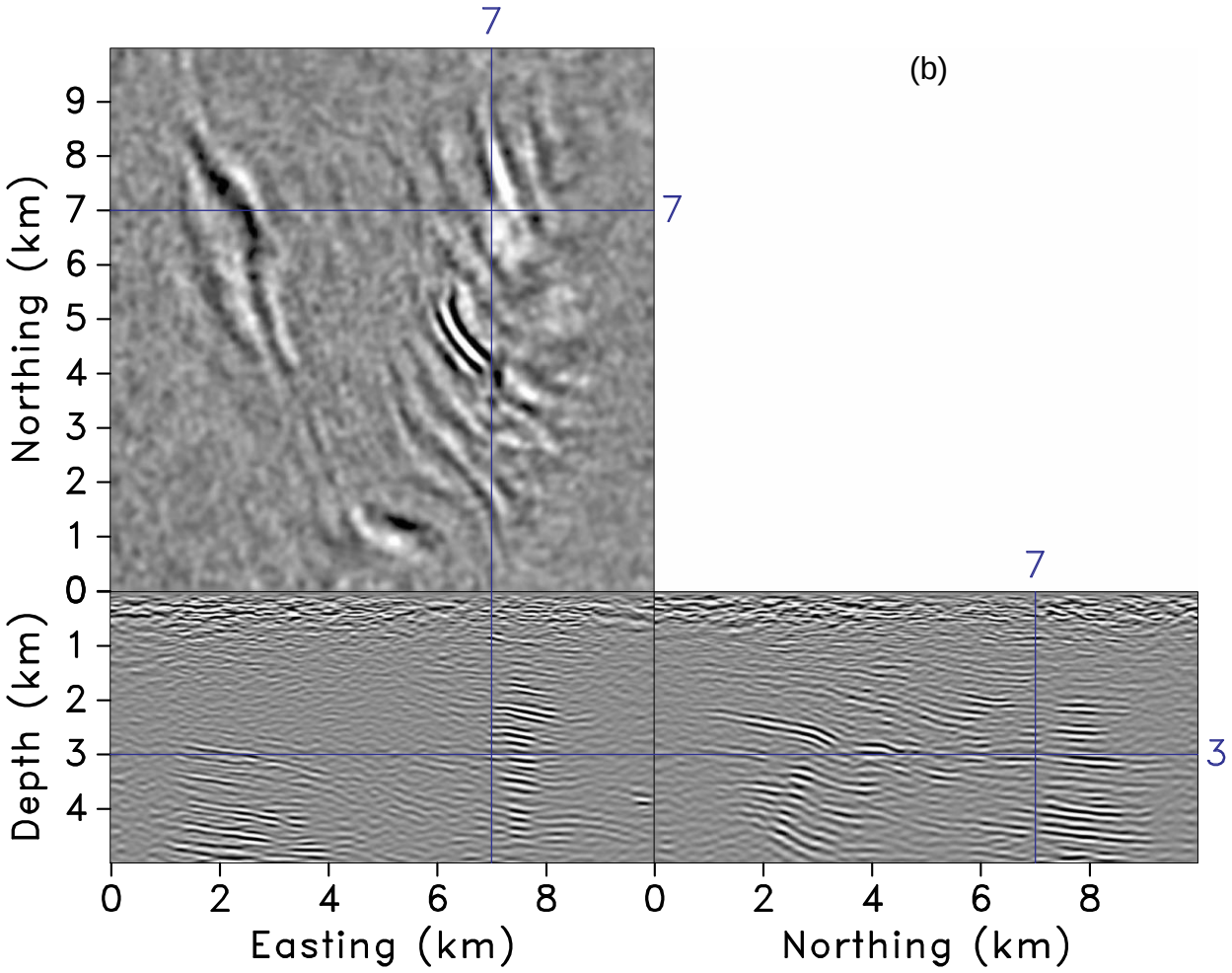

Figure 42. Comparison of two different PSDM results extracted at constant slices locations [x,y,z]=[7.0,7.0,3.0]km. Reverse-time migration (inverse-scattering imaging condition).

2.7. Diffraction imaging and steered migration

The assessment of subsurface structure and location of faults is key information for CO_2 geosequestration projects. In order to support the fault detection and decrease uncertainties on the structural framework, two additional imaging techniques have been applied to the 3D seismic volume. One is a diffraction imaging algorithm (Alonaizi et al, 2013), the other is a modified post-stack Kirchhoff migration – steered migration (Tertyshnikov et al, 2013). These algorithms are currently implemented in Matlab codes for 3D zero-offset/stacked data case.

2.7.1. Diffraction Imaging

The importance of diffractions for detection of geological heterogeneities has been studied for a long time (Krey, 1952; Trorey, 1970; Landa and Keydar, 1998). Local heterogeneities (faults, truncated interfaces, edges of CO_2 plume, fractures, etc.) are acting as scatterers (diffractors) in the recorded seismic field. Herein, the method of focusing the diffraction energy from scattering points on the common-diffractor-point volume (D-volume) (Alonaizi et al., 2013; Landa and Keydar, 1998) has been applied to identify and trace such geological features. The approach is defined by a procedure of measuring the coherency along a diffraction hyperboloid using semblance function (Taner and Koehler, 1969), which shows the weighted energy of the seismic signal at the location of the local diffractors on the D-volume. Diffractions from linear elements are formed by superposition of signals along hyperboloids generated from every scatter point on the object. In the case of edge diffractions, there is the 180 degree phase change across the point on the diffraction traveltime curve that corresponds to the reflected energy as well (Trorey, 1970). This fact can be used in order to separate edge diffractions from other wavefield components and to distinguish the diffraction produced from the edges of structural objects. The maximum semblance values obtained for every sample of the image form the D-volume are used for detection of geological targets. Diffraction from elongated objects is represented by overlapping of signals along diffraction hyperboloids. In such cases, only a part of every diffraction surface that is contributing to the total envelope of the overlapped hyperboloids along the linear segment has to be focused. The maximum semblance values are used to form the D-volume in order to emphasize orientation of the diffraction linear objects (fault, fracture zones).

The DMO corrected stack seismic volume has been used as an input to the diffraction imaging algorithm (we plan to expand existing post-stack diffraction imaging to pre-stack domain later).

To image the diffractions (to obtain the D-volume), the following workflow has been applied:

- The full range of possible orientations of a diffractor was divided into intervals of horizontal azimuths α. The interval increment Δα was 5°. (Figure 43)

- The diffraction hyperboloid was computed for every image point (trace and t_0).
- The lateral offset h from the line passing through the image point in the direction orthogonal to the direction of the analysis (expected orientation of the diffractor) was chosen for each trace. Data within the offset range ±h are using for the analysis. The offset 50 m was used. (Figure 43)
- In case of edge diffraction, the polarity of the signal along the line passing through the image point in the direction of the analysis is reversed.
- The semblance *W(a)* is computed from the time window along the part of the hyperboloid limited by the offset range ±h. The time window of 30 ms was used (trade-off between resolution and capturing most of the seismic energy within given period). Thus, for every direction of the analysis the semblance volumes are computed using the following equation:
- $$W(\alpha) = \frac{\sum_{k=-m}^{m}\left(\sum_{i=1}^{N} f_{s(t,i)+k,i}\right)^2}{N\sum_{k=-m}^{m}\sum_{i=1}^{N} f_{s(t,i)+k,i}^2} \qquad (2\text{-}1)$$

  where *i* is the trace number, *s(t,i)* is the sample number which corresponds to the diffracted wave travel time *t* in the i^{th} trace, $f_{j,i}$ is the j^{th} sample of the i^{th} trace, *2m* is the time window (given by the number of samples) and *N* is the number of traces in the selection.

- The last step is the estimation of the maximum semblance for corresponding azimuth that forms the D-volume.

The maximum semblance values obtained for every sample of the image form the D-volume, which is used for detection of geological targets. Diffraction from elongated objects is represented by overlapping of signals along diffraction hyperboloids. In such cases, only a part of every diffraction surface that is contributing to the total envelope of the overlapped hyperboloids along the linear segment has to be focused. The maximum semblance values are used to form the D-volume in order to emphasize orientation of the diffraction linear objects (fault, fracture zones). The robustness of the D-volume imaging in the presence of band-limited random noise for resolution in time (vertical resolution) has been shown by Alonaizi et al. (2013). Two types of D-volume can be defined: the first one is the volume computed with the phase change taken into account; another one evaluated without consideration of that phenomenon. Computation of the phase shift D-volume requires flipping of the

signal polarity along a line passing through the image point in the direction of the selected azimuth (fourth step of the workflow). Both types of the D-volumes can serve as an effective tool for reliable detection of local heterogeneities, linear and subvertical objects.

The final D-volume (computed without phase change, provided as Diffr_Energy_Distribution.sgy) is used to define the locations of the diffraction objects (fault, fracture zones).

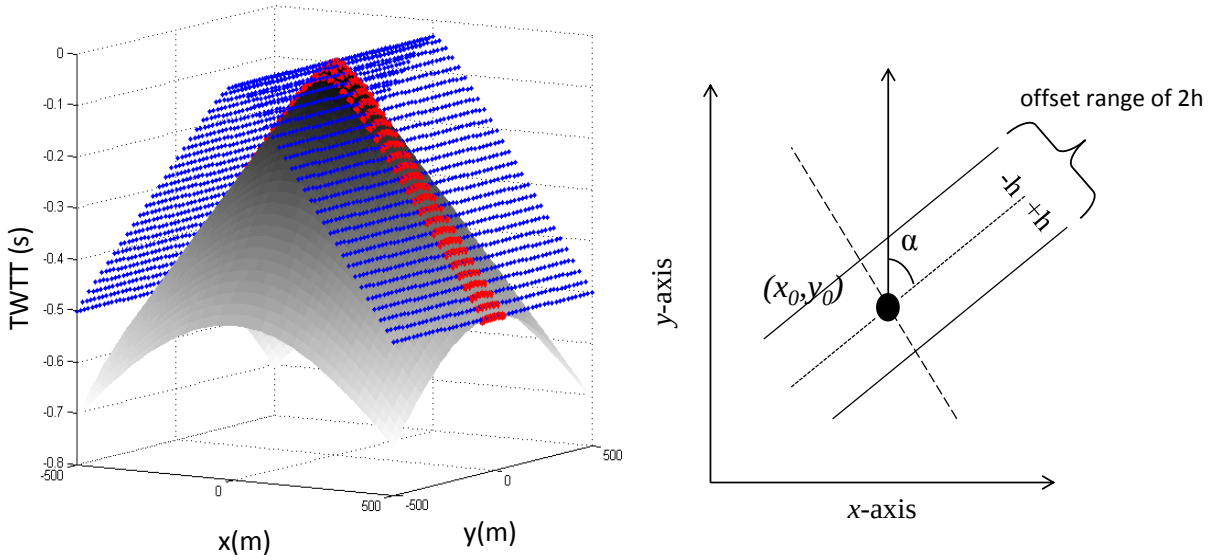

Figure 43. Left: Diffraction hyperboloid (grey) and a corresponding direction of the edge diffraction (blue). A limited offset (red) used to compute the D-volumes. Right: 2D projection showing the parameters used for D-volume computations, where α is the azimuth and the dashed line is where we split the diffraction traveltime for phase change. (Alonaizi et al, 2013).

Figure 44 and Figure 45 show examples of time-slices through the computed D-volume. Dark colours indicate the maximum of diffraction energy. The high diffractivity values correlate with the areas between the apparent faults in the migrated sections. The proper interpretation of the D-section will require more work and potentially use of the more accurate velocities obtained during the pre-stack migration process.

Figure 46 shows cross section 5095 through the D-volume.

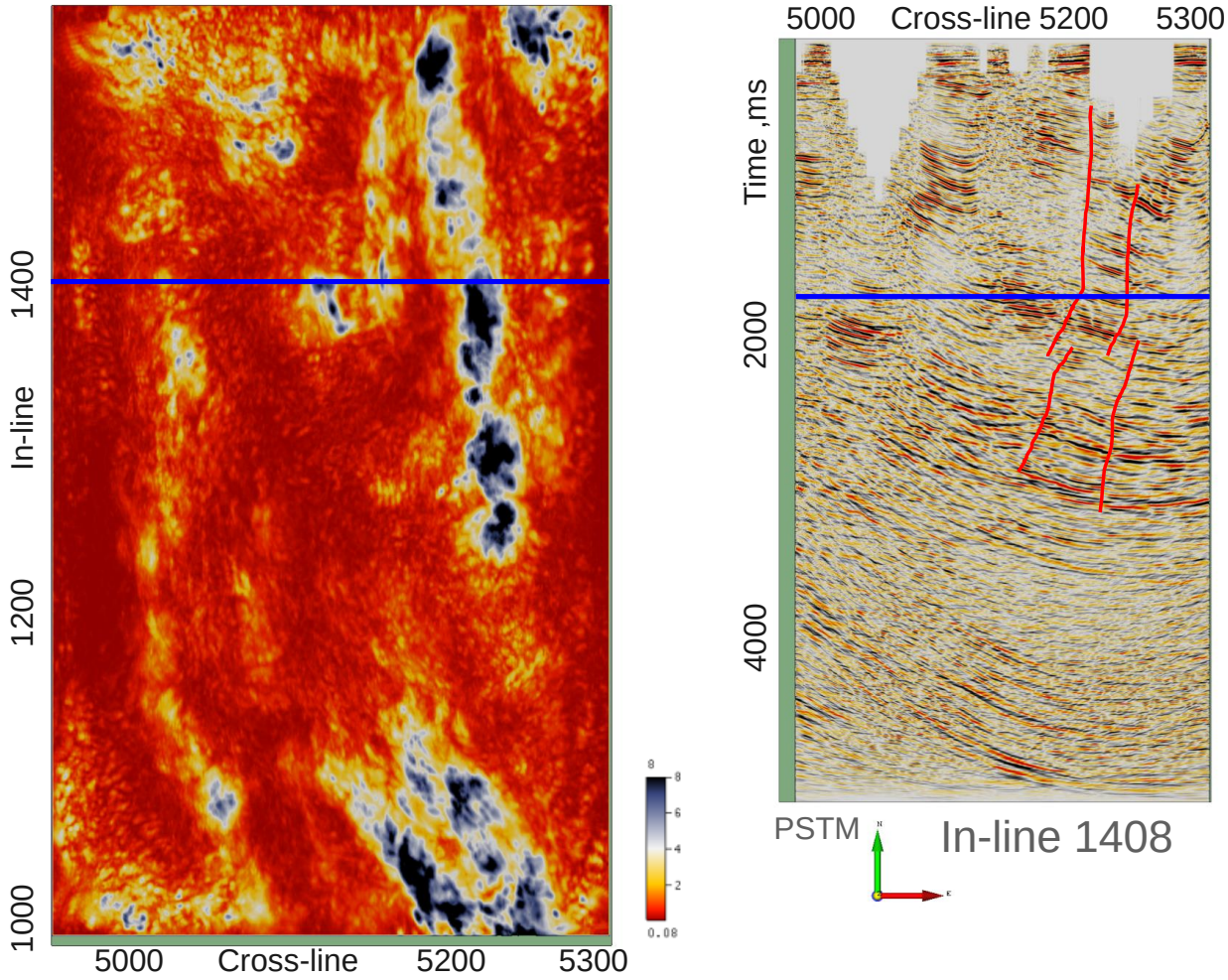

Figure 44. D-volume time-slice 1671 ms. Red lines indicate the appearance of faults on the migrated inline 1408 (PSTM_volume_.sgy). Blue line on the time-slice indicates a location of the corresponding inline 1408 and vice versa.

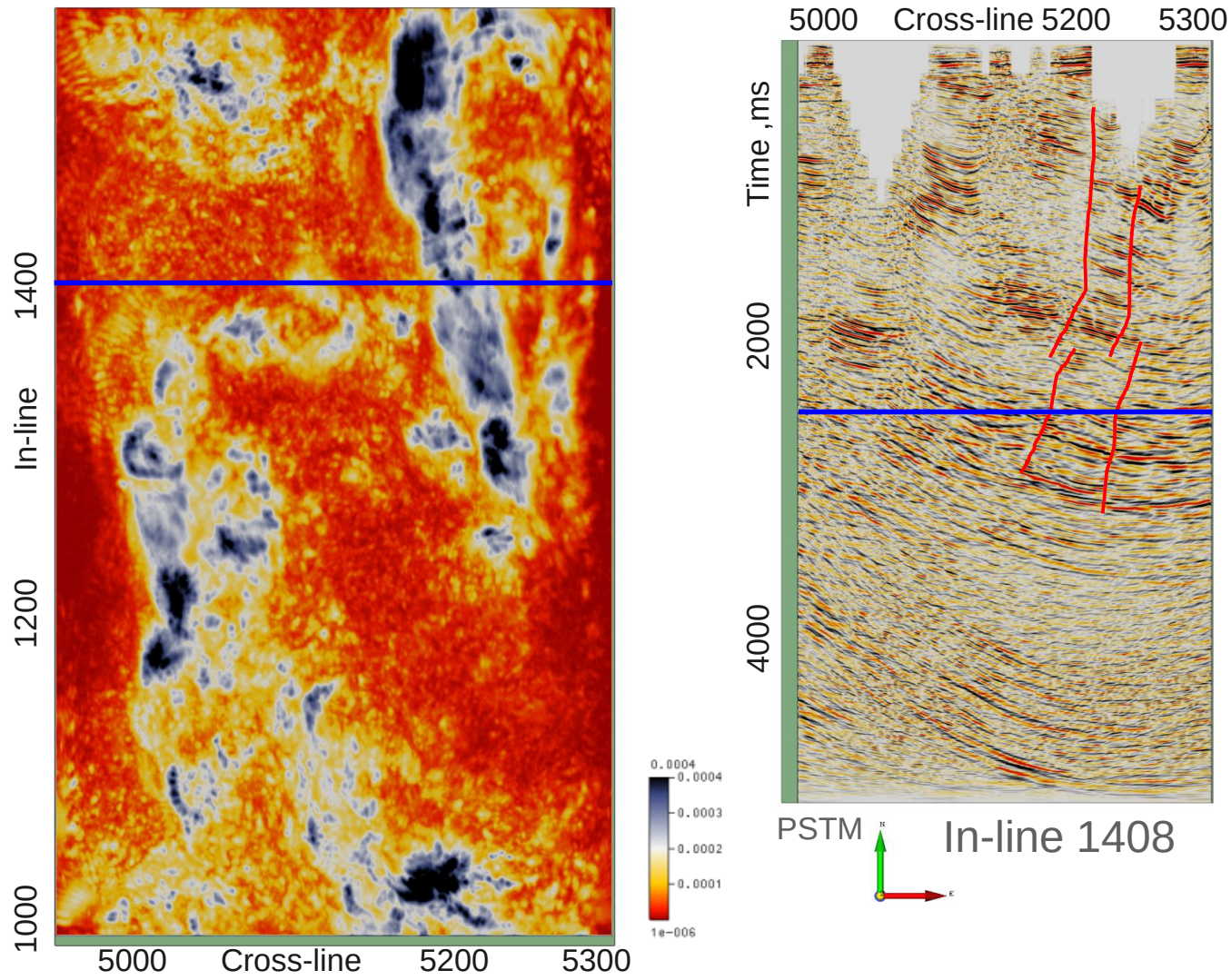

Figure 45. D-volume time-slice 2424 ms. Red lines indicate the appearance of faults on the migrated inline 1408. Blue line on the time-slice indicates a location of the corresponding inline 1408 and vice versa.

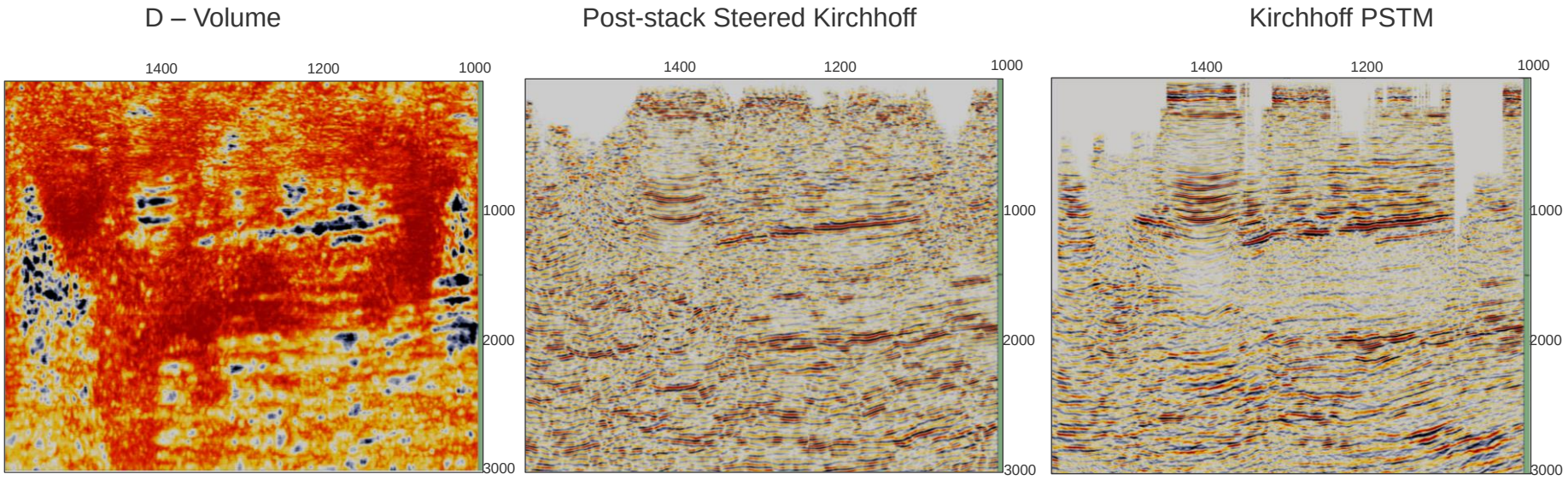

Figure 46. Cross-line 5095. D-volume - left panel. Steered Kirchhoff migration – central panel (Steered_Migration_volume.sgy). PSTM – right panel (PSTM_volume_.sgy).

2.7.2. Steered Migration

A modification of the 3D Kirchhoff post-stack migration algorithm which utilizes attributes obtained from the diffraction imaging algorithm to weight or steer the main Kirchhoff summation (Tertyshnikov et al, 2013) has been applied to the 3D seismic volume to enhance appearance of faults and continuity of the formation interfaces. The DMO corrected stack has been used as input for the steered migration.

A reflected wave from an interface can be viewed as superposition of the waves diffracted from every point of the interface. This means that the offset–travel-time curve (or surface in 3D) of the diffracted waves is tangent to the offset–travel-time curve (surface) of the specular reflection. Therefore all Kirchhoff migration algorithms comprise several common steps (Bancroft 2007):

1. For each output location, define a travel-time curve of the diffracted wave.
2. Compute a weighted sum of the input samples along this travel-time curve.
3. Place this sum into the output location.
4. Apply a wave-shaping filter.

For the 3D post-stack case, the data corresponding to a given reflected or diffracted wave belongs to an offset–travel-time surface. Conventionally, at the second step, the summation will occur along the complete diffraction travel-time surface, possibly with some corrections for the aperture. This surface is tangent to the actual travel-time surface of the specular reflection only along a certain contact curve/point. All corresponding input samples along the surface will contribute to the summation, whereas the actual signal energy is concentrated along one curve/direction only. The main idea of the steered migration is to detect this direction and give the higher summation weights to the input samples close to this direction. By doing this, those areas of the diffracted-wave travel-time hypersurface that do not have sufficient signal energy are effectively excluded and consequently the signal-to-noise ratio of the output is increased (coherent noise, such as multiples, will, obviously, be treated by this

approach as part of the signal, however we believe that the uncorrelated noise is a bigger issue for the Harvey 3D data).

The steered migration is taken the DMO corrected stack volume as input. The algorithm comprises of the following steps:

The first step of the migration is to compute an offset–travel-time curve of the diffracted wave for every output location. Then, for each horizontal direction (azimuth) α, the portion of this travel-time surface limited by a lateral offset h (this parameter should be chosen based on actual data) from the straight line passing through the scatterer in this direction is selected. The following step is to estimate the semblance W(α) in the time window use the selected portion of data. The next step is to compute a weighted sum of the input samples along this travel time curve using W(α) as a weighting function. Final step is to place this sum into the output location and apply a wave-shaping filter.

The following parameters have been used for the steered algorithm:

- angle increment for diffraction azimuth scanning α is 5°,
- lateral offset limit for the searching directions h is 50 m,
- time window used for semblance function calculation is 30 ms.

The actual parameter testing was largely done during tuning of the diffraction imaging algorithm (as the only difference is in the fact that we do not flip polarity of the signal over the apex of the diffracted wave while computing the semblance function for azimuthal weighting).

Figure 47 shows the comparison of two post-stack algorithms: phase-shift migration and steered migration. One can note that faults are much more pronounced on the steered migrated section and continuity of formation interfaces is significantly improved.

Figure 48 shows results of the pre-stack time migration and the steered time migration. Although the quality of the PSTM section is understandably higher, some faults are better defined on the steered migration section.

In order to verify the appearance of faults on the steered migration data we compared results with a minimum similarity attribute that has been derived from the PSTM volume. This attribute that sharpens the faults and suppresses non-fault discontinuities was designed by integrating dip attributes, similarity attributes, median dip filter and diffusion

filter (dGB, 2012). The minimum similarity attribute has been calculated from the PSTM seismic volume. Figure 49 shows the cross-line 5243 with results of the steered migration (the left section) and minimum similarity attribute (the right section). The set of anomalies of the similarity attribute (circled red) can be observed along the fault which is detected on the steered migration data. This might support the fault interpretation of the steered migration data.

Phase Shift Migration

Steered Migration

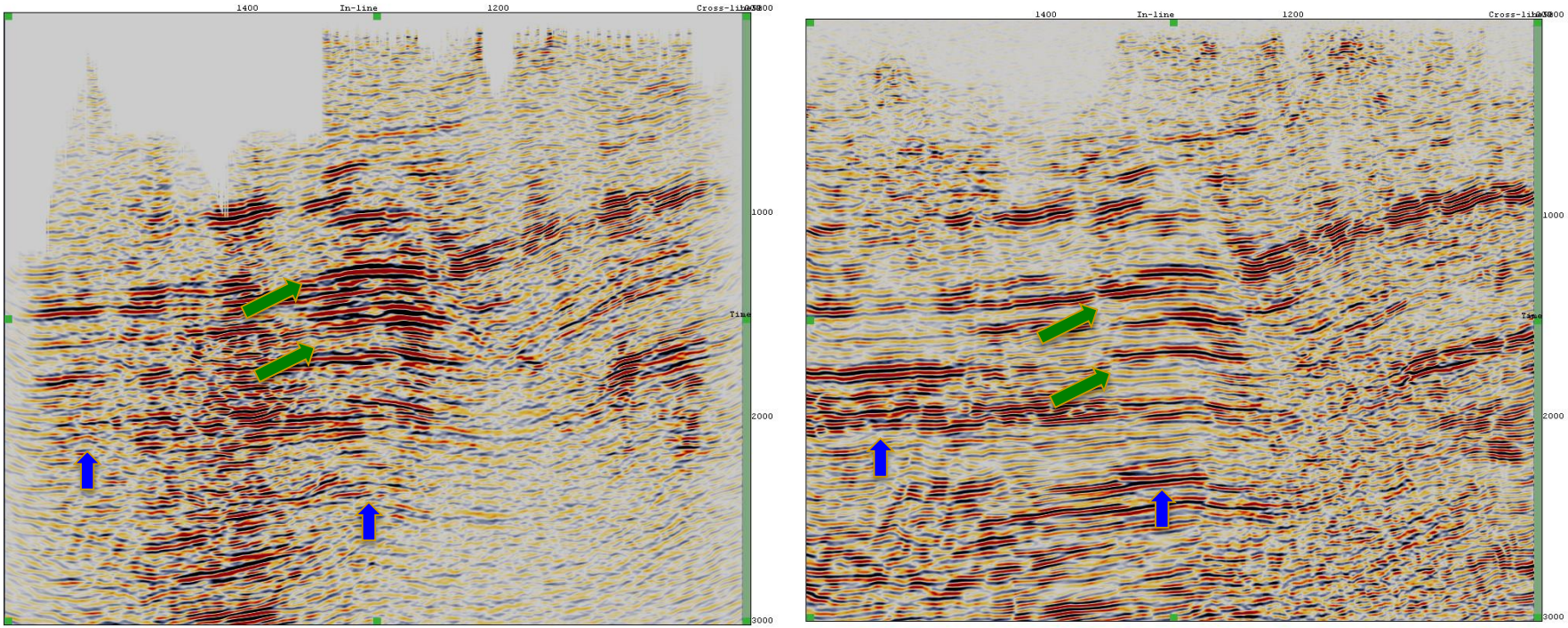

Figure 47. Comparison of two post-stack migrated volumes. Cross-line 5243. The left one is a result of the phase-shift post-stack migration. The right is a result of the steered Kirchhoff migration. Green arrows indicate the improvement of a fault image. Blue arrows indicate the improvement of interfaces continuity.

Kirchhoff PSTM

Post-stack Steered Migration

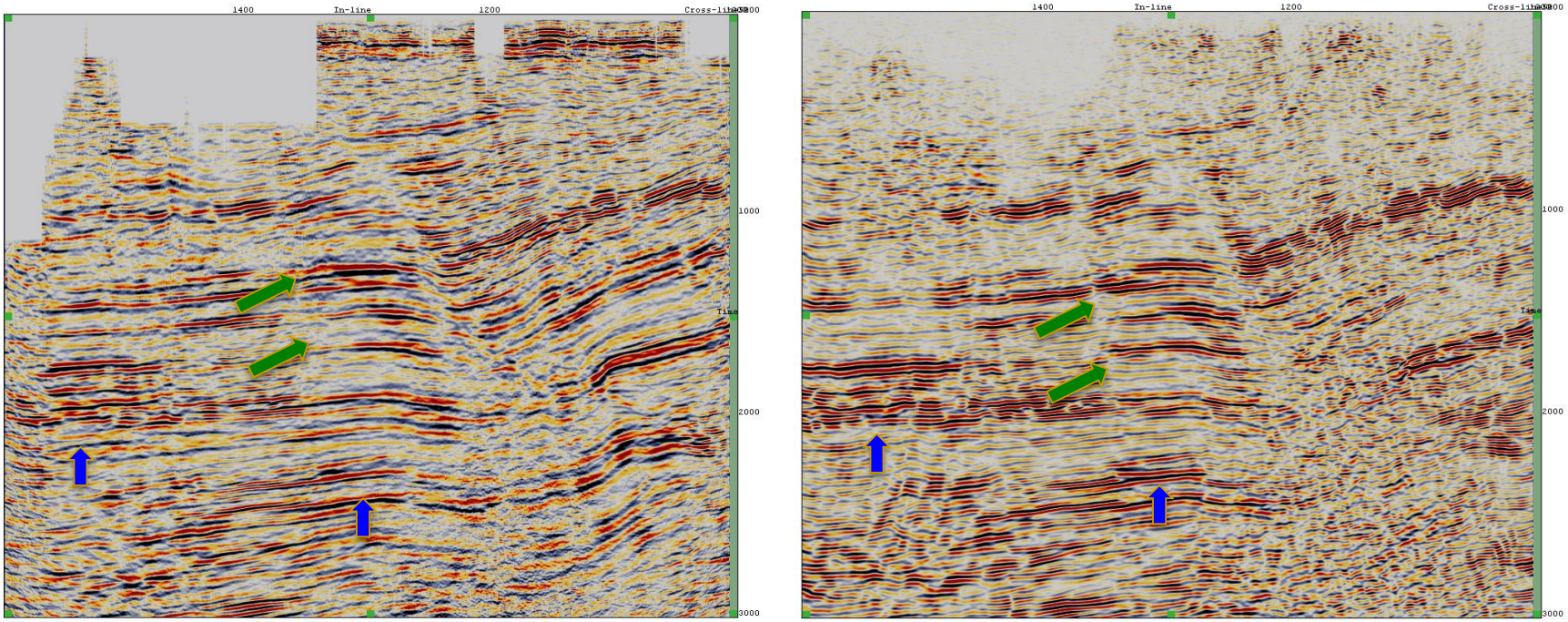

Figure 48. Results of PSTM and steered migration. Cross-line 5243. The left one is a result of the pre-stack time migration. The right is a result of the steered Kirchhoff migration. Green arrows indicate the improvement of a fault image. Blue arrows indicate the improvement of interfaces continuity.

Post-stack Steered Kirchhoff

Minimum similarity
derived from the PSTM volume

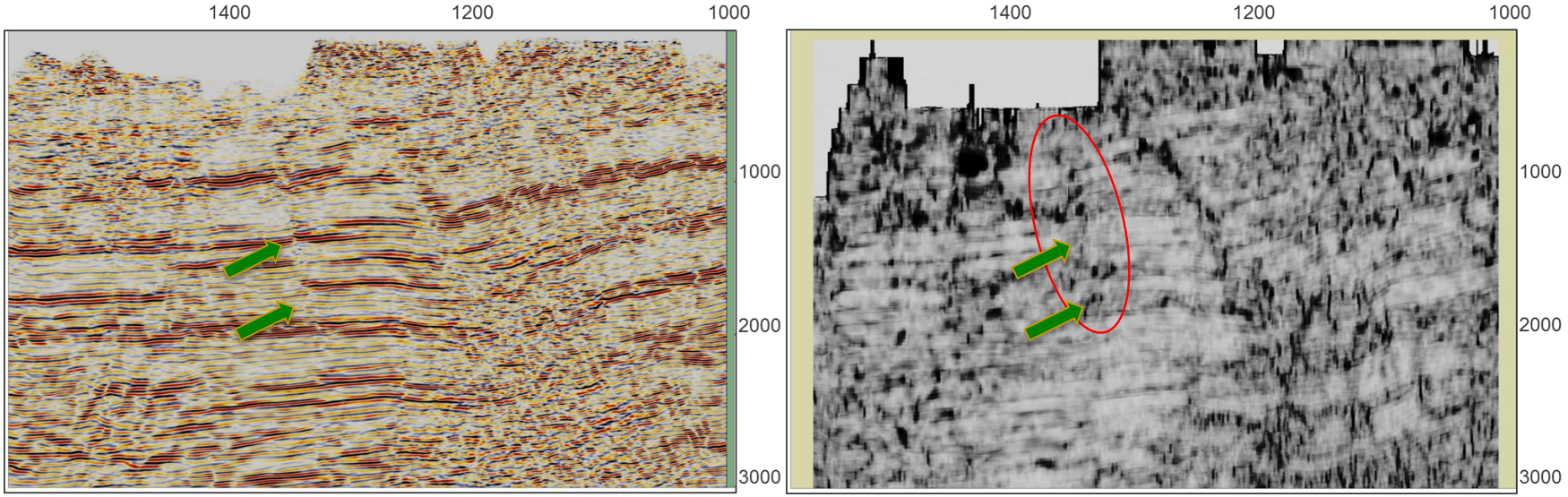

Figure 49. Results steered migration and minimum similarity attribute derived from the PSTM volume. Cross-line 5243. The left one is a result of the steered Kirchhoff migration. The right one is a minimum similarity attribute derived from the PSTM volume. Green arrows indicate the improvement of a fault image. Red circle indicates a set of anomalies along the interpreted fault.

2.8. Near-surface characterisation using surface-wave analysis

Imaging of shallow faults is an important aspect of carbon storage risk assessment, since knowledge of the extent of the faults indicates how recently the faults were active.

In order to investigate potential near surface expression of shallow faults, we have performed analysis of surface waves. The hypothesis is that if the fault reaches the upper tens of meter of the subsurface, the lateral changes in the elasticity properties (mostly shear wave velocity contrast) would be detectable by the analysis of the dispersion of the surface waves.

2.8.1. Methodology

There are several possible approaches of the surface wave dispersion analysis that can be generally divided into two groups: Spectral Analysis of Surface Waves (SASW) that is generally based on two receivers, and Multi-channel Analysis of Surface Waves (MASW) that usually utilises multitude of receivers. Herein we focus on MASW that provides more robust dispersion analysis than SASW.

McMechan and Yedlin (1981) were probably the first ones to use multi-offset analysis of surface waves by introducing the slant-stack in the Fourier domain to calculate the dispersion graphs. Now commonly used term MASW was first used by Park et al. (1999). A concise introduction to MASW is given by Park and Ryden (2007a) and Miller et al. (2008). Forbriger (2003) gives a good overview of the dispersion graphs, including aliasing and resolution discussion. Luo et al. (2007) show that that it is important to consider not only the receiver range of offsets within the spread, but also the location of the source.

The standard method for obtaining the dispersion curves for MASW analysis relies on a fixed range of receiver offset for all frequencies considered. The resolution of the dispersion graphs is directly related to the maximum offset from the source and the frequency; the lower the frequency, the lower the resolution. Good resolution at the low frequencies is often very important due to the fact that that the low frequencies carry the

information about the deeper parts of the subsurface. As discussed in presentation by Bona and Pevzner (2014), we can improve the resolution at low frequencies while ensuring that the inhomegeneities captured by higher frequencies stay resolved by using a variable range of receivers for different frequencies will allow us to maintain the resolution of the dispersion graphs at all frequencies. Park and Ryden (2007b) did use a variable window length and starting offset proportional to the wavelength of the plane waves used for computation of the dispersion graphs. This approach does take into account the near-field effects by limiting the near offsets as well, however it does not preserve the resolution across the values of the slownesses and frequencies. We use a combination of the two methods, where the near offsets are proportional to the wavelength and the maximum offset is controlled by the fixed resolution.

Figure 50 shows the basic principle behind the dependency of the resolution of the dispersion curves on the frequency *f* and the range of offsets x_{max} used to compute the dispersion graph. The blue line in the figure corresponds to the actual slowness of the depicted wave. If we do the slant-stack along one of the red curves – corresponding to the slowness plus-minus the resolution – the stack would result in the waveforms cancelling each other. The resolution of the dispersion graphs is given by the following relation:

$$\Delta p = \frac{T}{2x_{max}} = \frac{1}{2fx_{max}}$$

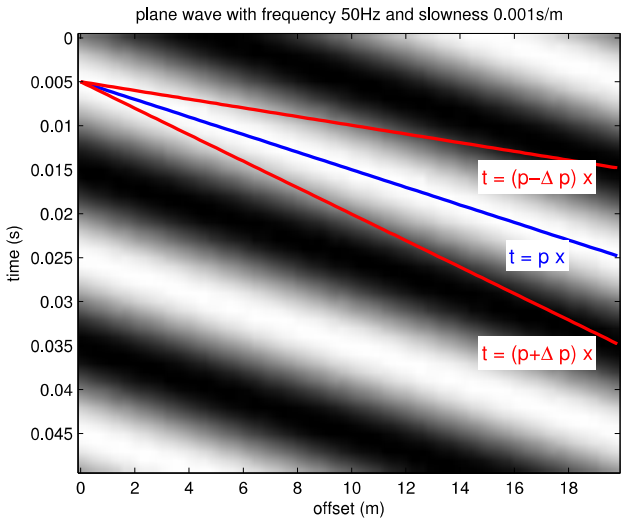

Figure 50 Schematic showing the effect of the maximum offset and frequency on the resolution of the dispersion curves.

Thus to improve the resolution of the dispersion graphs, we could increase the maximum offset x_{max}. This would, however, reduce the resolution of the heterogeneities in the subsurface. The natural compromise is to change the range of offsets depending on the frequency of the waves: lower the frequency the longer the offset range. Broadly consistent with this approach is the suggestion of Park and Ryden (2007b), who proposed to use offsets depending on the wavelength of the surface waves. Their empirical suggestion is to use offset range $h \in (0.1\,\lambda\,, 5\,\lambda\,)$.

The near offset limit is to avoid near-field effects of the source. One of the potential drawbacks of this approach is that the resolution of the dispersion graph changes with the slowness of the waves. We propose to use a combination of the two approaches, where the near offset is limited by the wavelength to avoid the near-field effects and the far offset is limited by the frequency to maintain the resolution of the dispersion graphs:

$h \in (0.1\lambda, 1/2f\Delta p)$.

2.8.2. Field data analysis

The analysis of surface waves benefits from relatively dense spacing of the geophones in order to avoid spatial aliasing in the seismic records. The “large” 3D survey by Geokinetics used receiver spacing of 50m, which would result in aliasing of all

wavelengths shorter than 100m. However, the nested 3D survey acquired by Curtin University as part of ANLEC R&D project number 7-1213-0224 has receiver spacing of 15m provides much better protection from aliasing. The effects of aliasing on dispersion curves for the two different receiver spacing is exemplified in Figure 51. The aliasing is the main reason we chose to use this survey for the analysis of the surface waves.

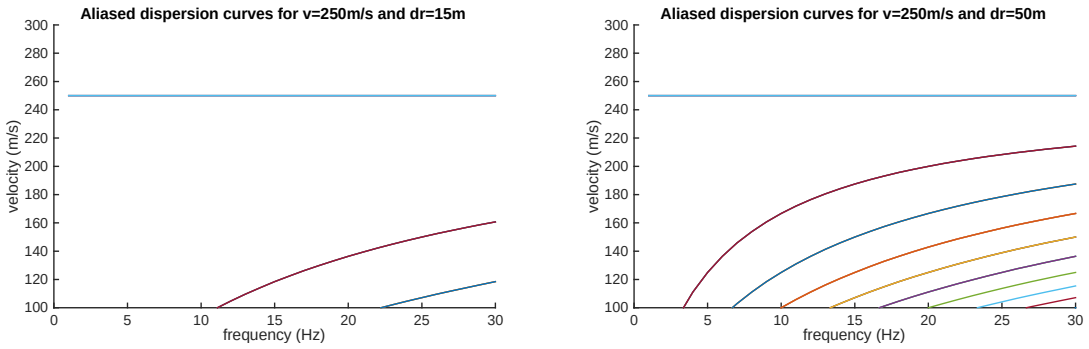

Figure 51 Effect of receiver spacing on aliasing visible in dispersion curves. This example shows a nondispersive wave with velocity of 250m/s (shown in blue) aliased as dispersive waves (shown as the differently coloured curves).

Figure 52 shows the layout of the survey, where the red squares indicate the locations of the sources and the blue crosses indicate the locations of the receivers. The median spacing between the neighbouring sources is 15m, the same as the spacing between the neighbouring receivers. The median line spacing is 90m. More detailed information about the survey can be found in ANLEC R&D report for project number 7-1213-0224.

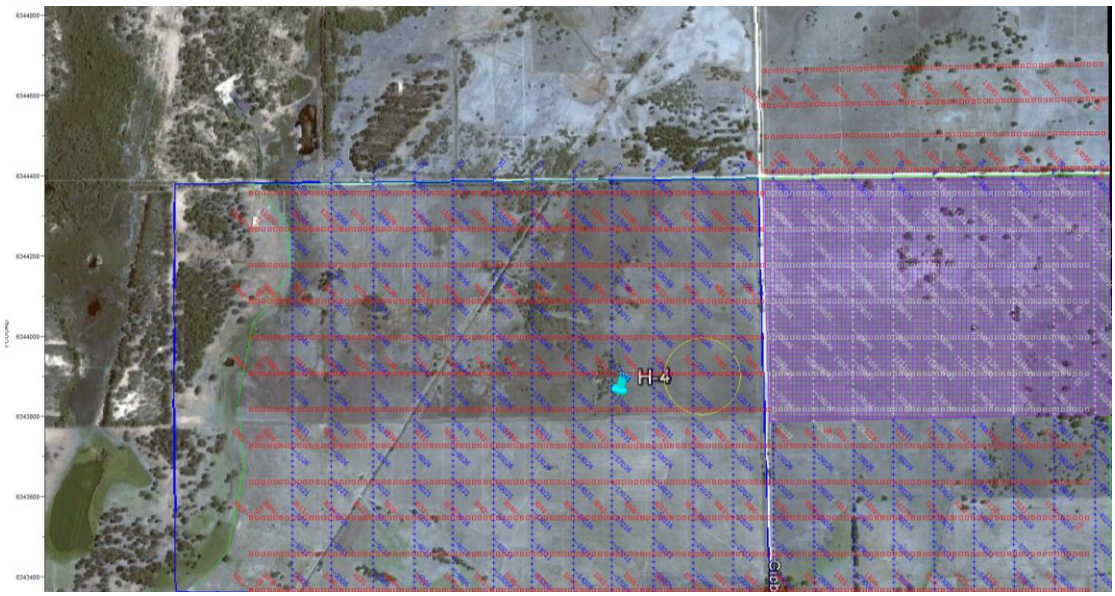

Figure 52 Layout of the seismic survey that was used for the surface wave analysis.

The locations at which we chose to investigate the dispersion of the surface waves were determined by the locations at which the sources were exactly located at the receiver lines. This restriction is to ensure that the surface waves propagate along the line and do not arrive at an oblique angle that would result in faster apparent velocity of the waves.

We applied the methodology described in Methodology section to the data to produce the dispersion curves. The quality of the curves varied from receiver to receiver; two representative examples of the curves are shown in Figure 53.

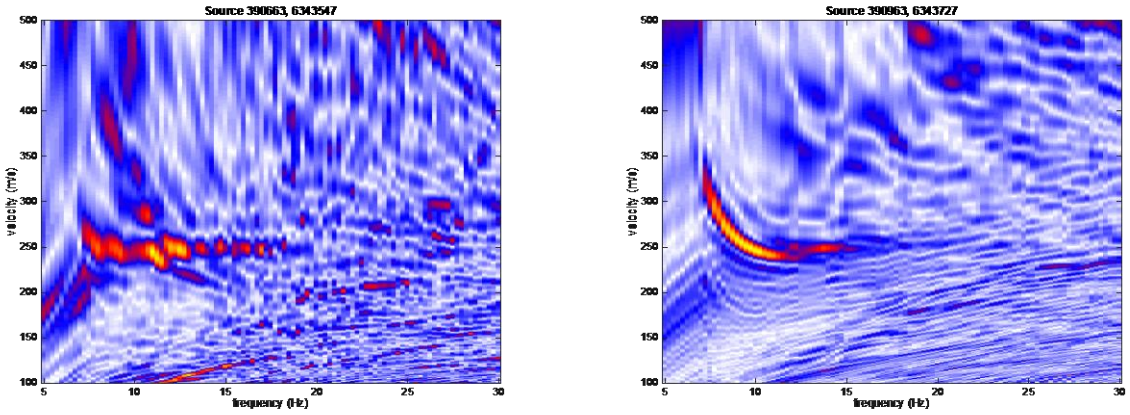

Figure 53 Examples of dispersion curves with different clarity of various surface wave modes. Figure on the left shows the first aliased dispersion curve similar to that modelled in Figure 51.

The resulting dispersion curves were imported into RadExPro software to invert them for shear wave velocity profiles. The required parameters for the inversion included assumed density (2000 kg/m3), Poisson's ratio (0.35) and number of layers (7). An example of part of the workflow is shown in Figure 54. The results of the inversion of the dispersion curves for the shear velocity profiles are discussed in the following section.

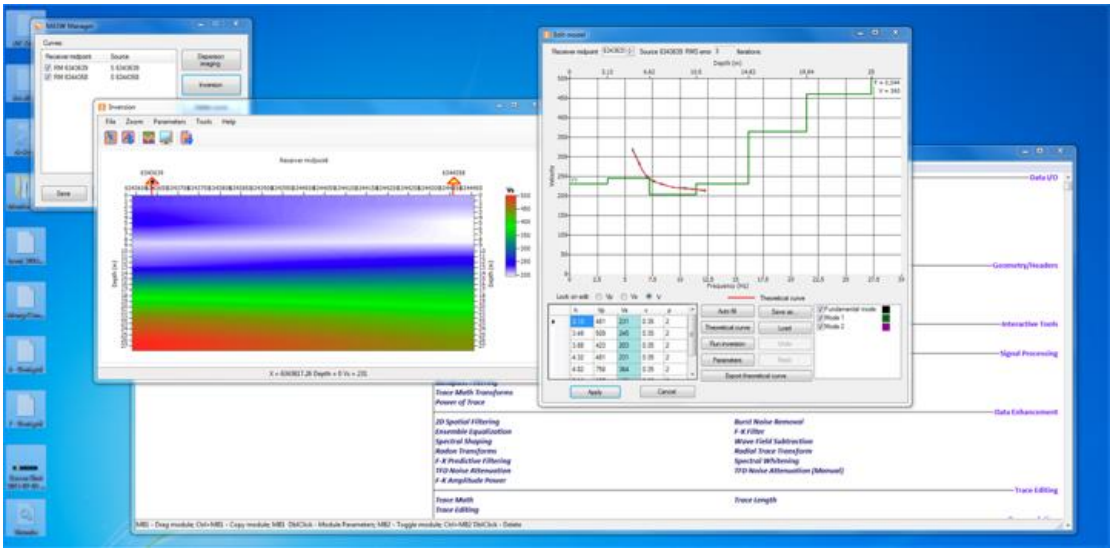

Figure 54 Example of workflow of the dispersion curve inversion in RadExPro.

2.8.3. Results

The results of the inversion are summarised by the depth slices shown in Figure 55 and Figure 56. The black circles indicate the locations of the 1D inversion. We performed 2D natural neighbour interpolation between the inversion points for each depth slice.

Application of the MASW to the Nested Harvey 3D data allowed to reconstruct high resolution shear wave velocity distribution in the top 30 m. We observe significant lateral velocity variation; we can expect to have similar order lateral variations in P wave velocity and significant variability in coupling conditions. Such lateral near-surface variations are likely to cause significant spatial variations on most of the seismic amplitude-based attributes, which should be taken into account in the true amplitude processing flow.

One of the reasons to undertake the MASW analysis of the data was to evaluate the hypothesis of presence of the faults in the shallow subsurface in the vicinity of Harvey 4. In this particular case lateral variations of the shear wave velocity is unlikely to be related to the faulting.

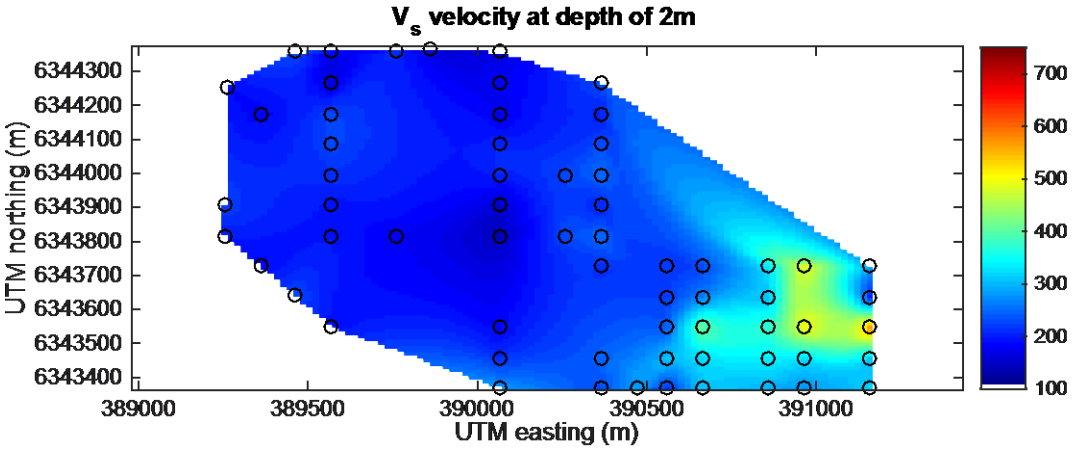

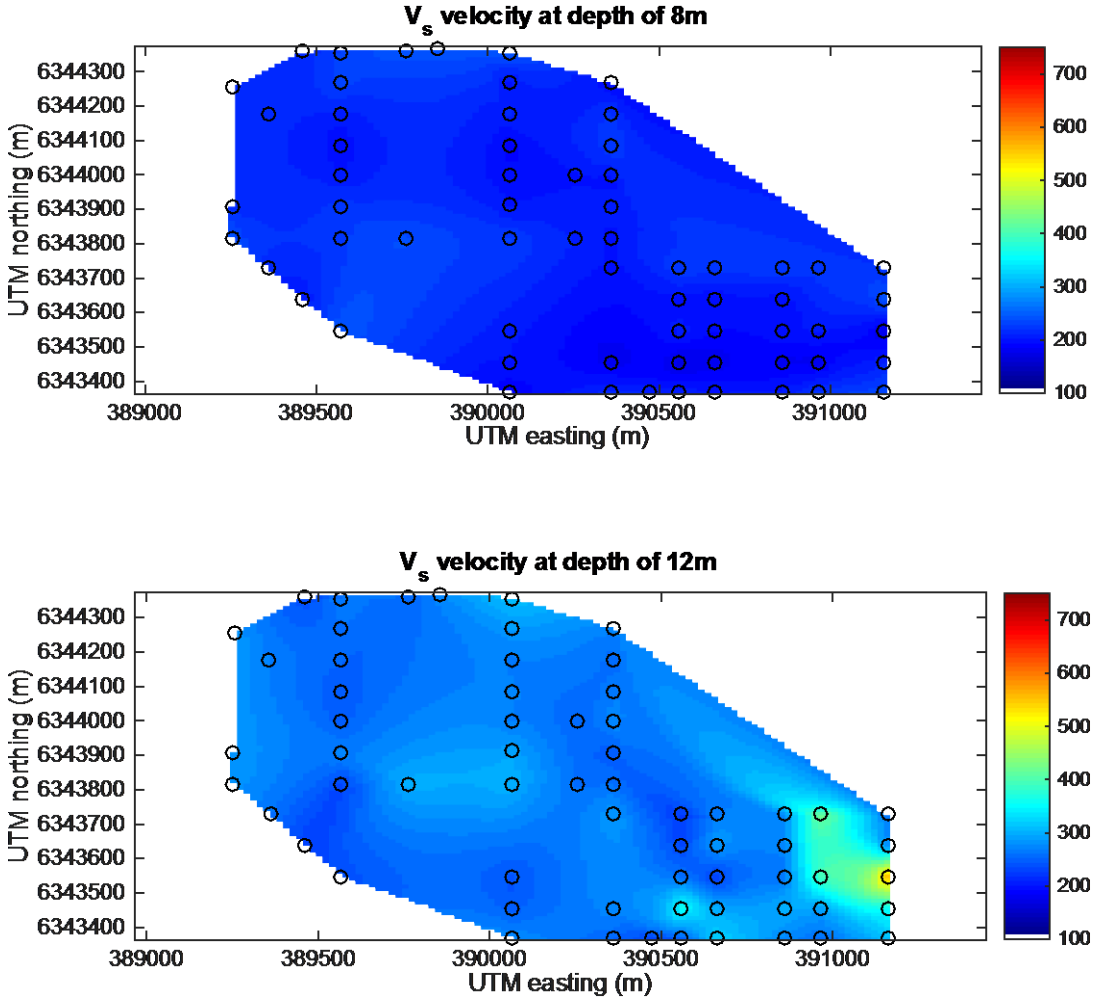

Figure 55 Shear wave velocity profiles obtained from surface wave analysis at depths of 2m, 8,m, and 12m.

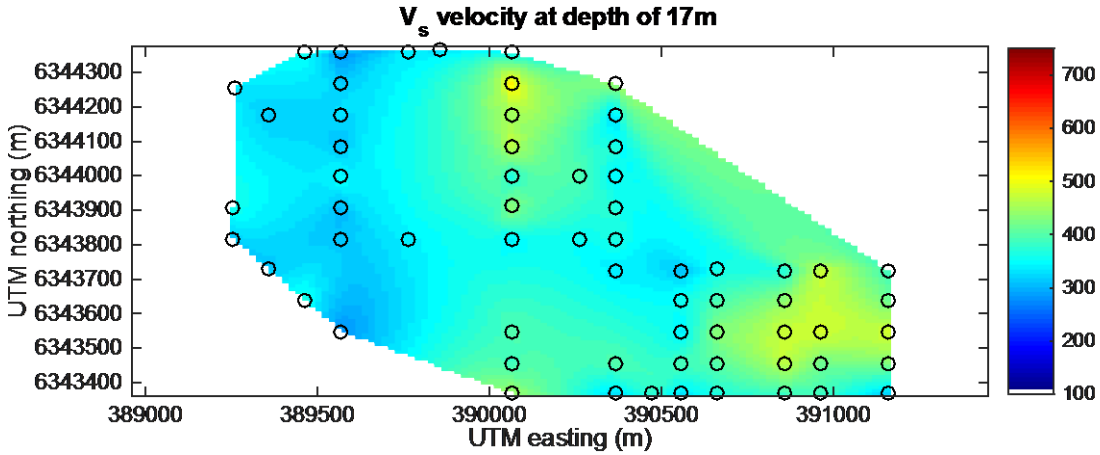

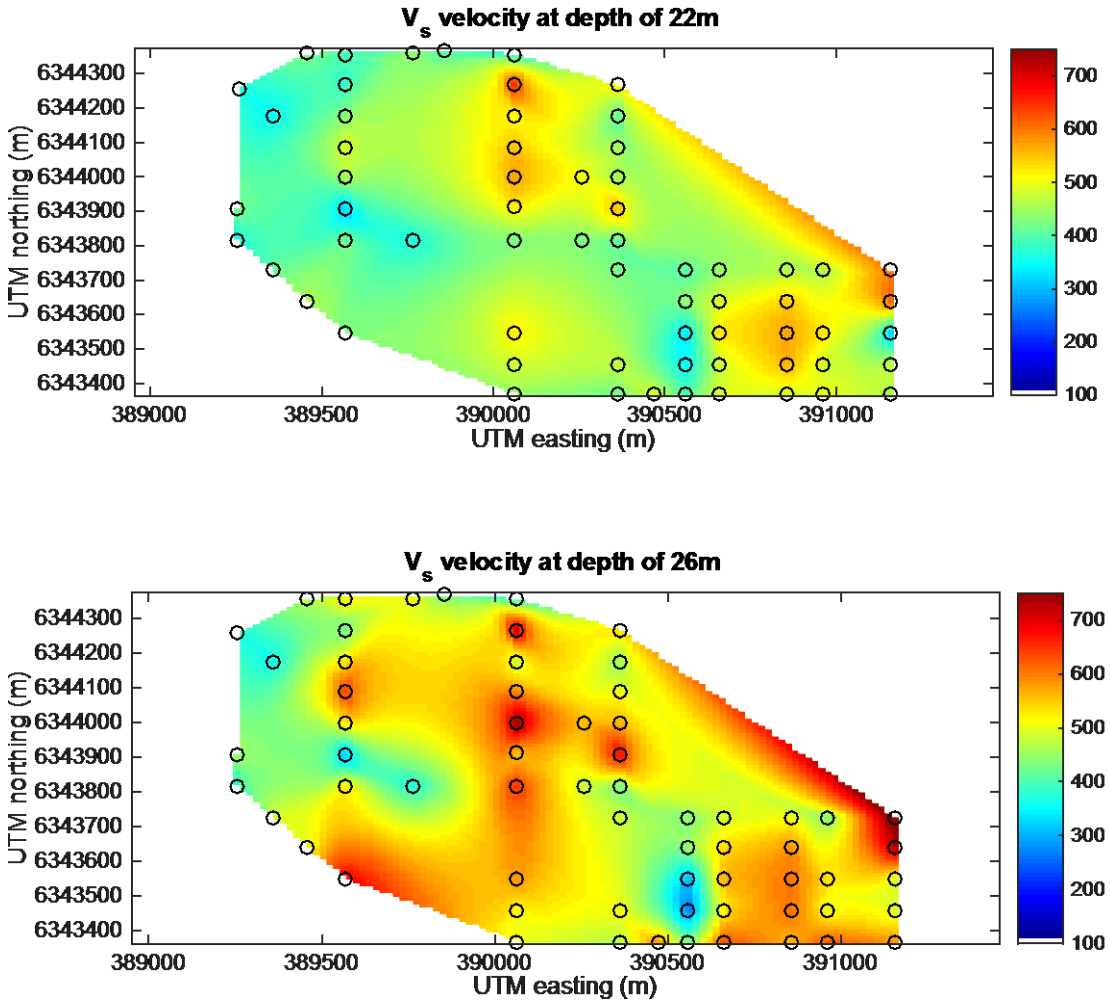

Figure 56 Shear wave velocity profiles obtained from surface wave analysis at depths of 17m, 22m, and 26m.

3. Structural analysis for CO_2 containment risk for the SW Hub, Western Australia

Subsurface data for the SW Hub, Mandurah Terrace, Perth Basin (Figure 57), clearly indicates that multiscale faults (10s of m to 10s of km) are present in the target CO_2 storage reservoir (Wonnerup Member) and the potential top seals (Yalgorup Member and basal Eneabba Formation) (Figure 58). Globally, there have been many examples of seismicity apparently induced by fluid injection in oil fields (see the review by Grasso, 1992) and it is known that changes in the pore pressure and stress field cause by fluid injection could alter the initial seal of a reservoir by either (1) overcoming the fault(s) membrane seal capacity leading to circulation of CO_2 by migration across or along the fault (e.g., Bretan et al., 2011; Ciftci et al., 2012), (2) by triggering slip on pre-existing fault(s) delimiting trap(s) or within the caprock leading to the potential loss of CO_2 by migration up the fault (e.g., Streit and Hillis 2004; Rutqvist et al. 2007; Chiaramonte et al. 2008; Bretan et al., 2011) or (3) by hydraulically fracturing the caprock (e.g., Secor, 1965, 1969).

In 2013, Langhi et al. proposed a new geological model for the SW Hub consistent with the integration of new 2D seismic reflection survey with the vintage seismic surveys, available geophysical data and Harvey-1 well data. For the ANLEC project 7-1111-0201 *Integration of data from Harvey-1 well to support decision*, they carried out a first-order assessment of the CO_2 containment potential for the SW Hub.

This work continues this initial assessment of the CO_2 containment potential by integrating the newly acquired 3D seismic dataset acquired by Geokinetics in 2014 and available data from Harvey-2 and Harvey-4 wells. We investigate the structural architecture of the SW Hub, potential for lateral and vertical circulation of CO_2, geomechanical controls on reactivation and sub-seismic fractures affecting structural permeability in the Wonnerup and Yalgorup Members.

In case of juxtaposition of the Wonnerup Member against another aquifer across a fault, the membrane (or capillary) seal (Jennings, 1987; Watts, 1987) is assessed using the

Shale Gouge Ratio (SGR) predictive algorithm (Yielding et al., 1997; Freeman et al., 1998) that is considered as a proxy of up-scaled fault-rock composition (Bretan et a., 2011). Empirical calibration is used to derive a fault-seal failure envelop and to calculate a maximum fluid column height able to be trapped by a fault without leaking (Yielding, 2002; Bretan et al., 2003). Ciftci et al. (2012) demonstrate that SGR calculated on faults intersecting, but not offsetting completely, a caprock can also be used to qualitatively assess along-fault hydrocarbon migration potential and caprock bypass.

The relationship between the modelled faults and the present-day stress field is investigated to analysis the effects of stress field changes on fault kinematic behaviour and to define which critically stressed fault segments are most likely to be forced into failure with pore-pressure build-up. Areas of fault reactivation are associated with an increase in structural permeability and therefore with the potential for along-fault flow (Ferril et al., 1999, Mildren et al, 2005, Bretan et al., 2011).

Elastic dislocation theory (Okada, 1985; 1992; Dee et al., 2007) is used to predict the spatial distribution, orientation and mode of sub-seismic fractures in the Wonnerup and the Yalgorup Members and assess their relative likelihood of reactivation under the present-day stress field.

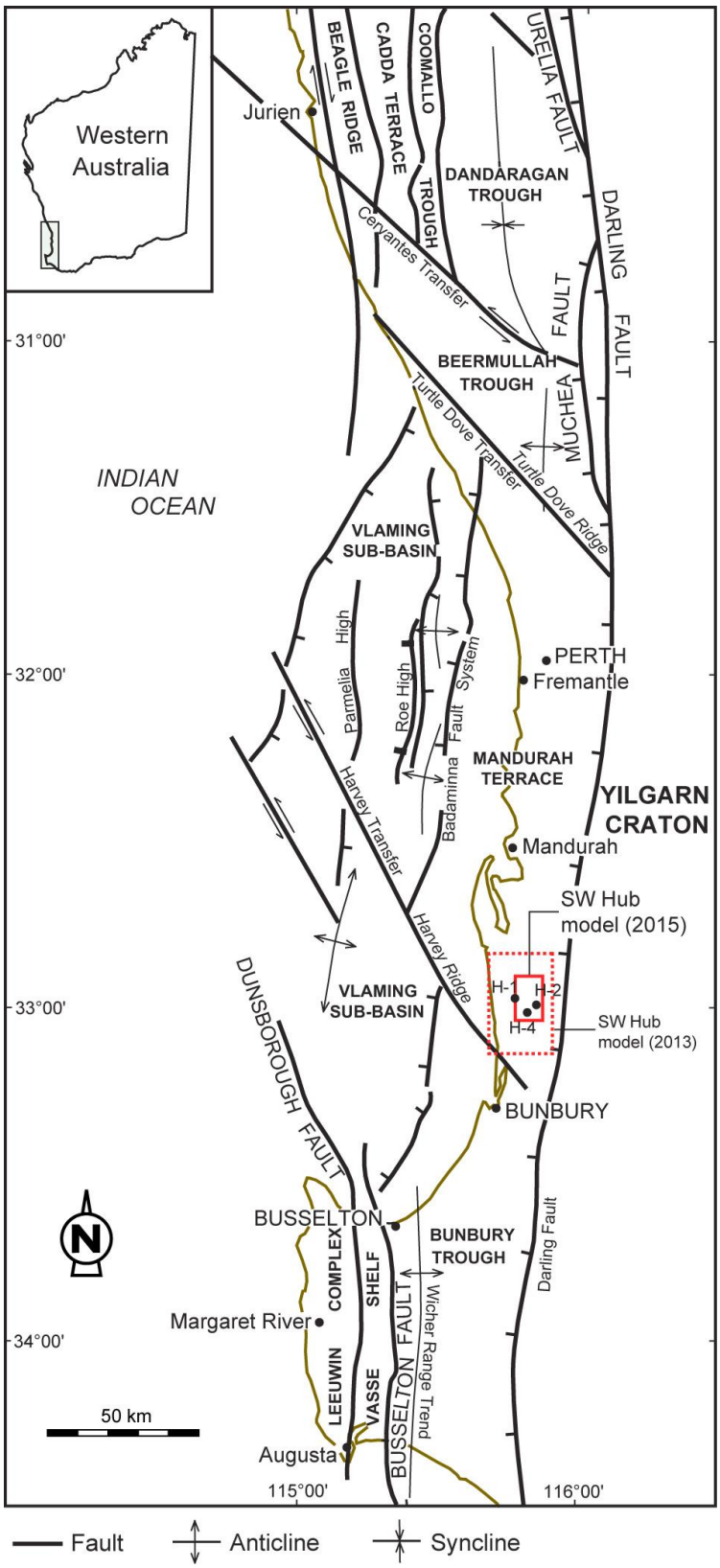

Figure 57: Perth Basin subdivision, tectonic lineaments and location of the SW Hub model. Modified form Crostella and Backhouse, 2000. The geological model from Langhi et al. (2013) is shown in red dotted line, the new geological model is in red plain line. H-1 = Harvey-1, H-2 = Harvey-2, H-3 = Harvey-3.

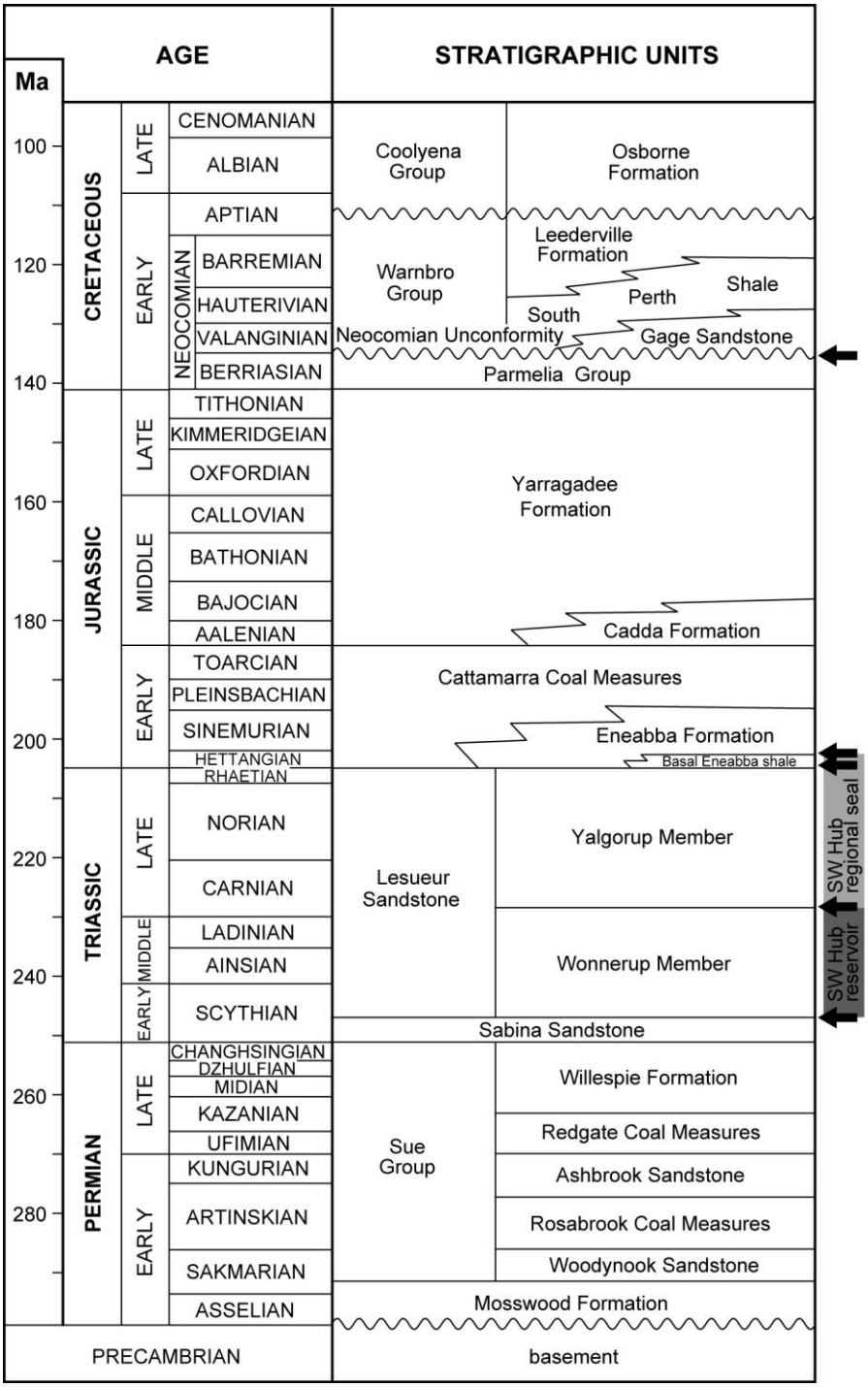

Figure 58: Stratigraphy of the central and southern Perth Basin and definition of the proposed CO_2 containment reservoir and top seal for the SW Hub. Modified form Crostella and Backhouse, 2000. The arrows indicate the mapped seismic horizons.

3.1. Geological setting

The SW Hub is located in the central part of the onshore Perth Basin, at the south end of the Mandurah Terrace (Figure 57, Crostella and Backhouse, 2000). The Mandurah Terrace forms a terrace in comparison to the offshore Vlaming Sub-basin to the west and is bounded to the east by the Darling Fault System. To the south the Mandurah Terrace is bounded by the Harvey Ridge that is a broad (> 10km) NW-trending basement high associated with normal and strike-slip deformation in the Phanerozoic sedimentary cover (G. Bernardel, pers. comm., 2012). Both the Darling Fault System and the Badaminna Fault bounding the terrace to the east and west, respectively, trend to the N-NNE. The structural pattern for the southern Mandurah Terrace primarily shows NNE to NW trending features (Cockbain, 1990; Crostella and Backhouse, 2000; Iasky and Lockwood, 2004; Wilkes et al., 2011).

The reader is referred to Crostella and Backhouse (2000) for a detailed description of the stratigraphy of the central Perth Basin. Figure 58 synthetises the stratigraphy of the southern Mandurah Terrace. The oldest known sedimentary rocks are Permian in age and belong to the Sue Group. The Sabina Sandstone overlies the Willespie Formation with an apparently conformable contact, and is conformably overlain by the Lesueur Sandstone. The units intersected in Harvey-1 have been investigated by Delle Piane et al. (2013) and are listed in Table 8. The Wonnerup Member (lower Lesueur Sandstone) drilled in Harvey-1 well consists primarily of interbedded coarse to gravelly sandstones occasionally punctuated by fine to medium, sandstones and mudstone layers typical of fluvial environments. The Yalgorup Member (upper Lesueur Sandstone) represents an interbedded succession of mixed coarse to gravelly facies and fine to medium grained facies and siltstones and mudstone. A basal Eneabba Shale is interpreted in Harvey-1 well. Although the residual trapping is expected as the sealing mechanism, the Yalgorup Member and Eneabba basal Shale are believed to represent potential physical top seals for the reservoirs in the Wonnerup Member. Mory and Iasky (1996) described the overlying Eneabba Formation as a fluvial sandstone interbedded with conglomerate, claystone and siltstone. The Early Jurassic Eneabba Formation is unconformably overlain by the Neocomian Unconformity. Based on well data from the Bunbury Trough to the south and the Beermullah Trough to the north (Crostella and Backhouse, 2000) and vitrinite reflectance data (Iasky, 1993) we estimate that at least 1500m of Early to

Late Jurassic sediment might have been deposited on the southern Mandurah Terrace and then eroded during the Neocomian (i.e. Berriasian-Valanginian). The unconformity is overlain the Leederville and the Guilford Formations.

Tectonic evolution of the central Perth Basin is described in Cockbain (1990) Crostella and Backhouse (2000) or Iasky and Lockwood (2004). During the Late Carboniferous to Early Permian, north-trending regional rifting marked the beginning of sedimentation within the Mandurah Terrace (Crostella and Backhouse, 2000). During the Permian, Triassic, and Jurassic, the Darling Fault System acted as a growth fault, which resulted in Permian to Neocomian clastic sedimentation from the emergent Yilgarn Craton that thickens toward the fault. During the Late Jurassic to Early Cretaceous the onshore part of the Perth Basin was uplifted, with limited and/or discontinuous deposition, and by the Neocomian the final separation of Australia from India produced intense deformation, uplift and erosion (Neocomian Unconformity). This episode is responsible for the bulk of the deformation observed in the study area. Although fault movement drastically decreases after the Neocomian break-up, localised fault activity is possible due to differential compaction or Cretaceous and/or Tertiary stress regime.

STRATIGRAPHIC UNIT	TOP MDRT	TOP TVDSS
Guildford	5	+20
Leederville	36	-11
Eneabba	250	-225
Basal Eneabba shale	625	-600
Yalgorup	704	-679
Wonnerup	1380	-1335
Sabina	2895	-2870
Total depth	2945	-2920

Table 8: Harvey-1 well; formation tops.

3.2. Geological model

The geological model built for this project includes the seismically mappable faults and five stratigraphic horizons, i.e. the Neocomian Unconformity, the top basal Eneabba

Shale, the top Lesueur Formation (top Yalgorup Member), the top Wonnerup Member and the top Sabina Formation (Figure 58). The horizons are tied to the top formation markers from Harvey-1 (Table 8).

3.2.1. Dataset

The geological model has been build up around the 115 km^2 3D seismic survey acquired by Geokinetics in 2014 (Figure 59).

The bulk of the geological interpretation is carried out on the prestack time migration (PSTM) data processed within the scope of this project by Curtin University. The 3D PSTM data set has a line spacing of 25m x 25m and includes 588 inlines oriented N-S and 351 crosslines oriented E-W. The 3D PSTM data set has a record length of 5 sec TWT.

Prestack depth migration (PSDM) data processed within the scope of this project by UWA were compared with PSTM data (Figure 60). The PSDM data shows local decrease of reflector's continuity and does not enhance the visualisation of the subsurface architecture for the SW Hub.

Gamma-ray logs from Harvey-1, Harvey-2 and Harvey-4 are used to derive the volume of shale of the formations.

Harvey-1 vertical seismic profiling (VSP) data (Pevzner et al., 2013) is used to constrain the time-depth conversion.

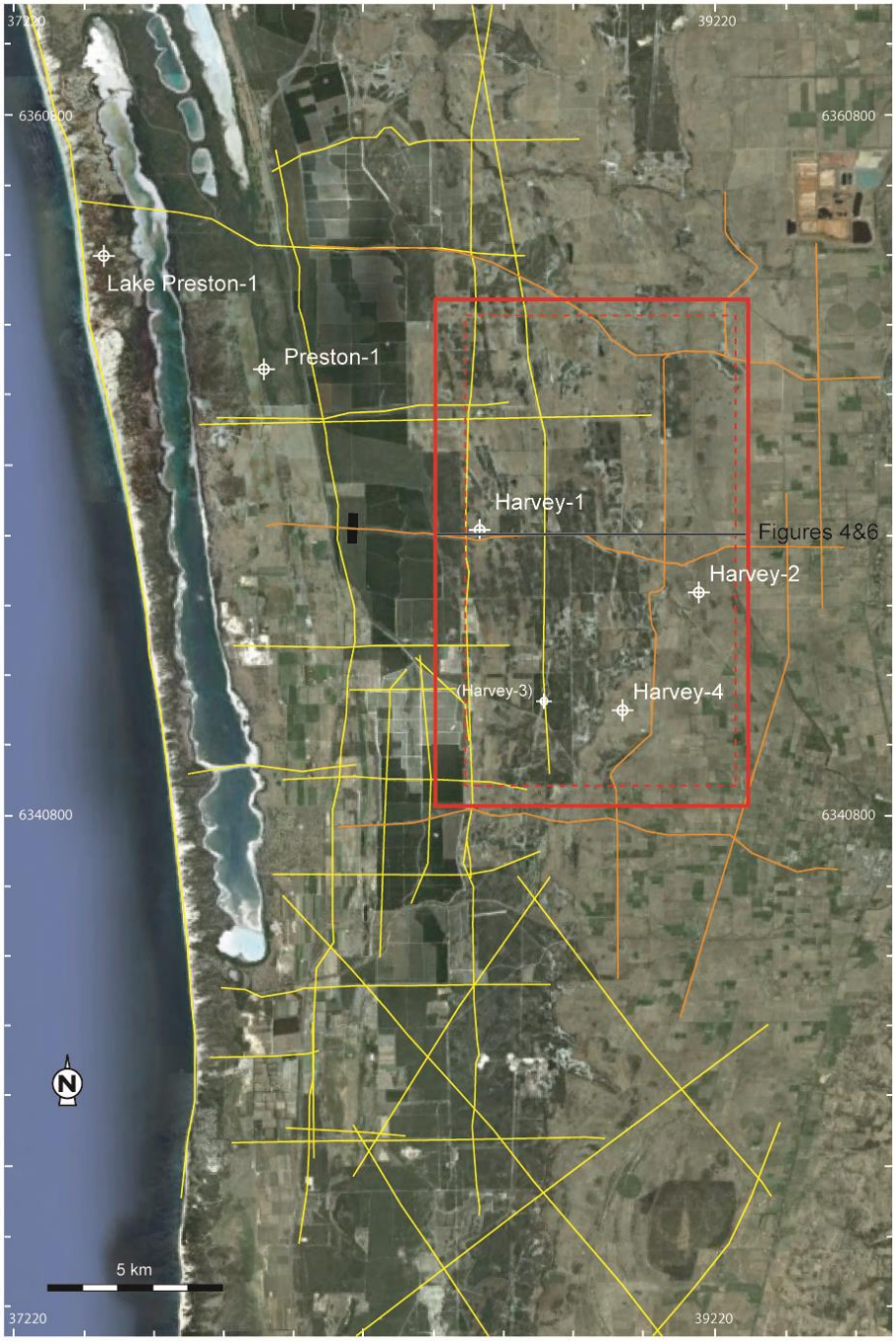

Figure 59: Modelled area for the SW Hub. The 2011 2D GA Lower Lesueur seismic survey is in orange, vintage seismic lines are in yellow and the 2014 3D seismic data is in red. The dotted red line represent the extent of the current geological model. Note that Harvey-3 is displayed but was not used in this work.

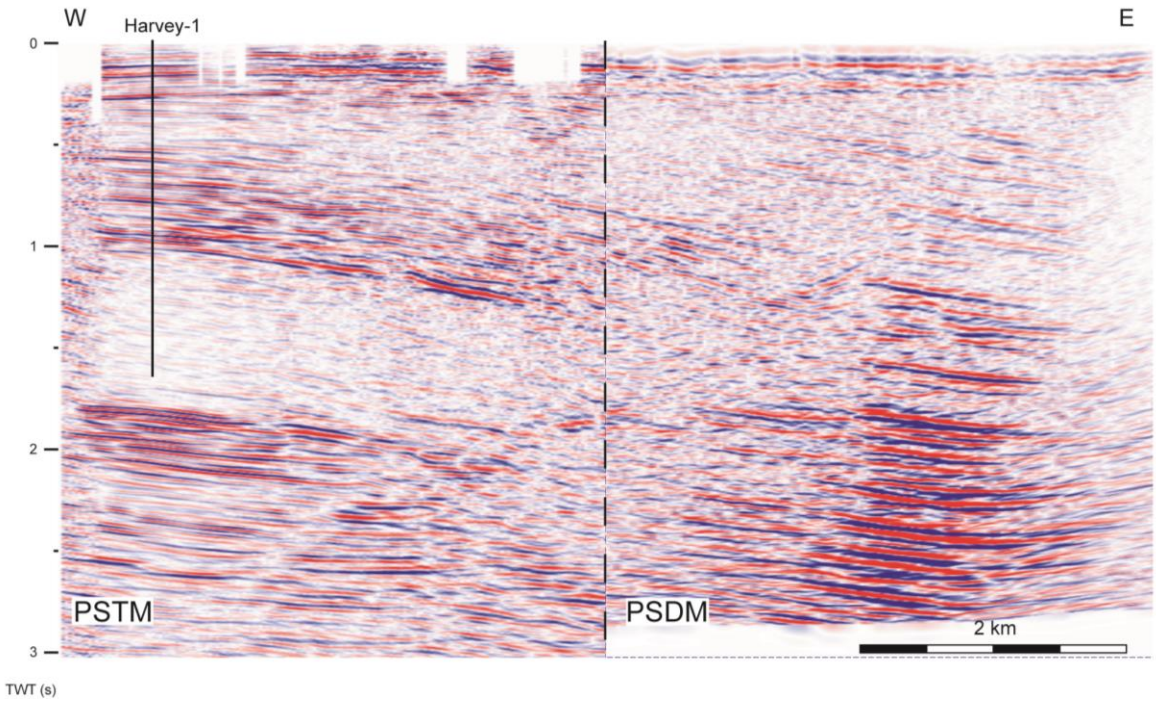

Figure 60: Comparison between PSTM and PSDM data on inline 1301.

3.2.3. Velocity model

A 3D average velocity model was provided by ODIN Reservoir Consultant. It represents a 3D grid comprising approximately 900,000 grid cells (250m x 250m bin) over 145 layers between 0 (seismic datum) and 5 seconds TWT.

This model was calibrated with Harvey-1 VSP data (Pevzner et al., 2013) to obtain an accurate fit at the well location (Figure 61). At the time of this study velocity data for Harvey-2 and Harvey-4 were not available.

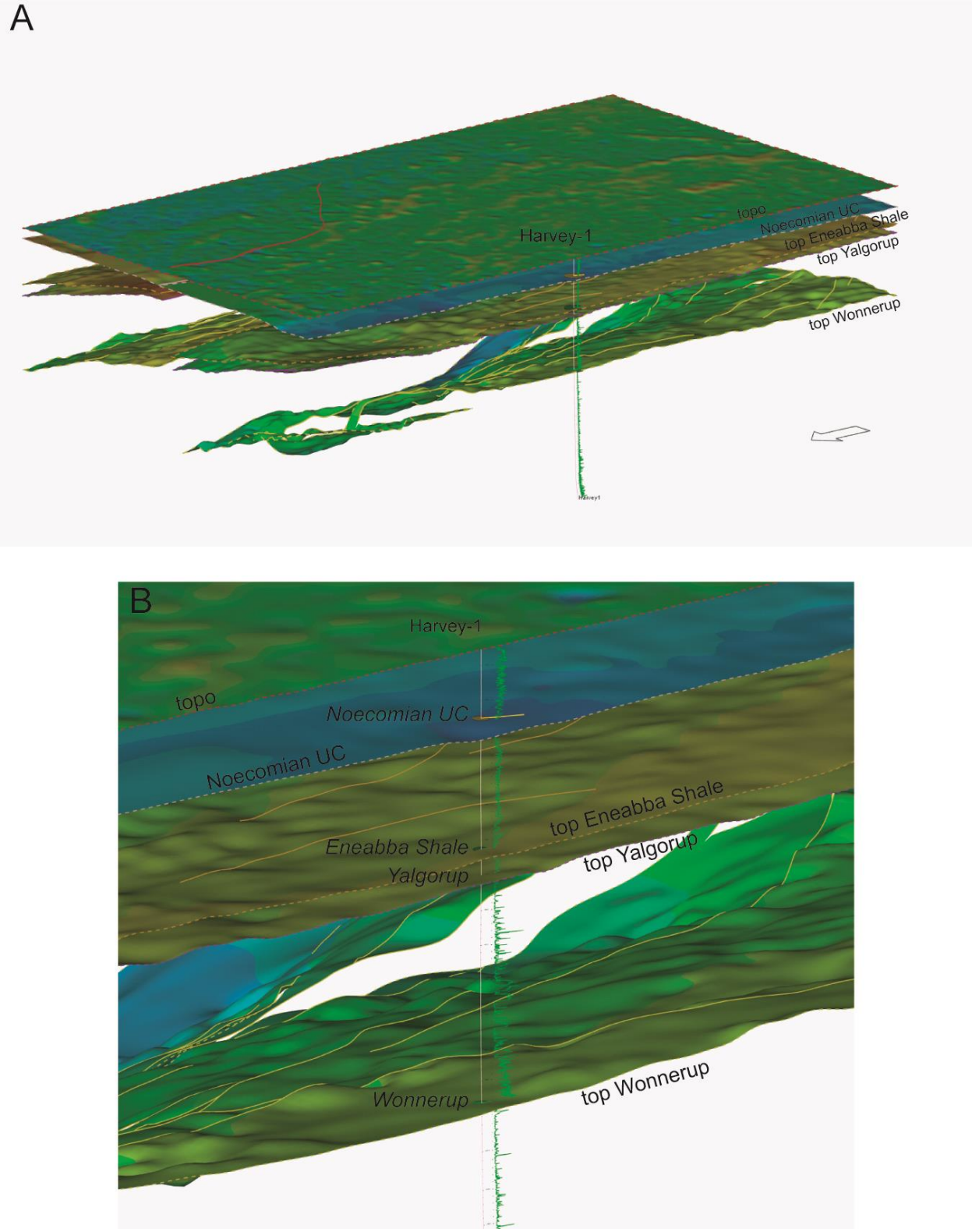

Figure 61: Depth conversion. A) Depth converted horizon model. B) Depth horizons tied to Harvey-1, top formations marker are in italic. Gamma ray log is shown in green.

3.2.4. Static geological model

The static geological model comprises five stratigraphic horizons (Figure 62):

- The Neocomian Unconformity (250mDRT in Harvey-1).
- The top basal Eneabba Shale (625mDRT in Harvey-1). The interpretation of this horizon still remains ambiguous due to the low contrast in acoustic impedance. Over the study area this horizon has been mapped as the second to third trough above the top Lesueur horizon (top Yalgorup).
- The top Lesueur (top Yalgorup, 704mDRT in Harvey-1). The Yalgorup Member is characterised by a typical seismic facies with high reflectivity and average to high continuity.
- The top Wonnerup Member (1380mDRT in Harvey-1). The interpretation of the top Wonnerup on the PSTM seismic data was compare with the interpretation done on the original 3D dataset (processed by VelSeis) and interpreted by Odin Reservoir Consultant. The interpretation form the PSTM data do not show major TWT differences (Figure 63); local differences are rather attributed to interpretation strategy than difference in seismic data.
  The top Sabina sandstone (2985mDRT in Harvey-1). This horizon represents the interface between the transparent Wonnerup Member and the more reflective and continuous Sabina sandstone and Sue Group.

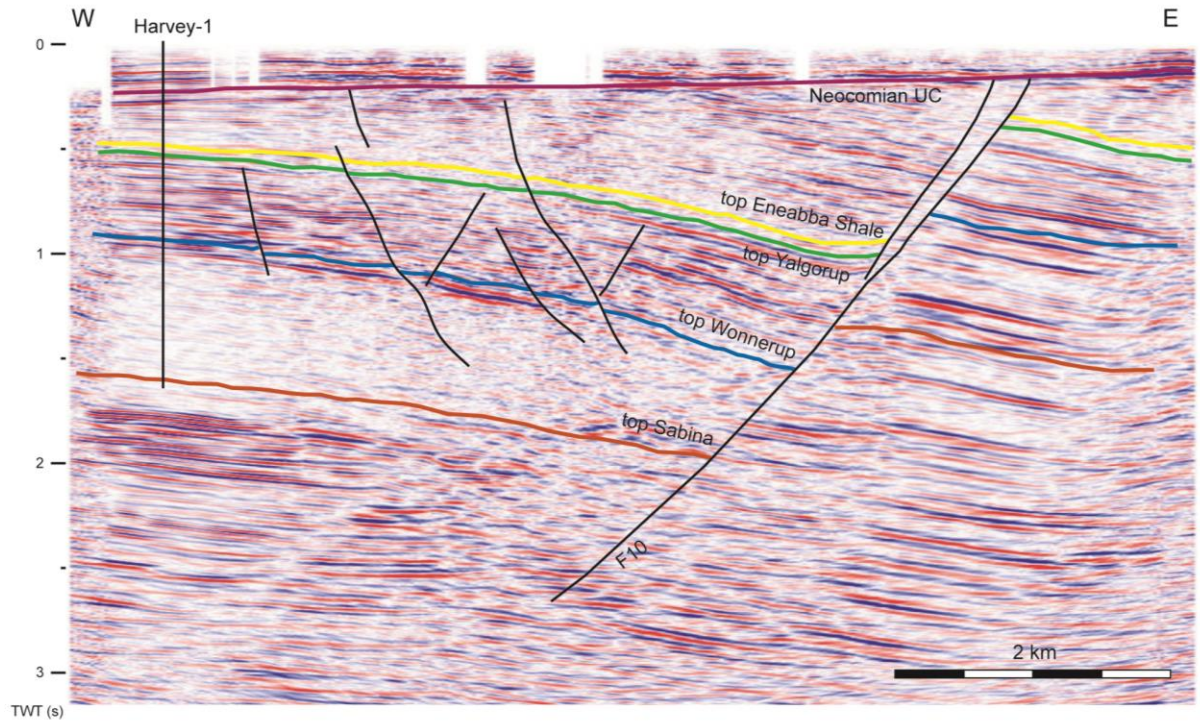

Figure 62: Inline 1301 (PSTM) through Harvey-1 showing the mapped horizons and faults. Location on Figure 3.

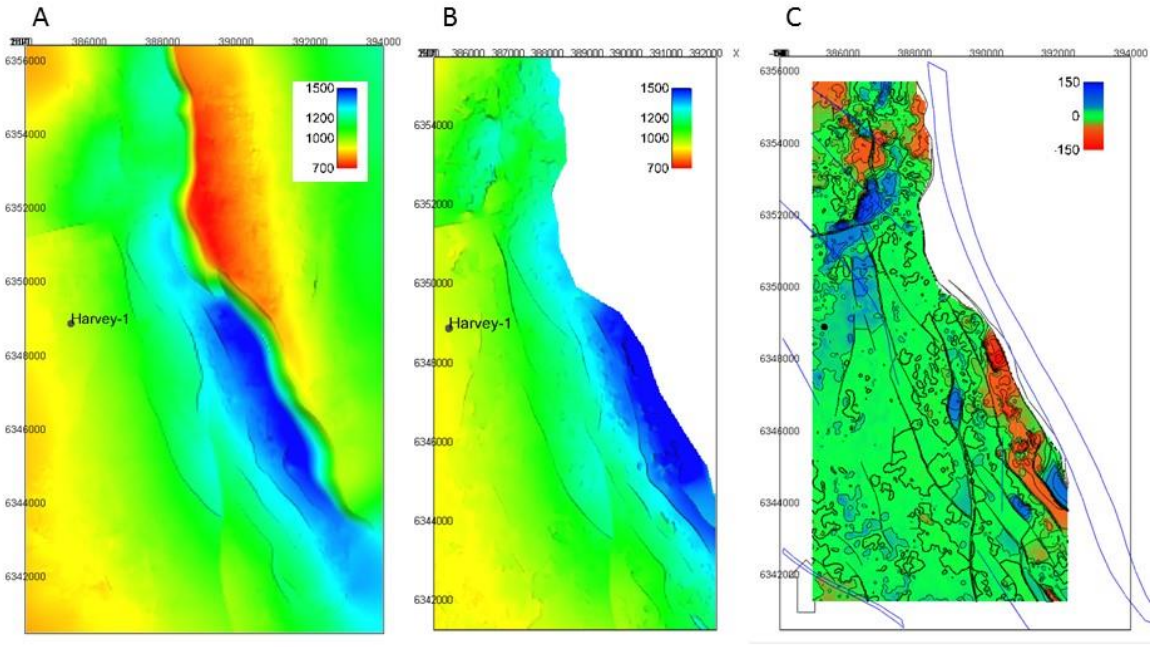

Figure 63: Interpretation comparison between original 3D seismic data and PSTM data. A) Odin Reservoir Consultant top Wonnerup surface (TWT ms). B) This study top Wonnerup surface west of fault F10 (TWT ms). C) Time difference between surfaces (TWT ms). Green areas represent difference =< 10ms (~<20m).

The main structural episode post dated the deposition of the Eneabba Formation and is mostly related to the break-up between Australia and India. The geological model is consistent with the stratigraphic interpretation, honours regional data (e.g. Le Blanc Smith 1993; Iasky and Lockwood, 2004; Causebrook et al., 2006; Nicholson et al., 2008; Wilkes et al., 2011) and includes 62 fault planes with a general NW-SE to N-S orientation (Figure 64 and Figure 65). The main structural feature is the F10 fault already reported by Langhi et al. (2013). It divides the SW Hub into two structural block with Harvey-2 located on the footwall block (Block A in Langhi et al., 2013) and Harvey-1, Harvey-3 and Harvey-4 to the west on the hanging wall block (Block B in Langhi et al., 2013) (Figure 64). The structural trend for the SW Hub is consistent with those interpreted from gravity and aeromagnetic data and from outcrop in the Collie Basin (Le Blanc Smith, 1993; Iasky and Lockwood, 2004; Wilkes et al., 2011). The north-west corner of the 3D seismic dataset shows low signal-to-noise ratio and therefore there is still high uncertainties on faults 94, 96 and 97 (Figure 64). The faults usually intersect the Mesozoic sedimentary succession and are truncated by the Neocomian Unconformity (Figure 62). The main F10 fault present maximum modelled offsets of 1500 m for the top Sabina and 1200 m for the top Wonnerup (Figure 66). Fault

movement is interpreted on seismic reflection data as mostly normal. The faults dip at around 60°.

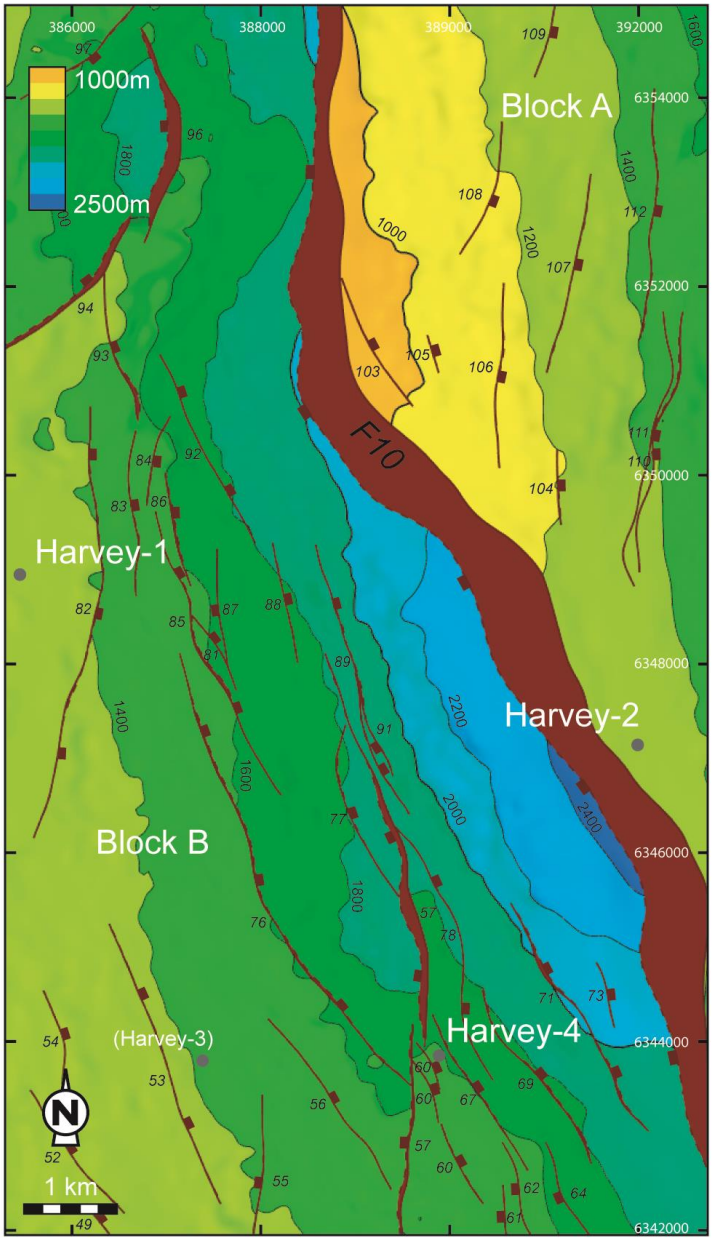

Figure 64: Depth structure map, top Wonnerup. Fault labels are in italic.

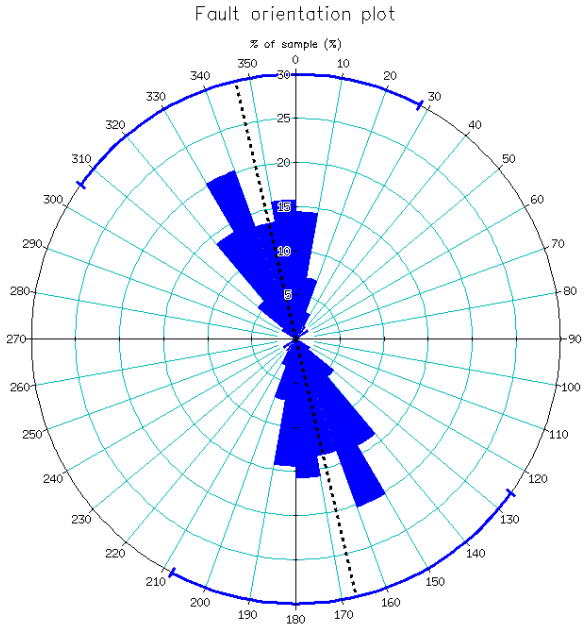

Figure 65: Fault strike orientation, top Wonnerup.

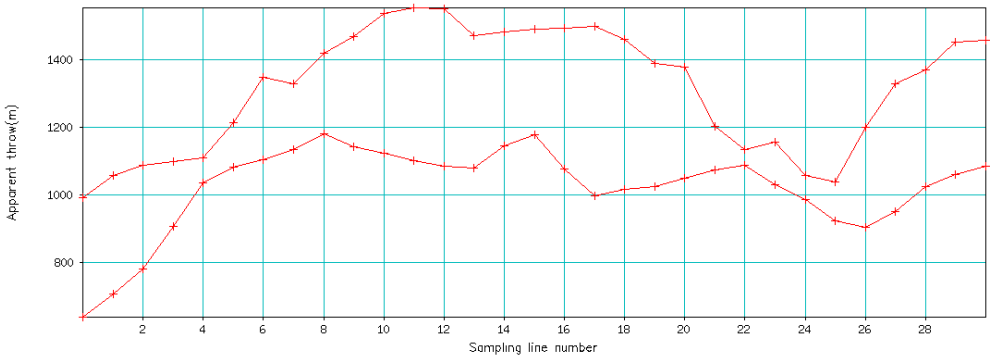

Figure 66: Apparent throw on F10 for the top Wonnerup (lower line) and the top Sabina (upper line).

3.3. Shale Volume

The distribution of the phyllosilicate content, or volume of shale (V_{sh}), represents a key factor in defining the membrane seal capacity of the faults (Knipe et al., 1997; Yielding et al., 1997; Sorkhabi and Tsuji, 2005; Underschultz, 2007) as it volumetrically relates to the shale gouge fraction of the fault rocks.

V_{sh} logs are derived from gamma ray index for Harvey-1, Harvey-2 and Harvey-4 by using standard oilfield petrophysical methods (Asquith and Krygowski, 2004) (Figure 67). The V_{sh} logs are then mapped to the faults planes. The contribution from each well is blended using a neural neighbour method.

This approach honours the data at the well location; however it simplifies the lateral distribution by ignoring the natural variation of the sedimentary depositional environment (Figure 68).

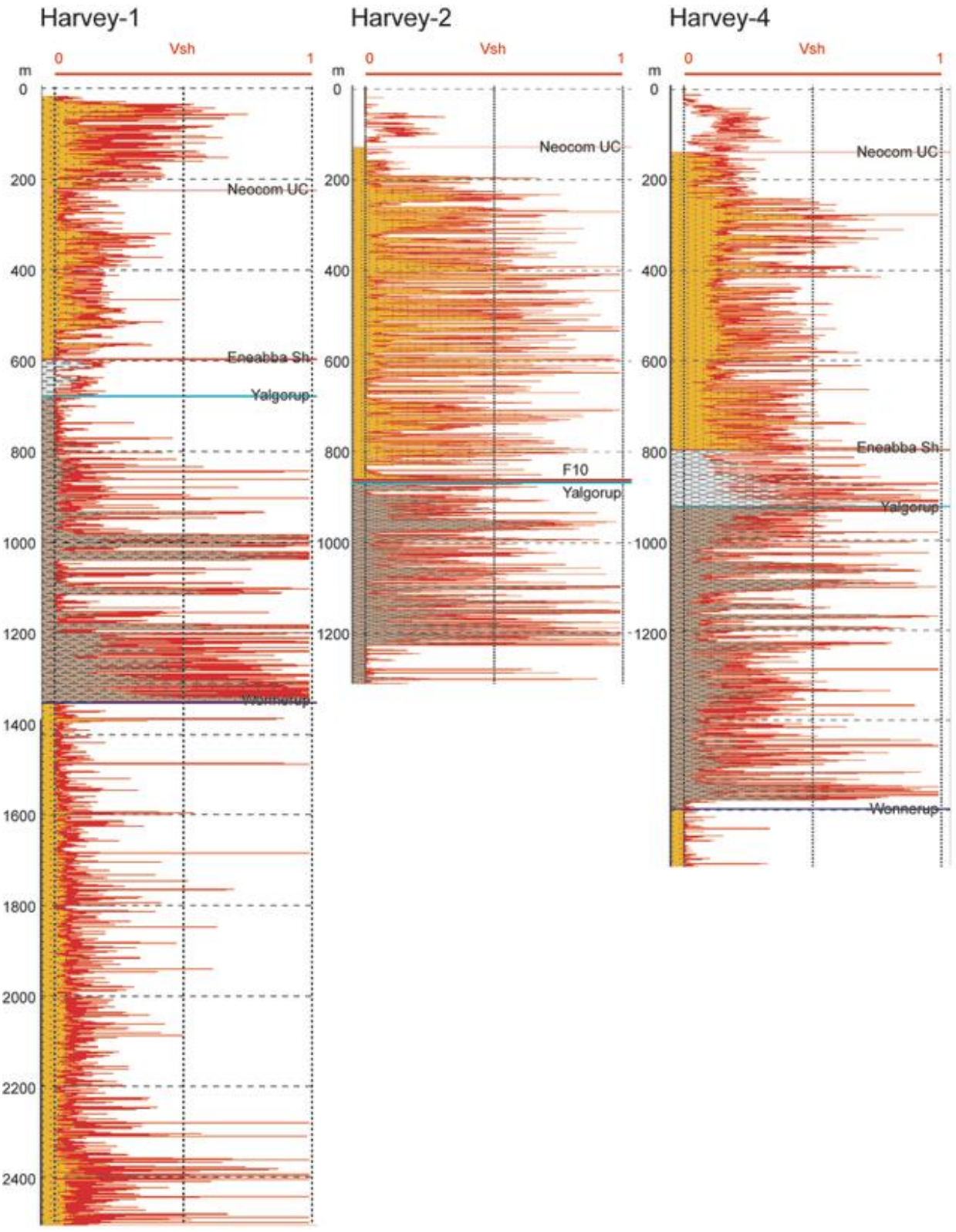

Figure 67: Vsh data for Harvey-1, Harvey-2 and Harvey-4. The basal Eneabba Shale is missing in Harvey-2 as the well intercepts fault F10 resulting in the juxtaposition of the Eneabba Fm against the Yalgorup Fm.

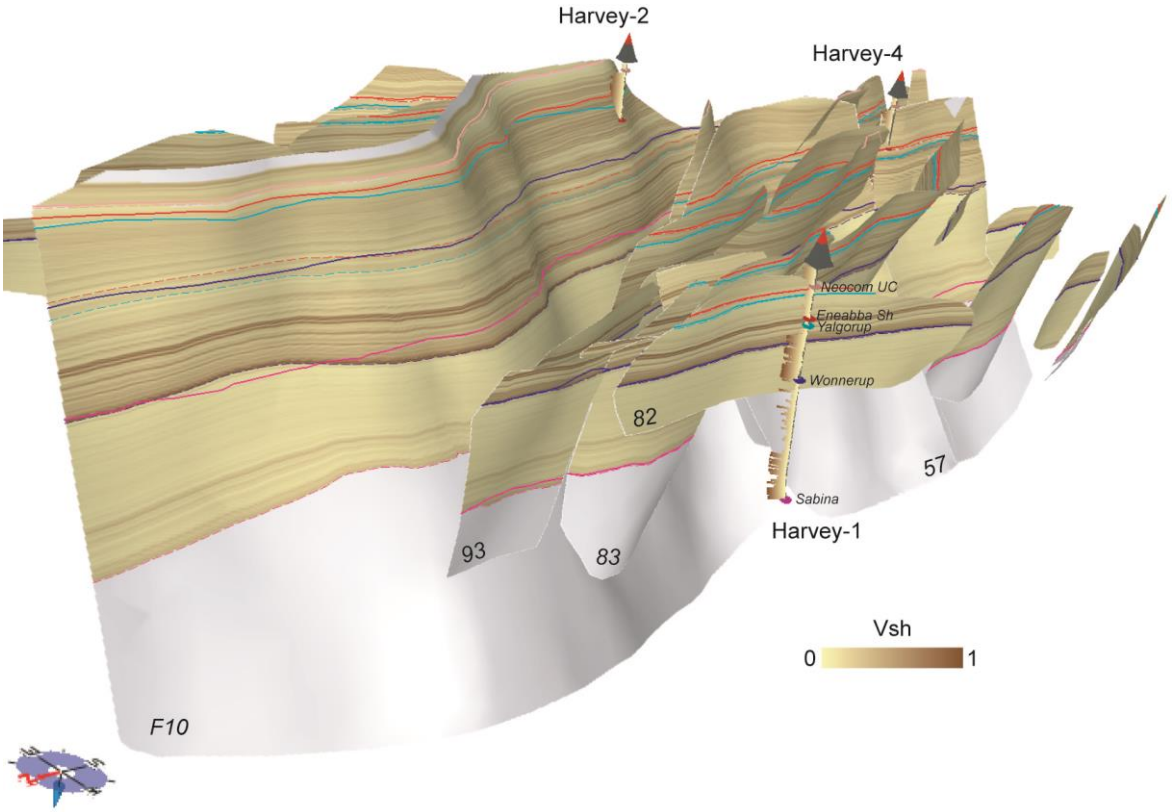

Figure 68: Vsh data mapped to the fault planes. Top formation markers are shown for Harvey-1.

3.4. Fault seal assessment

The assessment of the sealing behaviour of the faults to injected CO_2 relies on:

- The evaluation of the membrane fault seal potential to predict if a fault acts as a sealing lateral barrier thus permitting CO_2 to accumulate within a trap.
- The modelling of the stress state on the fault planes to predict the likelihood of fault reactivation under the present-day stress regime and if increasing formation pressure generated either by a CO_2 column (capillary pressure) or injection, is likely to trigger fault instability, reactivation and along-fault migration.

3.4.1. Membrane fault seal potential

The juxtaposition pattern of the lithology is the predominant influence on membrane fault seal in clastic sequences. It has been well documented in recent years for many hydrocarbon fields globally (e.g. Bouvier et al. 1989; Jev et al. 1993; Childs et al. 1997; Fristad et al. 1997; Fulljames et al. 1997; Yielding et al. 1997; Knipe et al. 1998; Yielding 2002; Bretan et al. 2003). Large faults (seismic scale) offsetting reservoirs and shale-rich sealing units may form seal if they juxtapose reservoir rocks against sealing

rocks (i.e., juxtaposition seal; Allan, 1989; Freeman et al., 1998; Yielding et al., 1997) or if the faulting process has generated a membrane seal, because of the presence of mechanically derived fault rock (i.e., gouge; Fisher and Knipe, 1998) that is of lower permeability and which impedes fluid flow (Bouvier et al., 1989; Knipe, 1992; Antonellini and Aydin, 1994; Gibson, 1994).

The generation of gouge is linked to the sliding of different lithologies past one another (Yielding et al. 1997). The first-order control on such fault-rock development is identified as the composition of the faulted lithologies and the amount of displacement on the fault (Fisher and Knipe, 1998). The capillary entry pressure of the fault-zone material is the critical parameter in determining whether a fault can successfully seal a non-wetting fluid accumulation (hydrocarbon or CO_2) when sands are juxtaposed. Leakage of hydrocarbons or CO_2 through the fault zone takes place when the difference in pressure between the water and hydrocarbon phases (buoyancy pressure) exceeds the pressure required for hydrocarbons or CO_2 to enter and pass through the largest interconnected pore throat in the seal (displacement or capillary entry pressure) (Bretan et al., 2003).

For the SW Hub the Shale Gouge Ratio (SGR) algorithm (Yielding et al., 1997; Freeman et al., 1998) is used to estimate the amount of phyllosilicates incorporated in the fault zones. A high SGR value is expected to correspond to more phyllosilicates in the fault zone (e.g. clay smear), and therefore to higher capillary threshold pressure and lower permeability (Bretan et al., 2011). Yielding (2002) observed that SGR>15–20% corresponds to faults that are sealing to hydrocarbons. A quantitative calibration of SGR against pressure difference data allows Yielding (2002) and Bretan et al. (2003) to derive a relationship between SGR and the maximum hydrocarbon column height supported by a fault:

$$h_{max} = 10^{(((SGR/27)-C)+5)}/(\rho_w - \rho_h)g \quad (1)$$

where C is 0.5, 0.25, 0 for increasing burial depths (see Bretan et al. 2003 for details), ρ_w and ρ_h are the densities of water and hydrocarbon and g is the acceleration due to gravity. Bretan et al. (2011) demonstrate the application of this fault seal methodology in the context of CO_2 storage.

East of fault F10 the Wonnerup Member juxtaposes against the Yalgorup Member or against itself.

The SGR values for the self-juxtaposition (i.e., the upthrown Wonnerup Member is juxtaposed against itself) are generally less than 15% which represent a low likelihood of membrane fault seal (i.e. <20 m of supported CO_2 column). An increase in SGR values from <15% to <35% is modelled near the bottom of the Wonnerup Member; however this variation results from projection of Harvey-1 V_{sh} data, located more than 6km away on the hanging wall block of F10, and that record increases in V_{sh} from 2300m to 2900m (Figure 67 and Figure 69). If confirmed laterally these increase in SGR could reflect local baffles able to support up to ~70 m of CO_2 given that a trap is present. The juxtaposition seals (Wonnerup Member juxtaposes against the Yalgorup Member) show SGR values between 20% and 50% which represent a moderate to high likelihood of membrane fault seal.

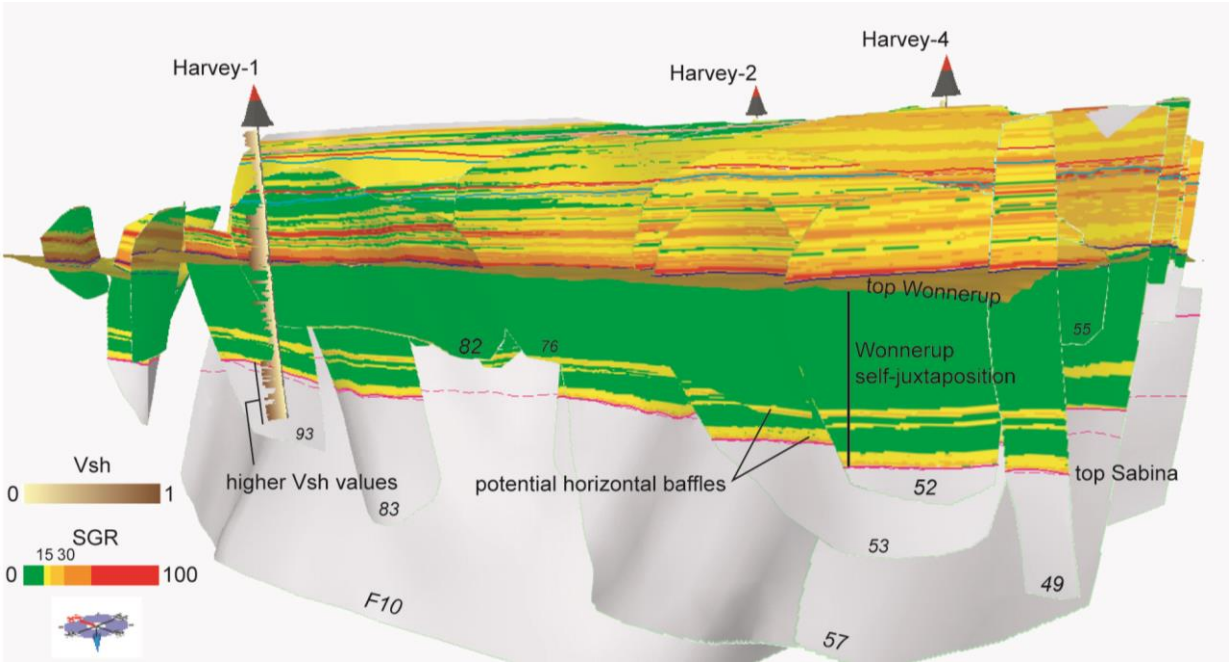

Figure 69: Wonnerup Member self-juxtaposition. SGR values are generally less than 15% but values up to 35% forming potential local baffles are modelled near the bottom of the Wonnerup Member. The largest leak potential is located to the north of Harvey-4.

As already defined by Langhi et al. (2013), fault F10 juxtaposes the Wonnerup Member against the Eneabba sandstone overlying the Yalgorup and basal Eneabba inferred top seals (Figure 70 and Figure 72). The SGR calculation for this fault segment generally exceeds 24% and is expected to be sealing (Yielding, 2002) and able to support a ~40 m CO_2 column.

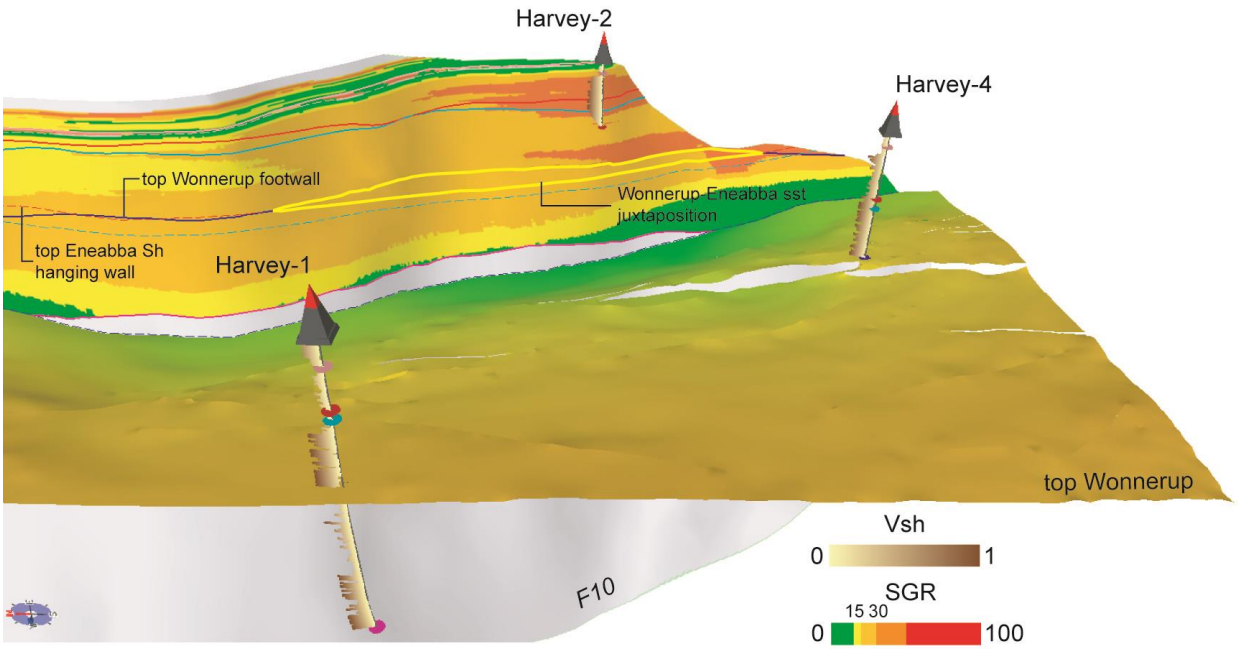

Figure 70: SGR distribution for the Wonnerup Member against Eneabba sandstone juxtaposition (yellow shape between the top Wonnerup footwall cutoff line (blue dotted line) and the top Eneabba Shale hanging wall cutoff line (green continuous line).

West of fault F10 (Block B) thirty-three faults displace the top Wonnerup with offset ranging from the seismic resolution (~15m) to 160m and with the upthrown Wonnerup Member juxtaposing against the Yalgorup Member (Figure 71) (faults 94, 96 and 97 in the north-west corner are ignored due to large uncertainties). These structures form physical traps if CO_2 is able to migrate to the top of the reservoir (Figure 64). The SGR values for these juxtapositions vary between ~15%, at the base of the juxtaposition and 30%-50% for the rest of the juxtaposition (average ~35%) (Figure 72). Slight decreases in SGR values are modelled for faults around Harvey-4. The SGR values represent CO_2 columns between 20m and 350m supported by the fault seal at the top of the Wonnerup reservoir where it juxtaposes against the Yalgorup member (average ~90m) (Figure 73).

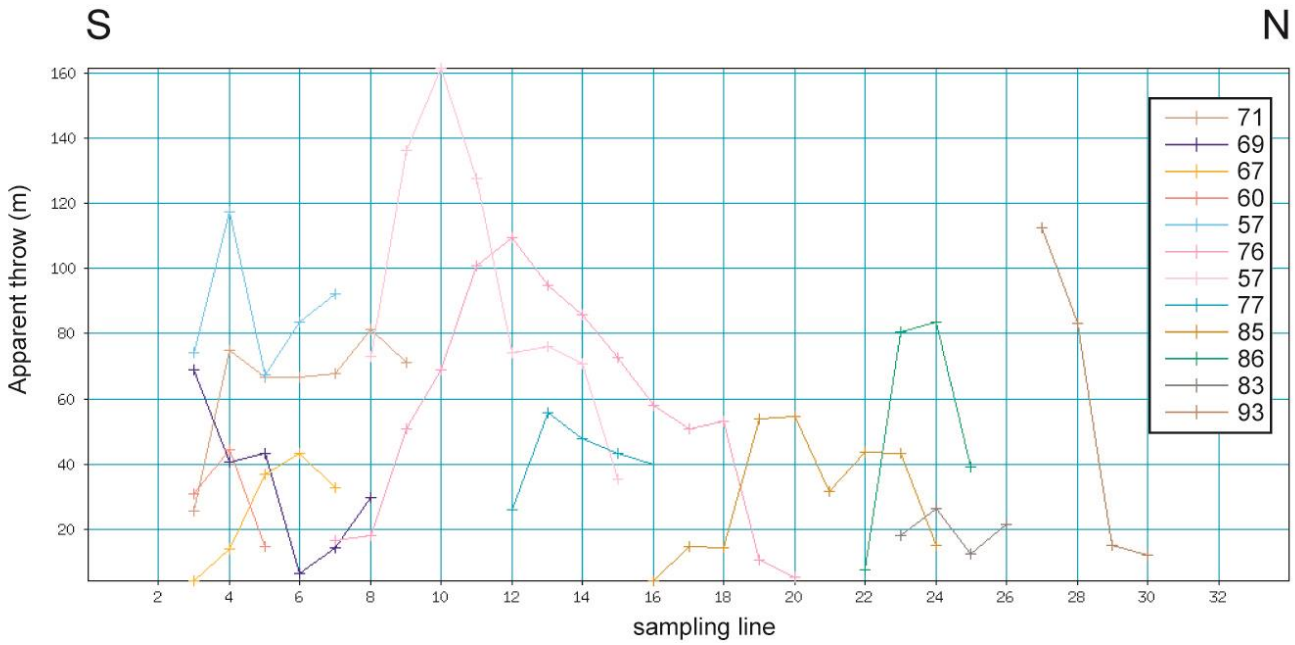

Figure 71: Displacement profiles of the main faults on Block B (Figure 64) that show an average displacement of the top Wonnerup of 70m.

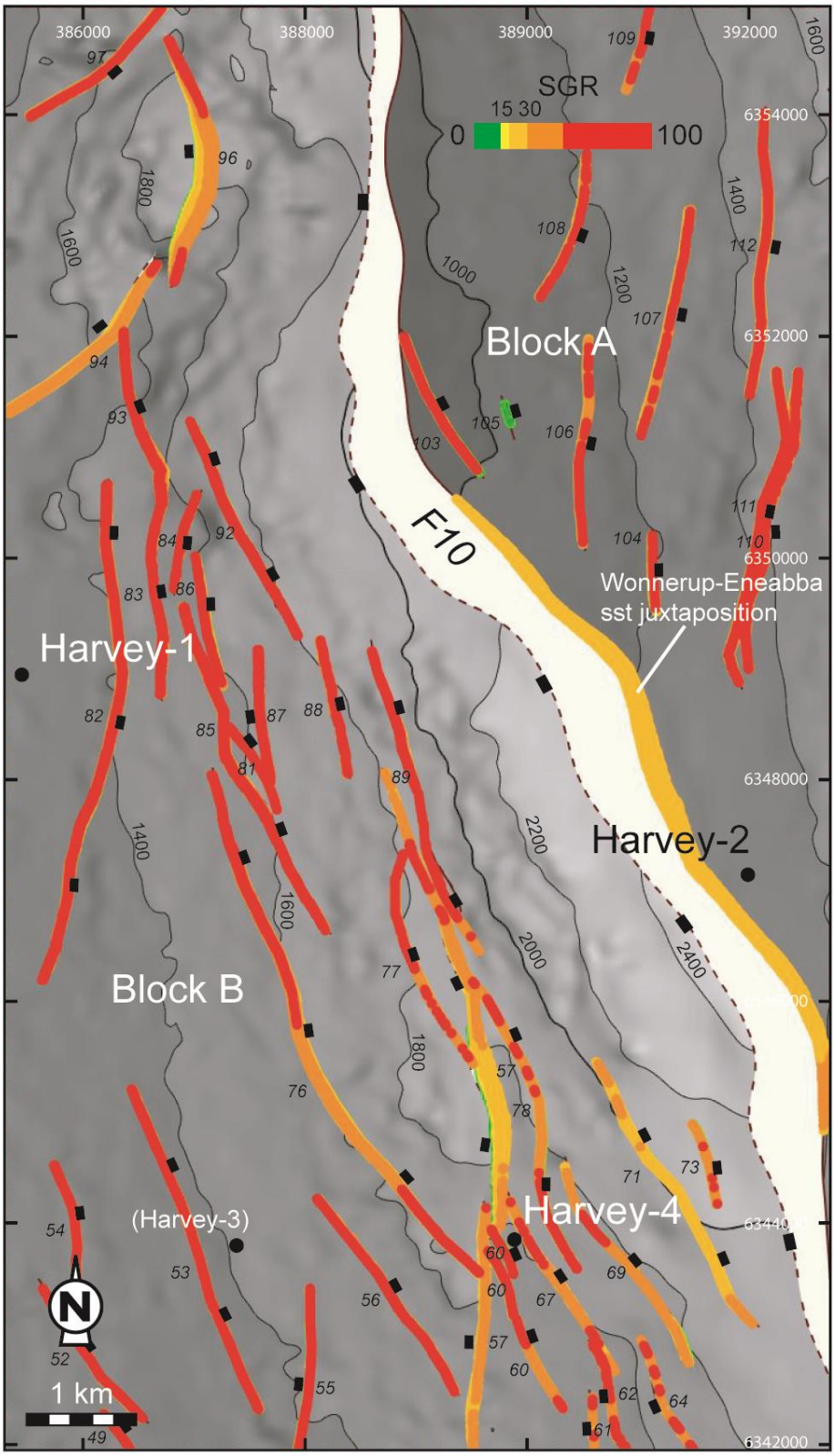

Figure 72: SGR distribution for the Wonnerup-Yalgorup juxtaposition in Block B.

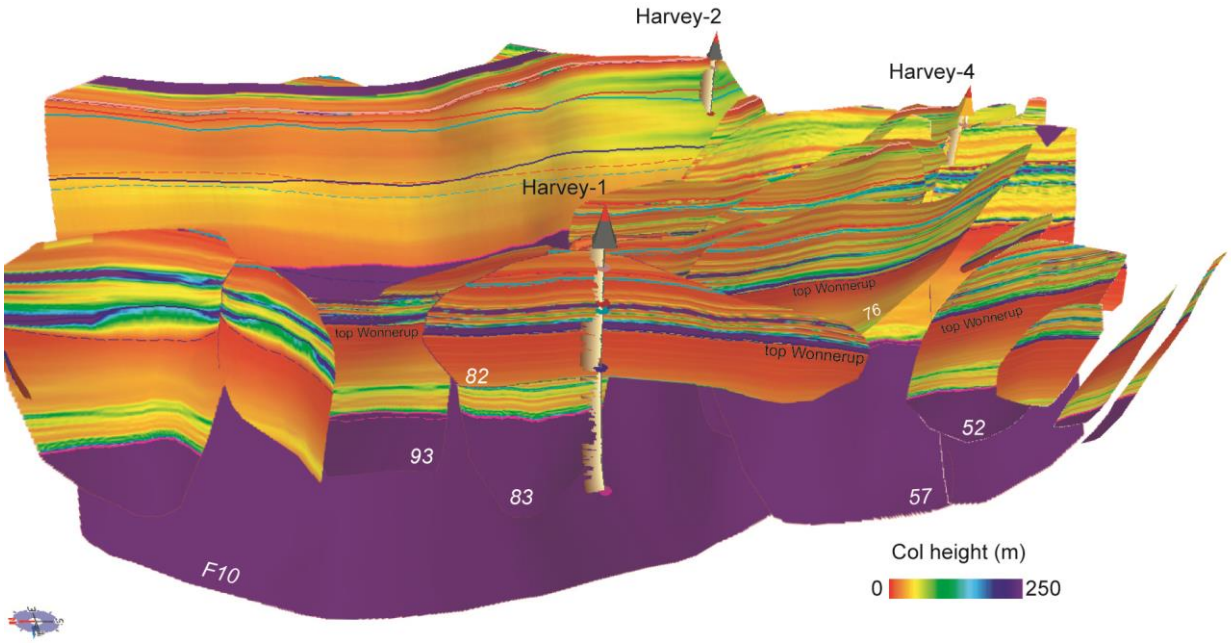

Figure 73: CO_2 column height supported by membrane fault seal for the Wonnerup-Yalgorup juxtaposition.

West of fault F10 (Block B) the SGR values for Yalgorup self-juxtaposition (i.e., the upthrown Yalgorup Member is juxtaposed against itself) vary from >65% in the lower and middle part down to <10% locally and mostly in the upper part (Figure 74. The SGR distribution for the Yalgorup self-juxtaposition suggest the presence of baffles throughout most of the formation and generally able to support >100 m CO_2 column.

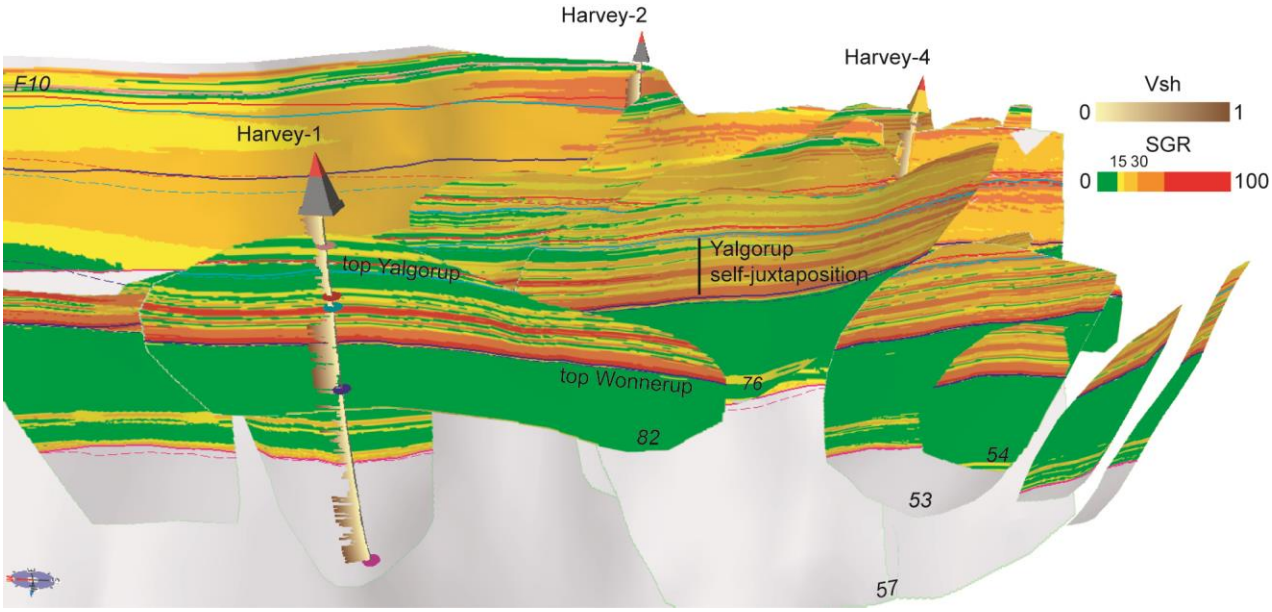

Figure 74: SGR distribution for the Yalgorup self-juxtaposition in Block B.

3.4.2. Geomechanical fault seal prediction

Active or critically-stressed faults intersecting the caprock are often cited as more likely to be fluid conduits whereas inactive or non-critically stressed faults are thought more likely to act as barriers (e.g. Sibson, 1987; Muir-Wood and King, 1993; Anderson et al., 1994; Barton et al., 1995; O'Brien et al., 1999; Sanderson and Zhang, 1999; Wiprut and Zoback, 2000; Zoback and Townend, 2001; Revil and Cathles, 2002; Ligtenberg, 2005; Wilkins and Naruk, 2007).

Characterising the stress state of a fault plane is a key aspect for assessing the risk of along-fault hydrocarbon leakage (Wiprut and Zoback, 2000). When plotted on a Mohr diagram (Figure 75), faults lying above the failure envelope are reactivated and likely to be conductive (Barton et al., 1995). This is supported by evidence showing that seal breach by fault reactivation represents a critical exploration risk for hydrocarbons in many petroleum provinces (Smith, 1966; Sibson, 1996; Abrams, 1996; Kaluza and Doyle, 1996; Dewhurst and Jones, 2002; Dewhurst et al., 2002, Gartrell and Lisk, 2005; Langhi et al., 2010).

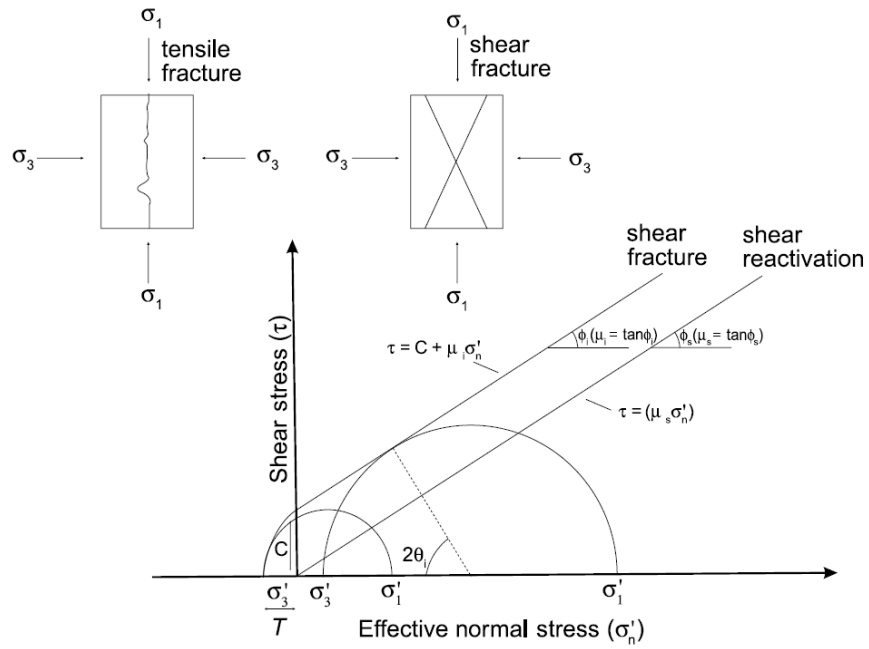

Figure 75: The effective normal (σ'n) and shear (τ) stresses leading to shear and tensile fracturing assuming a cohesionless Coulomb failure envelope (τ = μsσ'n) for shear reactivation of a pre-existing fracture and a composite Griffith (τ2 - 4T σ'n - 4T2 = 0) – Coulomb (τ = C + = μiσ'n) failure envelope for intact rock. The upper diagrams are schematic illustrations of the orientations of tensile and shear fractures in a rock sample. Shear fracturing occurs where differential stress (σ1 - σ3, the diameter of Mohr circle) is relatively large compared to the tensile or cohesive strengths and tensile fracturing at Fault Seal Risks Associated with Clay-rich Lithologies relatively lower differential stress. The symbol μs is the static friction coefficient along an existing plane of weakness; and μi is the internal coefficient of rock friction for intact rock (Mildren et al., 2005).

The SW Hub stress tensor is resolved onto the modelled faults to compute the shear and normal stresses, and the faults are colour-coded by the resultant value of slip tendency which is the ratio of resolved shear stress to resolved effective normal stress on a surface (Morris et al., 1996) and that determine the stability or failure risk of a plane of weakness (Morris et al., 1996; Lisle and Srivastava, 2004). Slip is likely to occur on a surface if resolved shear stress equals or exceeds the frictional sliding resistance.

$$T_s = \tau/\sigma_{n\,eff} \geq \mu \qquad (2)$$

where τ is the shear stress, $\sigma_{n\,eff}$ the effective normal stress (σ_n minus fluid pressure), and μ the coefficient of friction on a pre-existing fault plane. Byerlee (1978) shows that,

for an effective normal stress ≥ 10 MPa, μ is within the range 0.6-1.0. At a depth of 1500m (typical depth for top Wonnerup in Block B) the effective normal stress is between 13MPa and 23 MPa. Therefore a slip tendency of 0.6 corresponds to the (lowest) frictional strength of a cohesionless rock surface, and can be considered an approximate estimate of the stress state that would induce slip and therefore cause the fault to act as a fluid conduit (Bretan et al., 2011). The slip tendency analysis is a technique that permits rapid and easy visual assessment of stress states and related potential fault activity (Moeck et al., 2009). However this represents a relative measurement potential of fault activity. For planes that are under an overall similar in-situ stress an increase of slip tendency correlates with an increase in potential fault activity because on a Mohr diagram the fault plane is closer to the failure envelop. However for planes that are not under an overall similar in-situ stress (e.g., due to important variations of depth between the planes) an increase of slip tendency will not always correlate with an increase in potential fault activity because on a Mohr diagram the fault plane with the lower slip tendency value might be closer to the failure envelop than the one with higher slip tendency value.

A way to overcome this limitation is to use the fracture stability attribute (Mildren et al., 2005) that represents the critical pore pressure perturbation required to induce failure on a particular fault orientation. This attribute can be computed assuming a cohesionless frictional failure (e.g., Finkbeiner et al., 2000; Wiprut and Zoback, 2000) or assuming faults with cohesive strength (Dewhurst and Jones, 2002; Jones et al., 2002). For the SW Hub the variation of depth to the top Wonnerup Member is as much as 1000 m, therefore the fracture stability is also used to quantify the possibility of reactivation-related seal breach. The pore-pressure increase might occur as a result of a new buoyant supercritical CO_2 column.

The critical column height corresponding to the pore-pressure increase P depends on the fluid densities:

$$h_{max} = P/(\rho_w - \rho_h)g \quad (3)$$

where ρ_w and ρ_h are the densities of water and buoyant fluid and g is the acceleration due to gravity.

The in-situ stress data used is the one defined by Langhi et al. (2013) (Figure 76) and comes from the integration of data from Harvey-1 (Pevzner et al., 2013). It represents a strike-slip regime (SHmax> Sv>Shmin) (Van Ruth, 2006) that transitions to a reverse regime at depth < c. 500m. For the calculation of the slip tendency and the fracture stability, the vertical stress (Sv) gradient is 0.0217 MPa/m and has been derived from the integration of density data form Harvey-1 (Pevzner et al., 2013) . The minimal horizontal stress (Shmin) is estimated using the bilateral constraint (Zoback, 2007) and the maximum horizontal stress (SHmax) is estimated from the frictional equilibrium criterion for the strike-slip fault regime (Zoback, 2007). The gradient used for the horizontal stresses (SHmax and Shmin) are set to 0.0261 MPa/m and 0.018 MPa/m respectively. This results, for the calculated stress attributes, in a stress state at 600 m below ground level characterised by Shmin=12.3 MPa, SHmax=15.2 MPa and Sv=13.0 MPa. These linear parameters give an unrealistic stress regime with SHmax<Shmin at depth shallower than 250m, therefore stress attributes should be ignored for that depth range. Based on borehole breakout analysis SHmax has orientations between 085° and 120° in Harvey-1 with an average orientation of 106° (Pevzner et al., 2013).

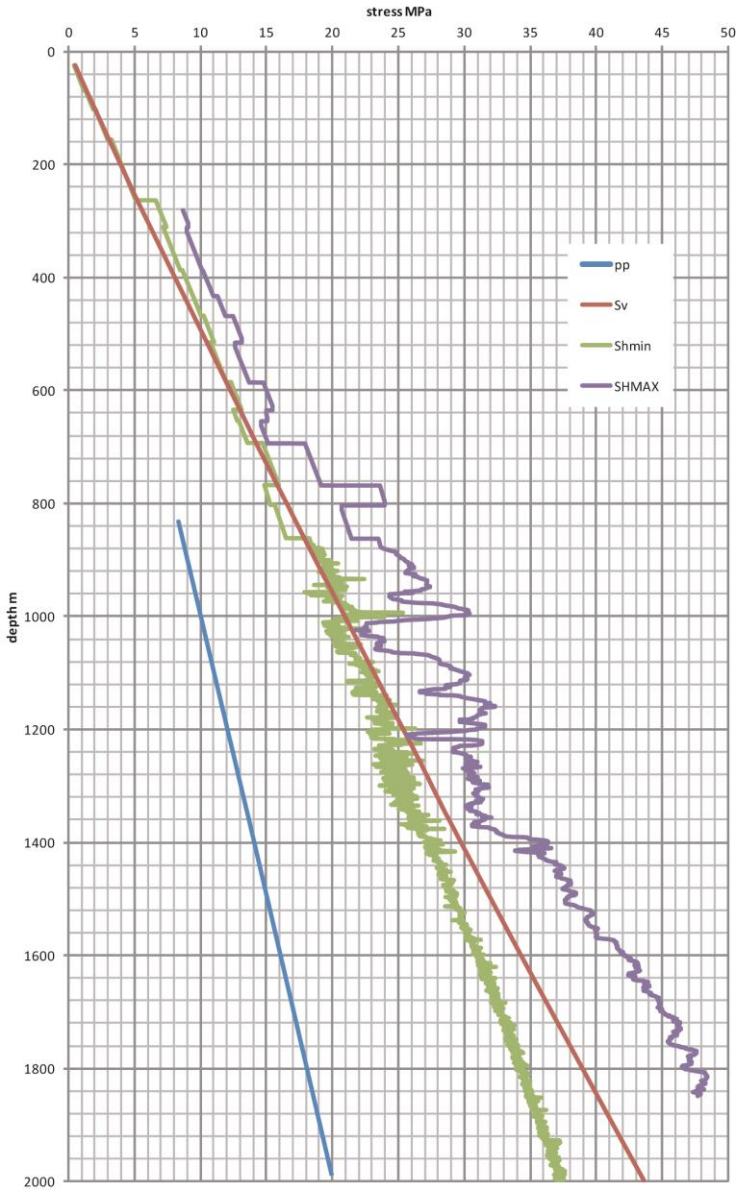

Figure 76: In-situ stress field derived from Harvey-1.

3.4.3. Stress state on fault planes

The slip tendency (T_S) values are minimum for faults striking parallel to SHmax and Shmin (105° and 195° respectively). T_S increases for strike orientation 50°-80° (SW-NE) and 130°-160° (SSE-NNW) (Figure 77). Using the strike-slip regime defined above, none of the faults modelled for the SW Hub are predicted close to failure with slip tendency values at the top Wonnerup Member lower than 0.6, typically between 0.15 and 0.3 (Figure 77 and Figure 78). Faults in the Block B as well as the large fault F10 to the east are partly optimally oriented (i.e., NW to NNW, Figure 77). However, the

maximum slip tendency is ~0.3 at top reservoir level well below the lowest frictional strength of a cohesionless rock surface and suggests a low risk of reactivation.

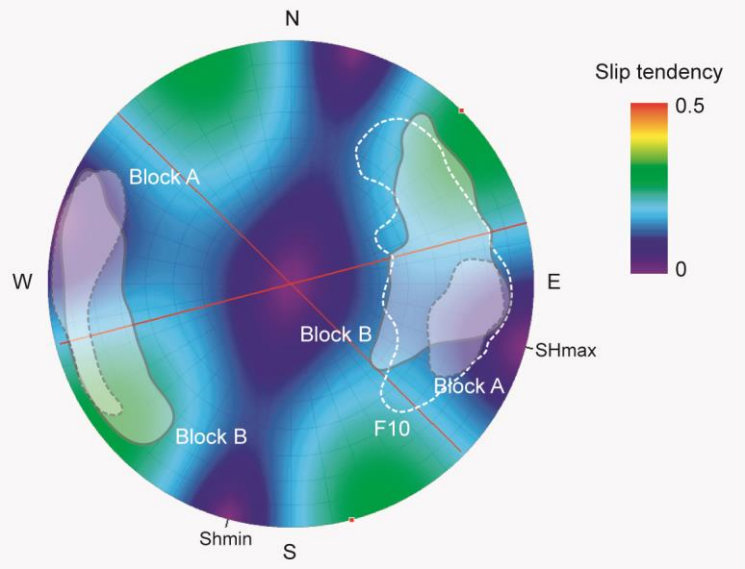

Figure 77: Slip tendency stereonet near the top Wonnerup (1500m). The poles of the faults from Block A and B and F10 are plotted on the stereonet.

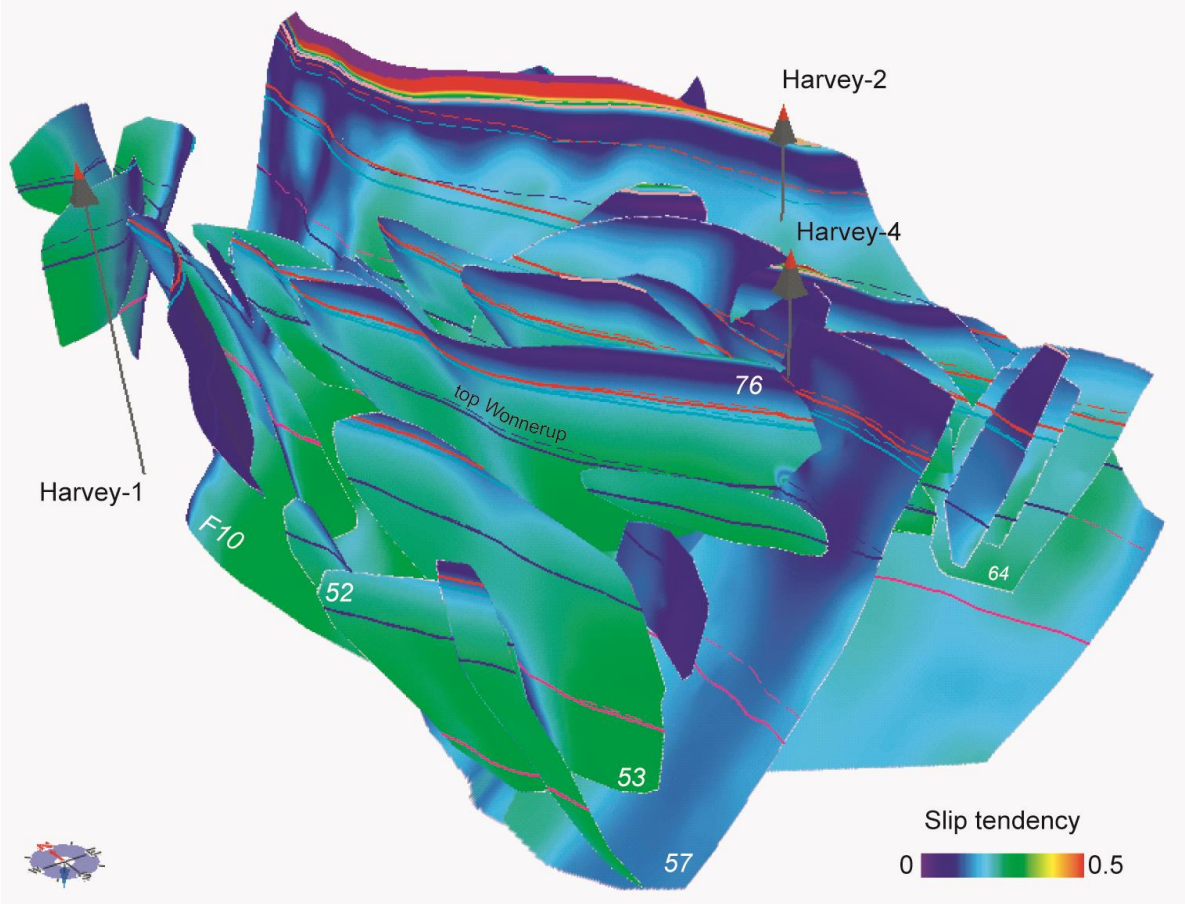

Figure 78: Slip tendency distribution. The cutoff lines for the top Wonnerup are in blue.

The fracture stability (i.e., pore pressure perturbation required to force a fault into failure) has been calculated using a coefficient of internal friction of 0.5 and a cohesive strength of 3 MPa (Figure 79) and then converted to an equivalent of maximum CO_2 column height using the equation (3) and a supercritical CO_2 density of 370kg/m^2 (Langhi et al., 2013). This shows the predicted amount of trapped CO_2 column that would be required to induce fault slip and therefore to cause up-dip fault leakage out of the Wonnerup Member (Figure 80). CO_2 column heights in excess of 2000m are needed to reach failure stress (at the top Wonnerup Member). The lowest column heights correlate with shallower top reservoir; this is visible in the south-west of Block B and on Block A.

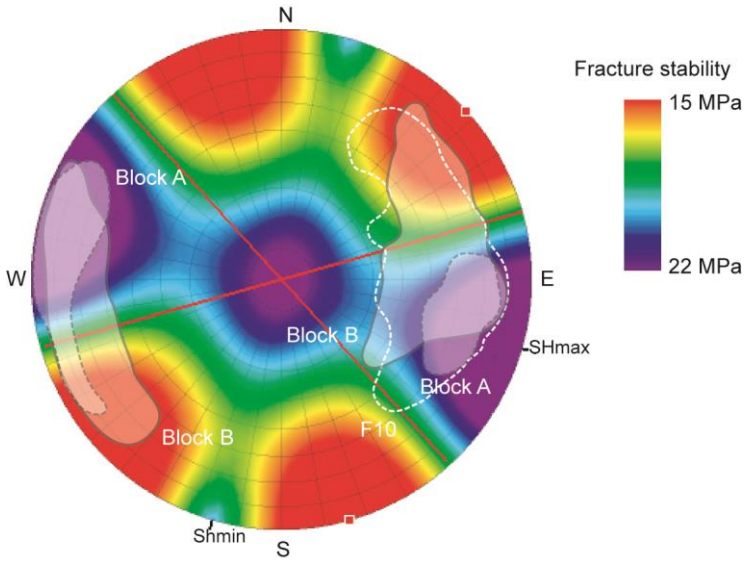

Figure 79: Fracture stability stereonet near the top Wonnerup (1500m). The poles of the faults from Block A and B and F10 are plotted on the stereonet.

The CO_2 column height can also be computed assuming cohesionless faults (cohesive strength 0). This could represent a conservative approach to evaluate reactivation potential due to increase of pore pressure. The overall column height distribution pattern is similar than with the fracture stability but CO_2 column height values decrease between 40% and 50% depending the depth.

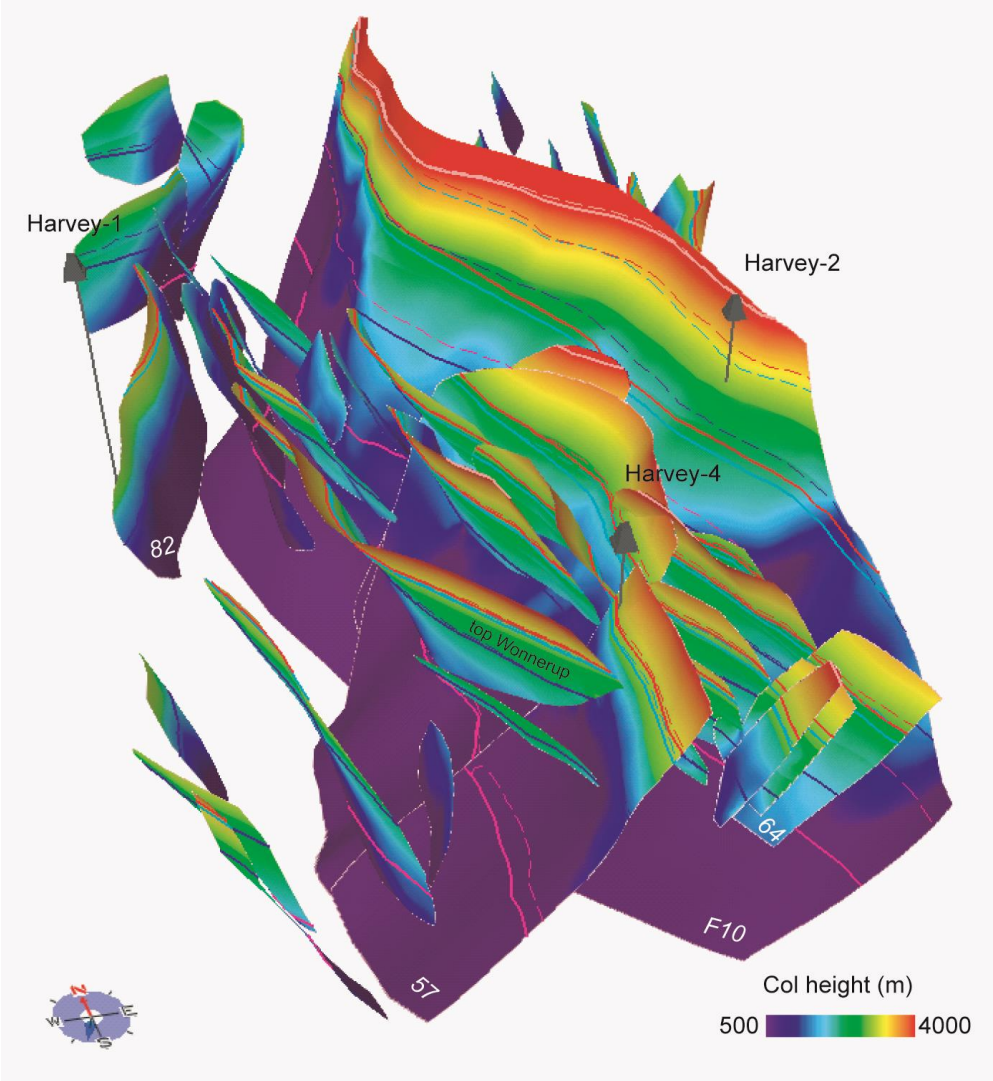

Figure 80: Supported CO_2 column height distribution. The cutoff lines for the top Wonnerup are in blue.

3.4.4. Implications of fault seal assessment for CO_2 storage

Migration of injected CO_2 in Block B in the SW Hub can be affected by fault seal by:

1. lateral migration of CO_2 between reservoir faults-bounded compartments,
2. lateral migration of CO_2 between reservoir and Yalgorup Member,
3. along fault migration of CO_2 between reservoir and overburden

The SGR model suggests that the connectivity between reservoirs compartments, in Block B, is high due to low likelihood of fault sealing potential within the Wonnerup Member. The low SGR values for Wonnerup self-juxtapositions reflect the cleanness of

this formation in Harvey-1, consisting mostly of high energy fluvial coarse sandstone (Delle Piane et al., 2013). Higher shale content in the lower part of the Wonnerup Member in Harvey-1 results in the modelling of a series of semi-horizontal baffles predicted for faults in Block B (Figure 68 and Figure 69).

The likelihood of lateral migration across faults between the upthrown Wonnerup Member and the Yalgorup Member is low. Locally the model predicts that the across fault migration potential can increase especially at the base on the juxtaposition and toward the south-east of the study area. This is likely to be attributed to misties between the top Wonnerup horizon and Harvey-4 data with the interpreted horizon slightly too deep (~50m) resulting in the base of the Yalgorup member to include clean sandstones. In overall, the model suggests that, for most of the Wonnerup-Yalgorup juxtaposition, migration is unlikely (Figure 72) and the faults can support an average CO_2 columns of 90m and up to 300m (Figure 73). Due to lower shale content in the Wonnerup Member in Harvey-4 (compare to Harvey-1) the faults near Harvey-4 in the southern part of Block B are associated with a slightly lower membrane seal potential (Figure 72).

Juxtaposition of the Wonnerup Member against the Eneabba Formation is only possible at fault F10. The potential of lateral migration of CO_2 is moderate using SGR as it generally exceeds the general 20% threshold (Yielding, 2002) (Figure 70 and Figure 72) and the fault could support a CO_2 column up to 40m. However the SGR algorithm assumes that the seismically derived throw is concentrated on a single plane and does not account for fault zone architecture. The fault F10 presents offsets of 900m-1200m at the top Wonnerup horizon and thicknesses of 160m-400m. Following the fault evolution model of Childs et al. (2009), the resulting displacement/thickness ratio of 2 to 6 suggests that for F10 could include, beside the fault gouge, fault zones (anastomosing network of through-going synthetic slip surfaces and associated fault rock) and possibly breach fault relays. These could significantly impact on the seal potential of fault F10. Currently, injection of CO_2 in Block A, east of F10, is not considered.

The likelihood of vertical migration along faults between the Wonnerup Member and the overburden is assessed using fault geomechanical attributes that are functions of the shear and normal stresses on the fault plane and the distance to the failure envelop (i.e., the pore pressure perturbation required to induce failure). Both these parameters

present uncertainties due to (1) the lack of rock physics data limiting the definition of failure envelops and (2) limitation of data for the calibration of the in-situ stress field.

Part of the faults in Block B and fault F10 are optimally oriented for failure (NNW and NW, Figure 77). However, the stress state at the depth of the Wonnerup Member results in a low slip tendency below the empirical typical threshold of 0.6 suggesting a low risk of fault reactivation under the present-day stress (Figure 77 and Figure 78).

The maximum CO_2 column height theoretically supported by a fault plane before failure (equation (3)) is marginally orientation-dependant with slightly lower values for strike orientations between 50° and 160° (SE-NW to ENE-WSW) and for fault with dip > 60°. However the depth has the most impact as an increasing depth corresponds to increasing pressures and moves the Mohr Circle away from the failure envelop and therefore increases the potential CO_2 column height. Based on the pore pressure perturbation required to induce failure on a particular fault orientation, the modelled smallest CO_2 column heights required to reach failure stress are located to the south-west of Blocks A and on Block B and represent 1900m or 1000m when assuming a cohesive and cohesionless fault respectively (Figure 79 and Figure 80). CO_2 column heights in excess of 2000m are needed to reach failure stress for faults, with a cohesive strength of 3 MPa, intersecting the Wonnerup Member in Block B.

The geomechanical fault seal assessment suggests that the faults in Block B are unlikely to fail and reactivate under the present-day stress field. An increase in pore-pressure equivalent to more than 1000m of CO_2 column would be required to force the fault planes in Block B into failure, assuming a cohesionless fault.

3.5. Fracture prediction

It is well established that small brittle faults are not reliably imaged by seismic reflection methods when their offset is less than the seismic resolution (i.e., about 20 m in most datasets, Dee et al., 2007). In recent years geomechanical approaches have been used to predict the likely distribution of subsurface strain, and then to transform it to stresses to predict the intensity and nature of brittle deformation (Bourne and Willemse 2001; Bourne et al. 2001; Maerten et al. 2002; Dee et al., 2007). We adopt here an approach

detailed by Dee et al. (2007) and use a boundary element method (BEM), in which faults are represented as dislocations embedded in an isotropic elastic medium (Crouch and Starfield 1983). We assume for the SW Hub that a dominant control on small-scale faulting is the strain perturbation around larger faults. Variations of rock properties that occur in layered sedimentary sequences are not considered in the strain modelling, only in the fracture criterion. Despite this limitation Dee et al. (2007) demonstrate that the method is useful in providing a process-driven prediction of small-scale faults and fractures.

The workflow used follows that described by Maerten et al. (2002) and Dee et al. (2007). The fault slip pattern mapped on seismic reflection data is the primary input data; the algorithms of Okada (1992) are then used to compute the displacement vector and fault-related strain tensor at any observation points in the surrounding rock volume. As the fault-related strains represent a local perturbation superimposed on the regional far field strain, this latter has to be defined and added at every observation point. The strain tensors are then used to calculate stress tensors and the effective overburden stress is added. The predicted rock fracturing resulting from the total stress is then computed by comparing the state of stress to a standard Mohr–Coulomb failure envelope, defined by appropriate coefficient of internal friction μ and cohesive strength C. to determine the mode of failure the Δχ method from Bourne and Willemse (2001) is used. The maximum Coulomb shear stress (MCSS, Jaeger and Cook 1979) is used as a proxy for fracture intensity (Maerten et al., 2002).

For the SW Hub, the elastic dislocation method (ED) is used to attempt to define a first order prediction of the small-scale subsidiary faults and fractures for the Block B within in the upper part of the Wonnerup Member and the Yalgorup Member representing the potential regional top seal (Figure 58). These two models use (1) the same observation surface to calculate strains due to faults displacement, (2) the same depth correction take into account real depth at the time of faulting, (3) the same regional strain to be superimposed to the ED strains and (4) two sets of rock properties Wonnerup Member and the Yalgorup top seal. The models parameters are as follows:

1. The observation surface is the interface between the Wonnerup and the Yalgorup Members.

2. The bulk of the displacement on the large faults pre-dates the Neocomian Unconformity and likely occurred during the Early Cretaceous. Based on stratigraphic correlation throughout the South Perth Basin (Crostella and Backhouse, 2000), vitrinite reflectance data from the nearby Lake Preston-1 (Iasky, 1993) and fluid inclusion pressure data from Pinjarra-1 (Bourdet et al., 2015), we assume that at the time of faulting, 1200 m of additional Late Jurassic sediments (Eneabba and Yarragadee Formations) were present. Therefore the depth is adjusted accordingly before generating the ED model in order to obtain the likely depth of the fault planes during slip.
3. A regional strain is estimated through the measurement of the cumulative slip across structures in the SW Hub. The maximum horizontal strain has an azimuth of N262 and an estimated magnitude of 5% (extension). The minimum horizontal strain has an estimated magnitude of 1% (extension). Assuming a preservation of volume the calculated vertical strain is 5.7% (shortening). This estimate represents the fault-related strain over a limited distance represented by the framework model and may underestimate the total fault related strain on the SW Hub and may not be representative of the South Perth Basin as a whole.
4. For the Wonnerup Member, static rock properties were estimated from geomechanical analysis of four cores from Harvey-1. For the Yalgorup Member, static rock properties (Poisson's Ratio and Young's Modulus) were initially estimated from velocity logs from Harvey-1 and calibrated with data from the Wonnerup Member. The values used for the ED models are shown in Table 9.

STRATIGRAPHIC UNIT	POISSON'S RATIO	YOUNG'S MODULUS (MPa)	DENSITY (KG/M3)	COHESIVE STRENGHT (MPa)	COEF OF INTERNAL FRICTION
Wonnerup Mbr	0.2	19250	2200	13.7	0.58
Yalgorup Mbr	0.33	8500	2000	11	0.38

Table 9: Static rock properties for the Wonnerup and Yalgorup Members for the fracture modelling.

The mode and orientation of predicted faulting is displayed in Figure 81. Within Block B, the imposed regional strain (extensional) produces dominantly high angle normal faulting (> 40°) within the Wonnerup and Yalgorup Members (shear failure shown in red). Overall, the orientation of the shear failure for the Wonnerup and Yalgorup Members within Block B is similar, with only local variations, and is consistent with observations of subsidiary faults within Block B. In the close vicinity of the large fault F10 (hanging wall) rotation of the strike direction occurs that also involves localised reverse and strike-slip shear failure planes in both the Wonnerup and Yalgorup

Members (Figure 81). The effect of the local perturbation of the stress field is likely to induce these types of failures in association with the dominant shear failure; however the methodology used here is also known to produce unstable result very close to the main deformation surfaces. Although a 100m blanking zone was used in the modelling around the main faults, the non shear failure observed in Block B near the fault F10 could represent numerically unstable values or could result from inaccurate interpretation of the observation surface (i.e. top Wonnerup horizon) near the fault F10.

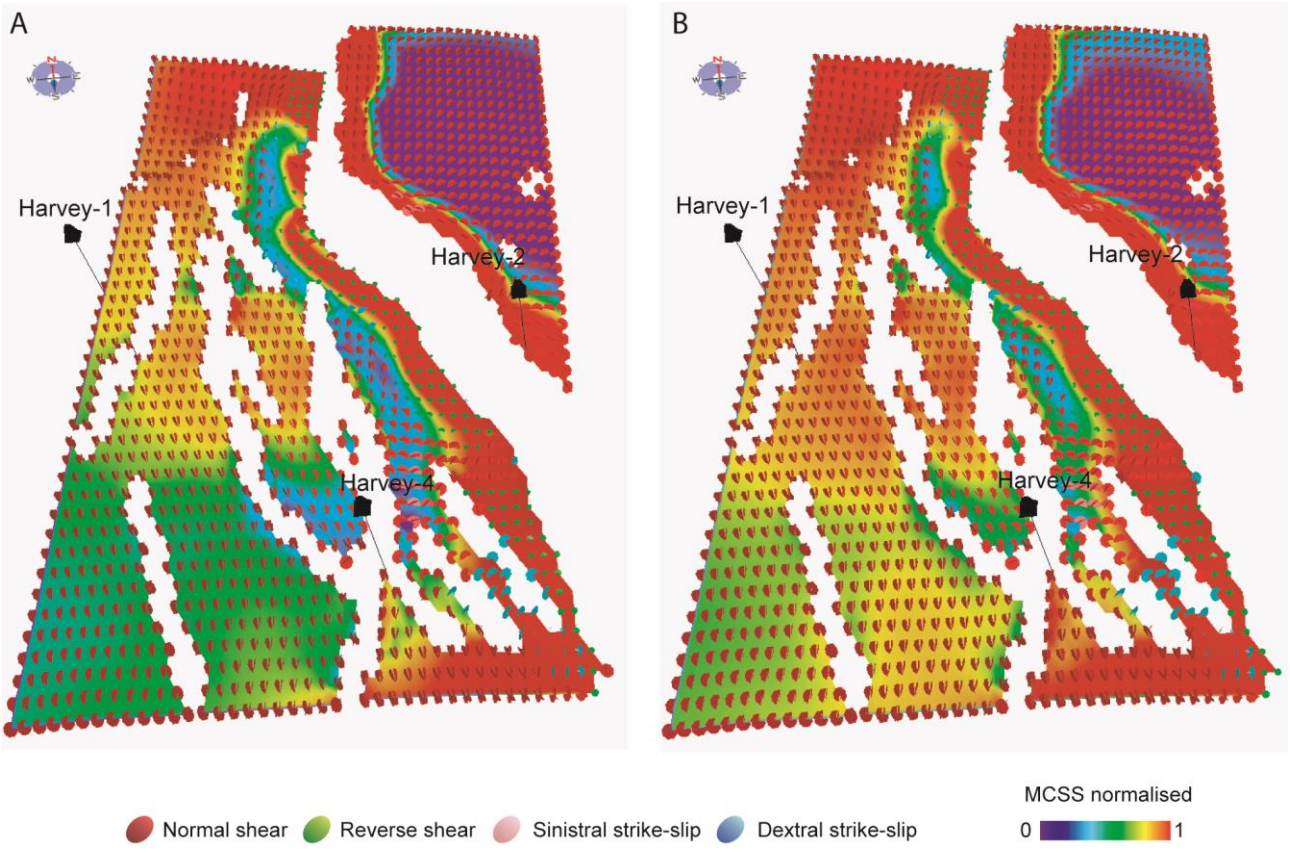

Figure 81: Modelled fractures, mode of failure and density represented by the normalised MCSS. A) Upper Wonnerup Member. B) Lower Yalgorup Member.

The azimuth of the σ_2 orientation in map view corresponds approximately to the predicted orientation of normal-fault strike in ED model (Dee et al., 2007). There is an overall correspondence between the predicted and the observed subsidiary fault orientation suggesting that the model achieved a reasonable match. The observed

discrepancy in the vicinity of F10 can result from inaccurate interpretation of fault displacement or inaccurate interpretation of the observation surface due to poor seismic signal; this will affect the definition of the strain tensor in the surrounding rock volume and thence the fracture prediction. Over a large part of Block B the predicted fault strikes are parallel to the main fault trends with predicted fault orientation varying from N-S to NNW-SSE. Due to local stress perturbation, SW-NE features are also predicted within the Wonnerup and the Yalgorup Members in Block B especially near F10 (Figure 82).

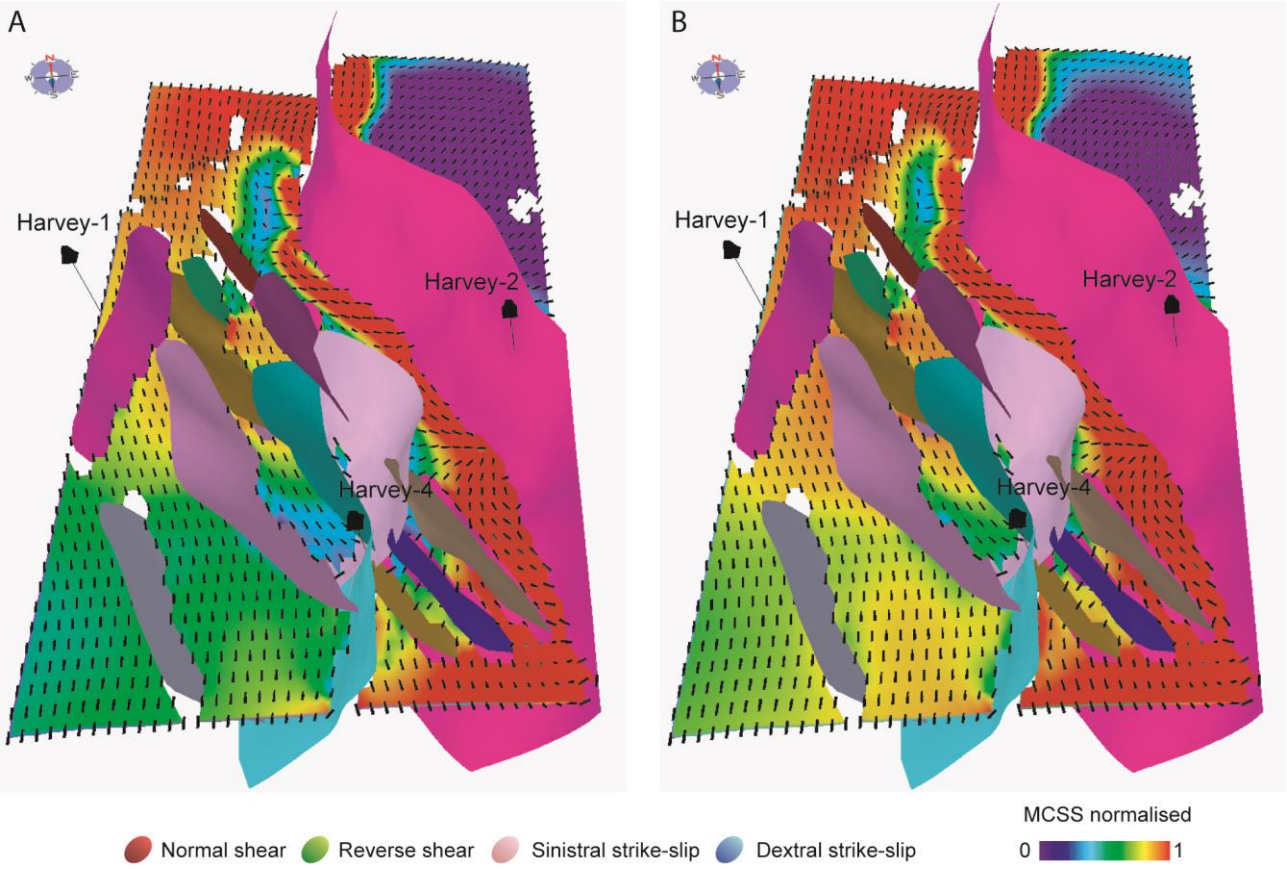

Figure 82: Modelled fractures, orientation. The azimuth of the σ2 orientation corresponds approximately to the predicted orientation of normal-fault strikes. A) Upper Wonnerup Member. B) Lower Yalgorup Member.

Figure 81 and Figure 82 show the computed normalised maximum Coulomb shear stress (MCSS) for the SW Hub for both the Wonnerup and the Yalgorup Members. Warmer colours indicated where, over many seismic cycles, the shear failure envelope has been exceeded repeatedly by the highest shear stresses (Dee et al., 2007) and is therefore related to higher fracture intensity potential (Maerten et al., 2002). The qualitative distribution of MCSS is similar within the Wonnerup and the Yalgorup

Members (Figure 81 and Figure 82). The main subsidiary faults mapped within Block B (i.e., mostly between Harvey-1 and Harvey-4) are aligned through the maxima in the MCSS distribution. Due to uncertainties related to the structural and stratigraphic interpretation in the north-west corner of the geological model, the results of the fracture modelling in the vicinity of faults 94, 96 and 97 should be disregarded and are not discuss here.

The predicted normal shear planes that represent most of the small-scale deformations in Block B can impact on the structural permeability at the time of tectonic activity (i.e. Early Cretaceous). However their impact on the CO_2 containment potential of the SW Hub has to be assessed using present-day in-situ stress data (Figure 76). Figure 83shows the normal shear fracture networks colour coded with the magnitude of slip tendency for the lower Yalgorup.

The slip tendency values for the fracture in the lower Yalgorup are lower than 0.6 in Block B. Orientations 50°-80° (SW-NE) and 130°-160° (SSE-NNW) and dip > 50° show the relative higher slip tendency (Figure 84). Some fractures optimally oriented north of Harvey-1 present slip tendency values up to 0.3 (Figure 83). However these still remain well below the empirical threshold of 0.6 for fault reactivation.

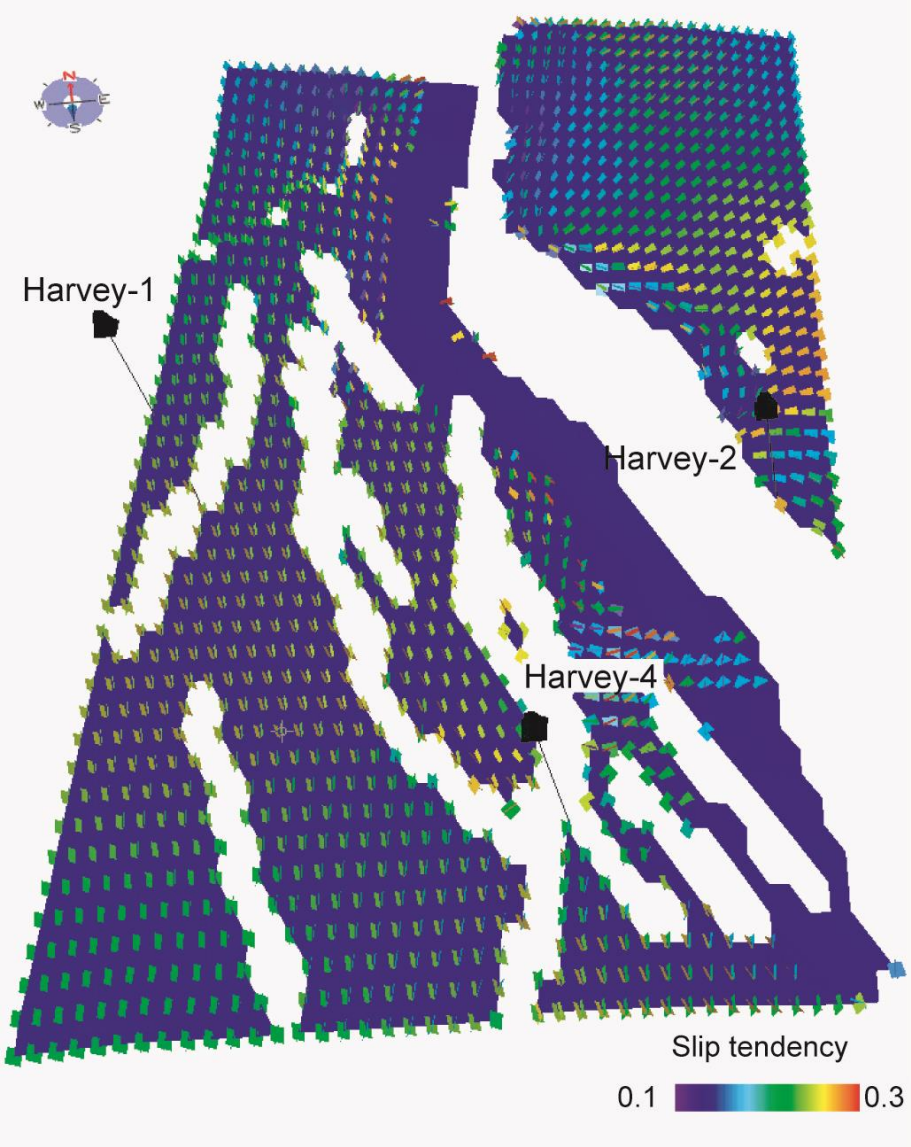

Figure 83: Slip tendency for normal shear fracture networks for the Lower Yalgorup Member. A) Slip tendency.

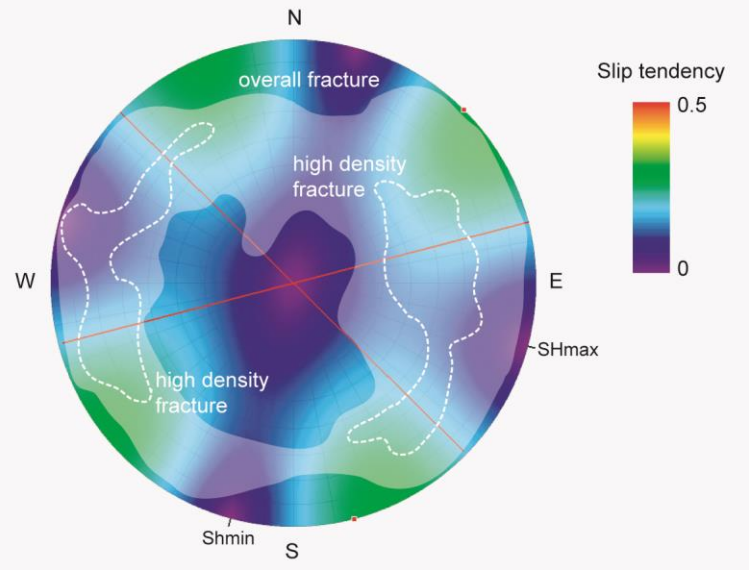

Figure 84: Slip tendency stereonet near the base Yalgorup (1500m). The poles of the fractures from Block A and B are plotted on the Stereonet with higher density of fracture delimited by the dotted line.

3.5.1. Implication of fracture prediction for CO_2 storage

The modelled small-scale faults in the SW Hub are assumed to develop due to deformation controlled by stress perturbation around larger faults which is most likely caused by Early Cretaceous slip episodes. The ED models predict dominant initial shear failures with a maximum density in the central part of Block B for both the Wonnerup Member and the Yalgorup Member (Figure 81). However, based on the present-day in-situ stress data, the model predicts that the fractures networks at the top of the reservoir or at the base of the Yalgorup Member are not critically stressed therefore less likely to be conductive for fluid flow under the present-day conditions.

4. CONCLUSIONS AND RECOMENDATIONS

The project was aiming to apply advanced seismic processing algorithms to improve quality of the imaging at SW Hub area, in particular to remediate the effects of the irregular geometry and presence of significant gaps due to the presence of 'NOGO' zones and, also, to improve fault imaging. The second principal goal of the project was to use to update fault seal analysis using the new data available, including the results of the seismic data processing and available well information. So here we group the conclusions according to these main goals.

Seismic data processing and analysis

One of the assumptions of 3D seismic data imaging is that offsets and azimuths have consistent distribution and that the trace density is regular. Hence straightforward processing of datasets that do not meet this requirement, can result in processing and imaging problems and artefacts. Harvey 3D is a dataset with irregular geometry. This was mitigated by utilisation of pre-stack Kirchhoff migration algorithm and by data pre-conditioning in the offset planes. Operations performed in the offset planes involved zeroing all the extrapolated migration artefacts. This comprehensive approach resulted in fully merged 3D seismic cube with continuous reflectors across the entire area. The methodology presented here can be used to merge seismic data vintages that may have vastly different acquisition geometries and source characteristics.

The post-stack diffraction imaging was used as a complimentary method for fault detection to conventional attribute-based detection of faults. The main use of the D-sections in the interpretation was not to localise the faults, but to use the attributes obtained during the diffraction imaging for steered post-stack migration of the data. The results clearly emphasize the discontinuities in the image compared to the standard post-stack migration and image certain faults even better than the pre-stack imaging.

CRS technology was tested on a portion of the full Harvey 3D data, but failed to produce significant uplift in information.

The 3D PDSM results demonstrate that 3D Kirchhoff migration operators are able to successfully image reflectivity from the large-scale 3D geologic structure contained within a target-oriented 10x10km2 area of the Harvey 3D seismic survey to depths of nearly 6km. The western half of imaged area shows a 1.5km-thick geologic unit of broad lateral extent with little internal reflectivity that dips slightly to the west. The eastern half of the image volume highlights a prominent fault reflector, presumably associated with the F10 fault. Overall, the 3D Kirchhoff PSDM results showed a modest uplift over the fast-track pre-stack time-migration (PSTM) results, and represent a worthwhile exercise to be applied at future Australian CO_2 geo-sequestration sites.

Imaging with 3D RTM operators was less successful than with the corresponding 3D Kirchhoff operators. The RTM image volumes generated demonstrated an ability to image reflectivity at depths greater than 1km; however, the numerical experiments indicated this technique was not that well suited due imaging issues largely associated with to the irregular source and receiver sampling and large acquisition holes. While 3D APEF interpolation within shot records was observed to improve the RTM results relative to non-interpolated data, the resulting RTM images were more band-limited and suffered from significant aliasing within the top 1km. Moreover, the 3D RTM analysis was roughly 3-4x computationally more expensive then Kirchhoff. Thus, even though RTM has become a mainstream 3D technique for imaging complex geologic structure in industry-oriented marine seismic settings, applying RTM in 3D land seismic scenarios may only be warranted for scenarios where: (1) data are more regular sampling throughout the full 5D seismic data volume; and (2) the true velocity models are of sufficient complexity to cause the breakdown of the approximations underlying Kirchhoff migration operators.

One of the original goals of the project was to try to predict level of time-lapse noise, providing that the 3D volume could be treated as a baseline survey for the future monitoring program. This has not been done due to the limitations imposed by the data quality and acquisition parameters.

Structural analysis for CO_2 containment risk for the SW Hub

The interpretation of the 115 km^2 3D seismic survey acquired by Geokinetics in 2014 allows to image adequately the stratigraphic and structural architectures of the SW Hub

and to build a constrained geological model. However the number of well data available for this study is not adequate to unambiguously model the facies distribution and the 3D variation of V_{sh}.

The CO_2 migration and containment potential is partly controlled by fault hydraulic behaviour and can result in lateral migration of CO_2 (1) between reservoir compartments, (2) between reservoir and the Yalgorup Member , (3) between reservoir and overburden and by (4) along fault migration of CO_2 between reservoir and overburden.

The limitations and the resulting uncertainties are:

- At the time of this work only two well (Harvey-1 and Harvey-4) are drilled in the Block B of the SW Hub and one in the Block A (Harvey-2) at the time of this work. Although this enables to generate a V_{sh} distribution model, this limits the development of a regionally meaningful 3D facies model.
- The absence of leak-off for the Leak-off test conducted in Harvey-1. The maximum and minimum horizontal stresses have to be defined using physically based relationships based on the frictional equilibrium criterion (Pevzner et al., 2013). This result is uncertainties on the in-situ stress field that affect the geomechanical fault seal assessment.
- The restricted geomechanical analysis performed on cores form Harvey-1. To date only 4 cores have been analysed for the Wonnerup Member. The rock properties for the Yalgorup Member are estimated from velocity data and initially calibrated with data from the Wonnerup Member. This leads to uncertainty in the geomechanical fault seal assessment and the sub-seismic fault prediction.

The geological model is characterised by a N-S to NW-SE structural trend. The main fault F10, already interpreted by Langhi et al. (2013), exhibit a maximum displacement of 1200m at the top Wonnerup and delimit the structural blocks A and B.

The large F10 fault is the only one that juxtaposes the Wonnerup with the Eneabba sandstone, overlying the regional seal. The SGR values on the fault plane are above 20% suggesting a moderate likelihood of across fault migration and a 50m supported CO_2 column before breaching the membrane seal. However the fault zone architecture could include network of slip surfaces and possibly breach fault relays.

All the other faults define a juxtaposition seal (Wonnerup Member is juxtaposed against the Yalgorup Member and Eneabba shale) or a self-juxtaposition of the Wonnerup Member. The likelihood of lateral migration of CO_2 across faults between the Wonnerup and the Yalgorup Members can be locally high at the base of the juxtaposition especially at the base on the juxtaposition and toward the south-east of the study area. However this likely an artefact to be attributed to misties between the top Wonnerup horizon and Harvey-4 data resulting in the base of the Yalgorup member to include clean sandstones. In overall, the model suggests that the Wonnerup-Yalgorup juxtapositions can support an average CO_2 column of 90m and up to 300m. The lowest values of SGR for the Wonnerup-Yalgorup juxtaposition are above 25% and are associated with faults near Harvey-4. The SGR values for the self-juxtaposition of the Wonnerup Member suggests high connectivity between reservoirs compartments, in Block B with possible baffles predicted in the lower part of the Wonnerup Member near Harvey-1.

Faults in Block B present a low risk of reactivation under the present-day stress (i.e., low likelihood to act as vertical pathways). The smallest CO_2 column heights required to reach failure stress are located to the south-west of Blocks A and on Block B and represent 1900m or 1000m when assuming a cohesive and cohesionless fault respectively.

The fracture models attempt to estimate the distribution, orientation and initial mode of failure of the subseismic faults that are predicted to have developed during the Early Cretaceous tectonic episode affecting the Wonnerup and the Yalgorup Members. The fracture models predict dominant normal shear failures with a maximum density in the central of Block B and adjacent to F10. Due to uncertainties related to the structural and stratigraphic interpretation in the north-west corner of the geological model, the results of the fracture modelling in the vicinity of faults 94, 96 and 97 should be disregarded. The stress state of these small faults and fractures suggests that there is a low likelihood of failure under the present-day in-situ stress field in Block B.

In light of these fault seal assessments, the locations associated with higher relative risks for CO_2 containment in the SW Hub are (Figure 85):

- The vicinity of the large fault F10; due to higher density of modelled sub-seismic faults and uncertainties related to the fault zone architecture that could include anastomosing network of through-going slip surfaces and possibly breach fault relays.
- The central part of Block B; due to relative higher density of modelled sub-seismic faults and the presence of fault planes optimally oriented for slip (relative high slip tendency values). However the maximum slip tendency is ~0.3 at top of the reservoir (i.e. well below the lowest frictional strength of a cohesionless rock surface and suggests a low risk of reactivation).
- The south-eastern part of Block B near Harvey-4; due to lower SGR values for the Wonnerup-Yalgorup juxtaposition seal and the planes optimally oriented for slip (relative high slip tendency values). However the maximum slip tendency is ~0.3 at top of the reservoir (i.e. well below the lowest frictional strength of a cohesionless rock surface and suggests a low risk of reactivation) and the SGR values are above 25%.
- The south-west of Block B; due to lower fracture stability values and lower CO_2 column required to induce fault slip and create vertical migration pathways. However CO_2 column heights in excess of 2000m are needed to reach failure stress at the top Wonnerup Member.

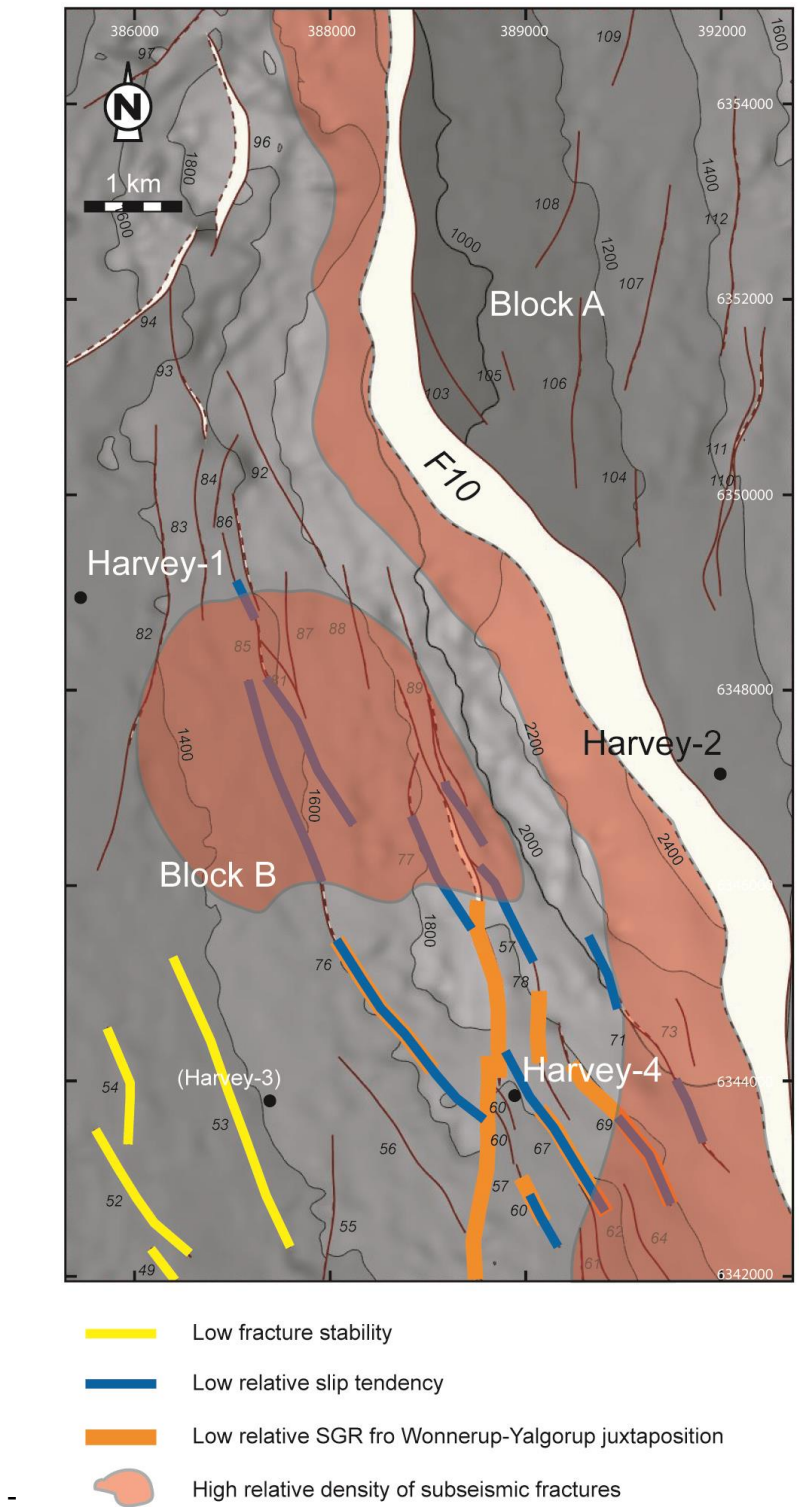

Figure 85. Locations associated with higher relative risks for CO_2 containment in the SW Hub. The vicinity of the large fault F10; the central part of Block B; the south-eastern part of Block B near Harvey-4 and the south-west of Block B. See text for discussion.

Recommendations

In light of the 3D geological modelling, the assessment of fault sealing potential and the modelling of sub-seismic faults for the SW Hub it is recommended to:

- Integrated data from newly drilled wells in order to (1) constrain the seismic interpretation (stratigraphic horizons and faults), (2) constrain the current Vsh distribution model.
- Integrate outcome from geophysical inversion work currently done to constrain the stratigraphic facies distribution and then the current Vsh distribution model.
- Refine the structural interpretation in Block B between Harvey-1, Harvey-3 and Harvey-4 and integrate outcome from geophysical inversion.
- Constrain the in-situ stress field.
- Acquire pressure data on fault compartments to constrain the across-fault pressure difference and calibrate the membrane fault seal calculations.
- Investigate cores from Harvey-2 intersecting the large fault F10 and define the geomechanical and petrophysical properties to constrain the geomechanical fault seal assessment.

LIST OF ABBREVIATIONS

AMO – Azimuthal Moveout

APEF – Adaptive Prediction Error Filter

CMP – Common middle point

DMO – Dip moveout

DMP / DMPWA - Department of Mines and Petroleum (Western Australia)

GPU – Graphics Processing Unit

LMO – Linear moveout

PSDM – Prestack depth migration

PSTM – Prestack time migration

PWD – Plane-wave Destructor

RTM – Reverse-time Migration

SW Hub – South West Hub

UWA – University of Western Australia

LIST OF TABLES

LIST OF FIGURES

SEGY FILES DESCRIPTION

Seismic 3D volumes (All volumes are in VelSeis geometry)

Headers mapping

Final datum is 40 m, replacement velocity is 2500 m/s.

No coordinate scalars.

CMP X and Y coordinates are at 73 and 77 bytes respectively.

Iline and Xline numbers are at 9 and 21 bytes respectively.

The sample rate is 4 ms (for time cubes) and 6.25 m (for depth cubes).

The bin size is 25x25 m.

The results of the Pre-Stack Time Migration:

1. File: 'PSTM_volume.sgy' – PSTM 3D seismic volume.

The results of similarity attribute analysis:

1. File: 'Similarity_Attribute.sgy' – 3D enhanced fault seismic cube (minimum similarity attribute).

The results of the Steered Migration:

1. File: 'Steered_Migration_volume.sgy' – the migrated 3D seismic volume.

2. File: 'D-volume_Diffr_Energy_Distribution.sgy' – distribution of diffracted energy (maximum semblance). Values are equalized by the average trace. The volume was computed without taking into account the phase change phenomena.

3. File: 'D-volume_Azimuths_Distribution.sgy' – the azimuths distribution volume. The volume was computed without taking into account the phase change phenomena.

The results of the Pre-Stack Depth Migration (10 by 10 km cube):

PSDM 3D seismic volumes converted to time form comparison with the PSTM results:

1. File: ‘PSDM_converted_in _time.sgy’ – PSDM migrated 3D seismic volume converted to time.

2. File: ‘PSDM_converted_in_time_AGC.sgy’ – PSMD migrated 3D seismic volume converted to time with applied AGC in 2 sec window.

PSDM 3D seismic

The sample rate is 6.25 m. The volume has spatial dimensions ~ 10x10 km.

1. File: ‘PSDM_volume_in_depth.sgy’ – PSDM migrated 3D seismic volume (in depth).

Velocity volumes: sample rate 30 ms

1. ‘Harvey_3D_NMO_VELS.sgy’ – velocity field after Interactive Velocity Analysis

2. ‘Harvey_3D_DMO_VELS.sgy’ – velocity field after DMO correction

3. ‘Harvey_3D_PSTM_VELS.sgy’ – velocity field for PSTM migration

REFERENCES

Abrams, M. A., 1996. Distribution of subsurface hydrocarbon seepage in near-surface marine sediments: AAPG memoir 66, 1–14.

Allan, U.S. 1989. Model for hydrocarbon migration and entrapment within faulted structures. AAPG bulletin, 73, 803–811.

Alonaizi, F., Pevzner, R., Bóna, A., Shulakova, V. and Gurevich, B., 2013. 3D diffraction imaging of linear features and its application to seismic monitoring. Geophysical Prospecting, 61(6): 1206-1217.

Anderson, R., Flemings, P., losh, S., Austin, J., Woodhams, R., 1994. Gulf of Mexico growth fault drilled, seen as oil, gas migration pathway: oil & gas journal, 92, 97–104.

Antonellini, M., Aydin, A., 1994. Effect of faulting on fluid flow in porous sandstones: petrophysical properties: AAPG bulletin, v. 78, p. 355– 377.

Asquith, G. Andkrygowski, D., 2004. Gamma ray, in Asquith, G. and Krygowski, D. Basic well log analysis: AAPG methods in exploration 16, p.31-35.

Audebert, F. L., and P. Froidevaux, 2005, Regularization of illumination in angle domains - a key to true amplitude migration: The Leading Edge, 24, 643-654.

Barton C.A., Zoback, M.D., Moos, D., 1995. Fluid-flow along potentially active faults in crystalline rock: geology, 23, 913-916.

Bancroft, J., 2007. A Practical Understanding of Pre/Poststack Migration, Society Of Exploration Geophysicists, pp. 486

Biondi, B., S. Fomel and N. Chemingui, 1998, Azimuth moveout for 3-D prestack imaging: Geophysics, 63, 574-588.

Bona, A., R. Pevzner, 2014, Use of a drill-rig as a source for multichannel analysis of surface waves, GEO Bahrain.

Bourdet, J., Conciadori, M. and Delle-Piane, C., 2015. Palaeo-gas discovery in Pinjarra-1, South Perth basin. AAPG conference, Melbourne, 2015.

Bourne, S. J., Rijkels, l., Stephenson, B. J., Willemse, E. J. M., 2001. Predictive modelling of naturally fractured reservoirs using geomechanics and flow simulation. Geoarabia, 6, 27–42.

Bourne, S. J., Willemse, E. J. M., 2001. Elastic stress control on the pattern of tensile fracturing around a small fault network at Nash Point, UK. Journal of structural geology, 23, 1753–1770.

Bouvier, J.D., Kaars-Sijpesteijn, C.H., Kluesner, D.F., onyejekwe, C.C., Van der Pal, R.C. 1989. Three-dimensional seismic interpretation and fault sealing investigations, Nun river field, Nigeria. AAPG bulletin, 73, 1397–1414.

Bretan, P., Yielding, G., Jones, H., 2003. Using calibrated shale gouge ratio to estimate hydrocarbon column heights. AAPG bulletin, 87, 397–413.

Bretan, P., Yielding, G., Mathiassen, O.M., Thorsnes, T., 2011. Fault-seal analysis for CO_2 storage: an example from the Troll area, Norwegian continental shelf. Petroleum geoscience,. 17 2011, 181–192.

Byerlee, j. D., 1978. Friction of rock. Pure & applied geophysics, 116, 615–626.

Causebrook, R., Dance, T., Bale, K., 2006. Southern Perth basin site investigation and geological model for storage of carbon dioxide. Co2crc report number: rpt06-0162.

Chiaramonte, l., Zoback, M.D., Friedmann, J., Stamp, V., 2008. Seal integrity and feasibility of co2 sequestration in the teapot dome eor pilot: geomechanical site characterization. Environmental geology, 54, 1667–1675.

Childs, C., Manzocchi, T., Walsh, J.J., Bonson C., Nicol, A. and Schopfer, M., 2009. A geometric model of fault zone and fault rock thickness variations. Journal of structural geology 31, 117–127.

Childs, C., Watterson, J., Walsh, J.J. 1997. Complexity in fault zone structure and implications for fault seal prediction. In: Møller-Pedersen, P. & Koestler, A.G. (eds) hydrocarbon seals: importance for exploration and production. Norwegian Petroleum Society (NPF) special publication, Elsevier, Singapore, 7, 61–72.

Ciftci, B.N., Langhi, L., Strand, J., Goldie-Divko, L., Miranda. J., O'Brien, G., 2012. Top seal bypass risk due to fracture systems, nearshore/onshore Gippsland basin. The APPEA journal and conference proceedings, 52, 397-413.

Claerbout, J., and S. Fomel, 2001, Image Estimation by Example: Stanford University.

Cockbain, A.E., 1990. Perth basin, geology and mineral resources of Western Australia, Geological Survey of Western Australia, memoir 3, 495-524.

Crostella, A., Backhouse, J., 2000. Geology and petroleum exploration of the central and southern Perth basin, Western Australia. Geological Survey of Western Australia report 57.

Crouch, S. L., Starfield, S. M., 1983. Boundary element methods in solid mechanics: with applications in rock mechanics and geological engineering. Allen and Unwin, Winchester, MA.

Dee, S. J., Yielding, G., Freeman, B. Healy, D., Kusznir, N. J., Grant, N., Ellis, P., 2007. Elastic dislocation modelling for prediction of small-scale fault and fracture network characteristics. In lonergan, l., Jolly, R. J. H., Rawnsley, K. & Sanderson, D. J. (eds) fractured reservoirs. Geological Society , London, special publications, 270, 139–155.

Delle Piane, C., Olierook, H.K.H., Timms, N.E., Saeedi, A., Esteban, L., Razaee, R., Mikhaltsevitch, V., and Lebedev, M., 2013, Facies-based rock properties distribution along the Harvey 1 stratigraphic well, CSIRO report number ep133710.

Dewhurst, D. N., and R. M. Jones, 2002. Geomechanical, microstructural and petrophysical evolution in experimentally reactivated cataclasites: application to fault seal prediction: AAPG bulletin, v. 86, 1383–1405.

Dewhurst, D.N., Jones, M.R., Hillis, R. R., Mildren, S.D., 2002. Microstructural and geomechanical characterisation of fault rocks from the Carnrvon and Otway basins: Australian Petroleum Production and Exploration Association Journal, 42, 167–186.

dGb, 2012, http://opendtect.org/images/PDF/faultenhancementfilter.pdf

Ferber, R. G., Sanders, B., and Yilmaz, O., 1996, Quick-look 3-D prestack time migration: 66th Ann. Internat. Mtg., Soc. Expl. Geophys., Extended Abstracts, 451-545.

Ferrill, D.A., Winterle, J., Wittmeyer, G., Sims, D., Colton, S., Armstrong, A., Morris, A.P., 1999. Stressed rock strains groundwater at Yucca Mountain Nevada. GSA TODAY, 9, 1–8.

Finkbeiner, T., Zoback, M., Flemings, P. B., Stump, B. B., 2000. Stress, pore pressure, and dynamically constrained hydrocarbon columns in the South Eugene island 330 field, Northern Gulf of Mexico: AAPG bulletin, v. 85, 1007–1031.

Fisher, Q.J., Knipe, R.J., 1998. Fault sealing processes in siliciclastic sediments. In: G. Jones, Fisher, Q.J., Knipe, R.J., (editors), faulting, fault sealing and fluid flow in hydrocarbon reservoirs. Geol. Soc., London, spec. Publ., 147, 117–134.

Fomel, S., 2002, Applications of plane-wave destruction filters: Geophysics, 67, 1946-1960.

Forbriger, T., 2003, Inversion of shallow-seismic wavefields: I. wavefield transformation: Geophysical Journal International, 153, 719–734.

Freeman, B., Yielding, G., Needham, D.T., Badley, M.E., 1998. Fault seal prediction: the gouge ratio method. In: Coward, M.P., Daltaban, T.S. & Johnson, H. (eds) Structural geology in reservoir characterization. Geological Society , London, special publications, 127, 19–25.

Fristad, T., Groth, A., Yielding, G., Freeman, B. 1997. Quantitative fault seal prediction: a case study from Oseberg syd. In: Møller-Pedersen, P. & Koestler, A.G. (eds). Hydrocarbon seals: importance for exploration and production. Norwegian Petroleum Society (NPF) special publication, Elsevier, Singapore, 7, 107–124.

Fulljames, J.R., Zijerveld, L.J.J., Franssen, R.C.M.W., 1997. Fault seal processes: systematic analyses of fault seals over geological and production timescales. In: Møller-Pedersen, P. & Koestler, A.G. (eds) Hydrocarbon seals: importance for exploration and production. Norwegian Petroleum Society (NPF) special publication, Elsevier, Singapore, 7, 51–59.

Gabriels, P., R. Snieder, and G. Nolet, 1987, In situ measurements of shear-wave velocity in sediments with higher- mode Rayleigh waves: Geophysical Prospecting, 35, 187– 196.

Gartrell, A. P., lisk, M., 2005. Potential new method for paleostress estimation by combining 3d fault restoration and fault slip inversion techniques: first test on the Skua field, Timor Sea, in P. Boult and J. K. Kaldi, eds., Evaluating fault and cap rock seals: AAPG hedberg series 2, 23–36.

Geokinetics (Australasia) Pty Ltd, 2014, 2013 Harvey-Waroona 3D Seismic Survey, Final report, 136 p.

Gibson, R.G., 1994. Fault-zone seals in siliciclastic strata of the Columbus basin, offshore Trinidad. Bull. Am. Assoc. Pet. Geol., 78: 1372–1385.

Grasso, J. R., 1992. Mechanics of seismic instabilities induced the recovery of hydrocarbons. Pure & Applied Geophysics, 139, 507–534.

Iasky, R. P., 1993. A structural study of the southern Perth basin, Western Australia: Western Australia Geological Survey report 31, 1993, 56p.

Iasky, R. P., Lockwood, A. M., 2004. Gravity and magnetic interpretation of the Southern Perth basin, Western Australia. Western Australia Geological Survey, record 2004/8, 32p.

Jaeger, J. C., Cook, N. G. W., 1979. Fundamentals of rock mechanics. Chapman & Hall, New York, 76p.

Jennings, J.B., 1987. Capillary pressure techniques: application to exploration and development geology. AAPG bulletin, 71, 1196–1209.

Jev, B.I., Kaars-Sijpesteijn, C.H., Peters, M.P.A.M., Watts, N.L., Wilkie, J.T. 1993. Akaso field, Nigeria: use of integrated 3D seismic, fault slicing, clay smearing, and RFT pressure data on fault trapping and dynamic leakage. AAPG bulletin, 77, 1389–1404.

Jones, R. M., D. N., Dewhurst, R. R. Hillis, S. D. Mildren, 2002. Geomechanical fault characterization: impact on quantitative fault seal risking. Society of Petroleum Engineers/International Society for Rock Mechanics, Rockmechanics conference, Irving, Texas, October 2002: SPE paper 78213.

Kaluza, M. J., Doyle, E. H., 1996. Detecting fluid migration in shallow sediments, continental slope environment, Gulf of Mexico: AAPG memoir 66, 15–26.

Kangan F., 1995, Prestack Kirchhoff migration: CREWES Research Report – Volume 7, 31.

Knipe R. J., Fisher, Q. J., Jones, M. R., Clennell, M. B., Farmer, A., Harrison, B., Kidd, E., McAlister, E., Porter, J. R., White, E. A., 1997. Fault seal analysis: successful methodologies, application and future directions, in P. Moeller-Pedersen, and A.G. Koestler, eds., Hydrocarbon seals: importance for exploration and production: Norwegian Petroleum Society special publications 7, 15-40.

Knipe, R. J., 1992. Faulting process and fault seal, in R. M. Larson, H. Breke, B. T. Larsen, and E. Talleraas, eds., Structural and tectonic modelling and its application to petroleum geology: Norwegian Petroleum Society special publication 1, Stavanger, p. 325– 342.

Knipe, R.J., Jones, G., Fisher, q.j. 1998. Faulting, fault sealing and fluid flow in hydrocarbon reservoirs: an introduction. In: Jones, G., Fisher, Q.J. & Knipe, R.J. (eds) Faulting, fault sealing and fluid flow in hydrocarbon reservoirs. Geological Society , London, special publications, 147, vii–xxi.

Krey, T., 1952. The significance of diffraction in the investigation of faults. Geophysics, 17(4): 843-858.

Landa, E. and Keydar, S., 1998. Seismic monitoring of diffraction images for detection of local heterogeneities. Geophysics, 63(3): 1093-1100.

Langhi, L., Ciftci, B., Strand, J., 2013. Fault seal first-order analysis – SW Hub. CSIRO report EP13879, pp. 50. http://www.anlecrd.com.au/announcements/media-release-research-project-drills-down-for-results

Langhi, L., Zhang, Y., Gartrell, A., Underschultz, J.R., Dewhurst, D.N., 2010. Evaluating hydrocarbon trap integrity during fault reactivation using geomechanical 3D modelling: an example from the Timor Sea, Australia. AAPG bulletin 94, 567-591.

Le Blanc Smith, g., 1993. Geology and Permian coal resources of the Collie basin, Western Australia. Western Australia Geological Survey, report 38, 86p.

Ligtenberg, J. H., 2005. Detection of fluid migration pathways in seismic data: implications for fault seal analysis. Basin research 17, 141–153.

Lisle, R.J., Srivastava, D.C., 2004. Test of the frictional reactivation theory for faults and validity of fault-slip analysis. Geology 32 (7), 569–572.

Liu, Y. and S. Fomel, 2011, Seismic data interpolation beyond aliasing using regularized nonstationary autoregression: Geophysics, 76, V69-V77.

Luo, Y., J. Xia, J. Liu, Y. Xu, and Q. Liu, 2007, Research on dispersion curves of MASW, in Research on Dispersion Curves of MASW: SEG, 1379–1387.

Maerten, l., Gillespie, P., Pollard, D. D., 2002. Effects of local stress perturbation on secondary fault development. Journal of structural geology, 24, 145–153.

Mayne, W. H., 1962, Common reflection point horizontal data stacking techniques: Geophysics,

McMechan, G., and M. Yedlin, 1981, Analysis of dispersive waves by wave field transformation: Geophysics, 46, 869–874.

Mildren, S.D., Hillis, R.R., Dewhurst, D.N., Lyon, P.J., Meyer, J.J., Boult, P.J., 2005. Fast: a new technique for geomechanical assessment of the risk of reactivation-related breach of fault seals. In: Boult, P. & Kaldi, J. (eds) Evaluating fault and cap rock seals. AAPG hedberg series, 2, 73–85.

Miller, R., J. Xia, C. B. Park, and J. Ivanov, 2008, The history of MASW: The Leading Edge, 4.

Moeck, I., Grzegorz, K., Zimmermann, G., 2009. Slip tendency analysis, fault reactivation potential and induced seismicity in a deep geothermal reservoir. Journal of structural geology 31, 1174–1182.

Morris, A., Ferrill, D.A., Henderson, D.B., 1996. Slip tendency analysis and fault reactivation. Geology 24 (3), 275–278.

Mory, A. J., Iasky, r. P., 1996. Stratigraphy and structure of the onshore northern Perth basin, Western Australia. Western Australia Geological Survey, report 46, 101p.

Muir-Wood, R., King G.C.P., 1993. Hydrological signatures of earthquake strain: Journal of structural geophysical research-solid Earth, 98, 22035-22068.

Nicholson, C.J., Borissova, I., Krassay, A.A., Boreham, C.J., Monteil, E., Neumann, V., di Primio, R., Bradshaw, B.E., 2008. New exploration opportunities in the Southern Vlaming sub-basin. The APPEA journal and conference proceedings, 48, 371-380.

O'Brien, G. W., Lisk, M., Duddy, I. R., Hamilton, J., Woods, P., Cowley, R., 1999. Plate convergence, foreland development and fault reactivation, primary controls on brine migration, thermal histories and trap breach in the Timor Sea, Australia. Marine and Petroleum Geology, 16, 6, 533–560

Okada, y., 1985. Surface deformation due to shear and tensile faults in a half-space. Bulletin of the Seismological Society of America, 75, 1135–1154.

Okada, y., 1992. Internal deformation due to shear and tensile faults in a half-space. Bulletin of the Seismological Society of America, 82, 1018–1040.

Park, C. B., and N. Ryden, 2007b, Offset selective dispersion imaging: Symposium on the Application of Geophysics to Engineering and Environmental Problems 2007, SEG, 910–915.

Park, C., and N. Ryden, 2007a, Historical overview of the surface wave method: Symposium on the Application of Geophysics to Engineering and Environmental Problems, 897– 909.

Park, C., R. Miller, and J. Xia, 1999, Multichannel analysis of surface waves: Geophysics, 64, 800–808.

Pevzner, R., Lumley, D., Urosevic, M., Gurevich, B., Bóna, A., Alajmi, M.A., Shragge, J., Pervukhina, M., Mueller, T., Shulakova, V., 2013. Advanced geophysical data analysis at Harvey-1: storage site characterization and stability assessment. ANLEC R&D project number 7-1111-0198.

Revil, A., Cathles iii, l. M., 2002. Fluid transport by solitary waves along growing faults. A field example from the South Eugene Island basin, Gulf of Mexico. Epsl 202, 321-335.

Rutqvist, J., Birkholzer, J., Cappa, F., Tsang, C.F., 2007. Estimating maximum sustainable injection pressure during geological sequestration of CO_2 using coupled fluid flow and geomechanical fault-slip analysis. Energy conversion and management, 48, 1798–1807.

Sanderson, D. J., and X. Zhang, 1999. Critical stress localization of flow associated with deformation of well-fractured rock masses, with implications for mineral deposits: Geological Society (London) special publication 155, 69–81.

Secor, D.T., 1965. Role of fluid pressure in jointing. Am J. Sci 263, 633-646.

Secor, D.T., 1969. Mechanics of natural extension fracturing at depth in the earth's crust. Pap. Geol., Surv. Can., 68-52, 3-48.

Sibson, R. H., 1996. Structural permeability of fluid-driven fault-fracture meshes. Journal of structural geology 18, 1031–1042.

Sibson, R.H. 1987. Earthquake rupturing as a hydrothermal mineralizing agent. Geology 15, 701-704.

Smith, D. A., 1966. Theoretical considerations of sealing and nonsealing faults: AAPG bulletin 50, 363-374.

Sorkhabi, R., Tsuji, Y., 2005. The place of faults in petroleum traps, in R. Sorkhabi and Y. Tsuji, eds., Faults, fluid flow and petroleum traps: AAPG memoir 85, 1-31.

Stolk, C., M. de Hoop, and T. O. Root, 2009, Linearized inverse scattering based on seismic reverse-time migration: Proceedings of the Project Review, Geo-Mathematical Imaging Group, 91108.

Streit, J.E. and Hillis, R.R. 2004. Estimating fault stability and sustainable fluid pressures for underground storage of co2 in porous rock. Energy, 29, 1445–1456.

Taner, M.T. and Koehler, F., 1969. Velocity spectra-digital computer derivation applications of velocity functions. Geophysics, 34(6): 859-881.

Tertyshnikov, K., Pevzner, R., Bona, A., Alonaizi, F., & Gurevich, B. (2013, June). Steering migration with diffractions in seismic exploration for hard rock environments. In 75th EAGE Conference & Exhibition incorporating SPE EUROPEC 2013.

Trorey, A., 1970. A simple theory for seismic diffractions. Geophysics, 35(5): 762-784.

Underschultz, J., 2007. Hydrodynamics and membrane seal capacity: Geofluids, 7, 148-158.

Urosevic, M., Ziramov, S., Pevzner, R., 2015, Acquisition of the Nested 3D seismic survey at Harvey. ANLEC R&D Project 7-1213-0224 Final report, Curtin University, 36 pp.

Van Ruth, P J. 2006. Geomechanics: Vlaming Sub-basin, Western Australia. CO2CRC Report number RPT06-0043.

Watts, N.L. 1987. Theoretical aspects of cap-rock and fault seals for singleand two phase hydrocarbon columns. Marine and petroleum geology, 4, 274–307.

Whitmore, N., and S. Crawley, 2012, Applications of RTM inverse scattering imaging conditions: Expanded Abstracts 31, Society of Exploration Geophysicists, 779-784.

Wilkes, P., Timms, N., Horowitz, F., Corbel, S., 2011. A new structural interpretation of the Perth basin and the Perth metropolitan area using gravity and aeromagnetic data, geomorphology and geology. Western Australia Geothermal Centre of Excellence report no ep117411, 65p.

Wilkins S. J., Naruk S. J., 2007, Quantitative analysis of slip-induced dilation with application to fault seal. AAPG bulletin, v. 91, 97–113.

Wiprut, D., Zoback, M.D., 2000. Fault reactivation and fluid flow along a previously dormant normal fault in the northern North Sea. Geology, 28, 595-598.

Yielding, G. 2002. Shale gouge ratio – calibration by geohistory. In: Koestler, A.G. & Hunsdale, R. (eds) Hydrocarbon seal quantification Norwegian Petroleum Society (NPF) special publication, Elsevier, Amsterdam, 11, 1–15.

Yielding, G., Freeman, B., Needham, T., 1997. Quantitative fault seal prediction. AAPG bulletin, 81, 897–917.

Yilmaz, O. 1987. Seismic data processing / Ozdogan Yilmaz. Tulsa, OK : Society of Exploration Geophysicists.

Zoback, M. (ed.) 2007. Reservoir geomechanics, Cambridge University Press, 448 p.

Zoback, M. D., Townend, J., 2001. Implications of hydrostatic pore pressures and high crustal strength for the deformation of intraplate lithosphere. Tectonophysics, 336, 19–30.